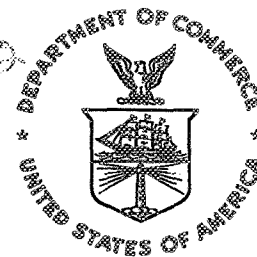# NOAA Technical Report NESDIS 58

Evaluating the Design of Satellite Scanning Radiometers for Earth Radiation Budget Measurements with System Simulations

Part I: Instantaneous Estimates

Washington, D.C.
October 1991

U.S. DEPARTMENT OF COMMERCE
National Oceanic and Atmospheric Administration
National Environmental Satellite, Data, and Information Service

NOAA TECHNICAL REPORTS

## National Environmental Satellite, Data, and Information Service

The National Environmental Satellite, Data, and Information Service (NESDIS) manages the Nation's civil Earth-observing satellite systems, as well as global national data bases for meteorology, oceanography, geophysics, and solar-terrestrial sciences. From these sources, it develops and disseminates environmental data and information products critical to the protection of life and property, national defence, the national economy, energy development and distribution, global food supplies, and the development of natural resources.

Publication in the NOAA Technical Report series does not preclude later publication in scientific journals in expanded or modified form. The NESDIS series of NOAA Technical Reports is a continuation of the former NESS and EDIS series of NOAA Technical Reports and the NESC and EDS series of Environmental Science Servives Administration (ESSA) Technical Reports.

NESDIS 5   A Statistical Technique for Forecasting Severe Weather from Vertical Soundings by Satellite and Radio-sonde. David L. Keller and William L. Smith, June 1983 (PB84 114099)

NESDIS 6   Spatial and Temporal Distribution of Northern Hemisphere Snow Cover. Burt J. Morse and Chester F. Ropelewski (NWS), October 1983. (PB84 118348)

NESDIS 7   Fire Detection Using the NOAA--Series Satellites. Michael Matson, Stanley R. Schneider, Billie Aldridge and Barry Satchwell (NWS), January 1984. (PB84 176890)

NESDIS 8   Monitoring of Long Waves in the Eastern Equatorial Pacific 1981-83 Using Satellite Multi-Channel Sea Surface Temperature Charts. Richard Legeckis and William Pichel, April 1984. (PB84 190487)

NESDIS 9   The NESDIS-SEL Lear Aircraft Instruments and Data Recording System. Gilbert R. Smith, Kenneth O. Hayes, John S. Knoll and Robert S. Koyanagi, June 1984. (PB84 219674)

NESDIS 10 Atlas of Reflectance Patterns for Uniform Earth and Cloud Surfaces (NIMBUS-7 ERB--61 Days). V. R. Taylor and L. L. Stowe, July 1984. (PB85 12440)

NESDIS 11 Tropical Cyclone Intensity Analysis Using Satellite Data. Vern F. Dvorak, September 1984. (PB85 112951)

NESDIS 12 Utilization of the Polar Platform of NASA's Space Station Program for Operational Earth Observations. John H. McElroy and Stanley R. Schneider, September 1984. (PB85 1525027/AS)

NESDIS 13 Summary and Analyses of the NOAA N-ROSS/ERS-1 Environmental Data Development Activity. John W. Sherman III, February 1985. (PB85 222743/A3)

NESDIS 14 NOAA N-ROSS/ERS-1 Environmental Data Development (NNEEDD) Activity. John W. Sherman III, February 1985. (PB86 139284/AS)

NESDIS 15 NOAA N-ROSS/ERS-1 Environmental Data Development (NNEEDD) Products and Services. Franklin E. Kniskern, February 1985. (PB86 213527/AS)

NESDIS 16 Temporal and Spatial Analyses of Civil Marine Satellite Requirements. Nancy J. Hooper and John W. Sherman III, February 1985 (PB86 212123/AS)

NESDIS 18 Earth Observations and the Polar Platform. John H. McElroy and Stanley R. Schneider, January 1985. (PB85 177624/AS)

NESDIS 19 The Space Station Polar Platform: Intergrating Research and Operational Missions. John H. McElroy and Stanley R. Schneider, January 1985. (PB85 195279/AS)

NESDIS 20 An Atlas of High Altitude Aircraft Measured Radiance of White Sands, New Mexico, in the 450-1050 nm Band. Gilbert R. Smith, Robert H. Levin and John S. Knoll, April 1985. (PB85 204501/AS)

NESDIS 21 High Altitude Measured Radiance of White Sands, New Mexico, in the 400-2000nm Band Using a Filter Wedge Spectrometer. Gilbert R. Smith and Robert H. Levin, April 1985. (PB85 206084/AS)

NESDIS 22 The Space Station Polar Platform: NOAA Systems Considerations and Requirements. John H. McElroy and Stanley R. Schneider, June 1985. (PB86 6109246/AS)

NESDIS 23 The Use of TOMS Data in Evaluating and Improving the Total Ozone from TOVS Measurements. James H. Lienesch and Prabhat K. K. Pandey, July 1985. (PB86 108412/AS)

NESDIS 24 Satellite-Derived Moisture Profiles. Andrew Timchalk, April 1986. (PB86 232923/AS)

NOAA Technical Report NESDIS 58
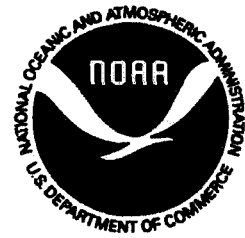
Evaluating the Design of Satellite Scanning Radiometers for Earth Radiation Budget Measurements with System Simulations

Part I: Instantaneous Estimates

Larry Stowe
Office of Research and Applications
Satellite Research Laboratory

Philip Ardanuy and Richard Hucek
Research and Data Systems Corporation
Greenbelt, MD 20770

Peter Abel
Standards and Calibration Office
NASA/GSFC Code 920.1
Greenbelt, MD 20771

Herbert Jacobowitz
Offfice of Research and Applications
Satellite Research Laboratory

Washington, D.C.
October 1991

TABLE OF CONTENTS

ACKNOWLEDGEMENTS

EXECUTIVE SUMMARY

A set of system simulations has been performed to evaluate candidate scanner configurations to fly as a part of the Earth Radiation Budget Instrument (ERBI) on the polar platforms during the 1990's (NOAA, 1988). The simulations begin with International Satellite Cloud Climatology Project (ISCCP) B-1 GOES-5 radiances for northern hemisphere summer and winter (Rossow et al., 1985). These radiances are navigated to the Earth's surface and located on a 0.1° latitude/longitude resolution grid at the top of the atmosphere (TOA). Having Earth-located the GOES observations, the counts are next calibrated into shortwave and longwave radiances, and then converted into broadband estimates using narrow-to-broadband models. Fluxes are obtained by invoking the Earth Radiation Budget Experiment (ERBE) anisotropic angular dependence models (ADM's) (Suttles et al., 1988; Suttles et al., 1989) after first determining the amount of cloud present through the use of the Maximum Likelihood Estimation (MLE) scene identification algorithm (Wielicki and Green, 1989). Orbits of the polar platform are then propagated across the domain with each of the proposed ERBI designs operated in scanning mode. The scanner field-of-view (FOV) footprints are located on the Earth, and simulated satellite measurements generated by use of the ISCCP-derived fluxes. After reduction to the TOA, the measurements contain errors induced by the spatial and angular sampling patterns, FOV size, and angular model use, which can be studied through comparisons to the reference flux fields.

In Part I of this study, we consider the simulation of instantaneous sampling (without diurnal averaging) of the longwave and shortwave fluxes at the TOA. After measurement and subsequent inversion to the TOA, the measured fluxes were compared to the reference fluxes for 2.5° latitude/longitude resolution targets. The reference fluxes at this resolution are obtained by integrating over the 25 x 25 = 625 grid elements in each target. The differences between each of these two resultant spatially averaged sets of target measurements (errors) are taken and then statistically summarized. Five different instruments are considered: (1) the Conically Scanning Radiometer (CSR); (2) the ERBE Cross-Track Scanner (ERBE); (3) the Nimbus-7 Biaxial Scanner (Nimbus-7); (4) the Clouds and Earth's Radiant Energy System-Instrument (CERES-I); and (5) the Active Cavity Array (ACA).

The two primary sources of error encountered in the simulation of measurements of radiation budget parameters from satellites are the nonuniform sampling of the TOA radiance field by the radiometer scanning design, and the use of incorrect ADM's in the inversion of the satellite altitude observations to TOA flux estimates. In the limit where the ADM errors vanish (due to the assumption of correctly specified ADM's), the accuracy of each candidate scanner design is determined by the instrument's ability to map out the TOA radiance field in a uniform manner. In this regard cross-track scanners (ERBE and CERES-I) do best. It may be possible, nevertheless, to improve their minimum error limit through attention to the design of the scanning pattern and to processing techniques which eliminate overlapping or widely scattered observations within a 2.5° target area. As errors in the ADM's are encountered, the total error exceeds the minimum spatial sampling-only error. These additional errors are due to the fact that only a finite number of mean ADM's for broad scene categories may be used while, in fact, each scene realization is composed of a unique ADM. By introducing systematic and random (at 10-km resolution) departures in the anisotropic component of the upwelling reference radiances from the mean ERBE models, biaxial scanning radiometers (CERES, CSR and ACA) are shown to be significantly less sensitive to ADM errors than a simple cross-track instrument (i.e., ERBE). This occurs through the cancellation of opposing ADM errors made at different viewing angles. Under conditions of large ADM variability (i.e., when large ratios, N, in the anisotropic component of the reference models to the ERBE models are present), they will yield the least errors in retrieved TOA fluxes. Our results show, however, that cross-track scanners are likely to outperform biaxial or conical scanners, for Earth radiation budget measurements, providing that realistic anisotropy scale factors for the atmosphere (N) do not exceed the range between 0.7 and 1.3 (error $\leq$ 30%).

A key issue that must be considered in interpreting the simulation results is the amount of systematic ADM variability (departures from the mean models) that is present at the 2.5° resolution of the ERBE target areas. Indications of the error magnitudes can be obtained from the ERBE models themselves by imposing systematic misclassifications of cloud amount by one cloud category (e.g., clear vs. partly cloudy, partly cloudy vs. mostly cloudy, etc.). We performed this exercise for both overestimation and underestimation of the cloud amount and found that systematic, long-term errors in the amount of anisotropy are likely to be less than 40%. Separate error analyses using ERBE scanner data (Barkstrom et al., 1989) are consistent with ADM errors of about 30%. Random components of the resultant ADM error (over small spatial or temporal scales) cancel quickly and are unimportant. If systematic ADM errors are indeed about 30%, then the CERES-I, ERBE and CSR, in order of increasing error, provide the most accurate instantaneous flux estimates, within 2 to 3 W/m² of each other in reflected shortwave flux. The magnitude of this error is near the 10 W/m² accuracy requirement of the user community (NOAA, 1988). However, because of a shortwave calibration error that underestimated the reference flux by about 20%, the instrument errors reported here also are underestimates (by about 20%) of the true errors produced when these scanners are flown over fields of more realistic shortwave radiation. Nevertheless, the relative accuracies of the radiometer estimates can still be examined and used to guide recommendations for improved instrument design configurations. In view of the fact that the error estimates provided in this report are too low, it appears necessary that the instrument scan and FOV designs and/or the data processing system require modifications in order to be able to satisfy the user requirement. The specific objective should be aimed at reducing spatial sampling error which, for all but the greatest perturbations in anisotropic reflectance, dominates ADM error. Longwave flux errors have been found to have the same space and time characteristics as errors in shortwave radiation, but only about 25% as large. These errors should be considered representative of the true values to be obtained for longwave radiation because, except for occasional scene identification errors, the longwave reference fields used were not affected by the shortwave calibration.

1. INTRODUCTION

1.1 THE NEED FOR AN EARTH RADIATION BUDGET INSTRUMENT (ERBI)

The exchange of radiative energy between the Sun, Earth, and space affects the Earth's climate and also is affected by the Earth's climate. Theoretical models indicate that increases in man-made greenhouse gases, such as carbon dioxide, over decadal and longer time scales, perturbs the equilibrium between the two components of the Earth's Radiation Budget (ERB): 1) the heat Earth absorbs from the Sun and 2) the heat Earth emits to space. This leads to changes in the global climate. For example, the 1983 report of the National Research Council entitled "Changing Climate" (NRC, 1983), indicated that a doubling of carbon dioxide concentration was likely in the next hundred years. This would cause the Earth to emit less heat than it absorbs which would subsequently increase the globally averaged surface air temperature by between 1.5 and 4.5°C. This change would occur as a result of a small imbalance between the two ERB components of less than 1 W/m^2, globally averaged. However, these same models indicate that each component would be changed by up to 4 W/m^2, globally averaged, with regional changes varying from about 20 W/m^2 in the tropics to as large as 100 W/m^2 for absorbed solar radiation at the poles. These large regional changes would be due to the effects of climate feedback on the ERB components, caused primarily by increased water vapor and decreased surface snow and ice cover at the poles, both the result of the warmer climate. Thus, with a long, uninterrupted time record of stable ERB measurements, it would be possible to detect climate change associated with increases in trace gas concentrations.

However, the predictions of climate change from computerized models of the climate system have large uncertainties, caused to a great extent by the lack of a complete understanding of the complex, non-linear interactions of all the physical processes involved. The potential impact that these predictions may have on society (for example, by forcing restriction or elimination of certain industrial activities) is severe. Because of this, and to overcome our lack of understanding of the underlying science, it is of crucial importance to measure accurately, on regional and global scales, and continuously in time, the fundamental physical quantities related to the Earth's climate. Only with such a measurement program shall we be able to monitor, understand, and predict the response of the Earth's climate to human activities with the confidence necessary to formulate wise environmental policy. The measurement of the components of the Earth's radiation budget are necessary to such a program.

1.1.1 Timeliness of ERBI

Regional and global measurements of ERB have been collected since the advent of satellites. NASA led the experimental development of instruments specifically designed to measure the total power/flux of the radiation from the Sun and Earth with so-called "broadband" instruments. NOAA has utilized operational satellite instruments which measure in a few selected intervals of the total spectrum, so-called "narrowband" instruments, to estimate the ERB components. These measurements have been considered inadequate by the climate community for measuring the Earth's radiation budget to the accuracies needed for the climate change problem. However, they are useful for filling gaps between measurements with broadband instruments and they are valuable for qualitative studies.

The most recent in the series of NASA experiments with broadband instruments, the Earth Radiation Budget Experiment (ERBE), will end with the deactivation of the NOAA-9 and -10 operational satellites in the next few years. A two-scanner system (CERES) has recently been funded by NASA for the Earth Observing System (EOS) of the late 1990's. There is also a Franco-Soviet program (ScaRaB) to measure broadband ERB components in 1992 with a scanning instrument. Currently, the climate community is left with, at best, a fifteen-year record of relatively homogeneous, low spatial resolution (2000 km)^2, broadband measurements that started with the ERB experiment on the Nimbus-6 satellite in 1975. After

ERBE, only narrowband instruments are sure to be available to extend these measurements into the future.

1.1.2 Applications of ERBI

ERB measurements constitute a key component of the set of radiative measurements that are needed to monitor the current state and variability of the climate system and to help detect and interpret anticipated changes in global and regional climate.

Numerical models of the atmosphere may be classified as short-range, medium-range, monthly, seasonal, and climatological, based on the implied length of the prediction. Within the last decade a number of weather centers have started making medium-range numerical weather prediction (NWP) forecasts to ten days routinely once per day. Increased use of satellite data offers the possibility of further improvement of initial data for NWP. Increased use of satellite data in the validation system for NWP models is essential for the improvement of model physical parameterizations (Krishnamurti, 1988).

The paucity of high spatial resolution $(250 \text{ km})^2$, broadband data sets for past years and the possible lack of such data for future years are of grave concern to the international meteorological and climatological scientific communities and organizations.

1.2 NOAA WORKSHOP (ERBRR-1987) SUMMARY AND RECOMMENDATIONS

The National Environmental Satellite, Data, and Information Service (NESDIS) of the National Oceanic and Atmospheric Administration (NOAA) hopes to eventually include an ERBI in its operational payload. To initiate planning for ERBI, NOAA organized an international workshop entitled "The Earth Radiation Budget Requirements Review-1987" (NOAA, 1988). The international importance of this problem is evident from the list of co-sponsors: the Radiation Commission of the International Association of Meteorology and Atmospheric Physics (IAMAP); the Commission on Space Research (COSPAR); the Joint Scientific Committee (JSC) for the World Climate Research Program; and the National Aeronautics and Space Administration.

From the workshop, a review of user requirements identified the following specifications for Earth radiation budget measurements at the top of the atmosphere (TOA) which are of particular interest for the current study:

    a.   Flux of broadband reflected solar and emitted thermal radiation for both average-cloudy and clear-sky conditions.

    b.   Spatial Resolution: 100 to 250 km.

    c.   Time Resolution: 3 hourly to daily.

    d.   Monthly and globally averaged fluxes should be accurate to 1 W/m^2 or better.

    e.   Regionally averaged fluxes should be accurate to between 2 and 10 W/m^2, depending on averaging time.

In order to test whether the ERBE instrument and data processing system meet the current user requirements and to evaluate alternative sampling and processing schemes, recommendations were made for the development of computer code to simulate the Earth's radiation, orbital and instrument design

configurations, and data reduction methods. Among the applications of the system simulation code would be its use to:

a.   Estimate error budgets for the current ERBE scanner and data retrieval systems;

b.   Guide decisions on design options to the basic ERBE scanner and flux retrieval algorithms;

c.   Evaluate satellite measurement errors using improved angular radiation models, alternate radiance-to-flux conversion schemes, ERB data from two or more polar satellites, an optimal design for the scanning instrument, higher spatial resolution target areas, parameterized models of diurnal processes, and geostationary data as a surrogate for ERB measurements missing from the diurnal cycle.

1.3 RESPONSE TO RECOMMENDATIONS OF NOAA WORKSHOP

1.3.1 Strategy of the Present Study

In response to the above user requirements and recommendations from this workshop, a complete computer system simulation of the ERB measurement process has been developed and applied. The system simulation was initially used to evaluate candidate scanner designs for the ERBI being considered by NASA for its system of polar platforms for the 1990's. It has also been used to study the other important issues identified above. These studies will be presented in subsequent reports.

Five candidate scanner configurations were simulated and evaluated by comparing their bias and regional RMS flux errors for atmospheric patterns of emission and reflectance which differ from the ERBE mean models used during TOA inversion. The different instruments considered are: (1) the Conically Scanning Radiometer (CSR); (2) the ERBE Cross-Track Scanner (ERBE); (3) the Nimbus-7 Biaxial Scanner (Nimbus-7); (4) the Clouds and Earth's Radiant Energy System-Instrument (CERES-I); and (5) the Active Cavity Array (ACA). Sampling rates and a short description of these candidates are depicted in Table 1.

When the study was initiated, it was believed that operational NOAA payloads would fly alongside NASA research instruments on the NASA Polar Orbiting Platform (NPOP), planned for launch by a Titan-IV booster from Vandenberg AFB in late 1996. This platform was intended for a sun-synchronous, 1:30 PM ascending-node, 824 km orbit. Due to various reasons, including the developmental nature of the platform, platform servicing uncertainties, and limited platform resources, NOAA has withdrawn its operational instruments from NPOP. NOAA is now planning to continue its independent program of polar orbiting spacecraft, now being termed "free-flyers". NOAA-N will be flown as an interim spacecraft prior to the launch of NPOP. The new series of afternoon free-flyers (NOAA-O, -P, and -Q) will fly at the same time as NPOP; both the free-flyers and the NASA polar platforms will use a set of common interfaces. These interfaces will facilitate the evolution of instruments from research/prototype operational (on NPOP) to fully operational (on free-flyers). NOAA will fly its operational instruments on the European Space Agency's Polar Platform (EPOP), which will be in an 824-km orbit, with a 10:00 AM descending-node.

Of the five candidate scanners simulated to take radiation budget measurements, one has now been formally selected by NASA to fly on NPOP (CERES-I) on EOS-A. Earlier published results from this simulation (Stowe et al., 1989) were used by NASA in making this decision. The original 824-km altitude for NPOP was specified based on operational NOAA requirements to view the entire Earth every

day with critical NOAA instruments. With the NOAA operational instruments on free-flyers, the new altitude for the NPOP is 705 km, same as Landsat, still with ascending-node at 1:30 PM.

Table 1. Summary Description of Five Prototype Scanners					
Radiometer	Scan Type	On-Earth Sampling Rate (sec⁻¹)[a]	FOV Type	Footprint Size (Equivalent Circular Diameter at Nadir, km)	Scan Period (sec)
ACA	Fixed array of multiple zenith/azimuth angles	90	Variable	150	3[b]
CERES-I	Two scanners: one cross-track and one azimuth-slew	50	Fixed	40	3
CSR	Conical scan at multiple zenith angles	35	Fixed	50	17
ERBE	Cross-track	14	Fixed	52	4
Nimbus-7	Biaxial	7	Variable	80	224

[a]Number of Earth samples per scan cycle divided by time of scan cycle.
[b]Sampling repeat cycle.

1.3.2 Goals and Objectives of the System Simulation

A computer system simulation of the measurement and retrieval procedure used in obtaining geophysical parameters from the ERBI observations permits the consideration of a wide range of effects. Each of these factors, some of which are listed below, are capable of impacting and degrading the original nature of the measurement and estimation process that retrieves the desired parameter from the six-dimensional (latitude, longitude, relative solar azimuth angle, satellite zenith angle, solar zenith angle, and time) incident radiance field emerging from the top of the atmosphere. The six general types of effects that may be simulated include: signal mixing between adjacent pixels/detectors (for certain types of instruments), spatial sampling (and navigation accuracy), angular sampling, temporal sampling, atmospheric effects, and instrument effects. Here, we will ignore signal mixing between pixels, detectors, and other instrument effects, as these are not usually related to the physical design of the instruments, or the spatial scales being considered. Instead, this system simulation concentrates on replicating the three effects that the authors believe most strongly impact the accuracy of past, present, and future measurements of the Earth's radiation budget: spatial sampling, angular sampling, and temporal sampling. Atmospheric properties such as cloud amount and height, total column ozone, aerosol size and density distributions, and the vertical profiles of temperature and humidity enter the simulation implicitly in that their effects are present in the GOES radiances used to derive TOA reference fields. Because they are not measured (except for ERBE cloud amount category), however, variations in the values of these quantities are considered only in the sense that they contribute to the variety of atmospheric angular radiance patterns that arise at the TOA. Their collective effects are introduced through the generation of angular dependence models (ADMs) that are normalized perturbations of the ERBE models. The perturbations

may be stratified by ERBE scene category, but variations within scenes, except randomly, and stratification by other measured quantities are presently not possible. In this study only simultaneous and equal perturbations to the ERBE scene ADMs are applied. Table 2 identifies the set of system properties that may be explicitly varied in this simulation.

In Phase I we consider the simulation of instantaneous sampling (without diurnal averaging) of the longwave and shortwave fluxes at the TOA. After measurement and subsequent inversion to the TOA, the observed fluxes are compared to the reference fluxes at a 2.5° (target area) resolution. We reject any of the target areas if they are sampled at the outer edge of the orbital scan swaths. This step is motivated by the recognition that, during measurements over many orbits, adjacent orbits will generally overlap. The differences between each of the resultant spatially averaged sets of measurements can be taken and then statistically summarized.

The days considered were July 15, 17, 18, 19, 20, and 21, 1983 and January 25-30, 1984. Images at 15Z, 18Z, and 21Z were used, though only the results of the 15Z and 21Z simulations are presented here, as they best represent morning and afternoon conditions in the GOES images.

Table 2. System properties that may be considered in a complete simulation.	
System Properties	Explicitly Included in this Simulation
SPATIAL SAMPLING AND NAVIGATION ACCURACY	
Scan pattern and IFOV distribution	Yes
Geometric effects due to topography or cloud altitude	No
Ignorance of true spacecraft position and attitude	No
ANGULAR SAMPLING	
Bidirectional reflectance distribution (BRD) uncertainties	Yes
Systematic BRD uncertainties	Yes
Random BRD uncertainties	Yes
Ignorance of precise scene type being viewed	Yes
Dependence of BRD function on sea and vegetation state	No
Dependence of BRD function on cloud amount	Yes
TEMPORAL SAMPLING	
Tape recorder systematic regional data losses	No
Downlink systematic regional data losses	No
Mode of operation systematic regional data losses	No
Conflicts in priorities	No
Random data losses	No
Bit error rate of downlink	No
Biased sampling of diurnal cycle	Yes
Product accuracy over weekly and monthly intervals	Yes
ATMOSPHERIC EFFECTS	
Ozone distribution in space and time	No
Aerosol distribution, particle size, and type	No
Total column precipitable vapor distribution	No
Cloud (liquid water or ice) distribution and properties	No
Vertical profiles of temperature and water vapor	No
Tradeoffs in sophistication of radiative transfer model	No
Other trace gas effects	No
SIGNAL MIX BETWEEN ADJACENT PIXELS/DETECTORS	
Atmospheric Scattering	No
Detector crosstalk	No
Detector point-spread function	No
Internal optical scattering and diffraction	No
OTHER INSTRUMENT EFFECTS	
Polarization sensitivity	No
Thermal transients	No
Noise-equivalent power and delta-T	No
A/D conversion and dynamic range of signal	No
Electronic crosstalk	No
Effects from and drifts in spectral band pass of filters	No
Total sensitivity drifts due to outgassing and solar UV	No
Interference from other instruments	No

2. TECHNICAL APPROACH

2.1 EARTH SIMULATION

2.1.1 Simulation Domain and Resolution

A geographic area, extending from 15° south to 45° north latitude and from 50° west to 120° west longitude, was chosen as a study site for the system simulation (Figure 1a). The area is shown in Figure 1b subdivided into 672 2.5° (in latitude and longitude) ERBE-size target areas. When combined with a 2° buffer on all sides, this domain occupies over 10% of the globe and is termed the M1 test site. It was further subdivided, to a scale of 0.1° latitude/longitude, in order to define a gridded area with a resolution of about 10 km. This choice corresponds closely to the nominal 8-km (at nadir) resolution of the International Satellite Cloud Climatology Project (ISCCP) GOES-5 B1 radiances (Rossow et al., 1985), which serve as the fundamental source of Earth radiation data for this study. The large area of coverage of the defined test site was chosen to encompass extended portions of ocean and land surfaces in both the tropics and mid-latitudes where sampling from a Sun-synchronous orbiter is sparser than in polar regions. This area includes a broad range of cloud types including the deep migratory convective bands of central America and the Amazon rain forests, low-lying stratus off the west coast of California, and the varied cloud forms associated with traveling mid-latitude cyclones.

A truth radiation field is required in which we specify the TOA distributions of longwave and shortwave fluxes, and their division into hemispherical radiances, on a spatial scale small compared to the minimum scanner footprint size to be studied. The summary description of the five candidate radiometers given in Table 1 shows that the smallest projected FOV size that we encounter at the TOA is the 40-km footprint of the CERES-I instrument at nadir. A sub 40-km resolution TOA truth field is then required. This we obtained through the ISCCP GOES-5 B1 radiance data set in which visible (VIS) and infrared (IR) narrowband data counts, centered about 0.6 μm and 11.5 μm, respectively, are provided at 8-km resolution at nadir. As illustrated in Figure 2, the raw counts are navigated to the Earth's surface and, after a series of calibration, classification, and conversion steps, are transformed to reflected and emitted TOA flux pairs and an associated bispectral cloud estimate at 10-km resolution. In re-mapping GOES-5 data to the 0.1 latitude/longitude elements of the M1 domain, oversampling occurs at nadir and some ISCCP data are discarded (see Section 2.1.2). Near the boundaries of the study area, the satellite data degrades in spatial resolution and undersampling of the grid elements occurs. In this case, data are generated at all grid boxes by interpolating the field of available GOES data. Knowledge of the underlying surface geography (i.e., ocean, land, or desert) and the cloud amount define an ERBE scene category, and its related angular dependence model (ADM), which we shall refer to as the reference models. Application of the reference ADM's, and normalized variations of them (Section 2.2.3), permit the redistribution of the estimated fluxes into a variety of patterns of upwelling hemispherical radiances. The result is a TOA radiation field which, while containing some error in the magnitude of the parameter estimates, provides a representative picture of the variability of the Earth on a 10-km scale and permits the study of the effect of instrument design and data processing methods on the accuracy of ERB measurements from space.

2.1.2 Navigation, Quality Control, and Interpolation

The ISCCP data are navigated to the Earth by means of an algorithm provided on the B1 data tapes (Smith and Phillips, 1972). The Earth-located data are mapped onto our 0.1° latitude/longitude resolution M1 grid and stored keeping only the last data value to fall within a grid element. This procedure eliminates the binning of multiple GOES-5 observations within a single grid element and preserves, since data averaging within a pixel is not performed, the discontinuities in radiances that occur across well defined

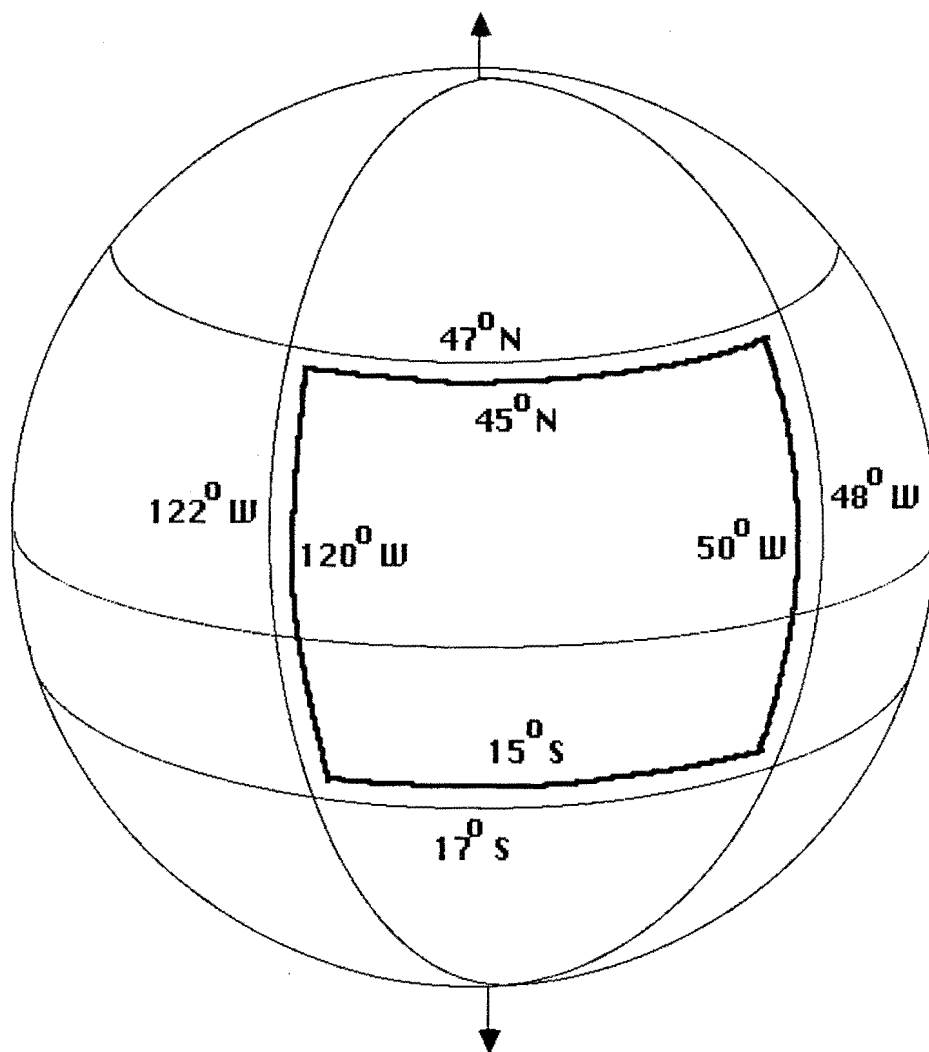**Domain of Simulation and Border Region**

Figure 1a. Domain of the system simulation, which extends across the southern tropics into the northern mid-latitudes and from the eastern Pacific Ocean to central South America.

M1 GRID 2.5 DEGREE RESOLUTION

LATITUDE / LONGITUDE

```
 45
    |  1 |  2 |  3 |  4 |  5 |  6 |  7 |  8 |  9 | 10 | 11 | 12 | 13 | 14 | 15 | 16 | 17 | 18 | 19 | 20 | 21 | 22 | 23 | 24 | 25 | 26 | 27 | 28
 40
    | 29 | 30 | 31 | 32 | 33 | 34 | 35 | 36 | 37 | 38 | 39 | 40 | 41 | 42 | 43 | 44 | 45 | 46 | 47 | 48 | 49 | 50 | 51 | 52 | 53 | 54 | 55 | 56
    | 57 | 58 | 59 | 60 | 61 | 62 | 63 | 64 | 65 | 66 | 67 | 68 | 69 | 70 | 71 | 72 | 73 | 74 | 75 | 76 | 77 | 78 | 79 | 80 | 81 | 82 | 83 | 84
 35
    | 85 | 86 | 87 | 88 | 89 | 90 | 91 | 92 | 93 | 94 | 95 | 96 | 97 | 98 | 99 |100 |101 |102 |103 |104 |105 |106 |107 |108 |109 |110 |111 |112
    |113 |114 |115 |116 |117 |118 |119 |120 |121 |122 |123 |124 |125 |126 |127 |128 |129 |130 |131 |132 |133 |134 |135 |136 |137 |138 |139 |140
 30
    |141 |142 |143 |144 |145 |146 |147 |148 |149 |150 |151 |152 |153 |154 |155 |156 |157 |158 |159 |160 |161 |162 |163 |164 |165 |166 |167 |168
    |169 |170 |171 |172 |173 |174 |175 |176 |177 |178 |179 |180 |181 |182 |183 |184 |185 |186 |187 |188 |189 |190 |191 |192 |193 |194 |195 |196
 25
    |197 |198 |199 |200 |201 |202 |203 |204 |205 |206 |207 |208 |209 |210 |211 |212 |213 |214 |215 |216 |217 |218 |219 |220 |221 |222 |223 |224
    |225 |226 |227 |228 |229 |230 |231 |232 |233 |234 |235 |236 |237 |238 |239 |240 |241 |242 |243 |244 |245 |246 |247 |248 |249 |250 |251 |252
 20
    |253 |254 |255 |256 |257 |258 |259 |260 |261 |262 |263 |264 |265 |266 |267 |268 |269 |270 |271 |272 |273 |274 |275 |276 |277 |278 |279 |280
    |281 |282 |283 |284 |285 |286 |287 |288 |289 |290 |291 |292 |293 |294 |295 |296 |297 |298 |299 |300 |301 |302 |303 |304 |305 |306 |307 |308
 15
    |309 |310 |311 |312 |313 |314 |315 |316 |317 |318 |319 |320 |321 |322 |323 |324 |325 |326 |327 |328 |329 |330 |331 |332 |333 |334 |335 |336
    |337 |338 |339 |340 |341 |342 |343 |344 |345 |346 |347 |348 |349 |350 |351 |352 |353 |354 |355 |356 |357 |358 |359 |360 |361 |362 |363 |364
 10
    |365 |366 |367 |368 |369 |370 |371 |372 |373 |374 |375 |376 |377 |378 |379 |380 |381 |382 |383 |384 |385 |386 |387 |388 |389 |390 |391 |392
    |393 |394 |395 |396 |397 |398 |399 |400 |401 |402 |403 |404 |405 |406 |407 |408 |409 |410 |411 |412 |413 |414 |415 |416 |417 |418 |419 |420
  5
    |421 |422 |423 |424 |425 |426 |427 |428 |429 |430 |431 |432 |433 |434 |435 |436 |437 |438 |439 |440 |441 |442 |443 |444 |445 |446 |447 |448
    |449 |450 |451 |452 |453 |454 |455 |456 |457 |458 |459 |460 |461 |462 |463 |464 |465 |466 |467 |468 |469 |470 |471 |472 |473 |474 |475 |476
  0
    |477 |478 |479 |480 |481 |482 |483 |484 |485 |486 |487 |488 |489 |490 |491 |492 |493 |494 |495 |496 |497 |498 |499 |500 |501 |502 |503 |504
    |505 |506 |507 |508 |509 |510 |511 |512 |513 |514 |515 |516 |517 |518 |519 |520 |521 |522 |523 |524 |525 |526 |527 |528 |529 |530 |531 |532
 -5
    |533 |534 |535 |536 |537 |538 |539 |540 |541 |542 |543 |544 |545 |546 |547 |548 |549 |550 |551 |552 |553 |554 |555 |556 |557 |558 |559 |560
    |561 |562 |563 |564 |565 |566 |567 |568 |569 |570 |571 |572 |573 |574 |575 |576 |577 |578 |579 |580 |581 |582 |583 |584 |585 |586 |587 |588
-10
    |589 |590 |591 |592 |593 |594 |595 |596 |597 |598 |599 |600 |601 |602 |603 |604 |605 |606 |607 |608 |609 |610 |611 |612 |613 |614 |615 |616
    |617 |618 |619 |620 |621 |622 |623 |624 |625 |626 |627 |628 |629 |630 |631 |632 |633 |634 |635 |636 |637 |638 |639 |640 |641 |642 |643 |644
-15
    |645 |646 |647 |648 |649 |650 |651 |652 |653 |654 |655 |656 |657 |658 |659 |660 |661 |662 |663 |664 |665 |666 |667 |668 |669 |670 |671 |672

   -120      -110      -100       -90       -80       -70       -60       -50
```
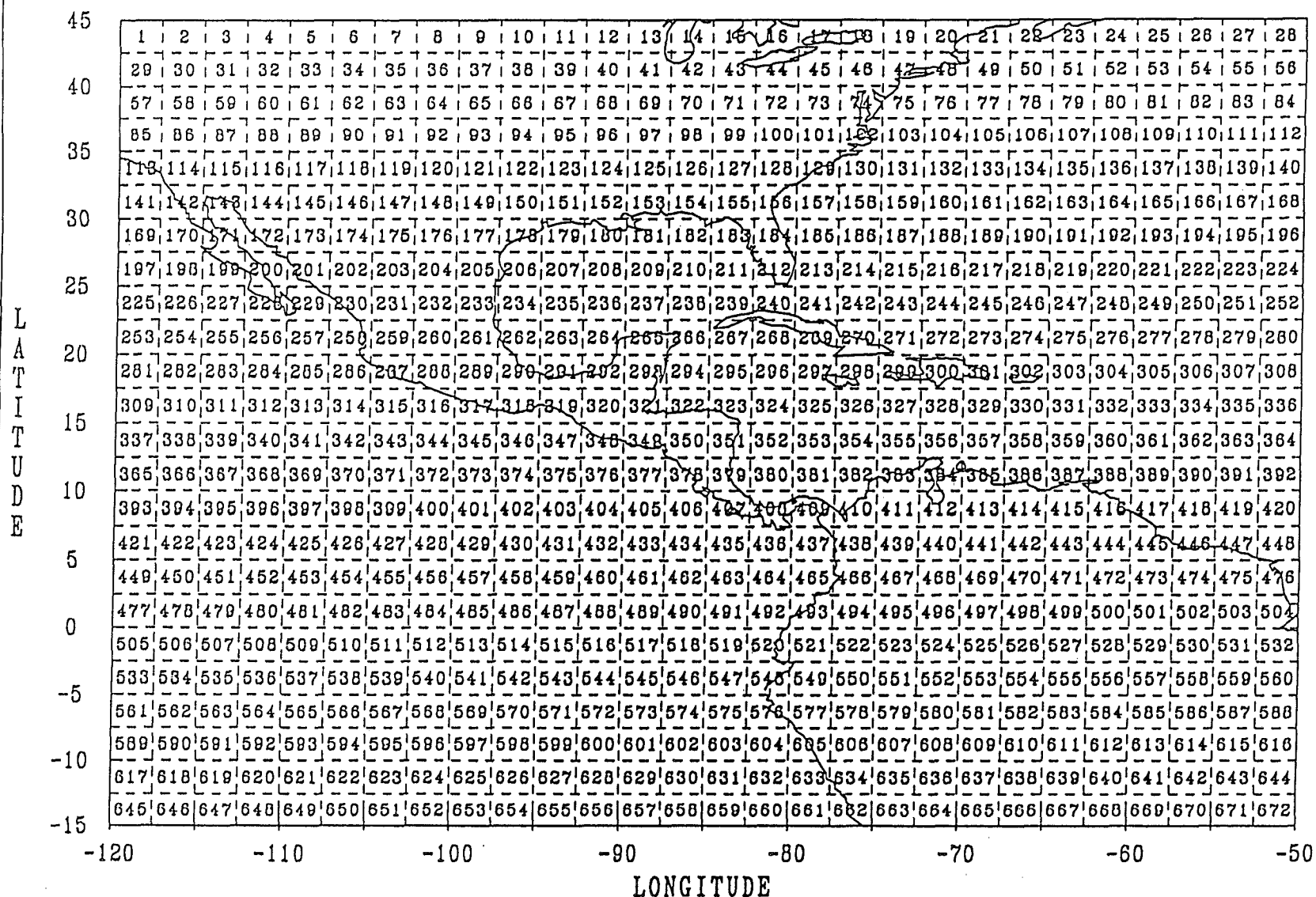
LONGITUDE

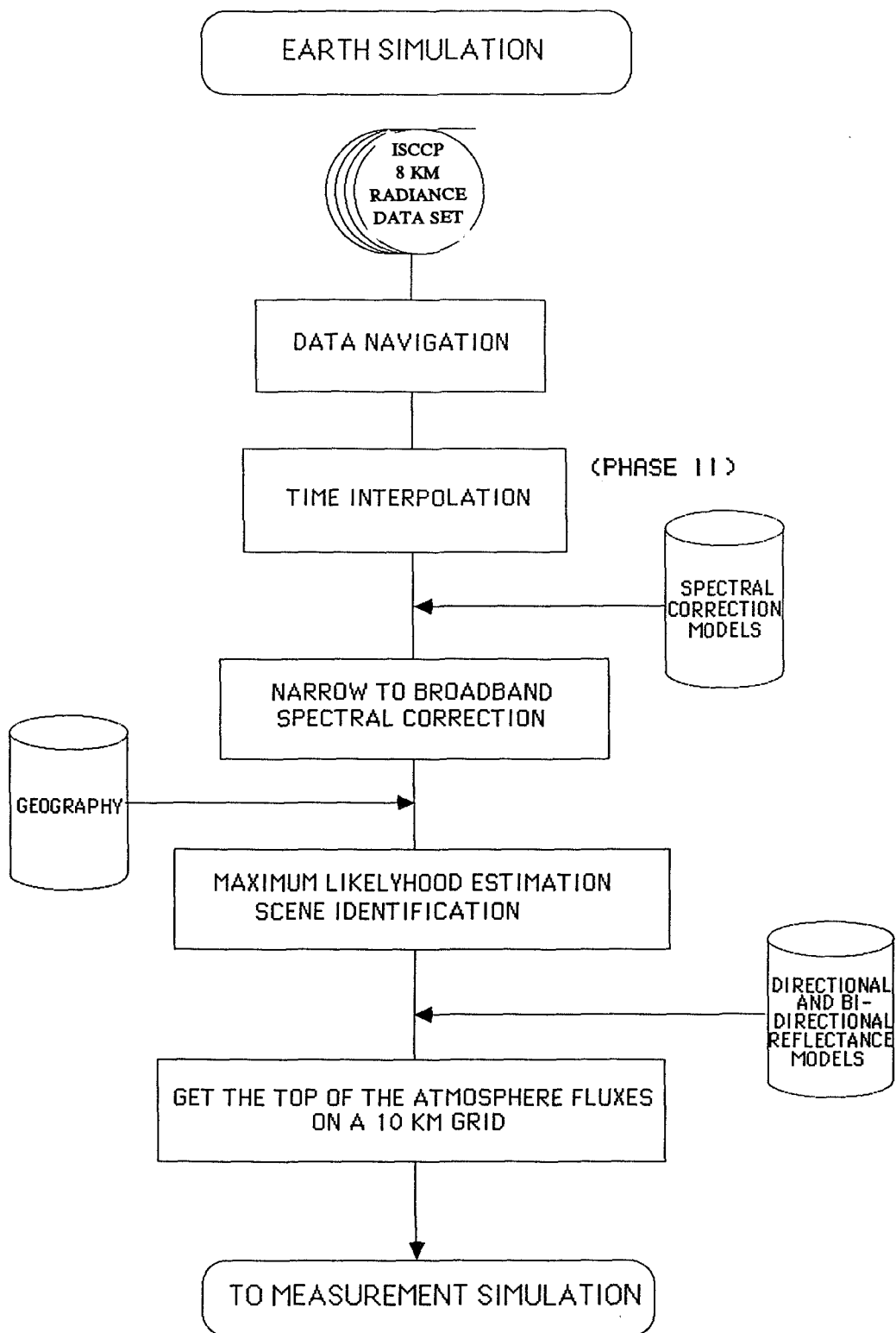Figure 1b. As in Figure 1a, but delineating the 672 2.5° study regions comprising the simulation domain.

Figure 2. The procedure for simulating the Earth, which is used as a reference or "truth" data set for the simulation. The steps involved in this procedure are the navigation of the GOES radiances, narrow-to-broad-band spectral correction, cloud fraction estimation, assignment of bidirectional models, and inversion of the radiances to recover fluxes at the top of the atmosphere.

scene boundaries. In this regard we note that multiple observations within an M1 pixel element would normally occur most frequently near the GOES-5 subsatellite point. Here the ISCCP data are densest (i.e., 8-km resolution) and the M1 grid resolution lowest (i.e., approximately 11 km at the equator). Near the boundaries of the M1 domain, on the other hand, and especially toward its northern edge, the grid resolution becomes higher than the data resolution. This occurs due to the combined stretching of the projected Earth positions of the B1 data away from the GOES-5 nadir point (0°N, 75°W) and to the increased longitudinal spatial resolution of the M1 grid toward the poles. In this region, the lack of available B1 data results in a characteristic missing value pattern which is most dense in the northwest corner of our domain, farthest from the GOES-5 subsatellite point. This is illustrated in Figures 3a and 3c, where missing values are seen to extend across the length of the northern boundary and southward from the northwest corner to a latitude of about 20°N.

Additional missing values are introduced during quality control checks on the gridded B1 counts. A search for data spikes at pixel resolution and for bad VISSR scan lines, which may extend across the entire width of the M1 domain, is carried out. Our interest here is to eliminate noticeably unphysical data values from further processing, but not to introduce an elaborate data validation scheme. With this in mind, the quality control procedures are kept simple with no attempt made to distinguish the absolute accuracy of borderline data values. Pixel values eliminated during quality control are marked as missing values and replaced, along with those arising during the mapping of ISCCP data to the M1 grid, by linear interpolation. Since, in the VISSR instrument, counts are related to radiance, an energy parameter, by a quadratic expression, a linear interpolation in counts squared is used. We consider the surrounding eight M1 grid values bordering a missing value and form an average among those which are not themselves missing. Pixel values which were once missing, but have subsequently been filled, are not included in the average. Occasionally only missing values are found among the eight pixels bordering a given missing value. In this case, it is necessary to widen the interpolation neighborhood to include a box of 24 surrounding pixels. Again, interpolation is performed by averaging only among data values which were not at one time missing. On rare occasions, however, even a box of 24 neighbors surrounding a missing value contains no nonfill data.

Interpolation is carried out, nevertheless, using the available already-interpolated data values. This last procedure produces a relatively flat and, perhaps, unrealistic local field, but it is necessary in the development of a TOA reference field which must be defined everywhere (Figures 3b and 3d).

2.1.3 Image Collocation

To ensure that the GOES infrared and visible images are precisely collocated after navigation, we examined the cross-correlation between a number of independent subdomains within the M1 grid. For each set of 40,000 pixels in 200 line x 200 pixel regions, we systematically displaced the infrared image relative to the visible image by 0, ±1, ±2, etc. lines and pixels. For the registration to be considered correct, the two images should exhibit the highest cross-correlation at no relative displacement. Both the raw counts and the final flux fields were examined. The raw counts values are preferable because they do not yet have the influence of what might be a possibly incorrect scene identification, while the flux values are preferable because the images have passed through the quality control, and any data errors have been screened out. As an example, for a subdomain near the image center of the 18Z image taken on January 29, 1984, a maximum correlation of 0.744 was obtained for the raw counts and -0.776 for the fluxes. The flux fields are normally negatively correlated because the presence of cloud acts to increase the albedo and hence the amount of reflected shortwave radiation, while at the same time decreasing the temperature of the emitting surface and thus the longwave flux. In both cases, the greatest magnitudes of the cross-correlations were obtained at no relative displacement between the two fields (see Table 3). To confirm these results, a number of independent tests were run for the flux fields at other
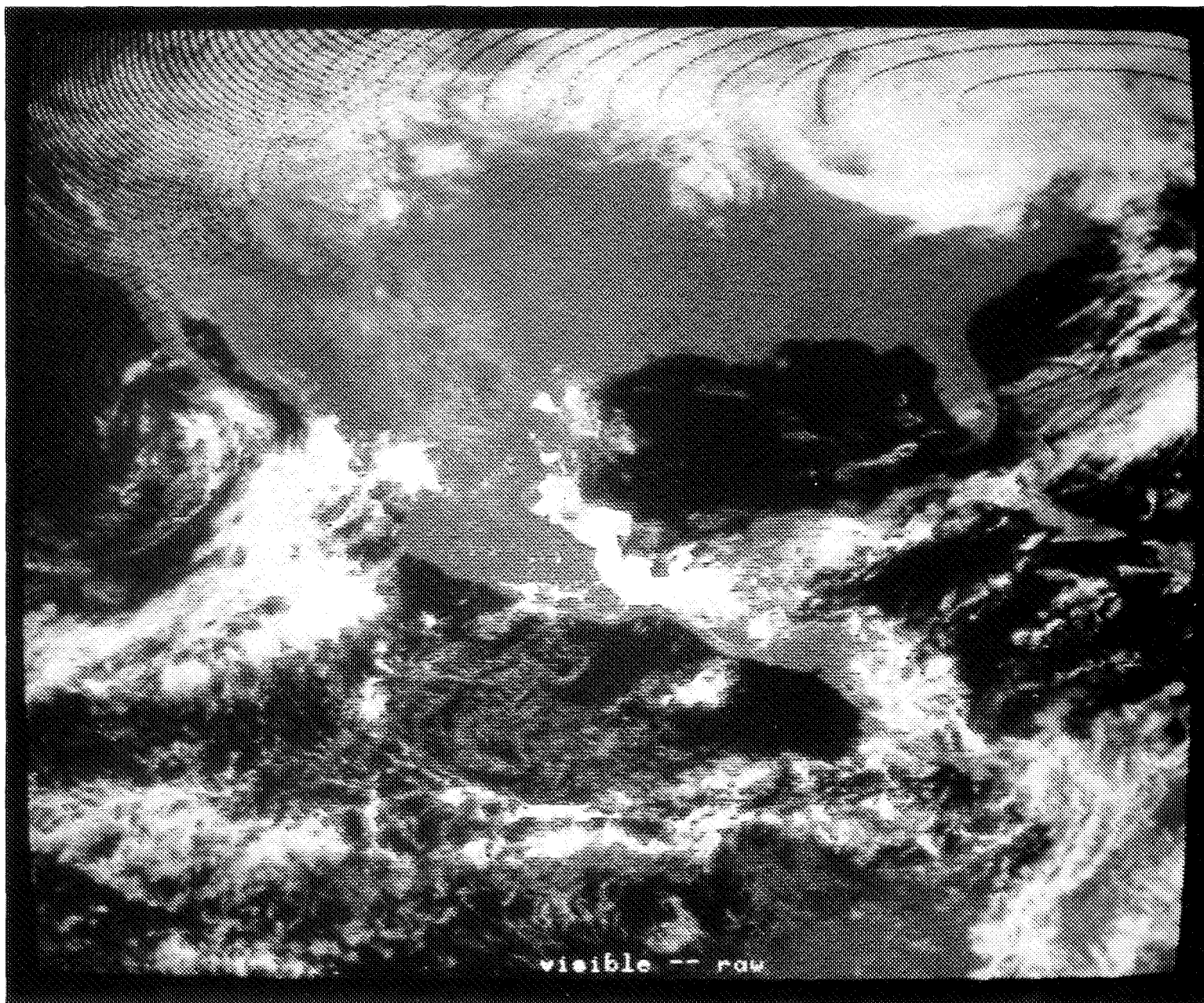
visible -- raw

Figure 3a. A 512 line x 512 pixel subset of the 640 line x 740 pixel reference field for visible reflected energy after navigation prior to interpolation.
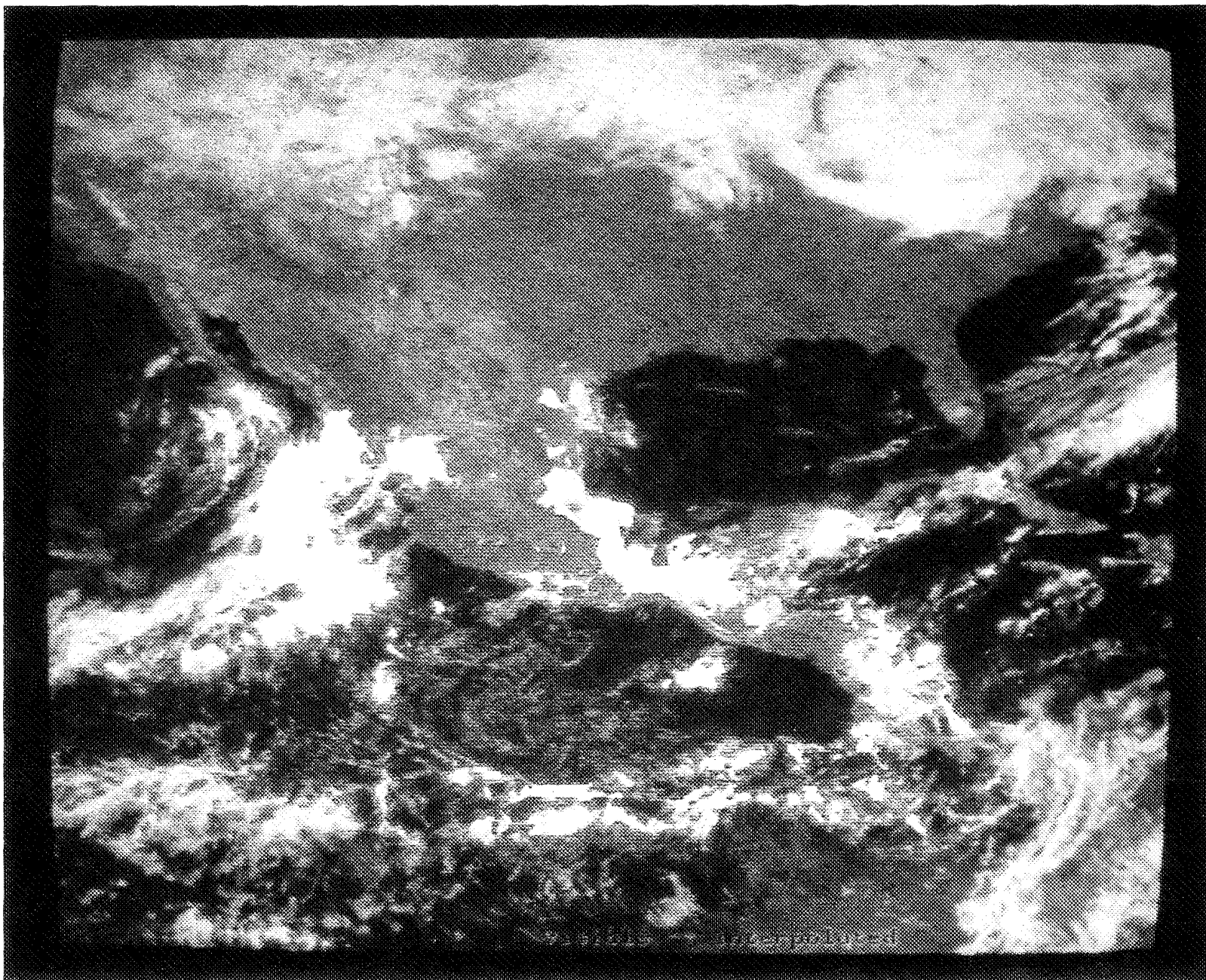
Figure 3b. As in Figure 3a, but subsequent to the interpolation to fill in the
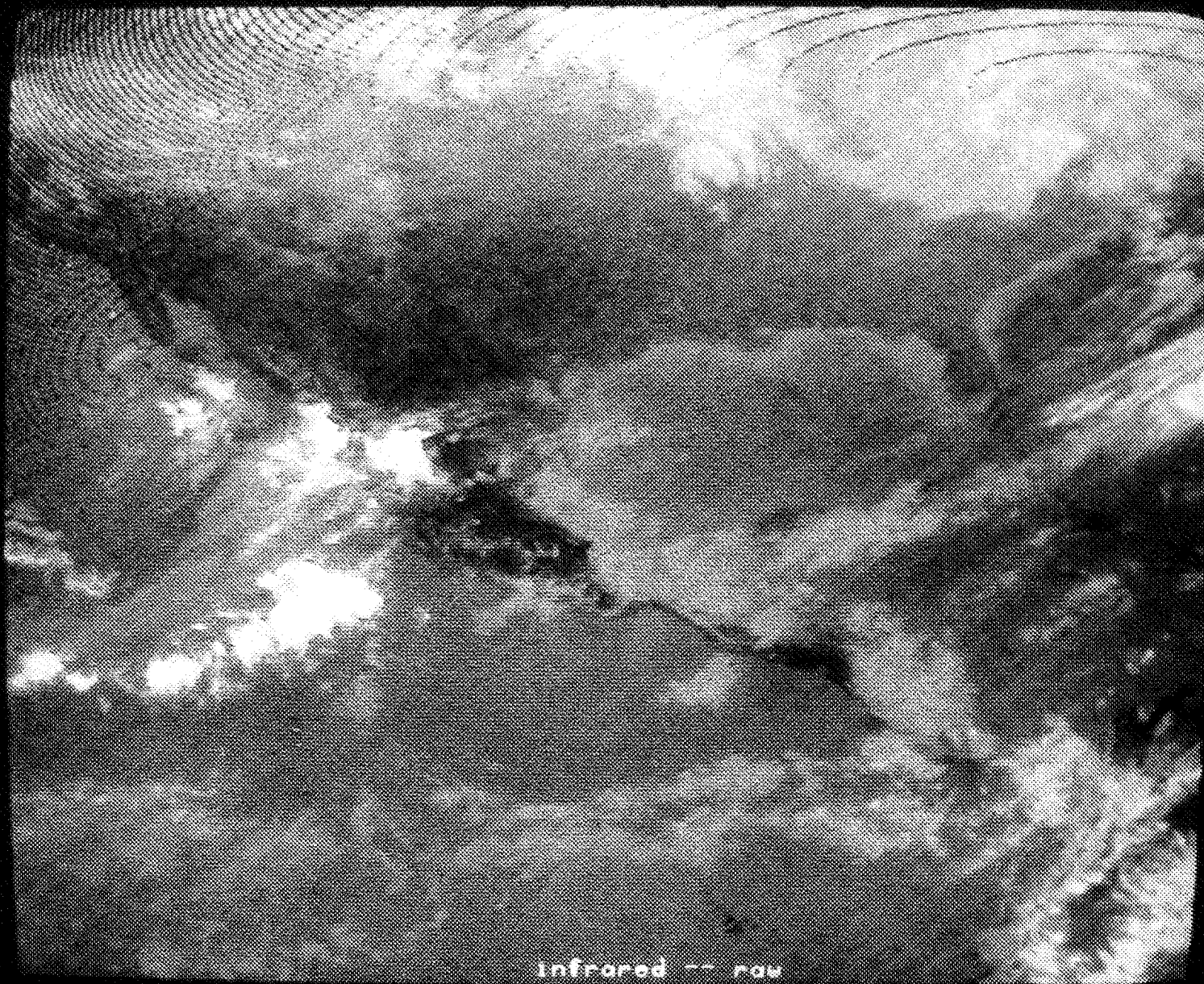missing pixels.

14

infrared -- raw

Figure 3c. As in Figure 3a, except for the thermal infrared radiation.
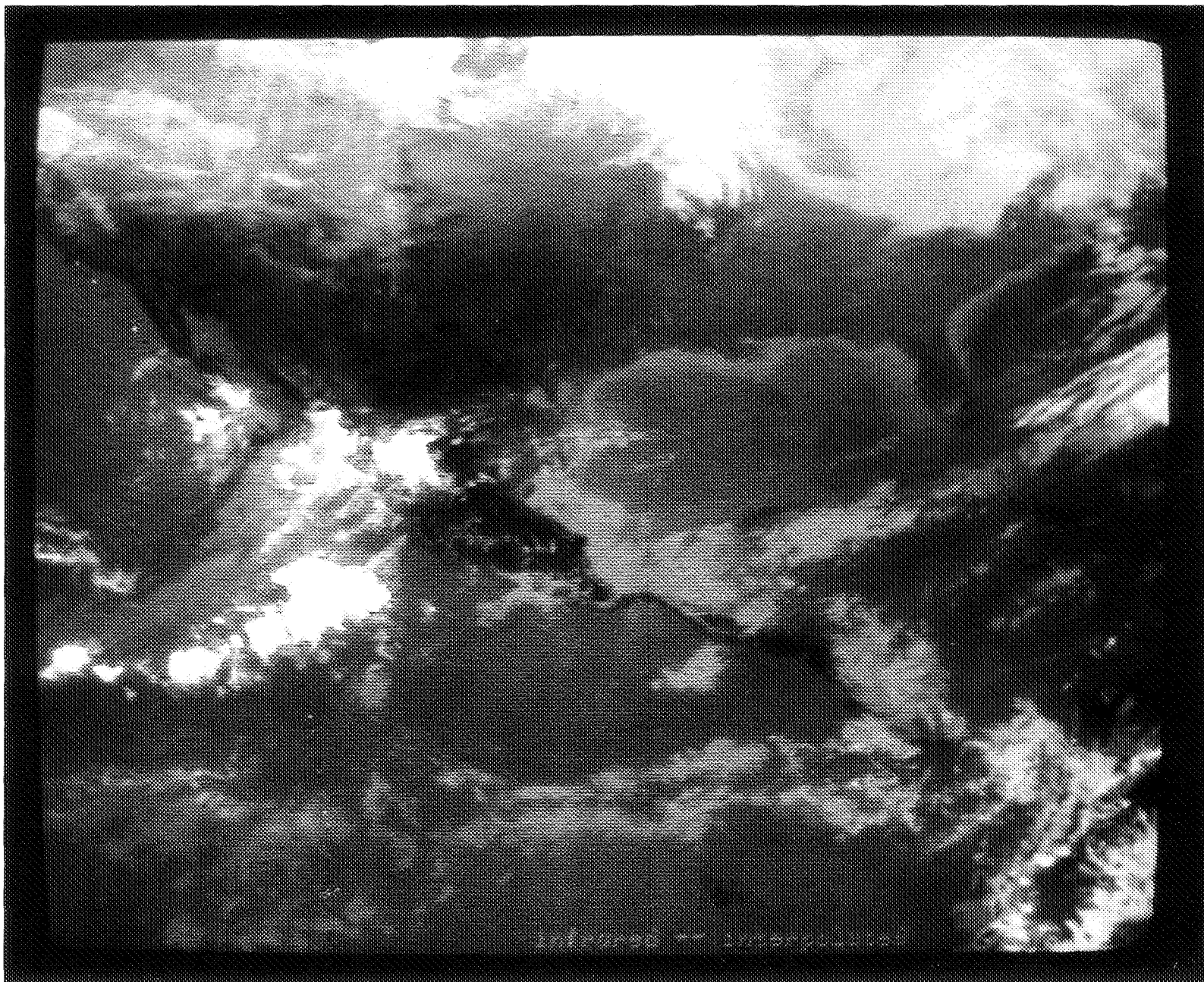
15

Figure 3d. As in Figure 3b, except for the thermal infrared radiation. A few bad pixels are evident off the coast of southern California extending into the Pacific Ocean, however, the impact of these is negligible.

neighboring 40,000 pixel subdomains. In four of these five additional tests, the highest correlations, with values of -0.769, -0.848, -0.749, and -0.767, were obtained at no relative displacement. In only one case was a possible one-half to one pixel displacement indicated, with a slightly increased amount of correlation in the fourth decimal place occurring with a one pixel shift between the two fields. This analysis confirms the collocation between the infrared and shortwave flux fields. Over the entire simulation data set, typical maximum displacements run from zero to two pixels, with the conclusion that the GOES images are well registered from the start.

Table 3. Cross-correlation between the shortwave and longwave count and flux fields illustrating the correct relative registration of the images.						
Pixels						
		-2	-1	0	+1	+2
Lines	+2	0.6058	0.6166	0.6175	0.6065	0.5845
	+1	0.6433	0.6671	0.6752	0.6537	0.6182
	0	0.6705	0.7142	0.7435	0.6928	0.6382
	-1	0.6720	0.7043	0.7169	0.6799	0.6333
	-2	0.6526	0.6643	0.6621	0.6408	0.6101
Counts Fields						
Pixels						
		-2	-1	0	+1	+2
Lines	+2	-0.6365	-0.6501	-0.6527	-0.6425	-0.6213
	+1	-0.6727	-0.6997	-0.7099	-0.6894	-0.6554
	0	-0.6974	-0.7443	-0.7757	-0.7282	-0.6761
	-1	-0.6967	-0.7331	-0.7496	-0.7155	-0.6715
	-2	-0.6754	-0.6916	-0.6935	-0.6753	-0.6475
Flux Fields						

2.1.4 Narrow-to-Broadband Radiance Conversion

On the ISCCP B1 tapes are VIS and IR narrowband data counts from which we require broadband radiances. For the VIS channel, the transformation from narrowband counts to broadband radiances is carried out using a two-step procedure in which we first convert ISCCP GOES-5 counts to equivalent GOES-2 counts and then apply the regression equations of Minnis and Harrison (1984a) to transform the GOES-2 counts to equivalent Nimbus-7 broadband radiances. Starting with ISCCP 8-bit words, we divide by 4 to recover the 6-bit count values measured by GOES-5. These can be related to GOES-2 counts through the calibration equations for the individual instruments given in the form

$$r = K^{-2} \cdot (C^2 - C_0^2)$$
(1)

where r is in units of reflectance (i.e., the energy reaching a satellite from a Lambertian reflector with an albedo of 1 when the Sun is at an overhead zenith position and 1 AU from the Earth), K is a sensitivity constant, C is measured counts and C_0 is an offset corresponding to the measured counts at the zero level of input power. The calibration constants, K and C_0, can be derived from preflight laboratory data for both GOES-2 and GOES-5, but they are subject to change when the radiometers are exposed to their inflight orbital environments. From Muench (1981) we find that K_2 (K for GOES-2) was measured in preflight tests to be 62.90 and that inflight studies show it remained relatively stable. For GOES-5 we examined the Santa Barbara Research Center (SBRC, 1980) calibration data and derived a preflight value of 61.33 for K_5. When this value is also assumed to hold for inflight conditions, as was approximately the case for GOES-2, a relationship between GOES-2 and GOES-5 counts is derived from Eq.(1) for equal values of r as

$$C_2^2 - C_{0,2}^2 = (K_2/K_5)^2 \cdot (C_5^2 - C_{0,5}^2)$$
$$= 1.026^2 \cdot (C_5^2 - C_{0,5}^2)$$
(2)

where only the inflight offset counts, $C_{0,2}$ and $C_{0,5}$ remain to be determined. These two constants are readily defined from inflight data by viewing empty space for which $C = C_0$. For GOES-5 we find $C_{0,5} = 6$ and for GOES-2, determined by Minnis and Harrison (1984a), we have $C_{0,2} = 2.5$. Eq.(2) then becomes

$$C_2^2 - 2.5^2 = 1.026^2 \cdot (C_5^2 - 6^2)$$
(3)

Instead of applying the calibration of Eq.(3), which is based upon inflight observations of $C_{0,2}$ and $C_{0,5}$, an alternate expression given by

$$C_2 - 2.5 = 1.026 \cdot (C_5 - 6)$$
(4)

was utilized. Eq.(4) differs from Eq.(3) in that the individual parameters and constants are not squared as before. This result was derived as an empirical correction to an initial algorithm ($C_{0,2}$ and $C_{0,5}$ derived from preflight calibration data) after it failed to produce regions of clear-sky scenes. Subsequently, it was recognized that Eq.(3) is the correct expression and a comparison of the two algorithms was made. Toward the high end of the counts spectrum, Eq.(4) yields a GOES-2 count value which can be low by as much as 3.5 counts. This leads to an underestimate of reflected broadband radiance in cloudy regions where measured counts are large. Toward the low end of the counts scale, corresponding to predominantly clear ocean regions, Eq.(4) yields nearly the same result as Eq.(3). The relationship between GOES-2 and GOES-5 counts for Eqs.(3) and (4) is shown in Figure 4. The curves indicate that the use of Eq.(4) introduces a negative error in the magnitude of GOES-2 counts for all values of
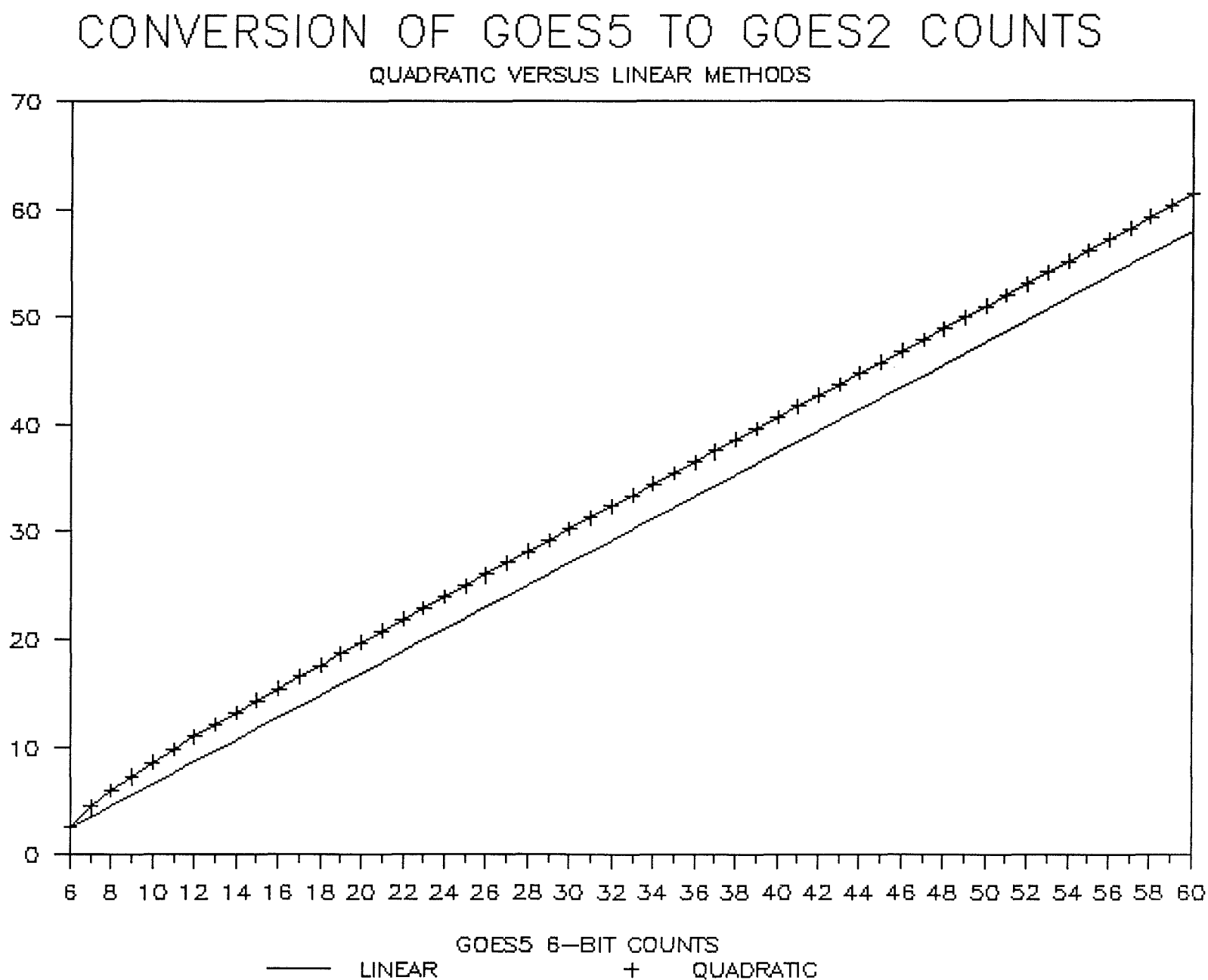
Figure 4. The relationship between GOES-2 and GOES-5 counts and the resultant conversion.

GOES-5. Although everywhere less than 3.5 in absolute value, these errors give rise to underestimates in SW radiance, which vary as the square of counts, of about 20% on average. Because the severity of this problem was not appreciated at the time, the reference fields used throughout this study were generated using Eq.(4). As a result, scanner shortwave flux sampling errors (to be reported in Section 3) will also be underestimated by about 20%, on average. This error should have little impact on the relative accuracy of the scanner estimates so they can be compared and used to indicate preferred scanning designs and data rates for the reduction of sampling error.

We have a simple linear expression relating the ISCCP GOES-5 counts to equivalent GOES-2 counts. The regression equations of Minnis and Harrison are now applied to the equivalent GOES-2 counts using Eq.(4) to yield broadband fluxes. These relationships were derived separately above and below a threshold value of 38 counts (6-bit digitization), and individually for ocean and land surfaces. They are included here for reference.

For $C_2^2 < 1450$

$$R_{sw} = 1.36 \cdot (C_2^2 - 6.25)^{1/2} + 0.0764 \cdot (C_2^2 - 6.25) \qquad ocean$$
$$R_{sw} = 1.92 \cdot (C_2^2 - 6.25)^{1/2} + 0.0616 \cdot (C_2^2 - 6.25) \qquad land$$

$$(5)$$

For $C_2^2 \geq 1450$ (land and ocean)

$$R_{sw} = 28.3 + 0.0923 \cdot C_2^2 \qquad (6)$$

where R_{sw} is shortwave broadband radiance (Wm^{-2}sr^{-1}), and 6.25 is the square of the GOES-2 offset constant, $C_{0,2}$.

The conversion of GOES-5 IR counts to broadband radiances is carried out using a multistep procedure in which we first transform measured counts at GOES-5 viewing geometry to spectral radiances at 11.5 μm. This is accomplished using a counts-to-blackbody temperature look-up table and, subsequently, converting temperature to spectral radiance by means of the Planck radiation equation evaluated at 11.5 μm. The temperature look-up table required for this procedure was provided by the University of Wisconsin and is included in Table 4. These narrowband radiances are then brought to overhead viewing estimates by applying the general narrowband limb darkening model of Minnis and Harrison (1984b). Regression equations relating GOES-2 overhead spectral radiances to Nimbus-7 overhead broadband radiances ($\theta=0$), also obtained from Minnis and Harrison (1984a), are now applied to derive a broadband nadir radiance estimate (Wm^{-2}sr^{-1}).

$$R_{lw} = 25.2 + 10.0 \cdot R_{BB} - 0.200 \cdot R_{BB}^2 \qquad ocean$$
$$R_{lw} = 24.0 + 9.43 \cdot R_{BB} - 0.133 \cdot R_{BB}^2 \qquad land$$

$$(7)$$

19

Table 4. Conversion table of GOES-5 infrared counts to blackbody temperature (K). Note that temperature, Temp, may be derived from Counts using two linear equations. For Counts $\leq$ 176, Temp $= 330 - 0.5 \cdot$ Counts; for Counts $\geq$ 176, Temp $= 418 -$ Counts.

Counts	Temp.	Counts	Temp.	Counts	Temp.	Counts	Temp.	Counts	Temp.
0	330.0	52	304.0	104	278.0	156	252.0	208	210.0
1	329.5	53	303.5	105	277.5	157	251.5	209	209.0
2	329.0	54	303.0	106	277.0	158	251.0	210	208.0
3	328.5	55	302.5	107	276.5	159	250.5	211	207.0
4	328.0	56	302.0	108	276.0	160	250.0	212	206.0
5	327.5	57	301.5	109	275.5	161	249.5	213	205.0
6	327.0	58	301.0	110	275.0	162	249.0	214	204.0
7	326.5	59	300.5	111	274.5	163	248.5	215	203.0
8	326.0	60	300.0	112	274.0	164	248.0	216	202.0
9	325.5	61	299.5	113	273.5	165	247.5	217	201.0
10	325.0	62	299.0	114	273.0	166	247.0	218	200.0
11	324.5	63	298.5	115	272.5	167	246.5	219	199.0
12	324.0	64	298.0	116	272.0	168	246.0	220	198.0
13	323.5	65	297.5	117	271.5	169	245.5	221	197.0
14	323.0	66	297.0	118	271.0	170	245.0	222	196.0
15	322.5	67	296.5	119	270.5	171	244.5	223	195.0
16	322.0	68	296.0	120	270.0	172	244.0	224	194.0
17	321.5	69	295.5	121	269.5	173	243.5	225	193.0
18	321.0	70	295.0	122	269.0	174	243.0	226	192.0
19	320.5	71	294.5	123	268.5	175	242.5	227	191.0
20	320.0	72	294.0	124	268.0	176	242.0	228	190.0
21	319.5	73	293.5	125	267.5	177	241.0	229	189.0
22	319.0	74	293.0	126	267.0	178	240.0	230	188.0
23	318.5	75	292.5	127	266.5	179	239.0	231	187.0
24	318.0	76	292.0	128	266.0	180	238.0	232	186.0
25	317.5	77	291.5	129	265.5	181	237.0	233	185.0
26	317.0	78	291.0	130	265.0	182	236.0	234	184.0
27	316.5	79	290.5	131	264.5	183	235.0	235	183.0
28	316.0	80	290.0	132	264.0	184	234.0	236	182.0
29	315.5	81	289.5	133	263.5	185	233.0	237	181.0
30	315.0	82	289.0	134	263.0	186	232.0	238	180.0
31	314.5	83	288.5	135	262.5	187	231.0	239	179.0
32	314.0	84	288.0	136	262.0	188	230.0	240	178.0
33	313.5	85	287.5	137	261.5	189	229.0	241	177.0
34	313.0	86	287.0	138	261.0	190	228.0	242	176.0
35	312.5	87	286.5	139	260.5	191	227.0	243	175.0
36	312.0	88	286.0	140	260.0	192	226.0	244	174.0
37	311.5	89	285.5	141	259.5	193	225.0	245	173.0
38	311.0	90	285.0	142	259.0	194	224.0	246	172.0
39	310.5	91	284.5	143	258.5	195	223.0	247	171.0
40	310.0	92	284.0	144	258.0	196	222.0	248	170.0
41	309.5	93	283.5	145	257.5	197	221.0	249	169.0
42	309.0	94	283.0	146	257.0	198	220.0	250	168.0
43	308.5	95	282.5	147	256.5	199	219.0	251	167.0
44	308.0	96	282.0	148	256.0	200	218.0	252	166.0
45	307.5	97	281.5	149	255.5	201	217.0	253	165.0
46	307.0	98	281.0	150	255.0	202	216.0	254	164.0
47	306.5	99	280.5	151	254.5	203	215.0	255	163.0
48	306.0	100	280.0	152	254.0	204	214.0		
49	305.5	101	279.5	153	253.5	205	213.0		
50	305.0	102	279.0	154	253.0	206	212.0		
51	304.5	103	278.5	155	252.5	207	211.0		

These are finally brought back to the GOES-5 viewing geometry using the broadband limb-darkening function of Raschke et al. (1973). We have represented the two limb-darkening models needed for this procedure by fifth degree polynomials in the satellite zenith angle, θ. These are expressed as

$$\lambda = C_0 + C_1 \cdot \theta + C_2 \cdot \theta^2 + C_3 \cdot \theta^3 + C_4 \cdot \theta^4 + C_5 \cdot \theta^5 \qquad (8)$$

where λ is the limb-darkening function, $R_{lw}(\theta)/R_{lw}(\theta=0°)$, and C_0 through C_5 are constants given in Table 5.

Table 5. Limb-darkening model coefficients used in the conversion of GOES-2 spectral radiances to Nimbus-7 broadband radiances.		
Limb-Darkening Coefficients		
Degree	Spectral Model	Broadband Model
0	1.0	1.0
1	-1.419×10^{-4}	-5.479×10^{-4}
2	2.435×10^{-5}	-3.169×10^{-6}
3	-1.295×10^{-6}	-5.795×10^{-7}
4	2.185×10^{-8}	1.195×10^{-8}
5	-1.327×10^{-10}	-1.039×10^{-10}

2.1.5 Scene Identification and the Derivation of a TOA Radiation Field

To infer cloud amount and a TOA radiation field from a single GOES-5-derived VIS and IR broadband radiance pair, we invoke MLE and the ERBE reference ADM's (Wielicki and Green, 1989). Although originally developed for spatial resolutions of 50 to 200 km, the ERBE ADMs are used here at 8 km and found to yield plausible patterns of cloud amount and reflected fluxes, except in regions of sunglint reflection. In this case, the relatively low resolution ERBE bidirectional reflectance models (Taylor and Stowe, 1984, 1986; Suttles et al., 1988, 1989) do not accurately capture the specularly reflected intensities that are observed within GOES pixels. As a result, overestimates in albedo may occur for regions of clear ocean whose sunglint reflection is visible from GOES-5. In this study, corrections for sunglint reflection were not applied because the scanning designs to be compared were each required to sample the same reference fields and only their relative accuracy is to be tested.

At each M1 grid element, surface geography and angular geometry (relating the Earth, Sun, and GOES-5 at the time of the B1 image) are known. This information together with the GOES-5-derived radiances is interpreted by MLE and the reference models to yield a cloud amount in one of the four broad ERBE categories: clear, partly cloudy, mostly cloudy, and overcast. The derived cloud estimate is taken as truth and used to complete the scene identification at a grid M1 element. TOA reference fluxes, F_{ref}, are obtained from the scene information and broadband radiances, R_{GOES}, using the relationship

$$F_{ref} = \frac{\pi \cdot R_{GOES}}{\rho_{ref}} \qquad (9)$$

where ρ_{ref} is the reference model anisotropic factor for the derived scene category and computed angular geometry. When averaged into 2.5° target areas, the fluxes of Eq.(9) represent the desired retrieval parameter of our system simulation.

For orbital simulations, we need to simulate errors in the bidirectional reflectance functions. To do this, upwelling radiances are required which are not necessarily related to the TOA fluxes by re-application of the reference anisotropic models. Instead, we consider a reasonable approach in which the Earth source radiation can be treated as systematically and/or randomly more, less, and as anisotropic as the ERBE reference models. For the more and less anisotropic cases, perturbed models (Green, 1980), ρ', are introduced which are related to the reference models in the form

$$\frac{\rho' - 1}{\rho_{ref} - 1} = N \tag{10}$$

where the isotropic component (i.e., $\rho = 1$) has been removed from both ρ' and ρ_{ref} and N is an anisotropy scale factor which may be systematically and/or randomly greater than, less than, or equal to unity. When Eq.(10) is rearranged and solved for ρ' we obtain

$$\rho' = N \cdot (\rho_{ref} - 1) + 1 \tag{11}$$

showing that ρ' is readily obtained from the existing ERBE reference models by simple algebra. From the form of Eq.(11), it is easy to verify that the perturbed models satisfy the normalization condition

$$\pi^{-1} \cdot \int_{2\pi} \rho' \cdot \cos\theta \cdot d\Omega = 1 \tag{12}$$

since the reference models, ρ_{ref}, are already normalized. Here θ is a polar angle measured from local zenith at a target on the Earth and $d\Omega$ is an element of solid angle of the outgoing hemisphere.

The perturbed anisotropic models of Eq.(11), together with the flux of Eq.(9), describe a complete radiance field at the TOA for all potential values of N. These experiments involve a redistribution of the total flux into the upwelling hemisphere, but do not affect the magnitude of the flux itself, which is determined uniquely from GOES-5 data using the reference models. For any given N experiment, radiances are determined from the flux using the familiar expression

$$R_{ref} = \pi^{-1} \cdot \rho' \cdot F_{ref} \tag{13}$$

where ρ' depends on the N value selected according to Eq.(11).

2.2 MEASUREMENT SIMULATION

The procedure for measurement simulation is illustrated in Figure 5. Orbits of a polar platform at 824-km altitude are propagated across the M1 grid in a series of experiments designed to test the sensitivity of the five scanners to conditions of solar illumination and ADM variability. Illumination conditions along the subsatellite track are, in part, determined by the choice of ascending node (AN) equator-crossing times of the satellite orbit and may be considered an adjustable parameter in planning for future satellite missions. ADM variability, on the other hand, is a property of Earth/atmosphere radiation which is not currently well-described. It is treated hypothetically in our study, therefore, as having the same potential range of variability for all seasons and illumination conditions. Although instrument noise has not been incorporated in the results of this study, it is an additional source of error that may be examined using the computer code developed. This is illustrated in Figure 5 where noise effects would be added to integrated satellite-altitude measurements.

2.2.1 Simulation of Spacecraft Motion

For orbital simulations we have generated the motion of a Sun-synchronous spacecraft with orbital parameters closely resembling those proposed for the polar orbiting platforms (POP's) of the Earth Observing System (EOS). The satellite flies at an altitude of 824 km above sea level and in a retrograde orbit of inclination 98.7° and period 100.7 minutes. For reference, the relationship between satellite zenith angle and Earth central angle for an 824-km orbiter is shown in Figure 6. AN equator crossing times in Phase I have been reserved as an experimental parameter with which to control solar illumination conditions across the viewed Earth. A complete test includes several overpasses of the M1 study site during hours of both morning and afternoon. These experiments were conducted using truth fields derived from GOES-5 synoptic data for 15Z and 21Z. The M1 grid, in extending from 50° to 120°W, spans a local time range from approximately three (50°W) to eight (120°W) hours earlier than Greenwich time. At 15Z, local times across the M1 grid vary from 7 AM to 12 noon and, at 21Z, they vary from 1 PM to 6 PM. By choosing satellite equator crossings that correspond to fixed positions within the M1 grid, varying local illumination conditions can be viewed within the same B1 data field. Using this strategy, we consider orbits with AN equator crossings of 63°, 86° and 109°W. At 15Z, these correspond to 11:15, 9:45 and 8:15 AM local time, respectively, at the equator. Similarly, at 21Z, they correspond to 4:45, 3:15 and 1:45 PM, respectively. Another way of looking at this is to imagine having a "fleet" of three satellites, each crossing the equator 23° in longitude apart.

2.2.2 Simulation of Scanner Operation

Five unique scanning concepts are studied which include a fixed array of radiometers (ACA), and biaxial (Nimbus-7), conical (CSR), cross-track (ERBE), and azimuth slewing scan combined with cross-track (CERES-I) scanning motions. All but the ERBE cross-track design employ some means of effectively viewing in two degrees of freedom about an axis along the spacecraft nadir direction. This is achieved for the ACA, Nimbus-7, and CERES-I, through the use of multiple radiometers for each broadband spectral interval in the design concept and, in practice, presents a challenging task in the overall maintenance and calibration of the instruments. The ERBE and CSR, on the other hand, use only a single observing radiometer for each spectral interval. The ERBE, however, is generally limited to one degree of viewing freedom, in satellite zenith angle, along a line ±90 degrees inclined to the direction of spacecraft motion. Individual scan patterns for specific designs of the five instruments used in this study are depicted in Figures 7 through 11, respectively, for the Nimbus-7, CSR, ERBE, ACA, and CERES-I radiometers. In the figures, only the location of the scanner FOV midpoints is shown. A description of overlap or gaps between footprints is indicated in each of the scanner description subsections which follow.
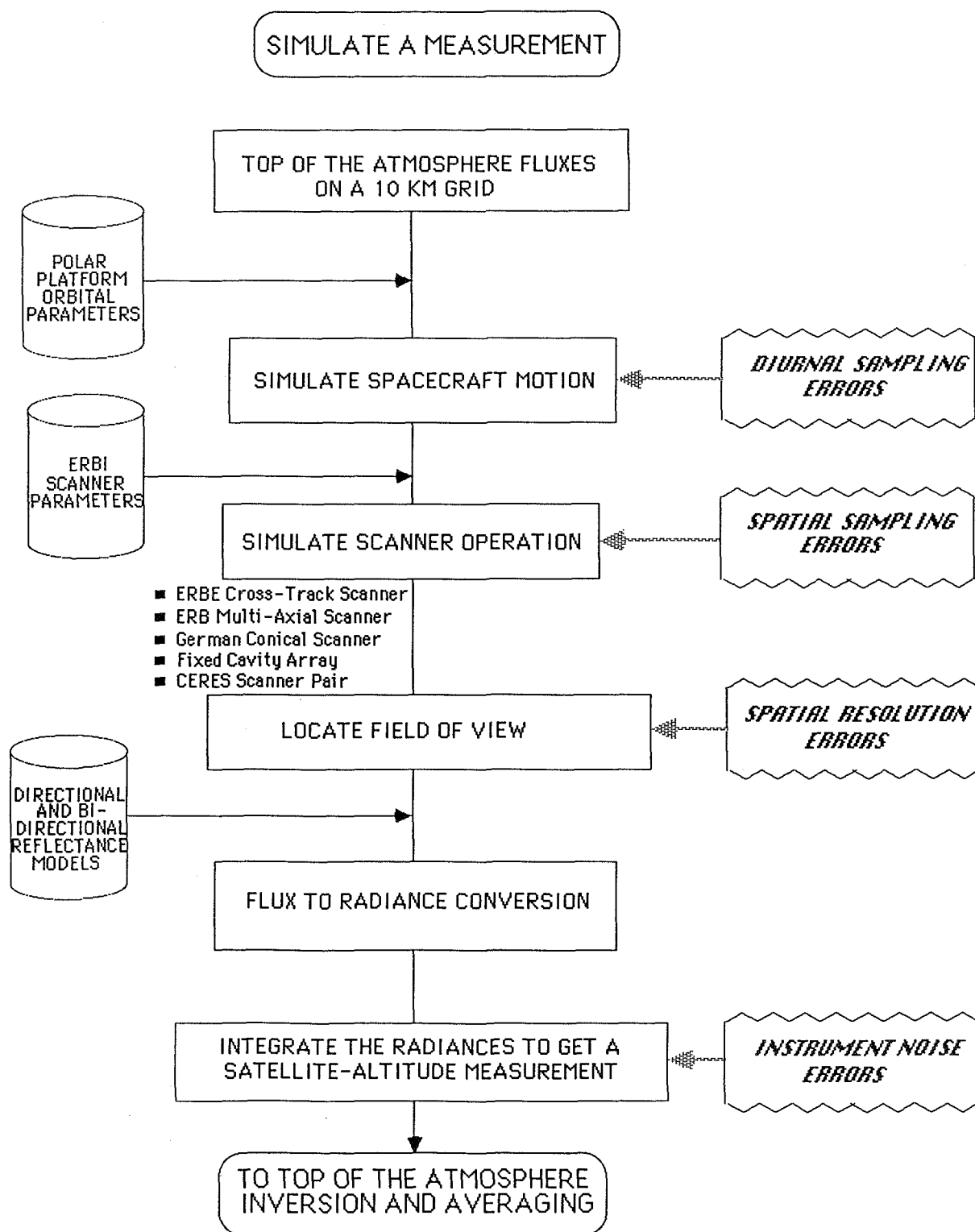
23

```
                   ╭─────────────────────────────╮
                   │   SIMULATE A MEASUREMENT    │
                   ╰─────────────────────────────╯
                                 │
                ┌────────────────────────────────────┐
                │   TOP OF THE ATMOSPHERE FLUXES     │
                │        ON A 10 KM GRID             │
                └────────────────────────────────────┘
   ┌─────────┐                   │
   │ POLAR   │                   │
   │ PLATFORM│──────────────────▶│
   │ ORBITAL │                   │
   │PARAMETERS│                  │
   └─────────┘   ┌──────────────────────────────┐
                 │  SIMULATE SPACECRAFT MOTION  │◀─── DIURNAL SAMPLING
                 └──────────────────────────────┘         ERRORS
   ┌─────────┐                   │
   │  ERBI   │                   │
   │ SCANNER │──────────────────▶│
   │PARAMETERS│                  │
   └─────────┘   ┌──────────────────────────────┐
                 │  SIMULATE SCANNER OPERATION  │◀─── SPATIAL SAMPLING
                 └──────────────────────────────┘         ERRORS
```

■ ERBE Cross-Track Scanner
■ ERB Multi-Axial Scanner
■ German Conical Scanner
■ Fixed Cavity Array
■ CERES Scanner Pair

```
                 ┌──────────────────────────────┐
                 │     LOCATE FIELD OF VIEW     │◀─── SPATIAL RESOLUTION
                 └──────────────────────────────┘         ERRORS
   ┌─────────┐                   │
   │DIRECTIONAL│                 │
   │ AND BI-  │                  │
   │DIRECTIONAL│─────────────────▶│
   │REFLECTANCE│                 │
   │ MODELS   │                  │
   └─────────┘   ┌──────────────────────────────┐
                 │   FLUX TO RADIANCE CONVERSION │
                 └──────────────────────────────┘
                                 │
                 ┌──────────────────────────────┐
                 │ INTEGRATE THE RADIANCES TO GET A │◀─── INSTRUMENT NOISE
                 │ SATELLITE-ALTITUDE MEASUREMENT  │         ERRORS
                 └──────────────────────────────┘
                                 │
                   ╭─────────────────────────────╮
                   │  TO TOP OF THE ATMOSPHERE   │
                   │  INVERSION AND AVERAGING    │
                   ╰─────────────────────────────╯
```

Figure 5. The procedure for simulating a measurement, the time series of which form the complete data set taken by each candidate radiometer. In this process, the orbit of the spacecraft is propagated across the domain of simulation, the scan pattern for the candidate radiometer is exercised, and the instantaneous fields of view for each channel are located at the top of the atmosphere. The truth fluxes at the top of the atmosphere within the radiometer's footprint are converted to radiances along the line of sight of the instrument and integrated over the field of view to yield a measurement.

Satellite Zenith Angle as a Function of
Earth Central Angle for Polar Platform
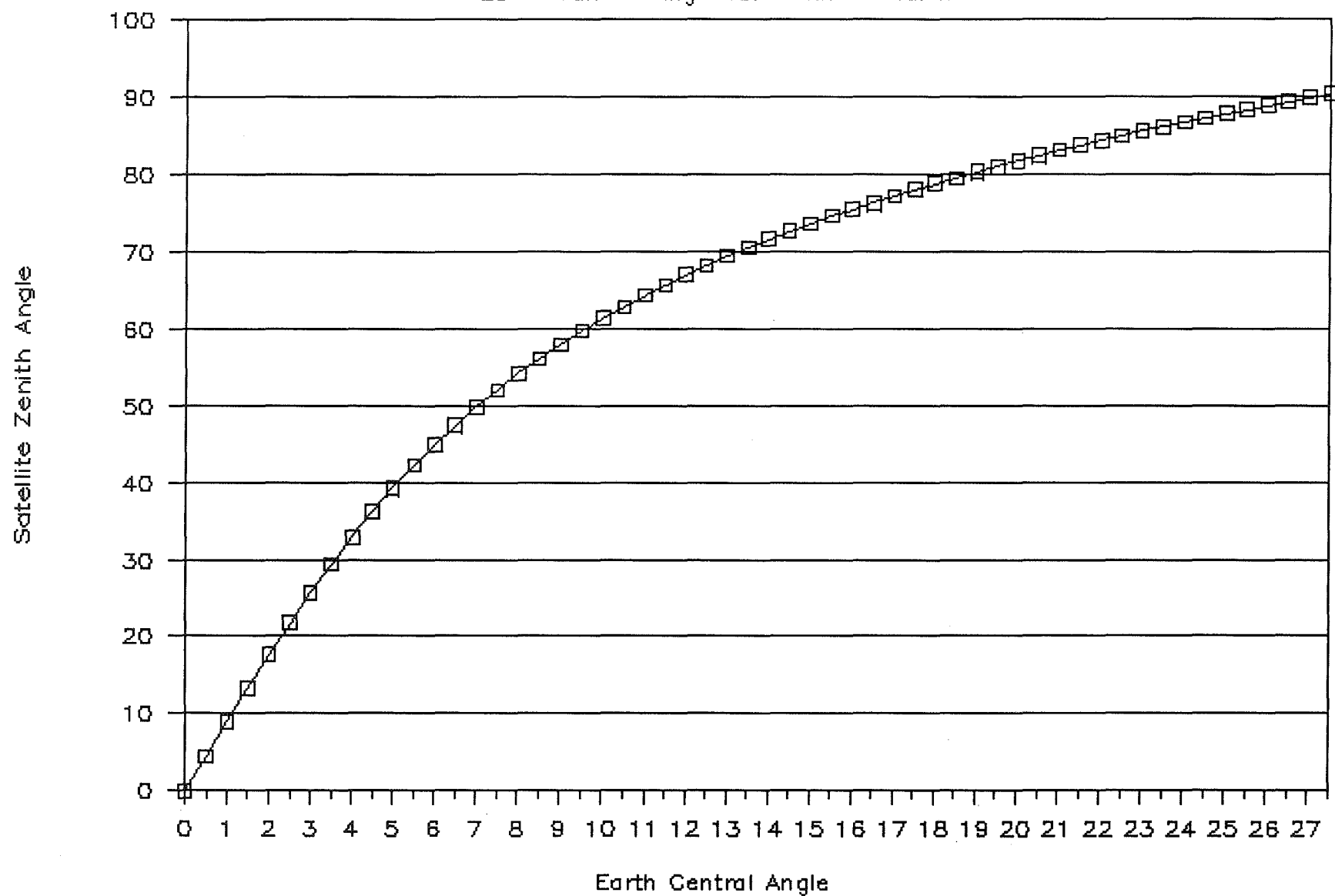
Figure 6. The relationship between satellite zenith angle and Earth central angle for an 824-km altitude orbit.

2.2.2.1 The Nimbus-7 Biaxial Scanner

The Nimbus-7 ERB scanner (Jacobowitz et al., 1978) consists of a four telescope array which cycles through a continuous series of 112-second scan modes. There are four unique scan modes and each is designed to measure radiances along the subsatellite track both ahead of and behind the spacecraft position, as well as toward one side of the orbit but not both. The consecutive, nearly square footprints align contiguously along a scan line and have a spatial resolution that varies from $(90 \text{ km})^2$ at nadir to about $(220 \text{ km})^2$ at the horizon. The capability to sample along both sides of the orbit is obtained by combining modes 3 and 4 in an alternating 112-second cycle to form a 224-second mode 5. In this configuration, the scanner sweeps both forward and backward from the subsatellite point to beyond the horizon and back, and to the sides from the subsatellite point out to a nadir angle of 56° and back. This scan mode yields the greatest azimuthal sampling and is the one used in this simulation. Typically, 50 to 60 observations are taken, during an orbital overpass, within 2.5° resolution target areas located near the orbital ground track and about 20 to 30 observations in target areas lying to the side. This is the lowest sampling rate (Table 2) of the five instruments tested and frequently leads to poor spatial sampling among targets at the edges of the orbital swath. Here the 224-second repeat period for side scanning is not sufficiently rapid to ensure that all 2.5° target areas can be observed perpendicularly from the orbital track (Figure 7).

2.2.2.2 The Conically Scanning Radiometer (CSR)

The CSR (Wirth et al., 1986) views the Earth at nadir and in five other elevation angle rings out to a maximum of 56° of nadir angle. In the design employed here the radiometer has a fixed circular FOV of 3.5° full cone angle and spends 2.41 seconds at each of six nadir angle positions and at one separate calibration position to complete a full scan cycle in 16.87 seconds. The sampling rate varies within each nadir angle ring and is adjusted so that consecutive observations (within a ring) overlap at roughly 50% coverage. Table 6 gives the six nadir positions of the CSR radiometer and the sampling rate and number of observations taken within each ring. When superimposed along the sub-orbital track, about 140 to 170 observations are collected within target areas located near the ground track. Toward the edge of the scan swath, Earth locations are viewed only when the radiometer is positioned to the highest nadir angle elevation. For these edge target areas, on the order of 50 data samples are taken during one satellite overpass (Figure 8).

2.2.2.3 The ERBE Cross-Track Scanner (ERBE)

The ERBE cross-track scanner (Barkstrom, 1984) completes a full scan cycle every 4 seconds, viewing the Earth for about 2 seconds and spending the remaining time in calibration and repositioning of the scan head. While moving across the Earth, the instrument rotates at 66-2/3 degrees of nadir angle per second and samples at the rate of 30 observations per second. Since the Earth subtends an angle of about 126° at 824 km, this corresponds to about 56 on-Earth observations per scan (i.e., 14 observations per second on average). As it scans, the radiometer samples the incident radiances using a fixed FOV that is projected perpendicular to the subsatellite track from horizon to nadir and through to the opposite horizon. In this study, the ERBE FOV is assumed to be circular and to occupy a 3.6° full cone angle. Near nadir, 70 to 90 observations fall within a 2.5° target area during one orbital pass. As the scanner approaches the horizon, the sampling decreases until only about 11 observations are obtained (Figure 9).

Figure 7. The simulated scan pattern for the Nimbus-7 ERB instrument, illustrating the center of the field of view for each of the four telescopes, for a small portion of an orbit.
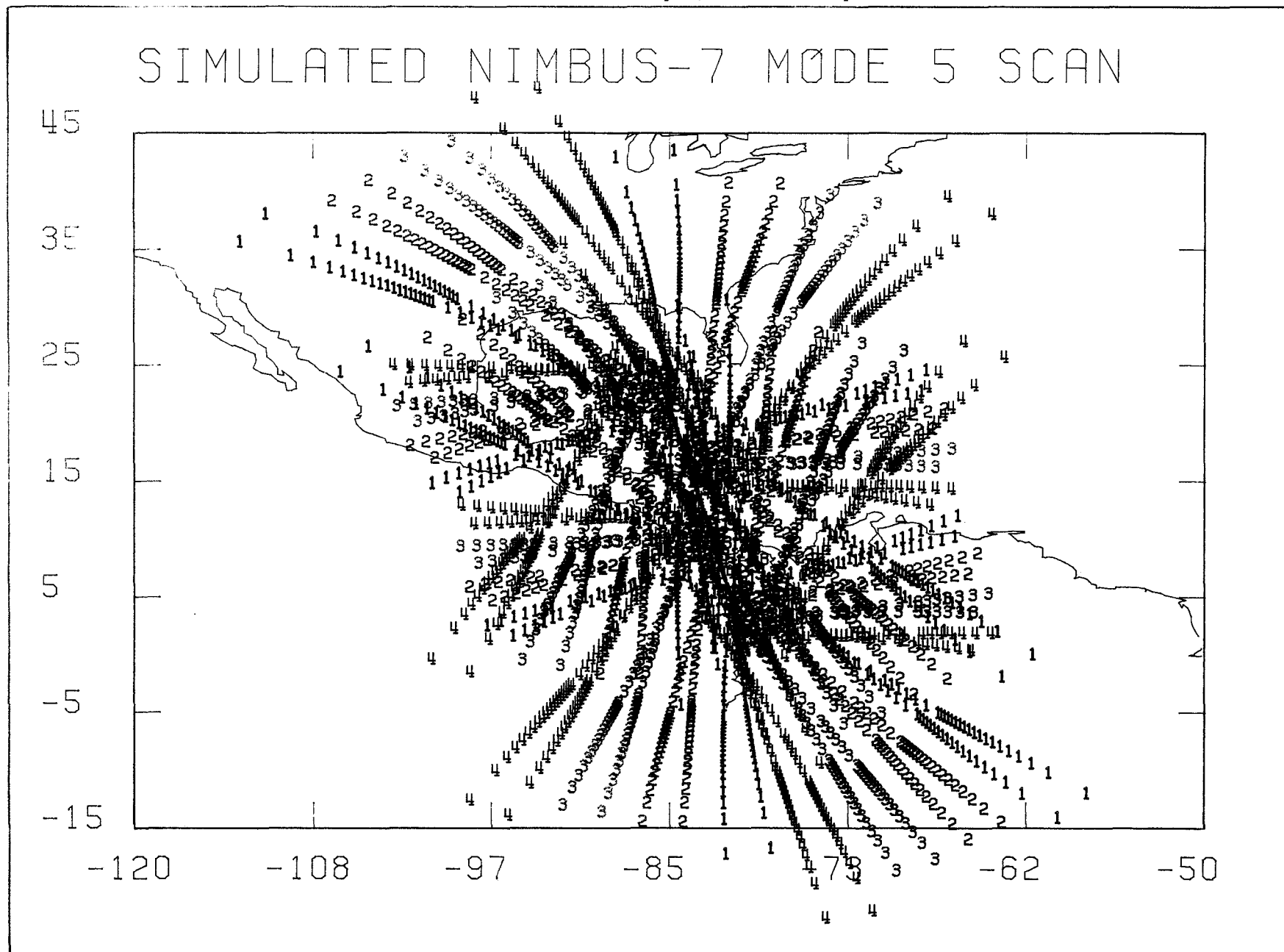

SIMULATED NIMBUS-7 MODE 5 SCAN

Figure 8. The simulated scan pattern for the Conically Scanning Radiometer, illustrating the center of the field of view for azimuth sweeps for each of the five telescope elevation angles for a small portion of an orbit.
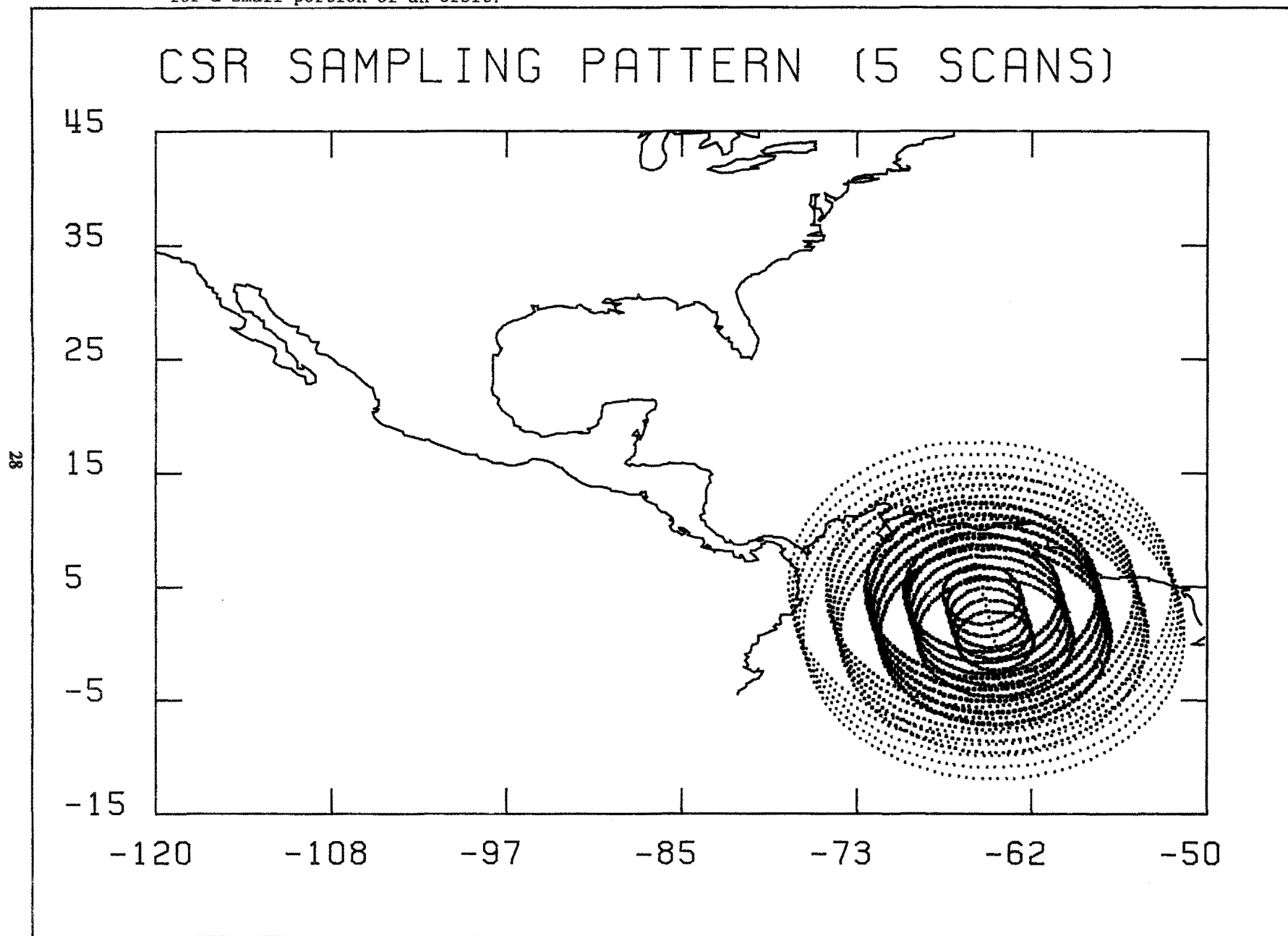

CSR SAMPLING PATTERN (5 SCANS)

ERBE SAMPLING PATTERN (33 SCANS)
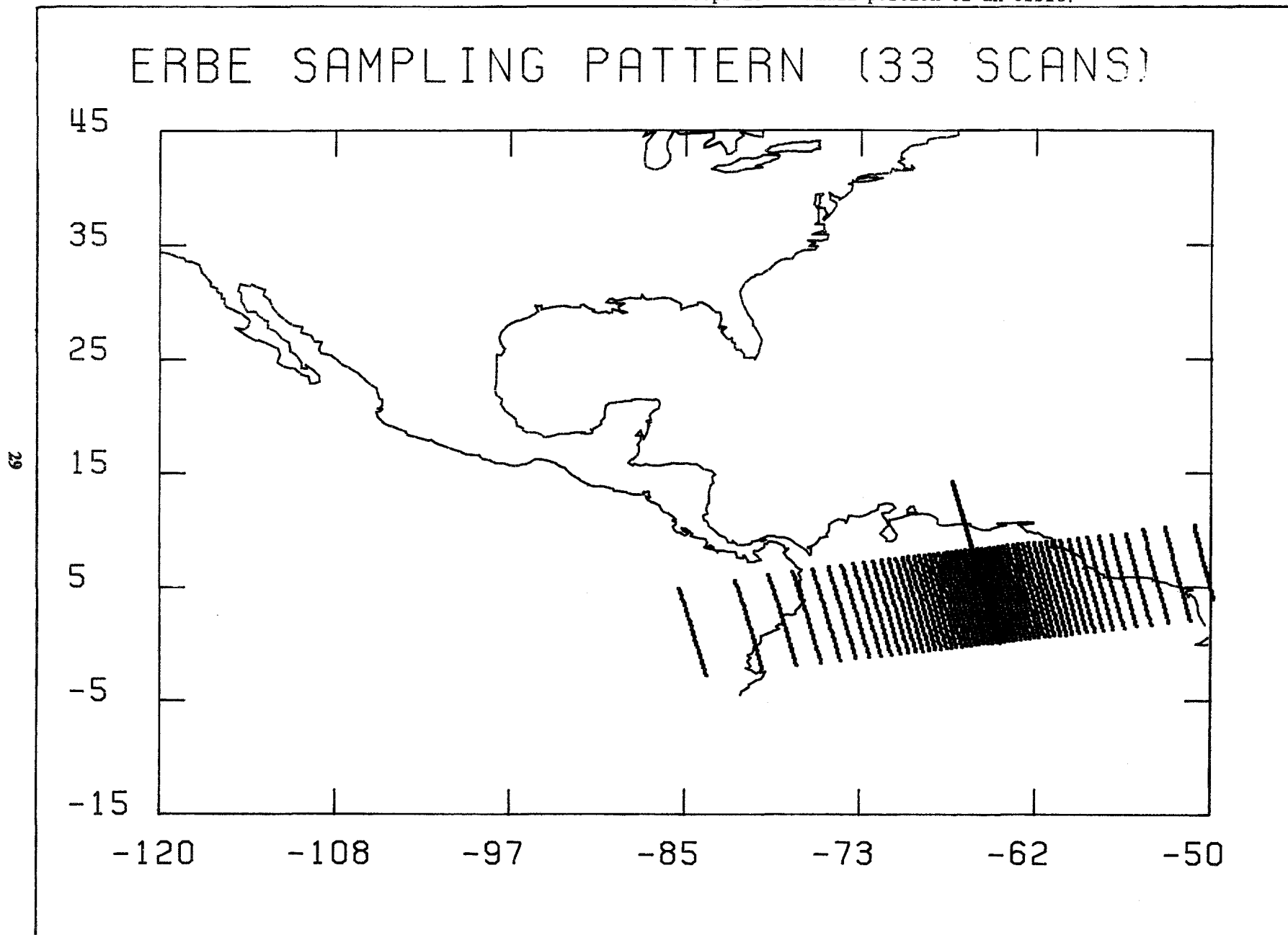
Table 6. Scan Characteristics of the Conical Scanning Radiometer			
Nadir Angle Position	Nadir Angle (°)	Sampling Rate (sec⁻¹)	Number of Observations
1	0	0.4	1
2	19.8	25	61
3	35.1	43	104
4	45.2	53	128
5	51.8	59	142
6	56.0	62	150

2.2.2.4 The Active Cavity Array (ACA)

The ACA (Hoffman, 1989) consists of a fixed array of radiometers which sample the entire visible Earth every 3 seconds. A biaxial scan is achieved by this sensor concept without any form of mechanical motion. Two configurations have been proposed: an 85-detector array with an effective resolution of 250 km and a 271-detector array with a resolution of about 150 km. In this work, we simulate the higher resolution 271-detector array. The individual detectors sample in 12-concentric rings about nadir, counting the nadir detector as a ring. Table 7 lists the nadir angle to the midpoint of each ring and the number of detectors required to cover the ring. In viewing the entire Earth disk, the ACA simulation samples radiances from approximately 300,000 M1 grid elements every three seconds. Due to the high sampling rate and contiguous nature of the fields of view, this simulation requires the processing of approximately two orders of magnitude more data than the other scanner designs (Figure 10).

2.2.2.5 The CERES-I Scanner

The CERES-I (Barkstrom, February 1988 personal communication) is derived from the ERBE cross-track scanner design, but with some significant changes. First, the scan parameters have been adjusted to increase the amount of data gathered by a cross-track scanner by almost 80%. This results from the combined effect of reducing the scan period from 4 to 3 seconds, increasing the angular scan velocity across the Earth from 66.7 to 88.9 degrees per second, and increasing the sampling rate from 30 to 53 observations per second. The CERES-I cross-track radiometers now collect 75 observations per scan or, on average, 25 observations per second. Secondly, the CERES-I FOV has been reduced from a 52-km diameter footprint at nadir to a 40-km diameter footprint, corresponding to a full cone angle of 2.7 degrees. In addition, the cross-track scanner has been complemented by a second identical scanner which observes along a scan azimuth which varies with time. For this second scanner, the azimuth angle changes at 5° per second. Thus, the second scanner rotates 180° and sweeps out a full 360° of coverage every 36 seconds. The radiometers of the CERES-I instrument sample each 2.5° target area near the subsatellite track approximately 300 times in one orbit. For target areas at the edge of the scan swath, this rate drops to about 20 samples (Figure 11).

2.2.3 Simulation of a Radiometer Measurement

Throughout the orbital simulations, an effort is made to portray the candidate radiometers in a form which closely resembles their conceptual designs. Scanning patterns and data rates, for example, are

Figure 10. The simulated scan pattern for the Active Cavity Array, illustrating the center of each of the fields of view for a 271 element configuration for a small portion of an orbit.

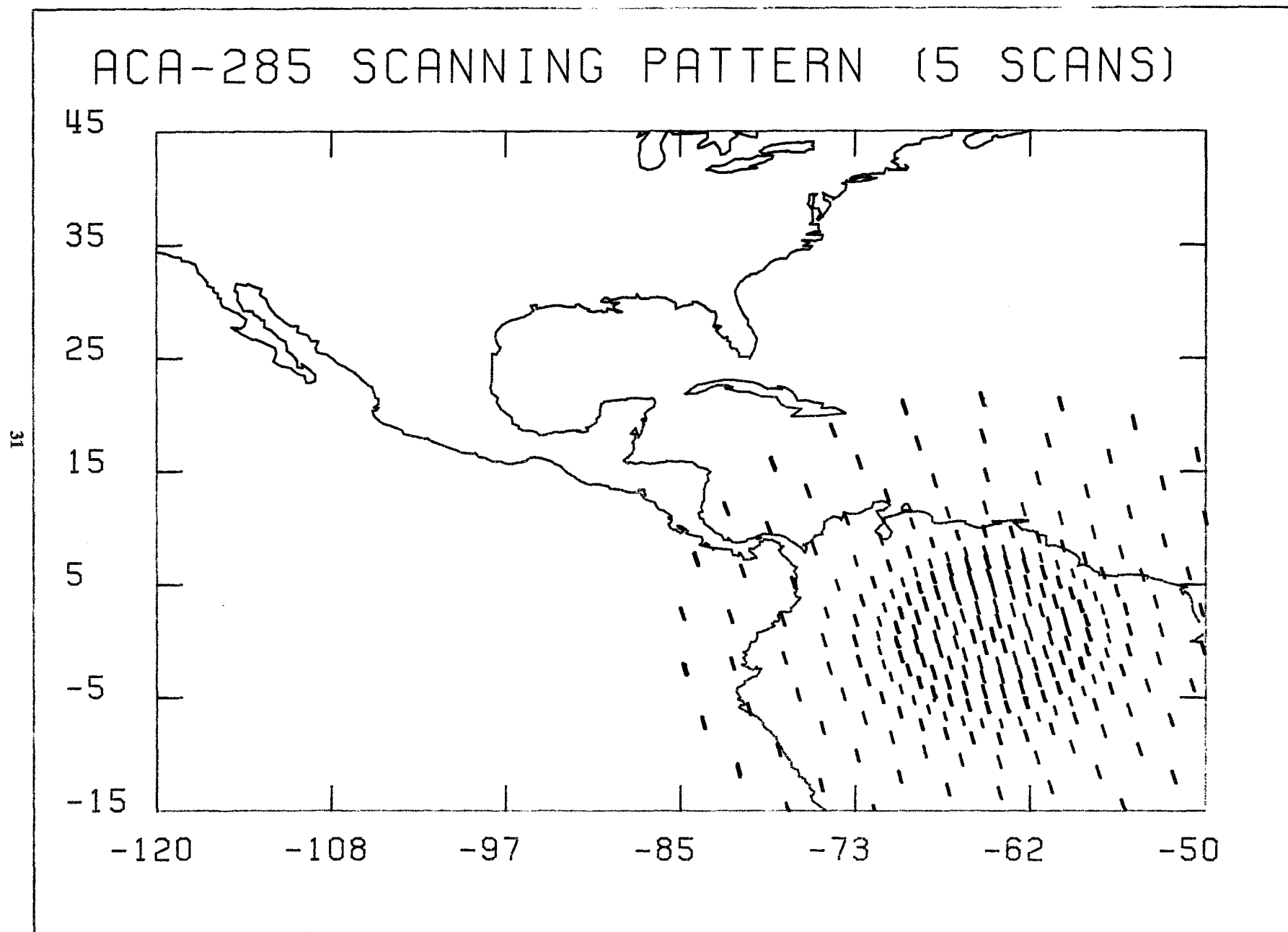

ACA-285 SCANNING PATTERN (5 SCANS)

Figure 11. The simulated scan pattern for the CERES-I Instrument, illustrating the center of the field of view for the cross track scanner and a similar, but azimuthally slewing, scanner for a small portion of an orbit.
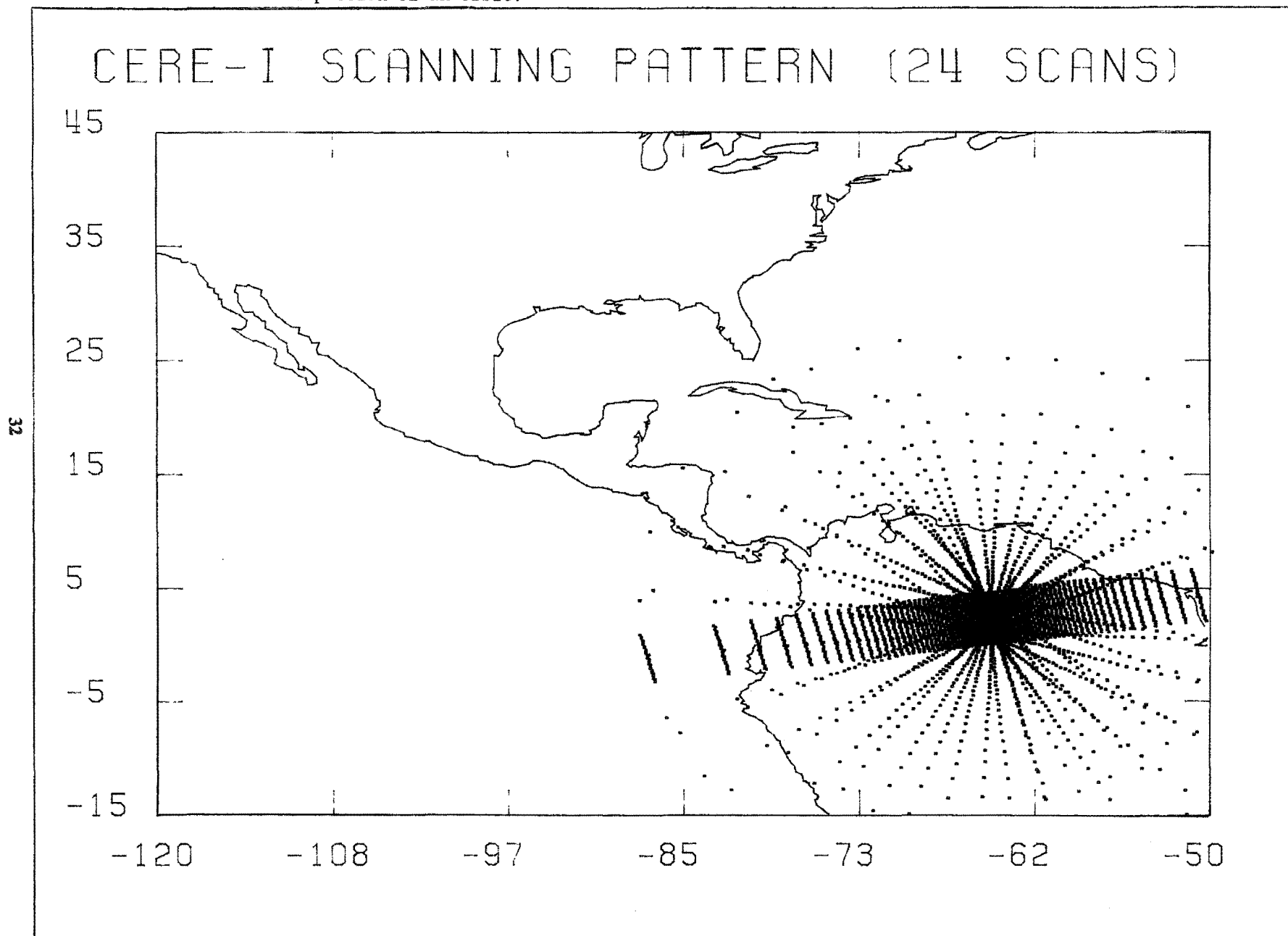
Table 7. Scanning characteristics of the Active Cavity Array radiometer.			
Nadir Angle Ring	Telescope Nadir Angle	Satellite Zenith Angle	Number of Detectors
1	0.0	0.0	1
2	10.2	11.5	6
3	19.7	22.2	13
4	28.0	31.8	19
5	34.9	40.1	25
6	40.6	47.0	31
7	45.2	52.9	38
8	49.4	58.6	32
9	53.7	65.0	28
10	57.6	71.7	26
11	60.4	77.9	26
12	61.9	82.7	26

rigidly adhered to and the projected Earth location of the radiometer optical axis is used to define the position of individual observations. Other characteristics, however, are more difficult to reproduce and are, therefore, represented by similar, but not identical, designs. Footprint shapes, for example, although not exactly reproduced in our simulation, are, nevertheless, represented by FOV's which conserve the solid angle of the IFOV and remain fixed or variable according to the basic prototype design. The CERES-I, CSR, and ERBE radiometers have circular or nearly circular, fixed FOV's which are represented as diamond shapes. The elevation angle of the corner points is determined so that at nadir, the same area is enclosed by the diamond shape as by the original circular FOV footprint. For the ACA and Nimbus-7 radiometers, the design FOV's have curvilinear shapes which terminate in four well defined corner points. These FOV's we represent by rectangular shapes whose sides terminate at the same corner positions as specified in the actual design. In this case, while individual footprints do not necessarily conserve area, over a complete scan cycle nearly the same total area is mapped out in our simulation as conceived in the radiometer design.

Scanner observations from space are modeled as an integral over the radiometer FOV in the form

$$m_{sat} = \int_{FOV} R_{ref} \cdot G \cdot d\Omega \qquad (14)$$

where the measurement value, m_{sat}, is the energy flux intercepted by the radiometer; R_{ref} is radiance at the TOA; G is the instrument point spread function including the time and angular response characteristics of the detector; and $d\Omega$ is an element of solid angle at the satellite. The instrument time response is assumed to be instantaneous and, for a flat plate sensor, the angular response varies as the cosine of the angle of incident radiation to the sensor normal. As the range in this angle is less than $5°$ for the FOV

apertures studied, it is set to unity for all scanners. In Figure 12, multiple observations from a passing polar orbiter are illustrated which view the same 10-km pixel element at the TOA from different look angles. Although the flux of this element was initially derived from GOES radiances using Eq.(9) and is the same for each observation, distinct upwelling radiances are viewed at each measurement and are obtained from Eq.(13). These radiances differ among themselves because the viewing geometry to the given pixel changes for each observation. They differ from the input GOES radiance for the same reason and also because the anisotropic models used to construct the reference radiances (ρ') are not necessarily the same as the ERBE models (ρ) used to derive the reference field flux. The integral of Eq.(14) used to obtain the satellite radiances is evaluated numerically as a discrete sum over all 10-km resolution elements whose midpoints fall within the instantaneous footprint of the radiometer. This is illustrated in Figure 13 where the four corners of a Nimbus-7 ERB FOV are shown projected to the TOA and geographically located. The sides of the footprint are defined by linear interpolation in latitude and longitude between the corner points. During numerical integration, small errors are incurred in the measurement value by including within the discrete summation contributions from portions of grid elements which lie outside the footprint boundary, and by excluding portions of other grid elements which lie within the footprint boundary. These errors tend to cancel for individual measurements and, more so, when many observations are averaged within 2.5° regional areas. Further treatment of this error source is given in the next section.

Without the need for an intermediate calibration step, the measurement values of Eq.(14) are converted directly to satellite measured radiances, R_{meas}. These are average values of the radiance over the radiometer FOV and are obtained from the measurement equation by bringing the mean radiance, $\overline{R}_{ref}$, outside the integral sign and rearranging in the form

$$R_{meas} = \overline{R}_{ref} = (\int_{FOV} d\Omega)^{-1} \cdot m_{sat} \tag{15}$$

where the instrument point spread function G no longer appears. Eq.(15) shows that satellite measurements are converted to measured radiances through normalization by the solid angle FOV of the radiometer. In practice this is a known design parameter, but in our simulation it is evaluated for each observation to account for the minor changes in FOV size that occur during numerical integration and the TOA interpolation used in defining footprint boundaries.

2.2.4 Discretization Error

Discretization error is depicted in Figure 13 where the exact, rectangular area of an observation footprint is approximated by the irregular shape shown shaded in the figure. In convolving radiances over the shaded area instead of within the correct boundary, an error in the measurement integral, Eq.(15), is made. This error is estimated by considering that the midpoint of grid elements lying along the footprint boundary have an equal, 50% probability of falling within the true rectangular outline. If they are within the boundary, they will be included as part of the discrete integration; otherwise they are omitted. This assumption, while not litterly correct for neighboring pixels whose probabilities are serially correlated, is useful nevertheless because it provides realistic variations in area for the random process of discretizing
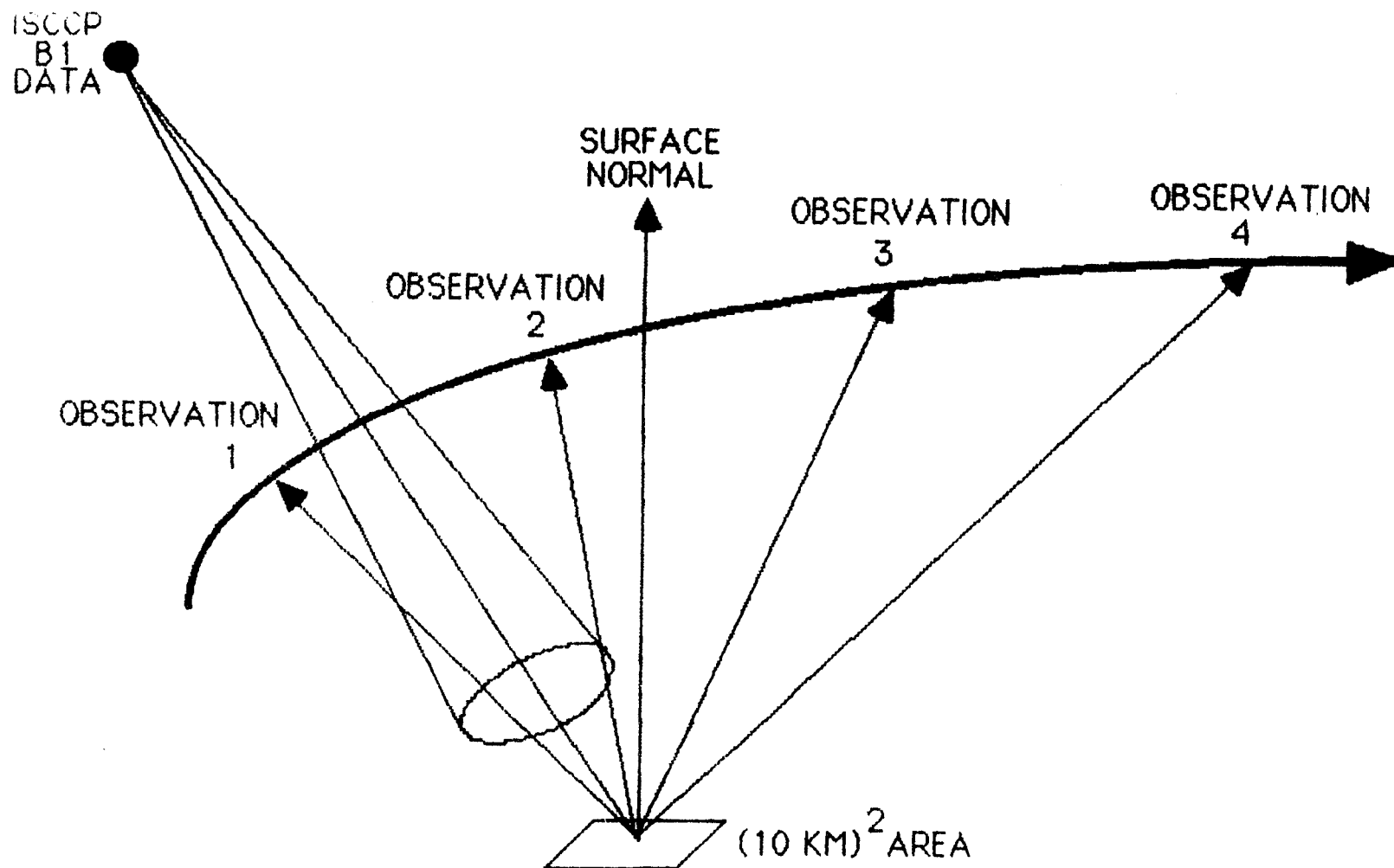
34

Figure 12. Depending on the scan pattern, multiple IFOV's may view individual elements of the truth field. The flux at the TOA, as derived from the ISCCP B1 data and coupled with a complete bidirectional reflectance model set, can be used to generate anisotropic radiances for each of the measurements.
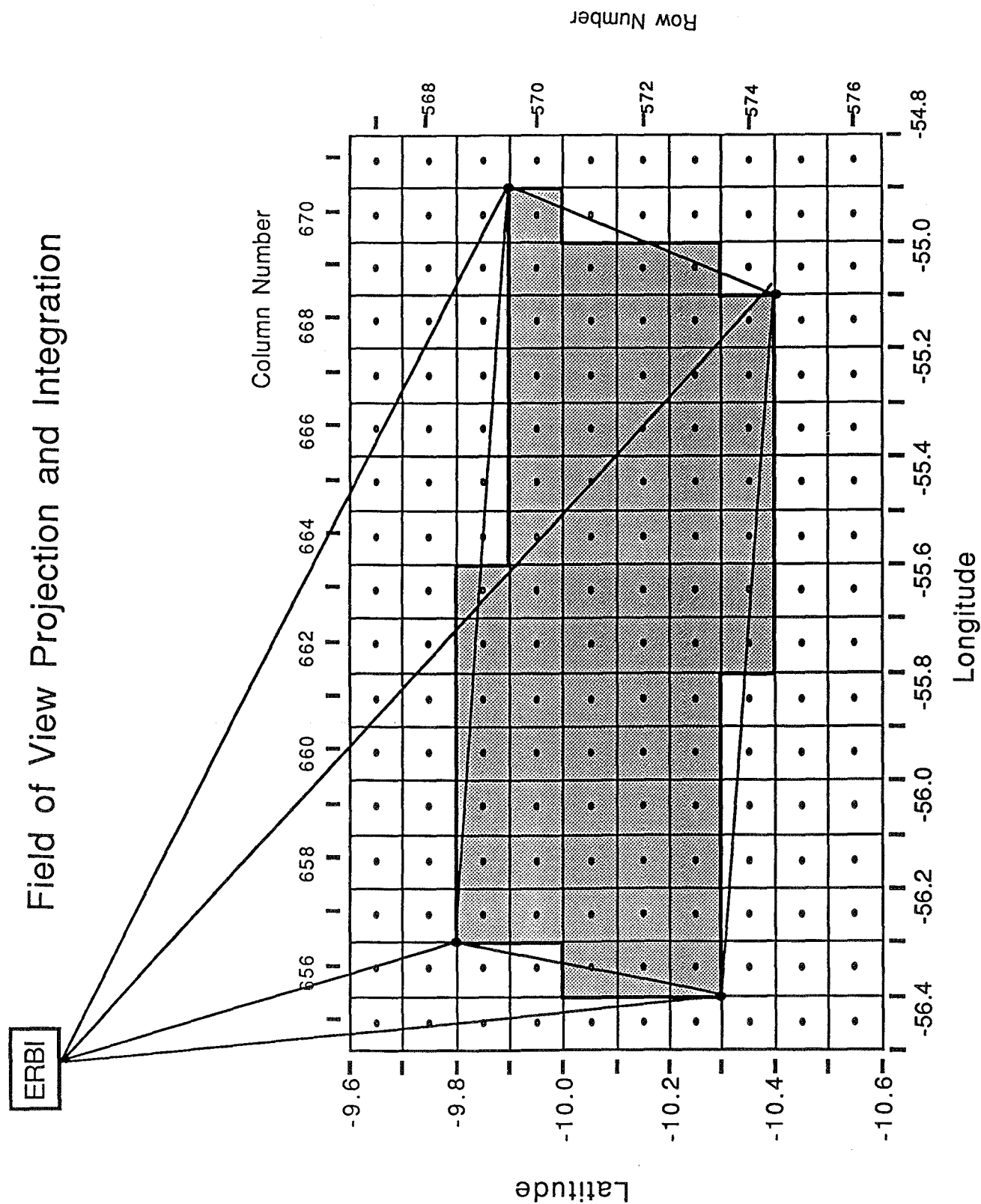
Figure 13. Illustration of the integration over the field of view of a single Nimbus-/ ERB scanner IFOV at the top of the atmosphere. For this observation, an area of about 7000 km² was viewed, allowing the radiances from 70 10-km truth elements to participate in the measurement integral.

36

a smooth boundary. This is done using the binomial probability distribution to obtain the mean, $\bar{n}$, and standard deviation, $\sigma_{\bar{n}}$, of the number of edge pixels included in a numerical quadrature when the total number of perimeter pixels is N. These are given by

$$\bar{n} = p \cdot N = \frac{N}{2} \tag{16}$$

$$\sigma_{\bar{n}} = \sqrt{p \cdot (p - 1) \cdot N} = \frac{\sqrt{N}}{2} \tag{17}$$

where p is the probability (taken to be 0.5) that any one pixel is included. From Eq.(16) we deduce that, on average, the area of the true footprint is preserved. This occurs because, although only half of all perimeter pixels are included in the numerical sum, the integration is over the full area of those selected. From Eq.(17) we note, however, that $\sigma_{\bar{n}}$ depends on $\sqrt{N}$ and, thus, the range of variation in footprint size differs for different FOV designs and satellite-viewing angles.

When a footprint is viewed as having a rectangular shape of n_s pixels on a side (i.e., a linear resolution n_s x 10 km), the measured radiance without discretization error, R_{WODE}, can be expressed as

$$R_{WODE} = \frac{SR}{n_s^2} \tag{18}$$

where SR is the summation of radiance over all n_s^2 pixels included within the footprint and variations in solid angle weighting are neglected. When discretization error is present, the summation represented by SR is extended or omitted over a number of pixels, $\sigma_{\bar{n}}$, located along the perimeter of the footprint. In this case a computed radiance with discretization error, R_{WDE}, is computed as

$$R_{WDE} = \frac{SR \pm \sigma_{\bar{n}} \cdot (R_{WODE} \pm \sigma_R)}{n_s^2 \pm \sigma_{\bar{n}}} \tag{19}$$

where σ_R is the standard deviation of the TOA radiance field and the sign of the first $\pm$ in the numerator is the same as the sign chosen in the denominator. The new terms appearing in the numerator and denominator of Eq.(19) represent the additional radiance and area that result when $\sigma_{\bar{n}}$ pixels are added to the correct measurement of Eq.(18). Eq.(19) is rearranged by factoring n_s^2 from the terms of the denominator and expanding the remaining factor in a Taylor series. After simplification and cancellation of terms, the discretization error, defined as

$$DE = R_{WDE} - R_{WODE} \tag{20}$$

becomes to first order in $\sigma_{\bar{n}}/n_s^2$

$$DE = \pm \frac{\sigma_{\bar{n}}}{n_s^2} \cdot \sigma_R \tag{21}$$

When expressed as a relative error, RDE, Eq.(21) becomes

$$RDE = \frac{\sigma_{\bar{n}}}{n_s^2} \cdot \left(\frac{\sigma_R}{R_{WODE}} \right) \tag{22}$$

Under most conditions σ_R/R_{WODE} is less than 0.5, but for a worst-case scenario we set this ratio to unity. Eq.(22) may now be evaluated for any of the radiometer designs. In particular, for the ERBE design at nadir, n_s is about 5 pixels and the number of perimeter pixels, N_{ERBE}, is approximately

$$N_{ERBE} = 2 \cdot n_s + 2 \cdot (n_s - 2) = 16 \tag{23}$$

Using this value in Eq.(17), we find that the standard deviation in the size of an ERBE footprint due to discretization error is 2 pixels or that $\sigma_{\bar{n}} = 2$. When this value is used in Eq.(22) and n_s is set to 5, we find that the discretization error of individual measurements for the ERBE instrument is typically 8% at nadir. When this error is present randomly in the 90 or so observations taken within 2.5° target regions, the relative error in regional mean satellite radiance, RDE($\bar{R}$) is approximately

$$RDE(\bar{R}) = \frac{8\%}{\sqrt{90}} \approx 1\% \tag{24}$$

2.3 TOP OF THE ATMOSPHERE MEASUREMENT INVERSION

The measured satellite radiances obtained during orbital simulations are reduced individually to TOA fluxes using MLE and the ERBE reference models. A schematic view of this procedure is illustrated in Figure 14 where a shortwave and longwave radiance pair, surface geography at the FOV midpoint and the ERBE models are used as inputs to MLE. These guide the selection of the most probable cloud amount category fitting the observed data and the identification of a scene category.

In this step we note that MLE cloud classification is based upon the ERBE reference models and the relationship of the measured radiances to the ERBE mean radiances for the four cloud categories. For anisotropic experiments in which $N \neq 1$ (Eq.10), the Earth source radiation is no longer accurately described by the reference models and, for these cases, there is no guarantee that the MLE-derived cloud selection is actually representative of the "true" cloud amount within an observation footprint. A scene identification is made, nevertheless, and TOA fluxes are derived using the ERBE reference models.
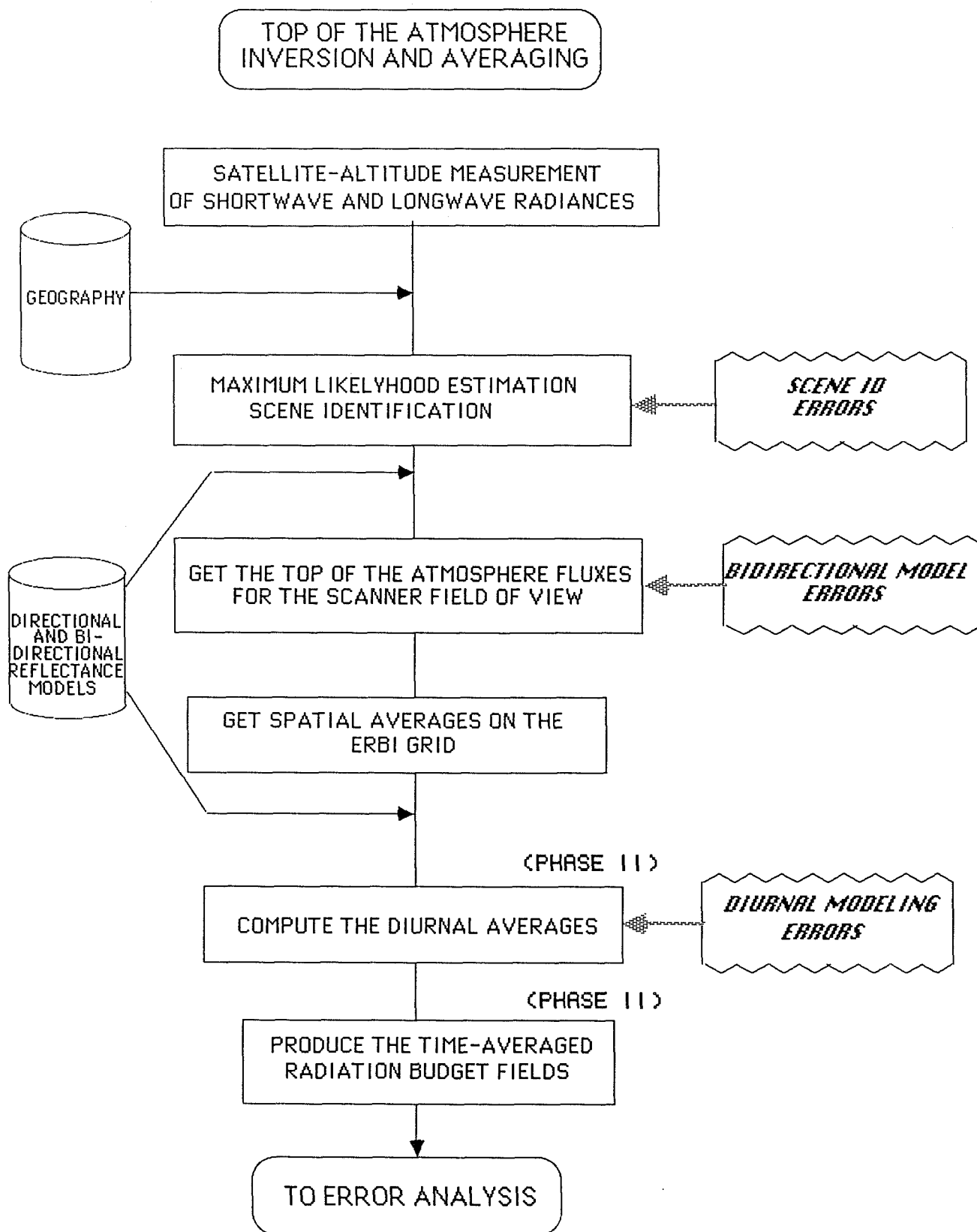
Figure 14. The procedure for generating TOA measurement fields from satellite altitude radiance measurements involves the scene classification to obtain cloud amount, the use of standard angular dependence models to recover TOA fluxes, and then spatial averaging of all observations within each 2.5° study region. The diurnal average errors will be presented in Phase II of this research, in a subsequent publication.

Again for anisotropic experiments in which $N \neq 1$, the reference models do not provide a correct picture of the angular distribution of the "true" source radiances and potentially large errors in flux estimates can occur. The individual FOV estimates are sorted into 2.5° target areas and averaged into regional flux estimates.

2.3.1 MLE Scene Identification

The probability that an ERBE scene category (i.e., surface geotype and cloud category) produces an observed longwave and shortwave satellite radiance pair, R_{sw} and R_{lw}, is determined from the relation for a normal distribution

$$P(ISCN) = (2\pi \cdot \sigma_{sw}(ISCN) \cdot \sigma_{lw}(ISCN) \cdot [1 - r^2(ISCN)]^{1/2})^{-1} \cdot \exp(-G/2) \quad (25)$$

where P is the probability density function, ISCN is a scene category index from 1 to 12, σ_{sw} and σ_{lw} are, respectively, shortwave and longwave standard deviations of the reference radiances describing the ERBE mean world, r is the correlation between the shortwave and longwave model reference radiances and

$$G = [1 - r^2(ISCN)]^{-1} \cdot [G1^2 - 2 \cdot r(ISCN) \cdot G1 \cdot G2 + G2^2] \quad (26)$$

where

$$G1 = \sigma_{sw}^{-1}(ISCN) \cdot (R_{sw} - \bar{R}_{sw}(ISCN))$$
$$G2 = \sigma_{lw}^{-1}(ISCN) \cdot (R_{lw} - \bar{R}_{lw}(ISCN)) \quad , \quad (27)$$

and $\bar{R}_{sw}$ and $\bar{R}_{lw}$ are the ERBE reference shortwave and longwave mean radiances. Throughout equations 25 through 27 the various ERBE model parameters depend not only on scene category but also on viewing and solar geometry. Indices denoting the latter have been omitted for clarity. The probability density in Eq.(25) is computed for the different scene types corresponding to the subset of four ERBE cloud amount categories for the given surface geotype at the FOV midpoint. The scene category yielding the largest probability is chosen as representative of the observation and used to select a model for the radiance-to-flux inversion. A detailed description of the MLE approach in the retrieval of TOA flux estimates from satellites is given in Wielicki and Green (1989).

In addition to probability calculations, the MLE procedure used here includes many of the refinements used in ERBE for the retrieval of TOA fluxes. Here they are applied both in the development of reference fields from GOES radiances and in the TOA inversion of simulated polar orbiter measurements. The implementation of these refinements for each application is compared in Table 8. Notice that in item four of the table, 8 W/m² were removed from the ERBE model LW fluxes in order to recover the archived Nimbus-7 data from which the ERBE models were derived (Suttles et al., 1989; page 4 and the footnote on page 6). When this is done, broadband radiances constructed from the mean fluxes and limb-darkening models are consistent with the Nimbus-7 radiances used by Minnis and Harrison in developing their GOES2-to-Nimbus-7 longwave spectral regression, Eq.(7). The rejection criteria (the last four items in the table) are also the same as used by the ERBE team in processing scanner radiances and are

followed here, as well, in the inversion to TOA. In the development of a truth field, none of the rejection criteria are used since we require flux estimates at all 10-km resolution grid elements of the study domain.

Table 8. Summary of the MLE Tuning for Application to the ERBI Simulation Study		
Tuning Parameter	Development of Truth Field	Inversion to TOA
Trilinear interpolation of SW anisotropic factors	Y	Y
Bilinear interpolation of LW anisotropic factors	Y	Y
Removal of the 8 W/m² bias shift added by the ERBE team to the LW mean fluxes	Y	Y
Diurnal LW adjustment over* land and desert (ERBE crude model) for all cloud amount categories	Y	Y
Clear thresholds for combinations of LW and SW radiances	Y	Y
Use of LW/SW correlation factor	Y	Y
Use of a priori cloud probabilities	N	N
Rejection of small probabilities (i.e., Q > 16σ	N	Y
Rejection of shortwave anisotropic factors > 2	N	Y
Rejection of satellite zenith angles > 70 @ FOV midpoint	N	Y
Rejection of solar zenith angles > 86 @ FOV midpoint for shortwave	N	Y

*Wielicki and Green (1989)

2.3.2 Computation of Satellite-Derived Fluxes

From MLE, a cloud amount and scene category are associated with every pair of simulated shortwave and longwave satellite radiances. Knowing the relative Earth-Sun-satellite geometry, the reference model anisotropic factors are interpolated to the solar zenith and satellite-viewing angles at the center of the observation footprint, as in the ERBE procedure, and a satellite-derived flux estimate, F_{meas}, computed as

$$F_{meas} = \rho_{ref}^{-1}(ISCN) \cdot \pi \cdot R_{meas} \tag{28}$$

where the explicit scene dependence of ρ_{ref} is indicated. Eq.(28) shows that, although variations in the Earth-atmosphere system give rise to measured radiances more or less anisotropic than the mean ERBE radiances for a given scene (i.e., $N \neq 1$), the radiance-to-flux inversion process is, nevertheless, carried out using the reference models. The MLE method used here provides no additional information from which to glean the relative anisotropy of the observed atmosphere relative to the ERBE mean atmosphere so that, by necessity, the inversion procedure relies on the mean reference models.

2.3.3 Spatial Averaging Procedure

After conversion to fluxes, individual measurements are sorted into 2.5° target areas according to the location of the M1 grid elements containing their FOV midpoints. Within a target area, observations are excluded from further processing if either their solar zenith angles are greater than 86°, their satellite zenith angles are greater than 70°, or their shortwave anisotropic factors are greater than 2; multiple observations located at the same M1 grid element are averaged. After these initial steps, a target area arithmetic mean is formed by averaging over the sampled 10-km grid elements. The resulting regional satellite flux estimates are compared against the TOA reference field which is averaged over all 625 M1 grid elements within a 2.5° region.

2.4 ERROR ANALYSIS

Discrepancies between satellite-derived, instantaneous regional flux estimates and their actual values at the TOA arise from two fundamentally different operational problems: One is sampling in space, while the other is sampling in angle about a given spatial position. These are referred to hereafter as spatial and angular sampling error components.

2.4.1 Spatial Sampling

In the case of spatial sampling, errors result from the nonuniform viewing of a given target region, due to orbital trajectory and radiometer scanning characteristics. Here an irregular distribution of observation points and satellite-viewing angles produce an assortment of scattered and overlapping footprints within the target area. A problem exists because it is not customary, under conventional data processing techniques, to consider the unequal viewing of the underlying field when combining these measurements to form an areal average. Typically, the satellite estimate is simply an arithmetic average over all individual observations whose FOV midpoints fall within the designated target area. This procedure yields a nonuniformly weighted mean of the TOA field rather than the desired equally weighted mean. Those elements of the field lying within multiple overlapping FOV's will appear many times in the satellite measurement average, while elements unviewed by any observations are absent entirely from the satellite average. Furthermore, there are always some observations falling near the boundaries of a target area whose FOV's spill over into surrounding neighboring targets. These observations, when included in the target mean, contaminate the estimate by adding extraneous data to the sum. If a suitable weighting procedure were initiated as, for example, a deconvolution technique, a surface fitting and integration procedure, or indirectly by eliminating or combining redundant observations, some improvement in remotely sensed fluxes could undoubtedly be made. If, however, observations are processed mainly by sorting and arithmetic averaging within target area regions, an inevitable error due to nonuniform sampling will result even in the hypothetical limit of infinite sampling rates. Of course, in this case, excess observations could be filtered to eliminate nonuniformities in spatial data coverage and thereby resolve the spatial oversampling problem.

In Figures 15a through 15d, sampling characteristics for the Nimbus-7 ERB, CSR, CERES-I, and ERBE scanners are summarized by giving the number of 0.1° area elements in a 2.5° target area that are

sampled a given number of times. By including the case of no samples taken, all area elements in a target area fall into one of the discrete sampling frequency categories given and, thus, the sum of all bar elements in the graph is 625. The pixel numbers given are average values for the 12 or so target areas lying east to west across a single orbital scan swath in the latitude zone from 2.5°S to the equator. The number of target areas seen varies slightly with scan design and on the equator-crossing longitude of the suborbital track. Within the zone, the population distribution varies from nadir to horizon, but only the average distribution is given in the figures. Under ideal conditions, viewing frequency populations would include no zeros, and would in fact be a spike with every truth-field element being considered the same number of times. Zero samples indicate that there are portions of the truth field which are not observed by the particular radiometer. Intuitively, one would expect that the characteristics of an ideal scanner would be: (1) one that views the Earth with no gaps in coverage; (2) one that views the Earth uniformly, with footprints that either do not overlap or that overlap 1/2 of an IFOV; and (3) one that has a sufficiently small FOV so that the boundary of the spatial cells (i.e., 2.5° in this case) is well resolved.

In the case of Nimbus-7 (Figure 15a), much of the domain is not sampled. When an element is viewed and participates in the formation of a measurement integral (an IFOV or footprint), it actually contributes to from one to six measurements. With the CSR (Figure 15b), a broad sampling distribution is obtained, as the multiple overlapping rings of observations do not yield a uniform imaging pattern. Near the subsatellite track, many observations can be taken, as portions of sequential scans overlap. Here more observations are taken than farther towards the edge of the orbit, as scans from different zenith angles view a given point on the Earth's surface. This broad pattern means that the TOA truth flux field will be quite unevenly weighted when the observations are added to form a 2.5° box average, suggesting that more advanced time and space processing strategies may be effectively employed here. With the ERBE cross-track scanner (Figure 15c), a tight imaging pattern is obtained. Each element is utilized about 3 ± 1 times, and practically all elements are viewed. This sampling pattern approaches the ideal distribution, where all elements of the truth scene contribute equally to the average. In the case of the CERES-I (Figure 15d), a pattern is obtained which is somewhat narrower and shifted to the left compared to the CSR pattern, yet somewhat broader than the ERBE pattern with a larger proportion of M1 elements unsampled. The cause of this pattern is the fact that the CERES-I is composed of a cross-track scanner similar to that of ERBE (though at a higher spatial resolution) combined with a second, slewing scanner. Although the proposed function of the slewing scanner is to collect angular data for the development of ADMs, its observations are grouped with those of the cross-track scanner throughout this study. Because of this, the spatial sampling characteristics of the CERES-I represented here may not be as favorable as for a simple, fixed-plane cross-track scanner alone. On the other hand, its angular sampling characteristics are likely to be better. Our purpose is to examine the magnitudes of the spatial and angular sampling errors that arise for the combined scanner observation dataset and to understand how changes in either radiometer component and/or the retrieval method might lead to reduced overall errors for the CERES-I. In the current design a sampling frequency of zero is seen to occur, on average, for 36 of the 625 area elements in a target area. This number may be misleading in that unsampled pixels occur only in target areas at the edge of the sampling swath. There the sampling has been cutoff at 70° of satellite zenith angle and numerous pixels toward the outer edge (i.e., farthest from nadir) of the target are now unsampled.

2.4.2 Simulation of Spatial Sampling Errors

During the processing of satellite data, observations are collected and averaged into target area regions. Regional errors in satellite flux estimates are defined by
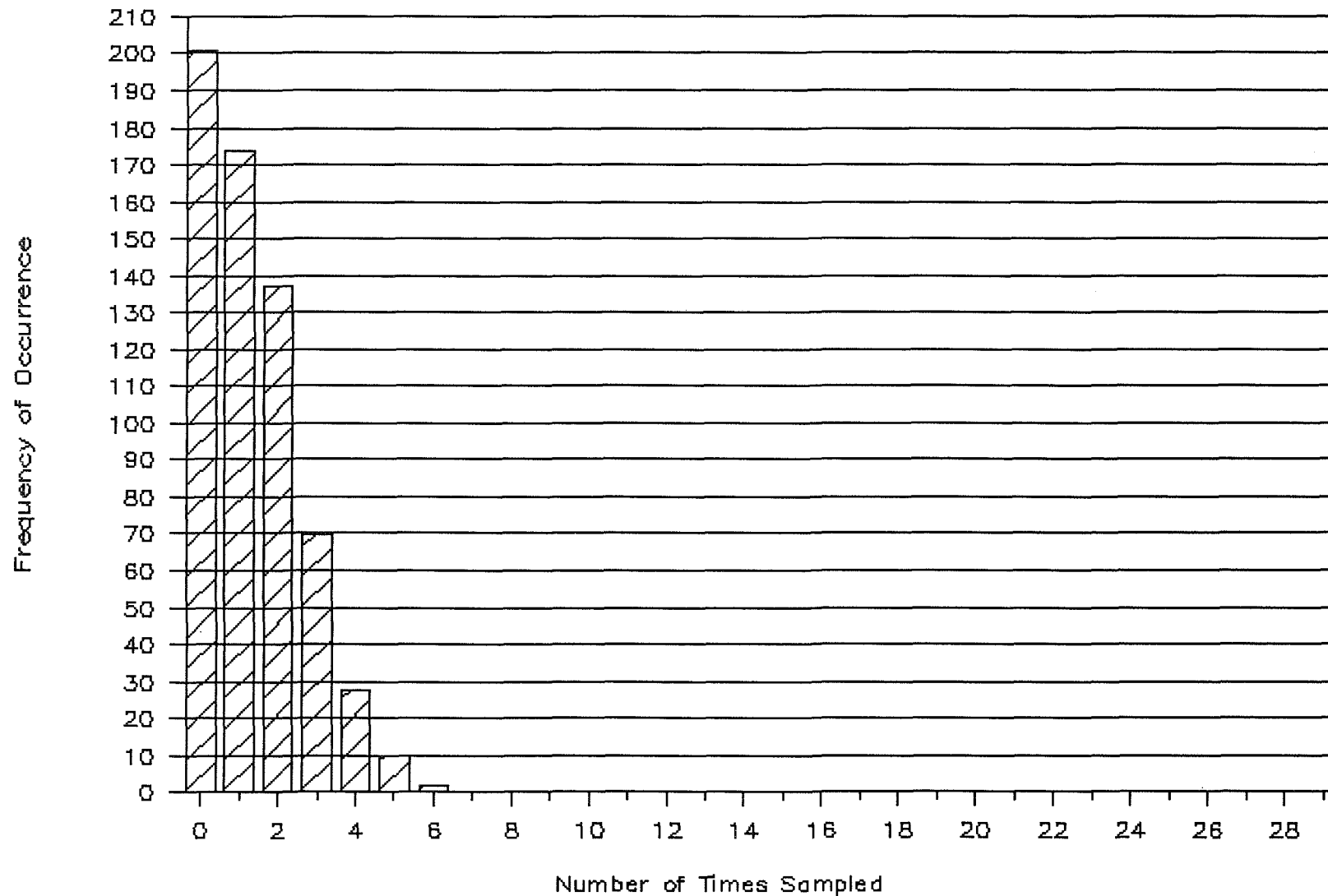
Figure 15a. A histogram of sampling frequency for the Nimbus-7 ERB scanner. This histogram illustrates the probability that individual truth elements in Band 19 (0° to 2.5°S latitude) will be viewed a given number of times for each orbit. For this scan pattern, many elements are not viewed while others are viewed one to four times.

44

Average Sampling Frequency for the 625

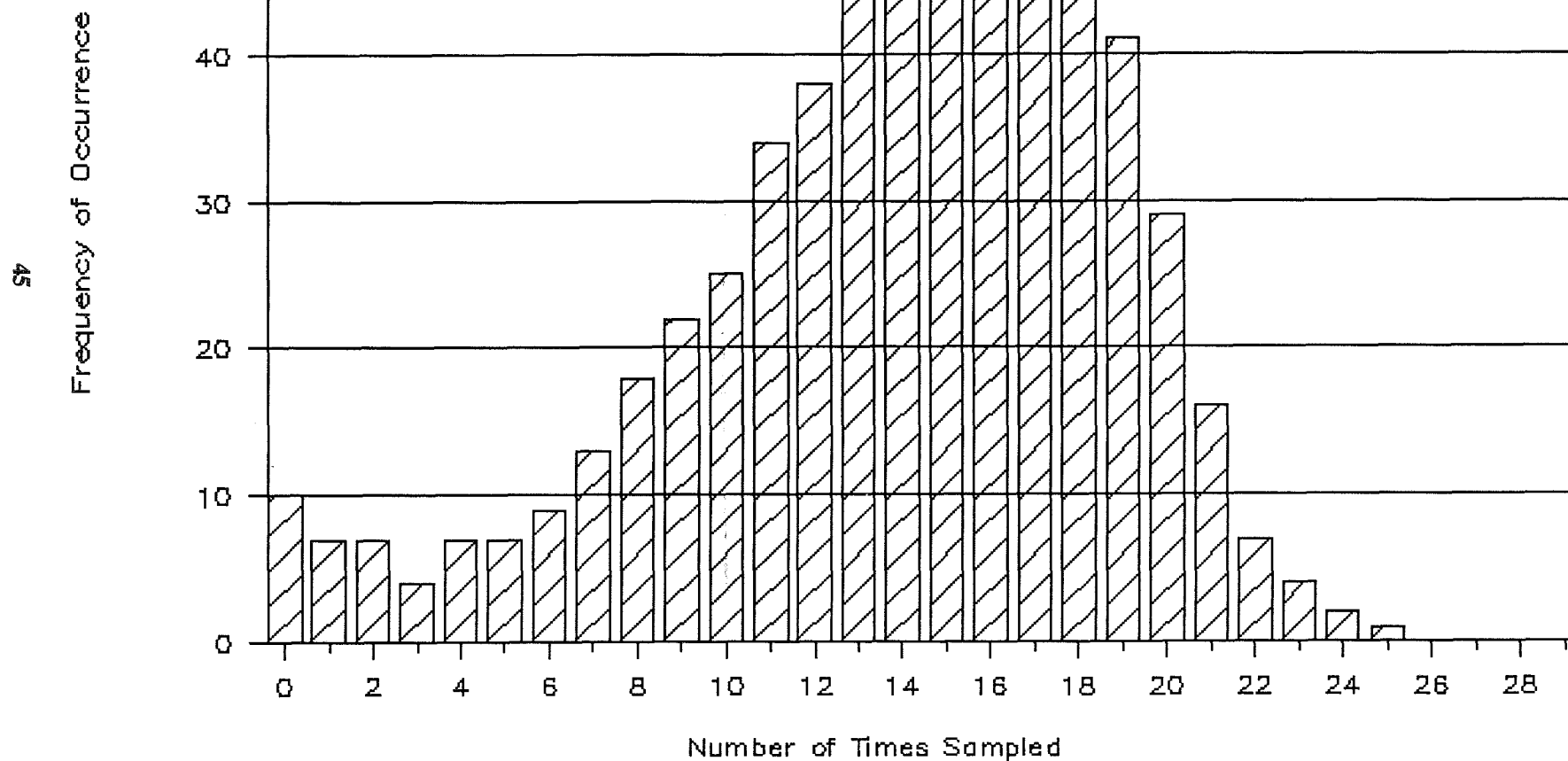## Grid Elements of a 2.5° Resolution Box: CSR—Band 19

Figure 15b. As in Figure 15a, but for the Conically Scanning radiometer. Here the quasi-random distribution of the IFOV's causes a wide range of sampling frequency.

Average Sampling Frequency for the 625

Grid Elements of a 2.5° Resolution Box: ERBE—Band 19
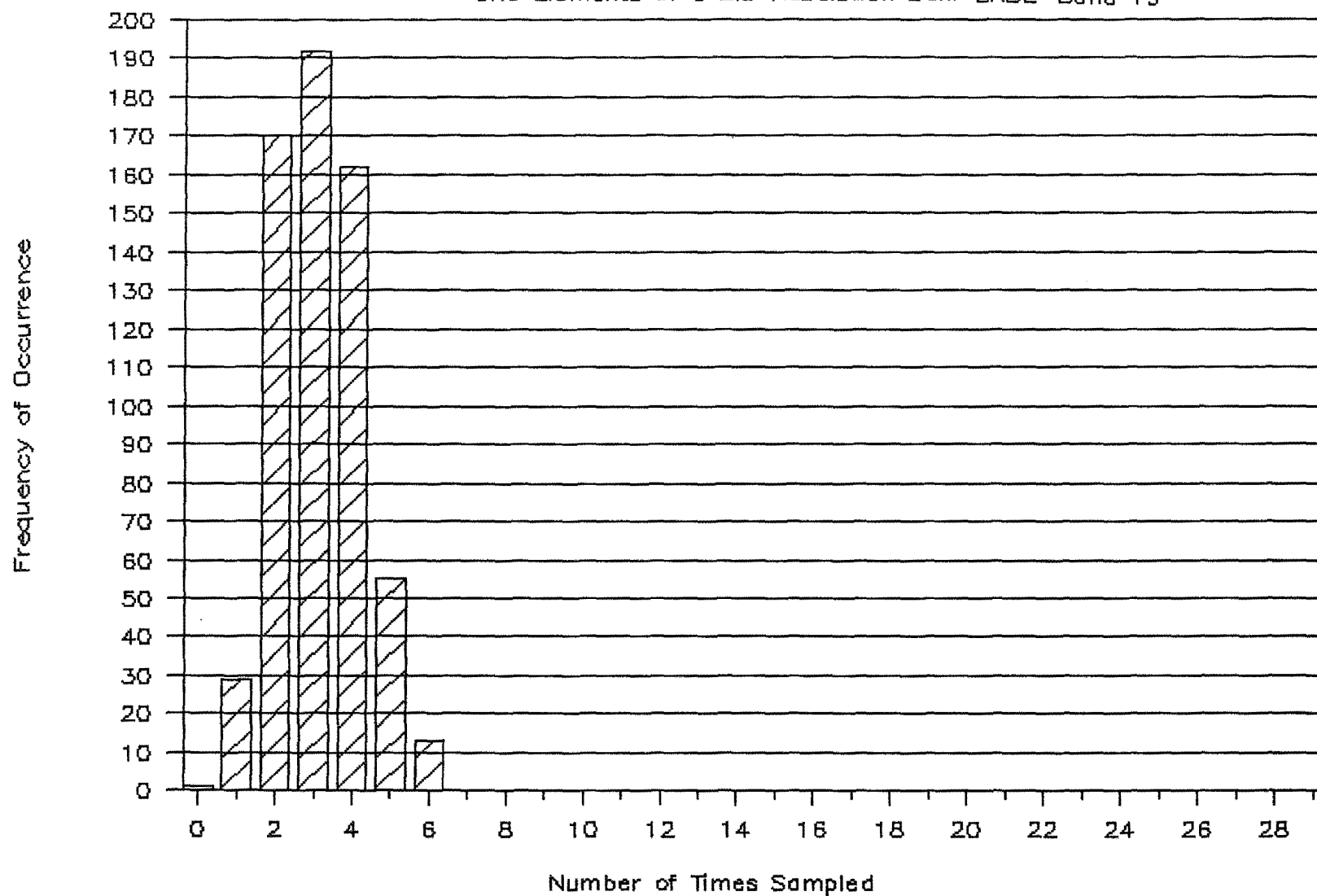
Figure 15c. As in Figure 15a, but for the ERBE Scanner. A cross track scanner is designed to optimize the spatial sampling characteristics, causing a very narrow (and highly desirable) distribution of sampling frequency.

Average Sampling Frequency for the 625

Grid Elements of a 2.5° Resolution Box: CERE—Band 19
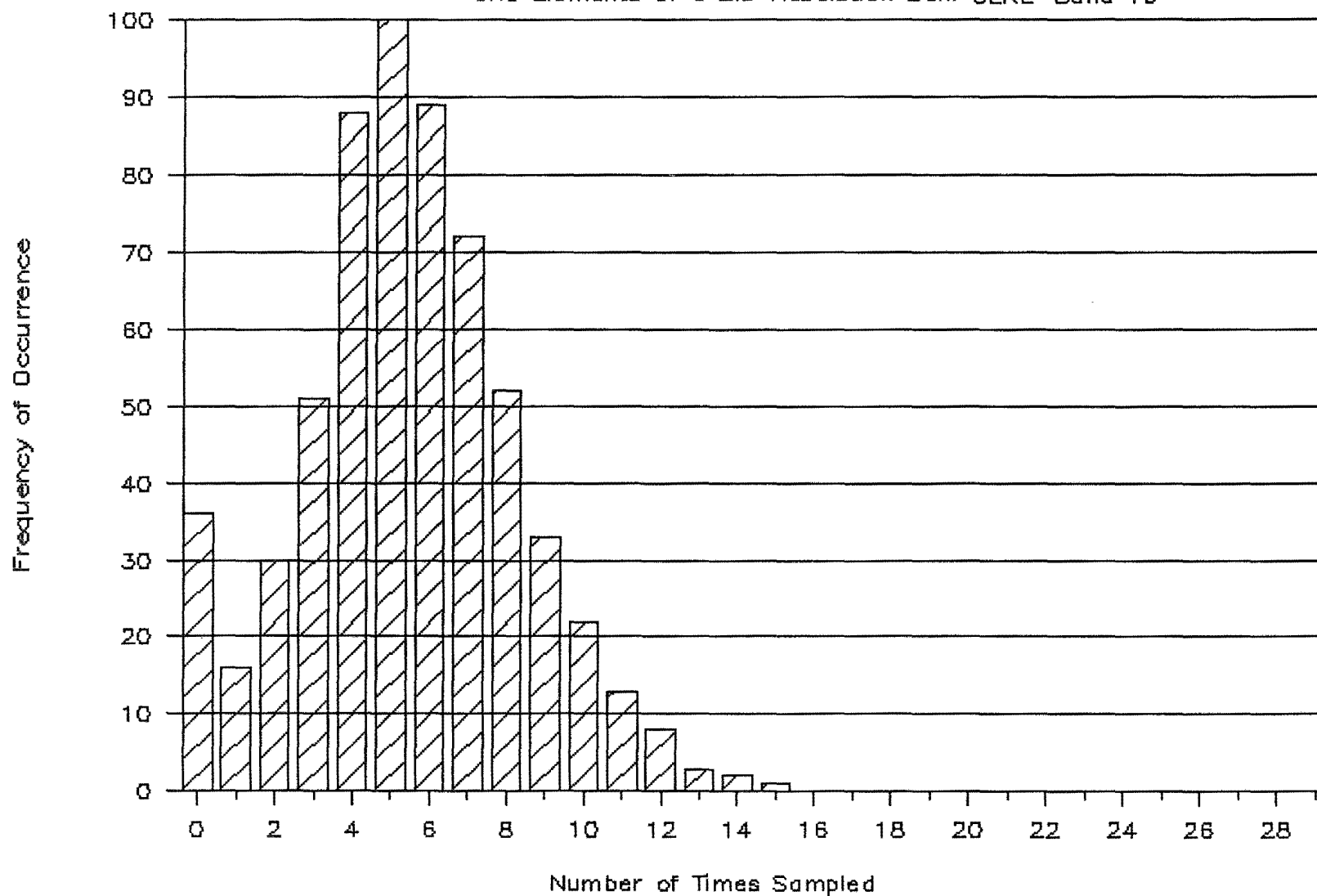
Figure 15d. As in Figure 15a, except for the CERES-I scanner. Due to the use of a pair of scanners, the sampling characteristics are a compromise between a conical scanner and a cross track scanner.

$$E = F_{MEAS} - F_{REF} \qquad (29)$$

where subscripts in capitals refer to regional parameter values. F_{REF} is the reference flux and is given by

$$F_{REF} = \frac{1}{625} \sum_{i=1}^{625} F_{ref,i} \qquad (30)$$

where the subscript i distinguishes the 25x25 10-km grid elements within a target area. F_{MEAS} is the satellite flux estimate and is obtained by averaging over the number, n, of sampled grid elements within the target (Section 2.3.3). F_{MEAS} is expressed as

$$F_{MEAS} = n^{-1} \cdot \sum_{i=1}^{n} F_{meas,i} \qquad (31)$$

where each FOV observation value, $F_{meas,i}$ is obtained from Eq.(28). Using successive substitutions of Eqs. (15), (14), and (13) in Eq.(28) with G set to unity, and extracting a flux and solid angle weight mean anisotropic factor, $\bar{\rho}'$, the equation becomes when evaluated numerically for j M1 elements within an FOV

$$F_{meas,i} = (\bar{\rho}'/\rho_{ref})_i \cdot \sum_{j} F_{ref,j} \cdot \Delta\Omega_j / \sum_{j} \Delta\Omega_j \qquad (32)$$

where the quotient of finite sums in Eq.(32) is the solid angle weighted mean reference flux, $\bar{F}_{ref,i}$, over the ith FOV. Eq.(32) is then conveniently written as

$$F_{meas,i} = (\bar{\rho}'/\rho_{ref})_i \cdot \bar{F}_{ref,i} \qquad (33)$$

and Eq.(29) becomes for the 2.5° latitude/longitude elements

$$E = \frac{1}{n} \sum_{i=1}^{n} (\bar{\rho}'/\rho_{ref})_i \cdot \bar{F}_{ref,i} - F_{REF} \qquad (34)$$

In the occasional circumstance where multiple scanner observations fall within the same 0.1° grid element, F_{meas} is defined to be the average of the individual measurement values (Section 2.3.3) centered

within the given pixel. For these grid elements, $\overline{F}_{ref,i}$ of Eq.(33) becomes an average over two or more FOV's and the ratio of anisotropic factors $(\overline{\rho}'/\rho_{ref})_i$ becomes an average flux-weighted mean ratio.

In Eq.(34), angular sampling errors are manifested through the ratio $\overline{\rho}'/\rho_{ref}$. If it were possible to correctly choose an inversion model in which ρ_{ref} were always equal to $\overline{\rho}'$, this ratio would become unity for all observations and the angular sampling problem would vanish. Any residual error would be attributable to the spatial sampling problem. This leads to a definition of the regional spatial sampling error as the discrepancy between satellite-derived TOA flux estimates and the underlying truth field when no uncertainty in the application of ADM's to the TOA reduction of the satellite observations exists,

$$E_{SPATIAL} = E(\rho_{ref} \rightarrow \overline{\rho}') = \frac{1}{n} \sum_{i-1}^{n} \overline{F}_{ref,i} - F_{REF} \tag{35}$$

Important to note in Eq.(35) is that spatial sampling errors involve only the FOV configuration of the radiometer, through the $\overline{F}_{ref,i}$'s, and its designed scanning pattern. No observed radiances nor ADM's are involved. In a simulation study, this error component is readily determined by using an isotropic source field at the TOA and corresponding isotropic reduction of simulated satellite measurements to the TOA. Under these conditions, both the $\overline{\rho}'$ and ρ_{ref} of Eq.(34) become unity for all observations and only the spatial error component remains. (Subsequently referred to as "N=0" experiment.)

2.4.3 Angular Sampling

Angular sampling from space is different from spatial sampling in that it is not possible to view, during any one orbital pass, the full range of hemispherical radiances exiting a fixed Earth location. This is true for a single satellite observing system and holds even in the limit of data rates tending toward infinity. To alleviate such an inherent sampling deficiency, ancillary scene identification algorithms, together with empirically derived, scene-dependent angular models, may be introduced into the data processing stream. These permit the inference of all upwelling hemispherical radiances, and the flux, with as little as a single scanner observation. Nevertheless, the angular models used can only be approximate for any individual observation since they are discrete and describe only the mean angular characteristics of a broad scene category. On the other hand, in nature there exists an infinite variety of angular models corresponding to a continuous transition of scene types over many category types (Figure 16). As a result, during any application of the discrete mean models, an error with respect to the prevailing true models, will be incurred. This error may be reduced by sampling at several satellite zenith angles. However, as illustrated in Figure 17, there is an upper limit to the hemispherical coverage that can be obtained from a single orbiting platform. Even when a radiometer is trained on a fixed point, only a single arc crosses the outgoing hemisphere during any one orbital overpass. Therefore, scene identification and associated angular models are needed to complete the angular coverage at any individual space point. Occasionally, scene miscategorization will occur and lead to errors. More important, however, are the systematic and random errors that occur by application of mean angular models to all variations of scene type existing within a given scene category. These errors cannot be completely removed by increased sampling rates. Rather, they require refinements in existing empirical models and their application methods.
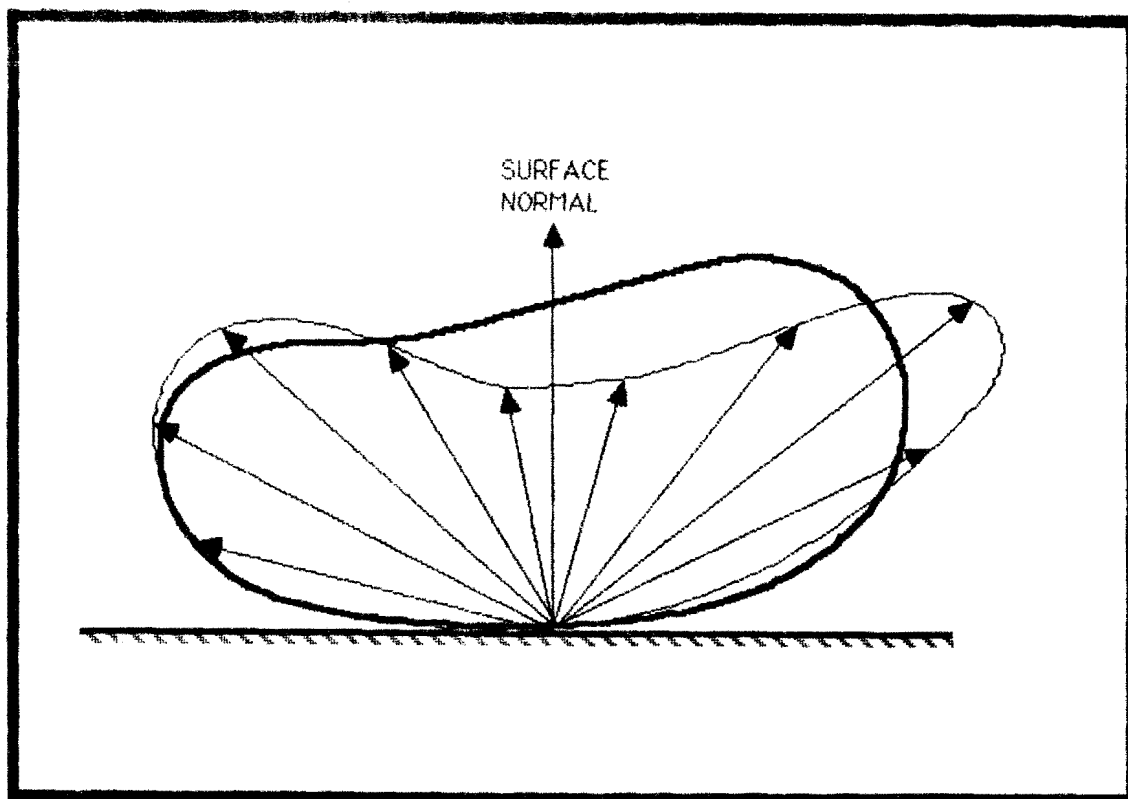
Figure 16. Conceptual diagram illustrating the difference between the outgoing anisotropic distribution of radiances from an ensemble mean surface type (dark line) and a somewhat different distribution of radiances reflecting off a surface during a single realization (thin line).
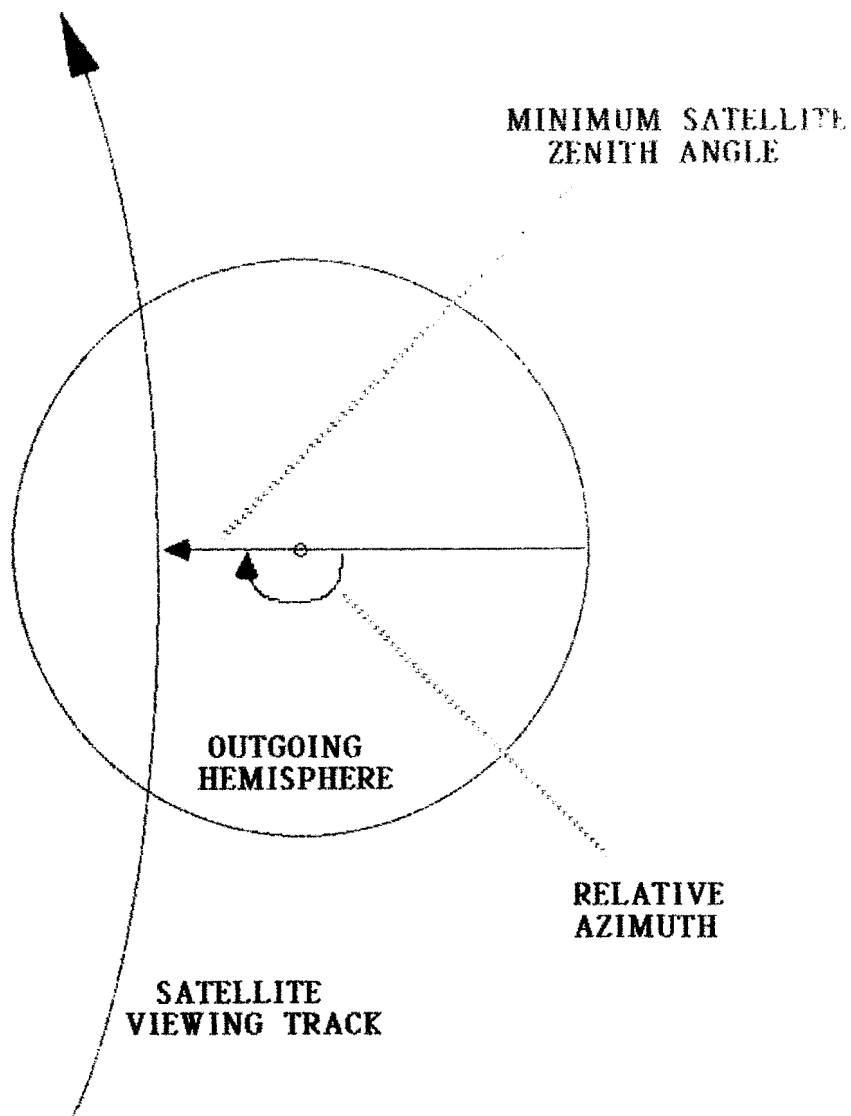
Figure 17. The complete set of viewing angles (relative azimuth and satellite zenith) that may be used to observe a target at TOA during a single orbit is limited to a set of points along a curved line mapped onto the outgoing hemisphere of radiances.

2.4.4 Simulation of Angular Sampling Errors

Angular sampling error is defined as the remaining component in Eq.(34) once the spatial error has been removed from the left-hand side. F_{REF} is expressed, with the help of Eq.(35), as $F_{REF} = 1/n \, \Sigma \, \overline{F}_{ref,i}$ - $E_{SPATIAL}$ and substituted in Eq.(34). After some rearrangement we obtain

$$E_{ANGULAR} = E - E_{SPATIAL} = n^{-1} \sum_{i=1}^{n} (\Delta \rho / \rho_{ref})_i \cdot \overline{F}_{ref,i} \tag{36}$$

where $\Delta \rho$ is given by

$$\Delta \rho = \overline{\rho}' - \rho_{ref} \tag{37}$$

As indicated by Eq.(36), an error will be incurred at every observation for which $\Delta \rho \neq 0$. This error will depend on the magnitude of N which may be varied in a series of experiments to demonstrate the sensitivity of a given scanning sequence to systematic and/or random ADM errors.

In contrast to spatial sampling errors, angular sampling errors arise only at the n observation positions within a target area. This error component we examine separately through the use of reduced-FOV experiments in which the spatial sampling does not contribute. In these experiments (see also Section 2.4.5) the radiometer footprint is adjusted to the resolution of the TOA M1 grid element size for all observations and the regional satellite flux estimates are compared against an "adjusted" reference flux which is averaged only over the n observation points. As seen in Eq.(35), $\overline{F}_{ref,i}$ reduces to $F_{ref,i}$ for each observation and the indicated summation becomes equal to the "adjusted" reference flux. Under these conditions, the spatial error vanishes and regional measurement errors contain an angular sampling component only which, we assume, is approximately equal to the angular error component of a full-FOV experiment. We have

$$E_{ANGULAR} = n^{-1} \sum_{i=1}^{n} (\Delta \rho_c / \rho_{ref})_i \cdot F_{ref,i} \tag{38}$$

where $\Delta \rho_c$ is similar to the $\Delta \rho$ of Eq.(37) except that now $\overline{\rho}'$ is replaced by ρ' at the center of the FOV. This is written as

$$\Delta \rho_c = \rho' - \rho_{ref} \tag{39}$$

When we compare Eq.(38) to Eq.(36) for a full-FOV experiment, we find that they differ only in the replacement of the FOV average terms, $\overline{\rho}'$ and $\overline{F}_{ref,i}$ of Eq.(36), with their values at the FOV midpoint in Eq.(38).

2.4.5 Consistency Checks

A consistency check is defined as an orbital simulation run in which: (1) the scanning radiometer FOV's are reduced to include only the M1 grid element containing the FOV midpoint; (2) the FOV midpoint is displaced, if necessary, to lie at the exact center of the M1 grid element in which it falls; (3) the generation of truth field radiances and the reduction of satellite measurements to the TOA are carried out isotropically; and (4) regional satellite estimates are compared against the truth field by averaging the truth field only among the M1 grid elements which have been sampled. Consistency checks were run repeatedly to debug the simulation code, since under the four stated conditions no ADM errors, no MLE scene misidentification errors, and no spatial sampling errors exist. Any disagreement between the regional truth and measured flux estimates was used to uncover software coding errors. These were corrected and additional consistency checks were performed until conformity was achieved between the truth and measured fluxes.

As discussed in Section 2.4.4 and further in Section 2.4.6, a variation of a consistency check is also used to estimate angular sampling errors inherent in the five scanning designs. In this case we refer to the simulation runs as reduced FOV experiments (or single-element FOV experiments). Of the four conditions stated previously for a consistency check, only the third no longer applies for a reduced FOV experiment. Here we wish to study the response of the various radiometers to different conditions of anisotropic emission and reflectance without the added complication of spatial averaging over the FOV footprint.

2.4.6 Computation of Sampling Errors Over an Orbital Swath

In analyzing regional sampling errors, we have subdivided the total error into spatial and angular components such that

$$E_{TOTAL} = E_{SPATIAL} + E_{ANGULAR} \tag{40}$$

Now we combine regional errors to form RMS errors over the domain contained within the scan swath of an orbiting radiometer. When this is done, we find that the spatial and angular components of Eq.(40) are nearly uncorrelated. This is illustrated in Table 9 where individual statistics for these components are given for a single satellite overpass of the study domain. An orbital simulation was conducted at 18 GMT ($\sim$ 13 local time) on January 29, 1984 using an anisotropy factor of N=1.3. In the table, total sampling errors are given for two derivations. Under the column labeled OBSERVED TOTAL we determine regional errors directly from the satellite measurements and the reference field, respectively, using Eqs. (21) and (22). RMS errors over the scan swath are then given by

$$RMS = (M^{-1} \cdot \sum_{j=1}^{M} E_{TOTAL,j} \cdot E_{TOTAL,j})^{1/2} \tag{41}$$

where M is the number of 2.5° regional areas viewed during the satellite overpass. Using a second approach we subdivide total regional sampling errors into spatial and angular components as in Eq.(40). The RMS error is then written

Table 9. Summary of spatial, angular, and total sampling errors in W/m^2 for five prototype instruments. The total error is compared to a computed total based on the assumption that the angular and spatial sampling errors are uncorrelated.

SAMPLING PERIOD: 18 GMT JANUARY 29, 1984

ANISOTROPIC SOURCE MODEL: N = 1.3

SW RMS ERRORS

RADIOMETER	SPATIAL SAMPLING[1]	ANGULAR SAMPLING[2]	OBSERVED[3] TOTAL	COMPUTED[4] TOTAL
ACA	14.30	3.05	14.37	14.62
CERES-I	9.77	7.34	12.01	12.22
CSR	13.09	2.98	13.54	13.42
ERBE	9.79	9.48	13.04	13.63
NIMBUS-7	26.99	6.87	27.15	27.85

LW RMS ERRORS

RADIOMETER	SPATIAL SAMPLING	ANGULAR SAMPLING	OBSERVED TOTAL	COMPUTED TOTAL
ACA	2.89	1.03	3.06	3.07
CERES-I	1.80	1.95	2.82	2.65
CSR	2.39	1.85	3.00	3.02
ERBE	1.88	2.25	3.10	2.93
NIMBUS-7	5.30	1.77	5.69	6.35

---

[1]Obtained from full-FOV isotropic experiments.
[2]Obtained from single-element FOV experiments.
[3]Obtained from full-FOV experiments.
[4]Obtained from the sampling and modeling errors by squaring each, adding and taking the square root.

$$RMS = (M^{-1} \cdot \sum_{j=1}^{M} (E_{SPATIAL,j}^2 + 2 \cdot E_{SPATIAL,j} \cdot E_{ANGULAR,j} + E_{ANGULAR,j}^2))^{1/2} \qquad (42)$$

The spatial and angular terms of Eq.(42) represent the total RMS errors obtained from individual simulation experiments designed to separately estimate the component terms. The spatial component is obtained from full-FOV isotropic experiments (Section 2.4.2) and the angular component from single-element FOV experiments. Under the assumption that $E_{ANGULAR,j}$ and $E_{SPATIAL,j}$ are uncorrelated over large areas, we computed the values under the column entitled COMPUTED TOTAL using the approximation

$$RMS = (RMS_{SPATIAL}^2 + RMS_{ANGULAR}^2)^{1/2} \qquad (43)$$

where $RMS_{SPATIAL}^2$ and $RMS_{ANGULAR}^2$ are RMS errors obtained from the independent simulations for, respectively, the spatial and angular components. We see that the two results agree to within 5% for all five radiometer designs indicating that $E_{SPATIAL}$ and $E_{ANGULAR}$ are nearly uncorrelated. A demonstration that this is true was necessary because, although errors in ADMs and spatial sampling enter the simulation study independently, their cross-product may not vanish due to separate causal relationships with a common third variable.

Eq.(43) is advantageous in that it permits us to infer the RMS statistics of a given radiometer and orbital pass for many anisotropic conditions using only the results of two relatively simple experiments: (1) an isotropic simulation to determine spatial sampling error and (2) a single-element anisotropic experiment to determine angular sampling error for an $N \neq 1$ experiment. From Eq.(35) spatial sampling error is independent of N and, once determined, is valid for all N experiments. Angular sampling error is a function of N, but from Eqs.(11), (39), and (38) we derive a relationship between the RMS statistics of angular sampling error for different N experiments. From Eqs. (11) and (39) we obtain

$$\Delta \rho_c = (N - 1) \cdot (\rho_{ref} - 1) \qquad (44)$$

and using this in Eq.(38) we obtain

$$E_{ANGULAR} = n^{-1} \cdot (N - 1) \cdot \sum_{i=1}^{n} \frac{(\rho_{ref,i} - 1) \cdot F_{ref,i}}{\rho_{ref,i}} \qquad (45)$$

Eq.(45) shows that regional angular sampling errors depend on the anisotropic condition of the source radiation only through the multiplicative factor, N-1. This holds for the RMS angular sampling error as well so that for two different anisotropic experiments we have the relationship

$$RMS^2(N_2) \cdot RMS^{-2}(N_1) = (N_2 - 1)^2 \cdot (N_1 - 1)^{-2} \qquad (46)$$

where the subscript ANGULAR has been omitted from RMS^2. RMS total sampling errors can be derived from Eq.(43) for any value of N_2 provided $RMS^2_{ANGULAR}$ for one $N \neq 1$ anisotropic experiment (N_1) and $RMS^2_{SPATIAL}$ are known. The equation relating total RMS errors for a given radiometer to different anisotropic experiments is given by

$$RMS(N_2) = (RMS^2_{SPATIAL} + (N_2 - 1)^2 \cdot (N_1 - 1)^{-2} \cdot RMS^2(N_1)_{ANGULAR})^{1/2} \qquad (47)$$

When experiments using 10-km random anisotropic departures from the ERBE reference models are conducted, we find that regional random ADM error components cancel almost entirely. This is illustrated in Table 10 where total sampling errors are compared for $N = 1.0$ and $N = 1.0 \pm 0.3$ experiments for an 18 GMT overpass of the study domain on January 29, 1984. From the $N = 1.0$ experiment we obtain a reference result for which no systematic or random ADM errors are included in the Earth simulation. Resultant RMS, STD (standard deviation), and BIAS errors are given for the five radiometers for both longwave and shortwave fluxes over the orbital scan swath (see Eq.(53) for definition). In the second experiment, a random anisotropic perturbation with a 30% STD about ERBE mean models is imposed on the upwelling Earth radiances at each M1 element. By comparing the RMS and BIAS error components of the two experiments, we see that no significant random error components remain for 2.5° resolution target areas.

2.4.7 Estimation of Likely Values of N

One of the types of measurement errors we are simulating arises through a propagation of the basic errors in the reference ADM's as used for the inversion of the observations. The total measurement error for each instrument is the sum of the spatial sampling error and this ADM-related error. The five candidate scanning instruments being considered will ultimately be ranked by their relative sensitivities to the two error types. However, the design of an instrument may be designed to optimize the performance relative to only one of the two error sources (e.g., the ERBE cross-track scanner when considering spatial sampling errors, and the ACA when considering angular sampling errors). The spatial sampling error is dependent on the spectrum of variance in the truth field, coupled with the projected IFOV of the instrument (footprint), and is not related to a free parameter of this system simulation (e.g., N). However, the angular sampling error will be driven by the amount of ADM errors introduced (i.e., the ADM of each truth field realization is made to depart from the ensemble-averaged models used for the measurement inversion). Thus, the relative performance and ranking of the five radiometers will depend on the degree of error present in the ADM's. It is important, therefore, to quantify the reasonable degree of ADM errors expected so that the simulation may be fairly and realistically performed.

CONCEPT 1: Variability in the ADM (realization versus ensemble average) is related to the standard deviation of the radiances originally used in producing the ERBE ADMs.

A factor for increased anisotropy in any one viewing direction is given by:

Table 10. Comparison of the total RMS and bias errors (W/m^2) of simulation results using unperturbed (N = 1.0) and randomly perturbed (N = 1.0 $\pm$ 0.3) ERBE ADM's. Errors are given separately for the five prototype radiometers and for both longwave and shortwave fluxes.

SAMPLING PERIOD: 18 GMT JANUARY 29, 1984

ANISOTROPIC MODEL: N = 1.0

SW STATISTICS[1]

RADIOMETER	RMS ERROR	STD OF ERROR	BIAS
ACA	25.03	25.03	0.03
CERES-I	13.26	13.26	-0.26
CSR	12.93	12.93	-0.20
ERBE	11.88	11.87	0.43
NIMBUS-7	24.50	24.46	1.41

LW STATISTICS[1]

ACA	5.49	5.49	-0.01
CERES-I	2.52	2.51	0.12
CSR	2.36	2.36	0.04
ERBE	2.25	2.24	-0.23
NIMBUS-7	5.21	5.21	0.01

ANISOTROPIC MODEL: N = 1.0 $\pm$ 0.3

SW STATISTICS[1]

RADIOMETER	RMS ERROR	STD OF ERROR	BIAS
ACA	---	---	---
CERES-I	13.30	13.30	-0.24
CSR	12.93	12.93	-0.23
ERBE	11.93	11.92	0.46
NIMBUS-7	24.54	24.49	1.55

LW STATISTICS[1]

ACA	---	---	---
CERES-I	2.52	2.52	0.12
CSR	2.36	2.36	0.04
ERBE	2.25	2.24	-0.23
NIMBUS-7	5.18	5.18	0.02

---

[1]Statistics are given for all satellite zenith angles, including those greater than 70°.

$$N - 1 + \frac{\Delta R/R}{1 - 1/\rho_{ref}} \tag{48}$$

where $\Delta R = \pm \sigma$ and is the standard deviation of the ERBE model mean radiances, $\overline{R}$, in the given direction. Note that ΔR may enter Eq.(48) as a positive or negative term. This expression is derived from the definition of ρ as the ratio of radiance to flux (scaled by π) and the definition of N in Eq.(10). When N is averaged over the upwelling hemisphere for any particular ADM realization, the sign of N-1 is not arbitrary for different viewing directions, but rather the normalization condition for ρ in Eq.(12) must be satisfied. One way to ensure this is to require that when $\Delta R > 0$ for angles in which $\rho_{ref} > 1$, ΔR must then be < 0 for angles in which $\rho_{ref} < 1$. Conversely, when $\Delta R < 0$ for angles in which $\rho_{ref} > 1$, ΔR must be > 0 for angles in which $\rho_{ref} > 1$. These additional requirements for averaging over the viewing hemisphere are met by modifying Eq.(48) to become

$$N - 1 \pm \frac{\sigma/\overline{R}}{|1 - 1/\rho_{ref}|} \tag{49}$$

where now either the plus or minus sign is chosen for all angles. Because Eq.(49) contains a singularity when $\rho_{ref}=1$, it is not suitable for averaging over the hemisphere. An alternate integral given by

$$N - 1 \pm \frac{\int \int (\sigma/\overline{R}) \, \mu \, d\mu \, d\theta}{\int \int |1 - 1/\rho_{ref}| \, \mu \, d\mu \, d\theta}, \tag{50}$$

where θ is zenith angle and $\mu = \cos(\theta)$ was used instead to estimate N. From the form of Eq.(50) the singularity at $\rho_{ref}=1$ is expected to produce an underestimate in the value of N because the delta function spike in the lower integrand will cause the denominator to be too large. It was found, however, that the computed values were so large that N became less than zero when the minus sign in Eq.(50) was used. Even when half the radiance variance was assumed to come from non-angular effects (e.g., cloud amount, etc.), a mean value of N=2.4 was obtained when averaged over separate computations for eight scene types and ten solar zenith angle bins. As a result, the N estimates from Eq.(50) are apparently too large and cannot be used.

From the ERBE models and consideration of physical constraints on reflected energy, a maximum possible range for N may still be determined. Because reversal in the sign of anisotropy (see Eq.(10)) is not permitted, N is restricted to positive values and a lower limit of N=0 is established. At the opposite extreme, the magnitude of anisotropic stretching may not be so great as to cause ρ' to become less than zero as this violates conservation of energy. A maximum N value is thus obtained from the ERBE models for clear ocean where the bidirectional reflectance factor may be as low as 0.41. Using Eq.(10) and setting ρ' to zero, a maximum N of 1.69 is found.

CONCEPT 2: Variability in ADM may be estimated from assumed cloud category misidentifications, based on differences in anisotropic factor from one cloud amount (A) to another, but with near-singular values screened (N > 2.4 or N < 0).

For four surface geography classifications (viz. ocean, land, desert, and coastal), an anisotropic ratio

$$N = \frac{\rho_{scn1} - 1.0}{\rho_{scn2} - 1.0} \qquad (51)$$

was computed between a given cloud amount category and the next higher cloud amount category (A_{SCN1} > A_{SCN2}). A similar ratio was also obtained between a cloud amount category and the next lower cloud amount (A_{SCN1} < A_{SCN2}). For a given geography type and scene misidentification sequence, a maximum of three cloud comparisons at 49 angular viewing bins and 10 SZA ranges can be made. These are analyzed below for over and under cloud misclassification and by surface type for the mean and standard deviation of the estimates of N.

OVERESTIMATING (i.e., A_{SCN1} > A_{SCN2})

Surface	# of Values	Mean	STD
Ocean	1304	0.72	0.32
Land	1212	0.86	0.44
Desert	1148	0.92	0.47
Coast	1286	0.80	0.36

UNDERESTIMATING (i.e., A_{SCN1} < A_{SCN2})

Surface	# of Values	Mean	STD
Ocean	1162	1.37	0.45
Land	1118	1.12	0.50
Desert	1096	1.02	0.51
Coast	1195	1.22	0.45

The ocean models are the most sensitive to systematic overestimation or underestimation of cloudiness, with errors in anisotropy in the range of 30% to 40%, while land and desert are less sensitive. These errors are somewhat smaller than the 70% errors (N=1.69) identified in Concept 1.

As presented during the Twenty-Fourth ERBE Science Team Meeting, comparisons between shortwave fluxes measured by NOAA-9 and ERBS ERBE scanners over 2.5° regions (including satellite nadir angles up to 40°) indicated an RMS difference of 15 W/m². This figure can be used to infer the amount of angular model error that may have been present in the observations. To do this, we assume that the observed RMS difference, when squared, can be partitioned into equal error contributions from NOAA-9 and ERBS. The RMS error for each ERBE instrument is thus 10.6 W/m². In our simulations, we consider an error as the difference between the satellite-derived flux and the true flux. This error is partitioned into contributions from spatial sampling errors and from angular modeling errors. Our experiments have indicated that the two effects are uncorrelated, which allows us to partition the squared error into the two contributions by ignoring the covariance term. Near nadir, the shortwave spatial

sampling error is on the order of 5 W/m² for the ERBE scanners (see Figures 18e and 19e). Subtracting the squared spatial sampling error from the squared total error, implies an angular modeling error of about 9.4 W/m². Our experiments also show that the ADM errors for two anisotropic scaling factors, N_1 and N_2, are related by (see Eq.(46))

$$E_{ADM}(N_1) = (N_1 - 1)/(N_2 - 1) \cdot E_{ADM}(N_2) \tag{52}$$

For the ERBE instrument with N_2 set to 1.69, we find (see Figures 21d and 22d) E_{ADM} is approximately 20 W/m². Using Eq.(52) and the above finding that $E_{ADM}(N_1) = 9.4$ W/m², we obtain for N_1 an approximate value of 1.3. Therefore, systematic errors in angular models of about 30% can be expected for 2.5° spatial resolution.

This very qualitative analysis indicates a probable degree of ADM errors that we can expect an ERB instrument to encounter and the typical values of N that are found. However, the absolute range of N values that occurs is not determined from these results. Because this study compares the relative sampling characteristic of various scanner designs over a broad range of atmospheric conditions, we chose an extreme range of N values to study. A minimum value of N=0, corresponding to isotropic emission and reflectance, is used to quantify spatial sampling error. A maximum value of 1.69, representing the physical limit for conservation of energy, is chosen as the largest value of N. RMS sampling errors for intermediate values of N can be estimated either by conducting additional orbital simulations for specific N values or by reference to Eq.(47).

3. RESULTS OF THE SYSTEM SIMULATION STUDY

Satellite-derived instantaneous TOA flux estimates are recovered from orbital simulations and compared against the reference fluxes as regional bias errors, Eq.(29), and over the domain of an orbital swath in terms of bias, RMS and STD of the errors. The "orbital" RMS error is defined in Eq.(41) while the bias error is the average of E_{TOTAL} in Eq.(40) when summed over all sampled target areas. The STD of the error is given for convenience and is approximated by

$$STD \approx \sqrt{RMS^2 - BIAS^2} \qquad (53)$$

The total sampling error from satellites depends on the anisotropy of the Earth source radiation field (i.e., N) and on meteorological and illumination conditions along the subsatellite track. For a given anisotropic experiment we consider orbital simulations for July and January, and for morning and afternoon overpasses of the M1 study domain. East to west across the M1 grid a local time change of five hours occurs with the eastern edge, at 50°W, located roughly three hours earlier than Greenwich time. At 15Z, the M1 grid extends from 7:00 to 12:00 local time, encompassing morning meteorological conditions, and at 21Z from 13:00 to 18:00 local time to include afternoon meteorological events. ISCCP data for these two synoptic times were used to generate reference fields for which orbital simulations were conducted at three different equator crossings, 63°W, 86°W, and 109°W longitude, for each image. These three equator crossings evenly subdivide the M1 grid and correspond to distinct conditions of solar illumination. Three anisotropic experiments were run in July corresponding to N values of 0, 0.59 (1/1.69), and 1.69 and two experiments in January with N values of 0 and 1.69. The N=0 experiments produce an isotropic source radiation field, Eq.(11), and are used, along with isotropic inversion to the TOA, to measure the spatial sampling error (Section 2.4.2) of each radiometer and scan pattern.

Angular sampling errors are computed, rather than measured independently (Section 2.4.4), using Eq.(40) to obtain regional bias errors and Eq.(43) to obtain "orbital" STD and RMS errors. In using Eq.(43) we use the fact that regional angular and spatial sampling errors are uncorrelated over a scan swath (Section 2.4.6). After computing the RMS error of the angular sampling for a value of N, we use Eq.(46) to compute the RMS error for any other value of N.

A set of contour plots illustrating regional TOA reference fluxes and satellite sampling errors for the 21Z GOES image with the platform ascending node at 86°W is provided here. Results are given for the shortwave measurements taken by all five candidate radiometers (ACA, CERES-I, CSR, ERBE, and Nimbus-7) for one day of each of the summer and winter simulation periods chosen (July 17, 1983 and January 30, 1984). Four categories of the TOA shortwave flux fields are considered: (1) the two truth fields independent of any spatial or angular sampling errors; (2) the spatial sampling of the radiometer in the absence of any bidirectional modelling error; (3) the angular sampling errors in the absence of any spatial sampling error; and (4) the total sampling error combining the spatial and bidirectional sampling errors.

3.1 SPATIAL SAMPLING ERRORS

Figure 18a shows the TOA truth shortwave flux field for 21Z July 17, 1983, and Figures 18b through 18f illustrate the spatial sampling errors associated with each of the five instrument types for this field. The scanners were simulated to be aboard a sun-synchronous polar orbiter at an altitude of 824 km (at 3:15 PM for this run). The ERBE pattern (Figure 18e) produces a highly regular array of observation

points within any viewed target area region. The result is an efficient sampling pattern which minimizes redundant overlapping footprints and leads to relatively uniform weighting of all TOA areal elements. The CSR scanning strategy, by contrast, is to view a given target region with as many as six widely spaced telescope nadir angles (Figure 18d). This tends to reduce angular modeling errors, but at the cost of generating an assortment of scattered and overlapping footprints within the various target area regions. As a consequence, different area elements of the TOA flux field enter the satellite-derived flux estimate a nonuniform number of times. This yields a weighted mean of the target area truth field rather than the desired arithmetic mean. As a result, cross-track scanners will generally achieve a lower spatial sampling error than biaxial scanners. Especially along the subsatellite track, the ERBE error contours do not exceed ± 5 W/m^2. For the CSR, on the other hand, contours above ± 10 W/m^2 are present. The CERES instrument (Figure 18c) also is capable of spatially sampling the truth fields with relatively little error, much as with the ERBE. The Nimbus-7 ERB instrument (Figure 18f), on the other hand, obtains relatively large sampling errors. This is a result of the relatively low data rate and scan design that were chosen, not so much for mapping the radiation budget, but to collect an angular data set for the development of ADMs. The ACA instrument is also not optimized for spatial sampling due in part to its relatively large fields of view. As a consequence, moderate spatial sampling errors are obtained with the ACA (Figure 18b). Figure 19a shows the TOA truth shortwave flux field for 21Z January 30, 1984, and Figures 19b through 19f illustrate the spatial sampling errors associated with each of the five instrument types for this field. The error patterns have similar characteristics to those shown for July, so no further discussion is required.

3.2 ANGULAR SAMPLING ERRORS

The total sampling error of an orbital simulation is varied through the anisotropy scale factor, N, of Eq.(10). These experiments involve a reapportionment of the total reflected energy into the upwelling hemisphere, but do not affect the magnitude of the flux field. Rather, a new distribution of radiances, ρ'_{TOA}, is defined which is related to the original ERBE models through Eq.(11). Figure 20 shows a plot of ρ'_{TOA} (for N = 0.59 and N = 1.69) and ρ_{ref} (the ERBE models) as a function of satellite zenith angle bin (using the ERBE bin scheme where bin 1 is nadir and bin 7 is horizon) for an ocean surface and a sun-target-satellite geometry corresponding to a solar zenith angle (SZA) of 57° and a relative azimuth (RELAZ) of 255°/75° on either side of zenith. For N > 1, in regions where the original ERBE models are greater than unity, $\rho'_{TOA} > \rho_{ref}$ and where they are less than unity, $\rho'_{TOA} < \rho_{ref}$. Figures 21a through 21e and 22a through 22e present the angular sampling errors associated with the five candidate scanning patterns for July and January, respectively, for N=1.69. As a result of the ADM errors, negative contours as large as -45 W/m^2 are seen in the ERBE error map of Figure 21d near the western coast of South America and Figure 22d over the central U.S. Here the ERBE observations are collected either over a highly anisotropic surface (ocean) or at high solar zenith angles (U.S.), but in the near-nadir (satellite zenith angle bins 1 and 2) where $\rho'_{TOA} < \rho_{ref}$. As a result, a relatively small satellite radiance is observed. Reduction to a TOA flux, nevertheless, is carried out using the ERBE reference (mean) anisotropic factor, since more complete knowledge of the real atmosphere, that might tell us that $\rho'_{TOA} < \rho_{ref}$, is not available. This leads to an underestimate by ERBE (cf Eq.(33)). The CERES instrument is not as sensitive to ADM errors as is the ERBE, due to the incorporation of an azimuth-slewing scanner (Figures 21b and 22b). To an even greater extent, large values are reduced in the CSR measurement error field of Figures 21c and 22c, as well as with the measurements of the ACA (Figures 21a and 22a). This favorable outcome is due to the multiple angular sampling capability of the CSR scanner and ACA which permits compensation of opposing anisotropic modeling errors made at different viewing angles. Compensation of errors is also evident in the case of the Nimbus-7 ERB (Figures 21e and 22e). It is important to remember that these simulation errors are larger than expected under real conditions, since N $\simeq$ 1.3, not 1.69 (cf 2.4.7) under those conditions.

Figure 18a. The TOA shortwave flux truth field for 21Z July 17, 1983 (the contour interval is 100 W/m^2).

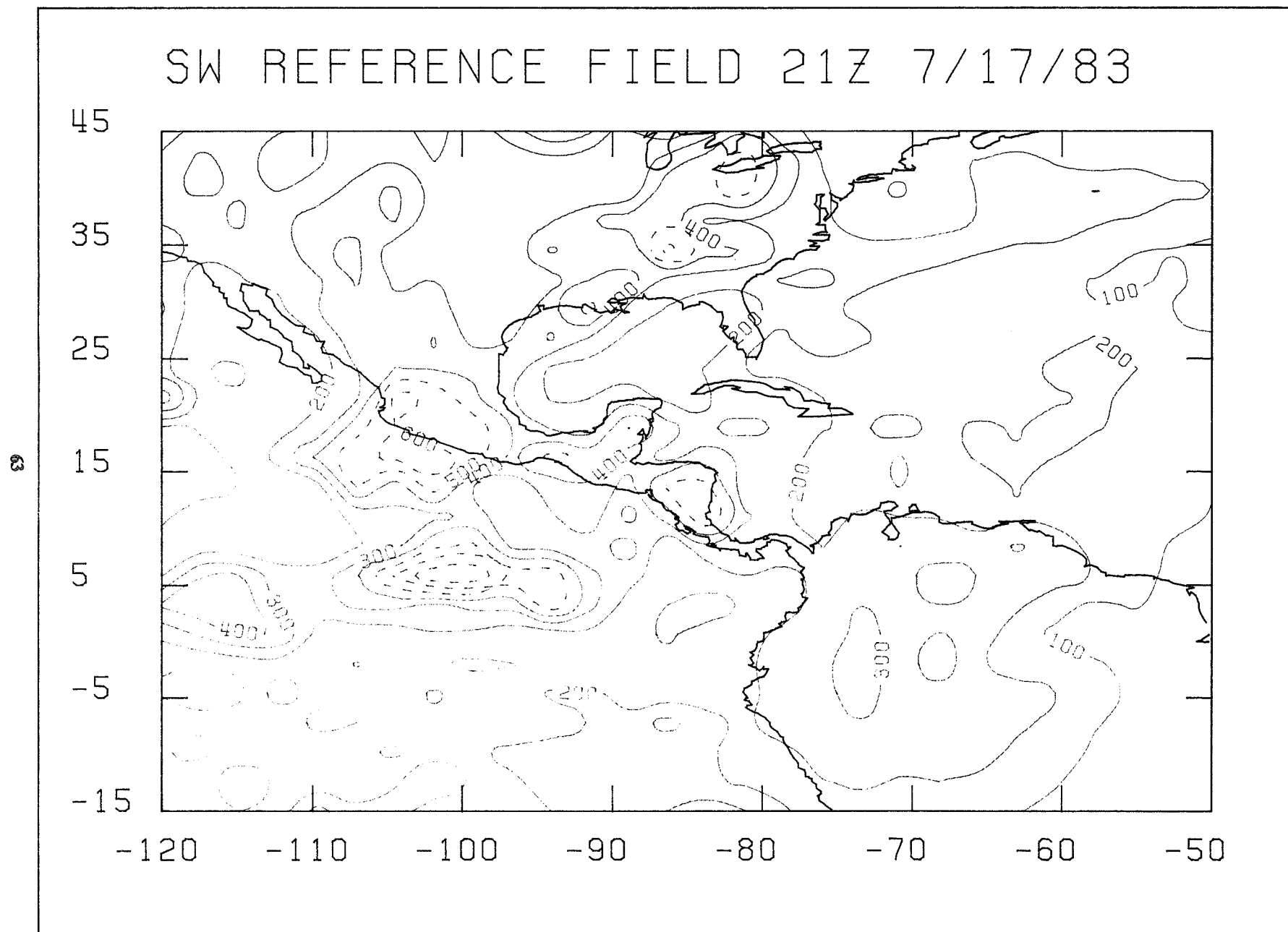SW REFERENCE FIELD 21Z 7/17/83

Figure 18b. The errors in shortwave TOA flux relative to the truth field for 21Z July 17, 1983, due to spatial sampling errors, as measured during a single orbit by the ACA (contour interval is 10 W/m^2, dashed contours are negative).
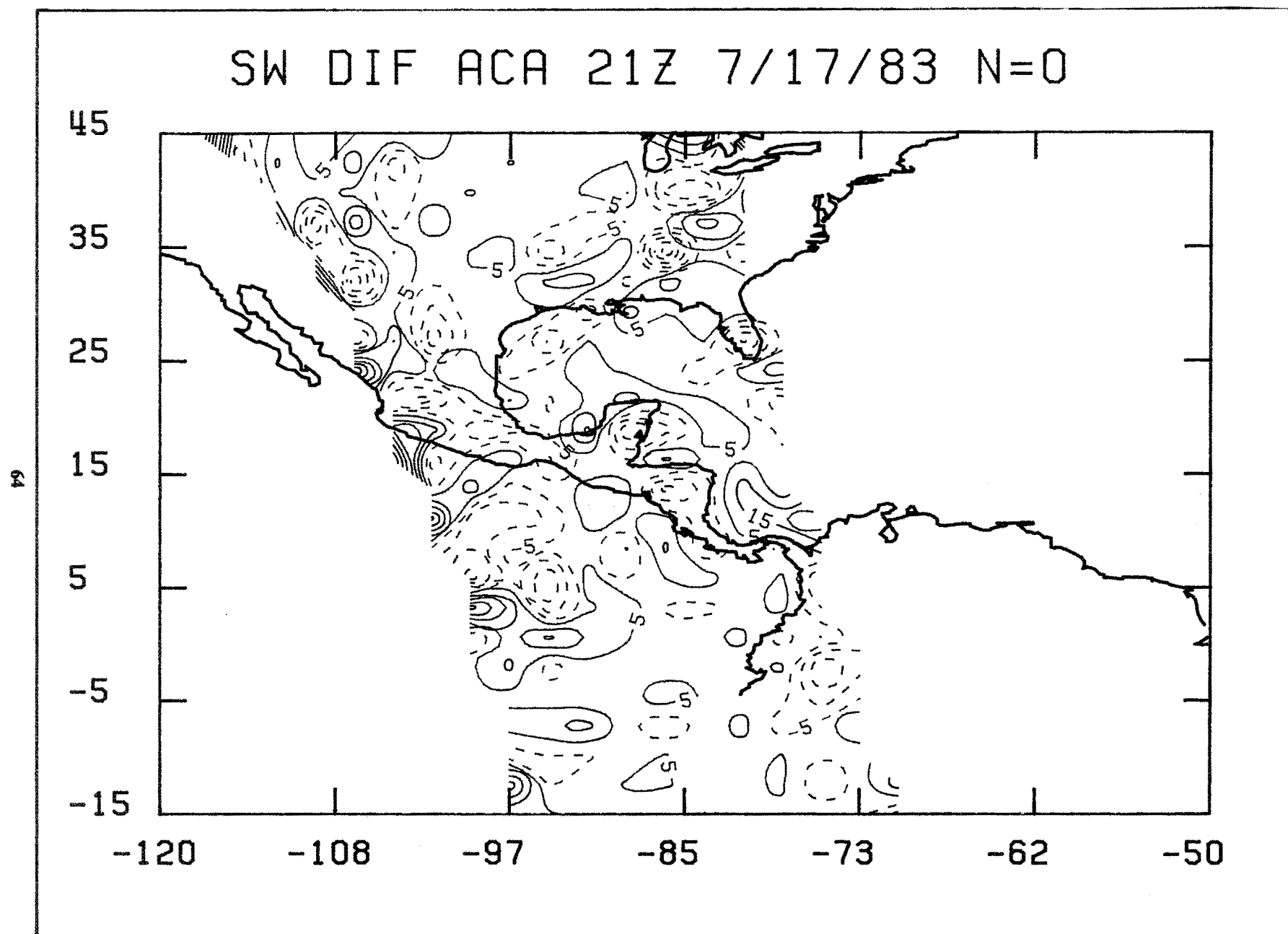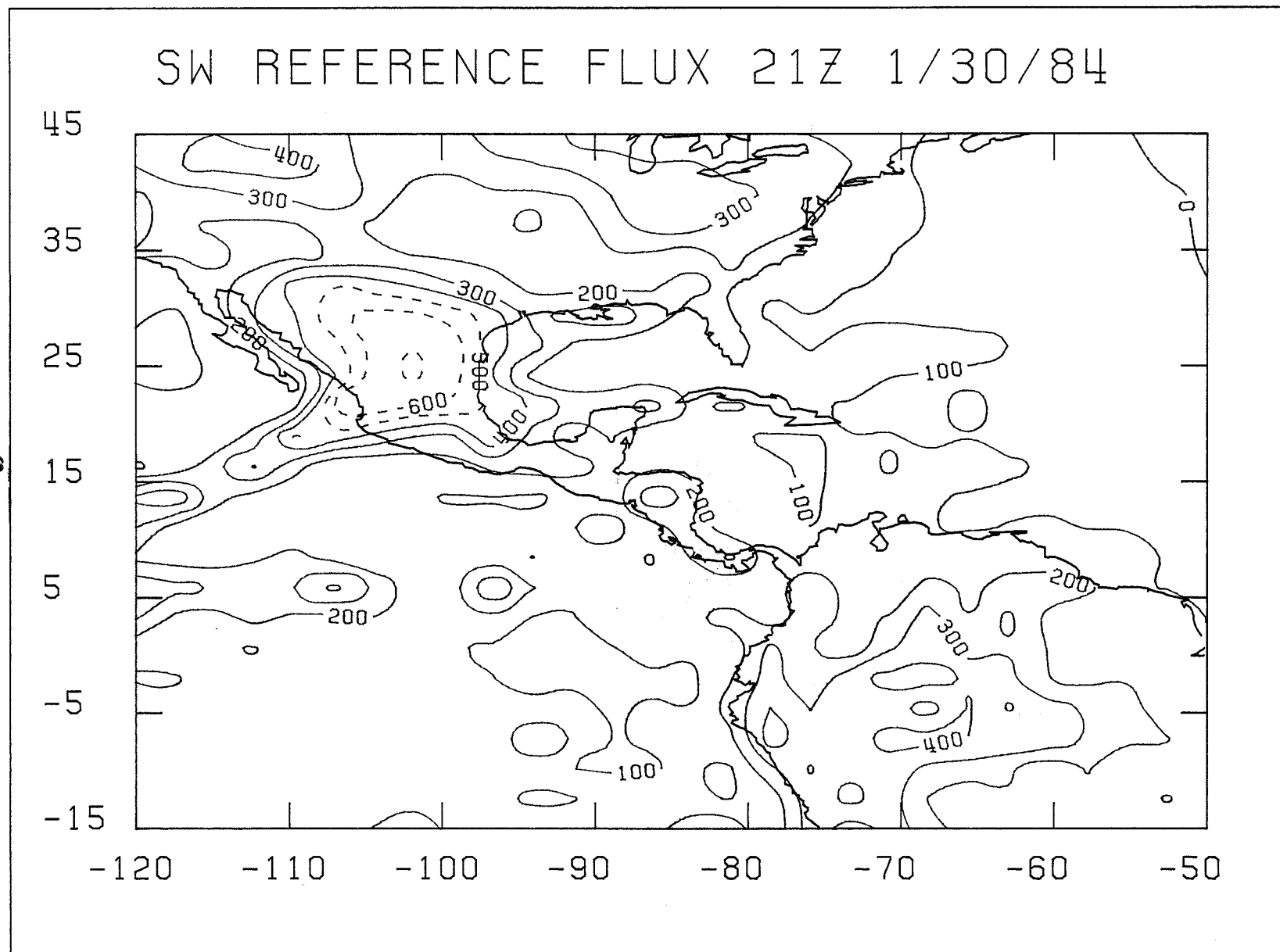

SW DIF ACA 21Z 7/17/83 N=0

SW DIF CERES 21Z 7/17/83 N=0

Figure 18d. As in Figure 18b, but as measured during a single orbit by the CSR.

SW DIF CSR 21Z 7/17/83 N=0

SW DIF ERBE 21Z 7/17/83 N=0

SW DIF NIMBUS-7 21Z 7/17/83 N=0
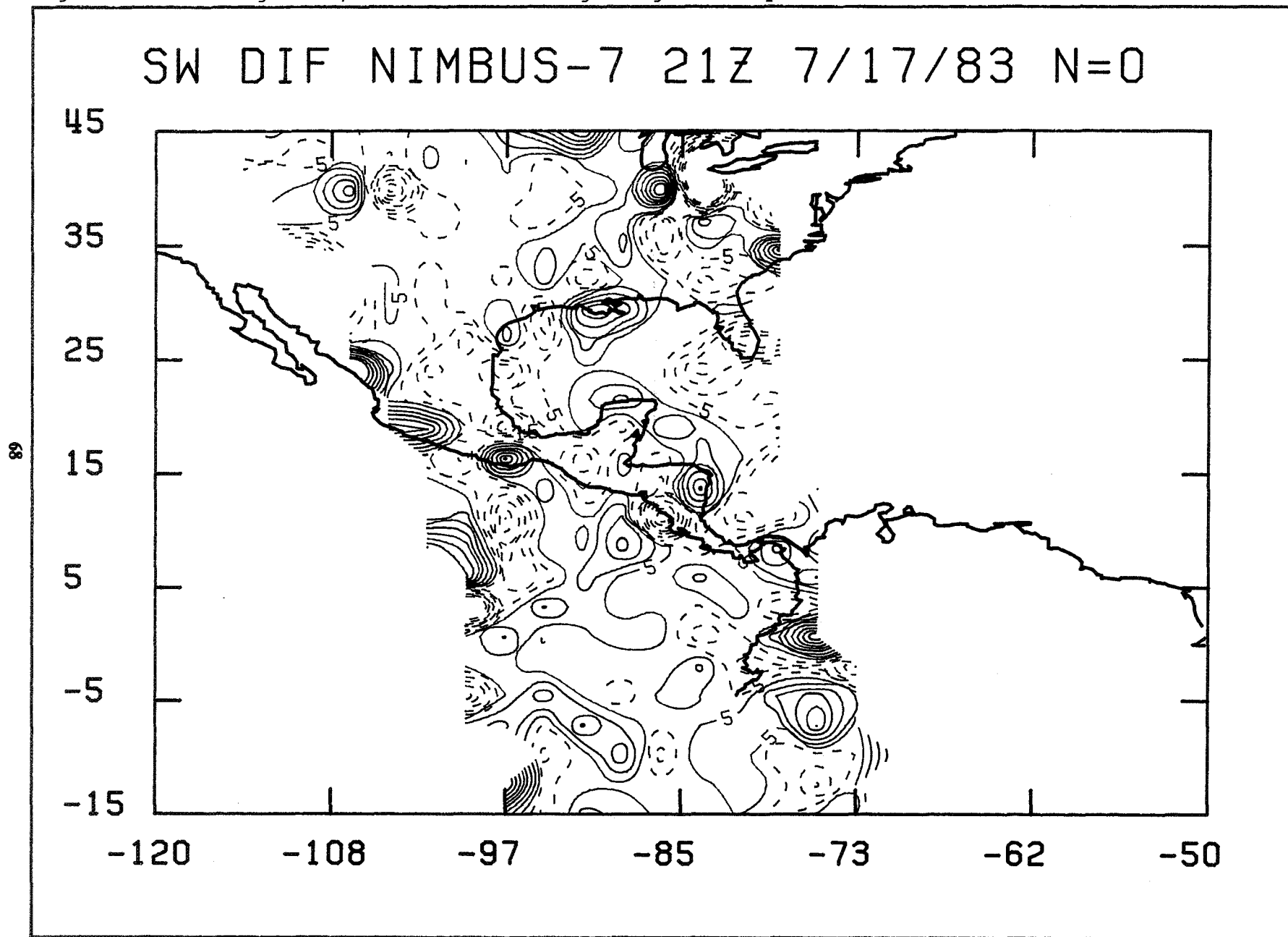
Figure 19a.   The TOA shortwave flux truth field for 21Z January 30, 1984 (the contour interval is 100 W/m^2).
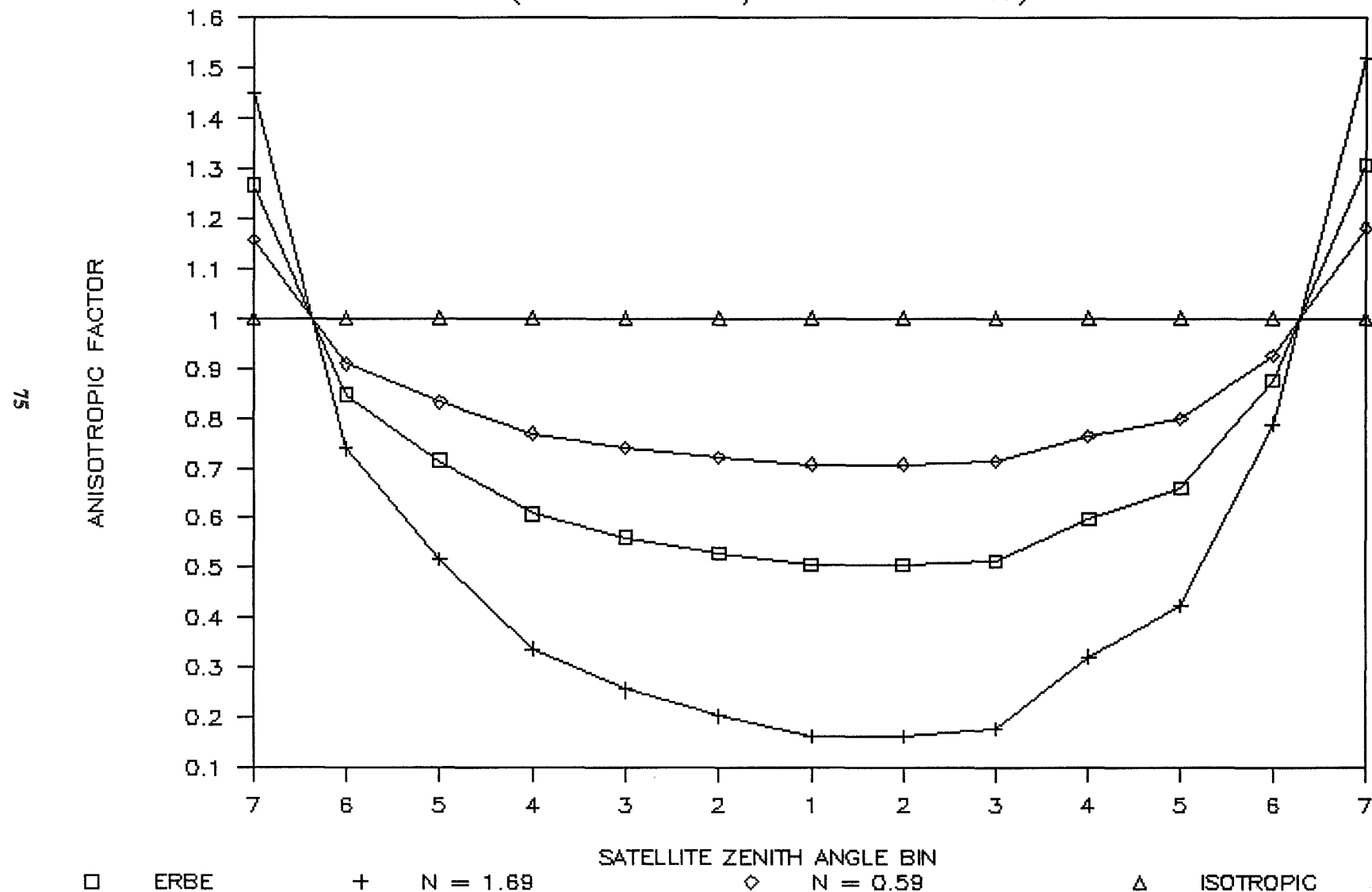

SW REFERENCE FLUX 21Z 1/30/84

Figure 19b.   The errors in shortwave TOA flux relative to the truth field for 21Z January 30, 1984, due to spatial sampling errors, as measured during a single orbit by the ACA (contour interval is 10 W/m^2).


SW DIF ACA 21Z 1/30/84 N=0

SW DIF CERES 21Z 1/30/84 N=0
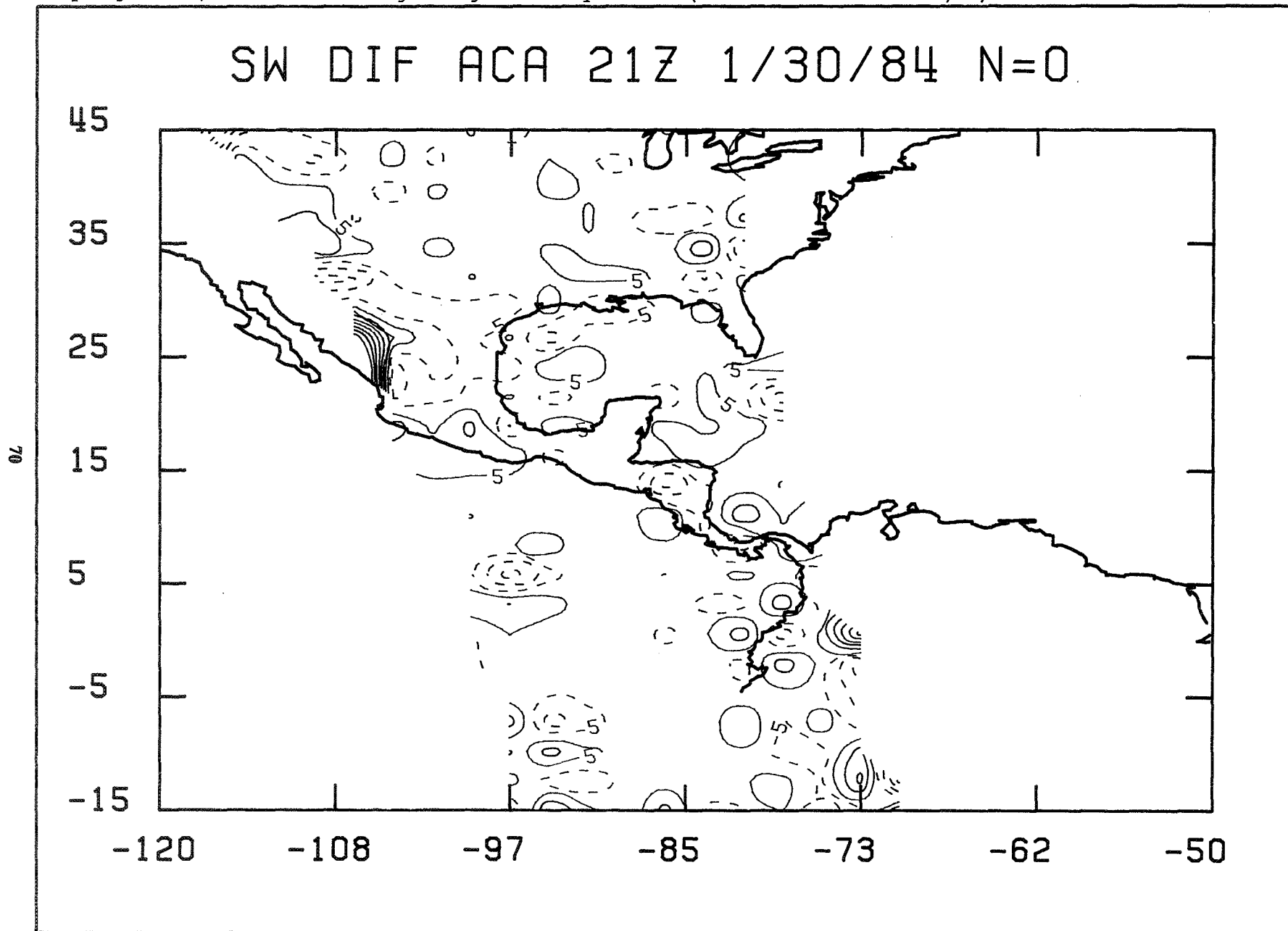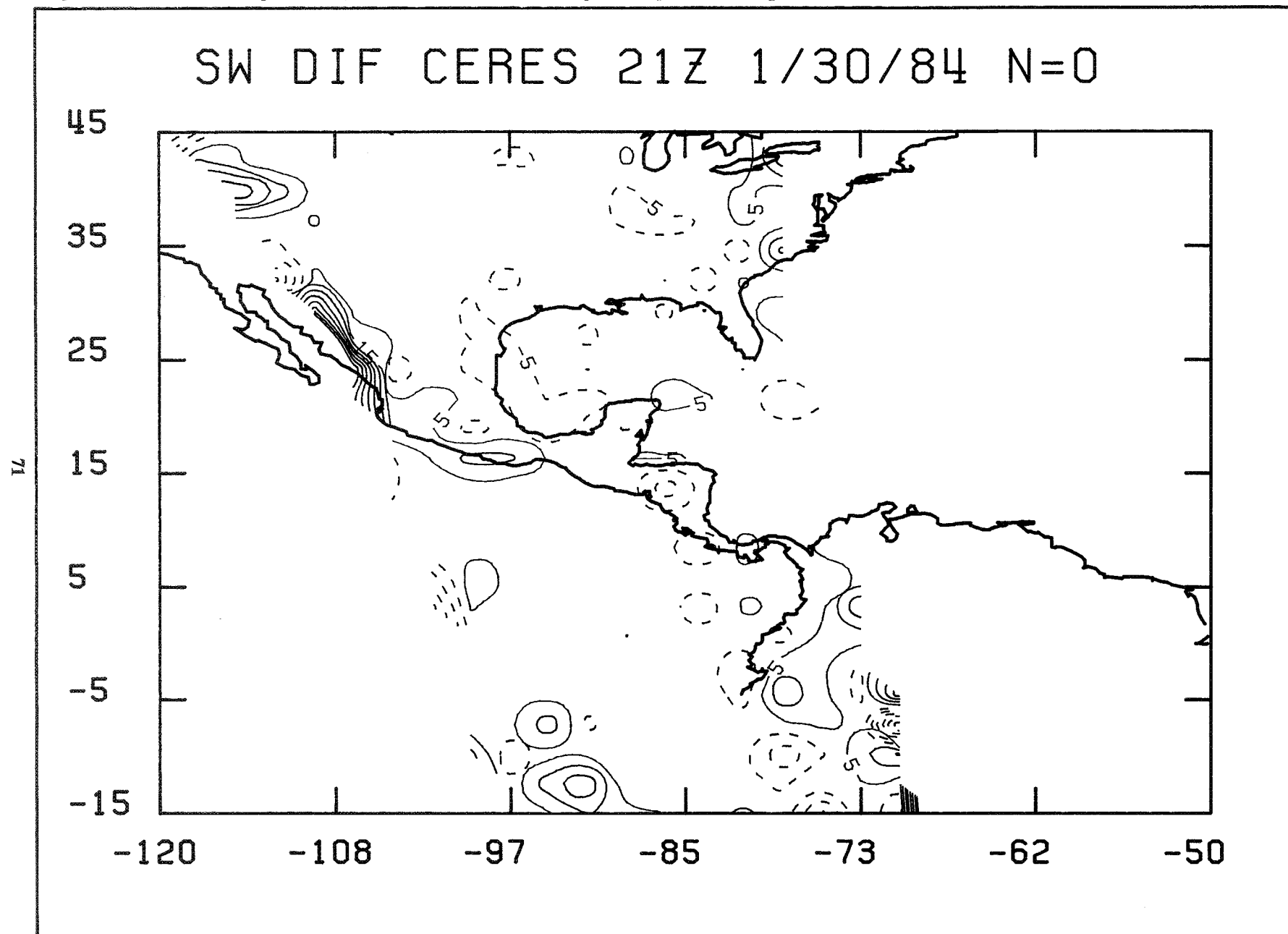
Figure 19d. As in Figure 19b, but as measured during a single orbit by the CSR.

SW DIF CSR 21Z 1/30/84 N=0
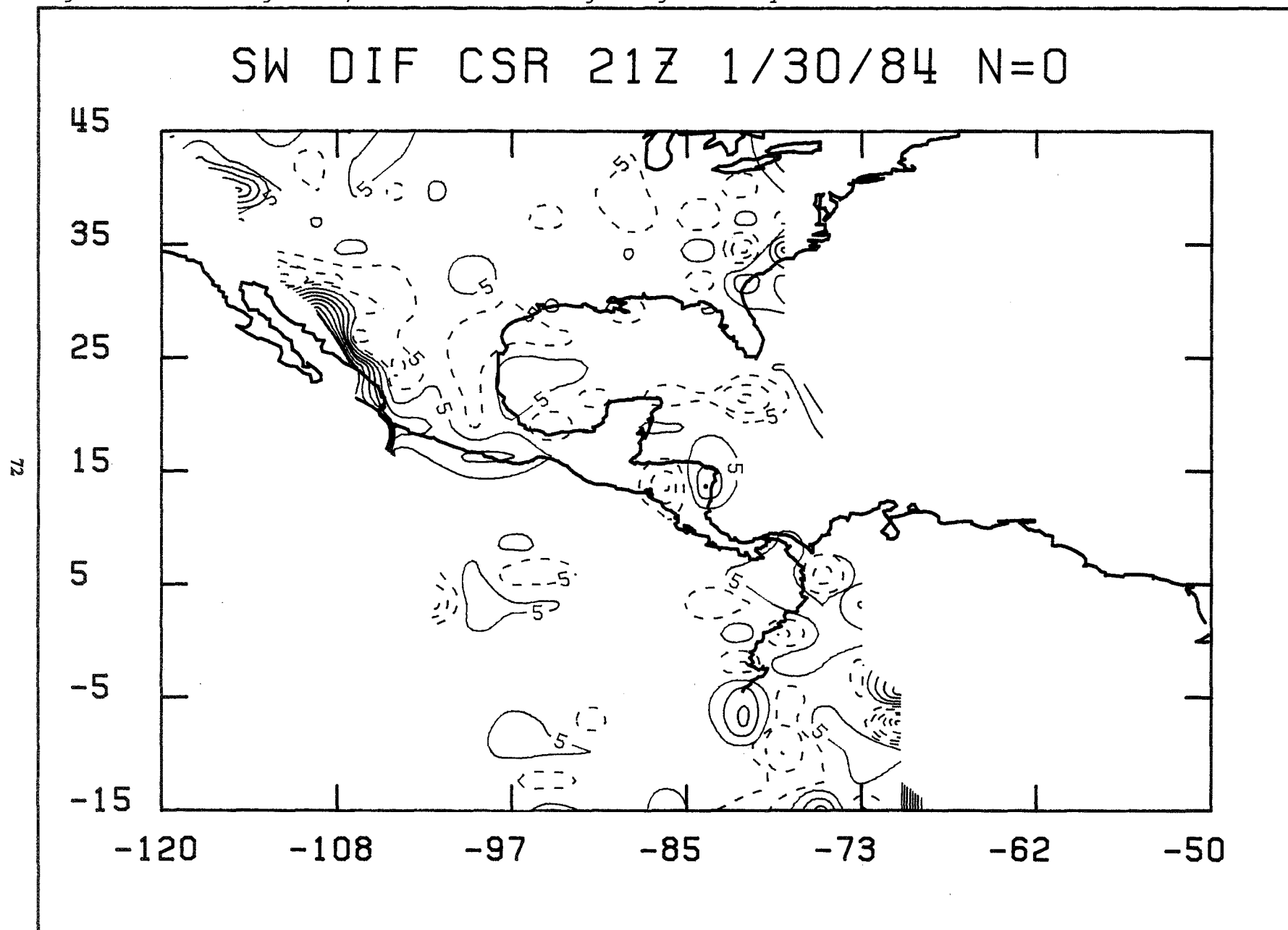
Figure 19e.   As in Figure 19b, but as measured during a single orbit by the ERBE.

SW DIF ERBE 21Z 1/30/84 N=0
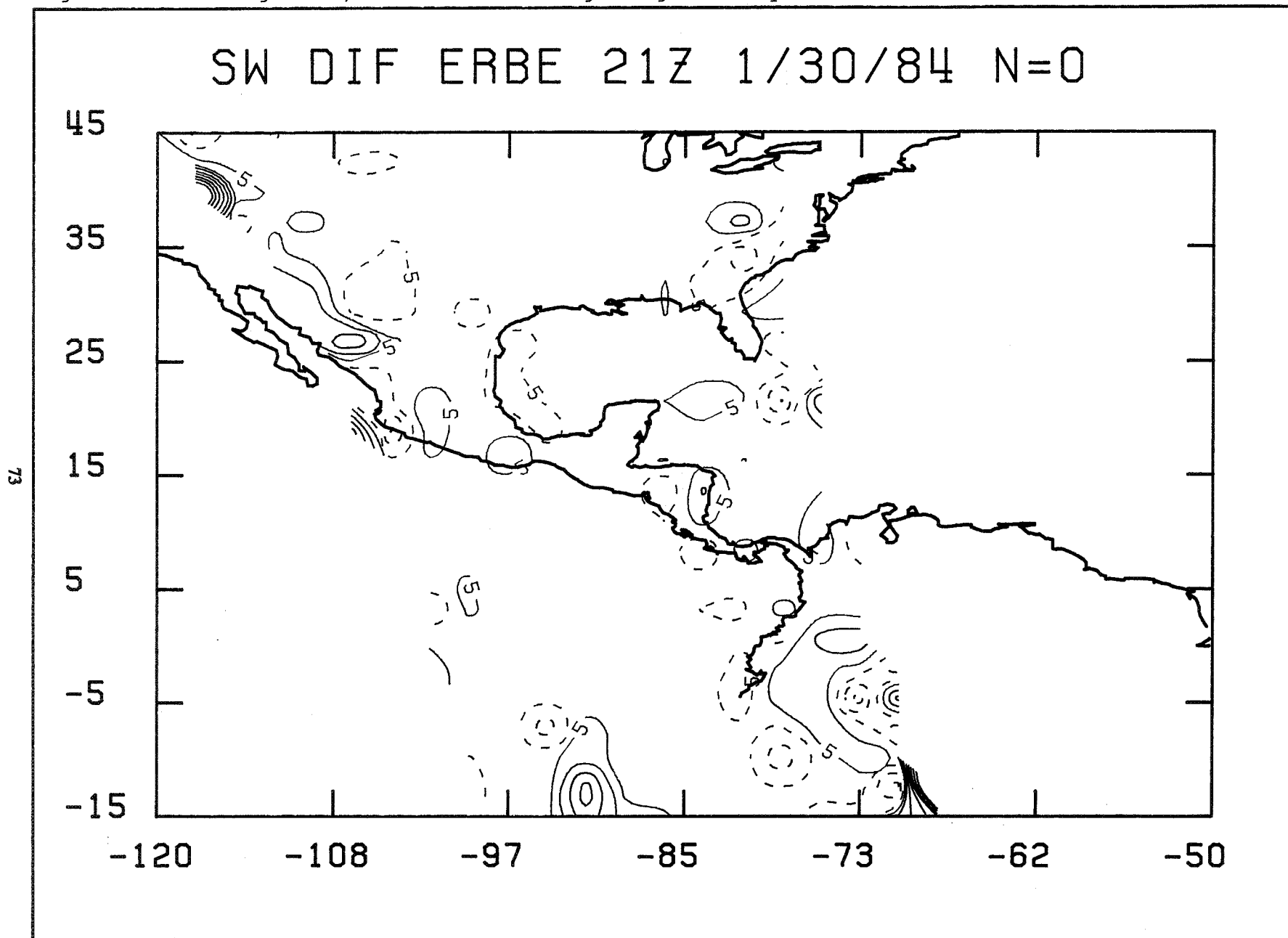
Figure 19f. As in Figure 19b, but as measured during a single orbit by the Nimbus-7 ERB.

SW DIF NIMBUS-7 21Z 1/30/84 N=0
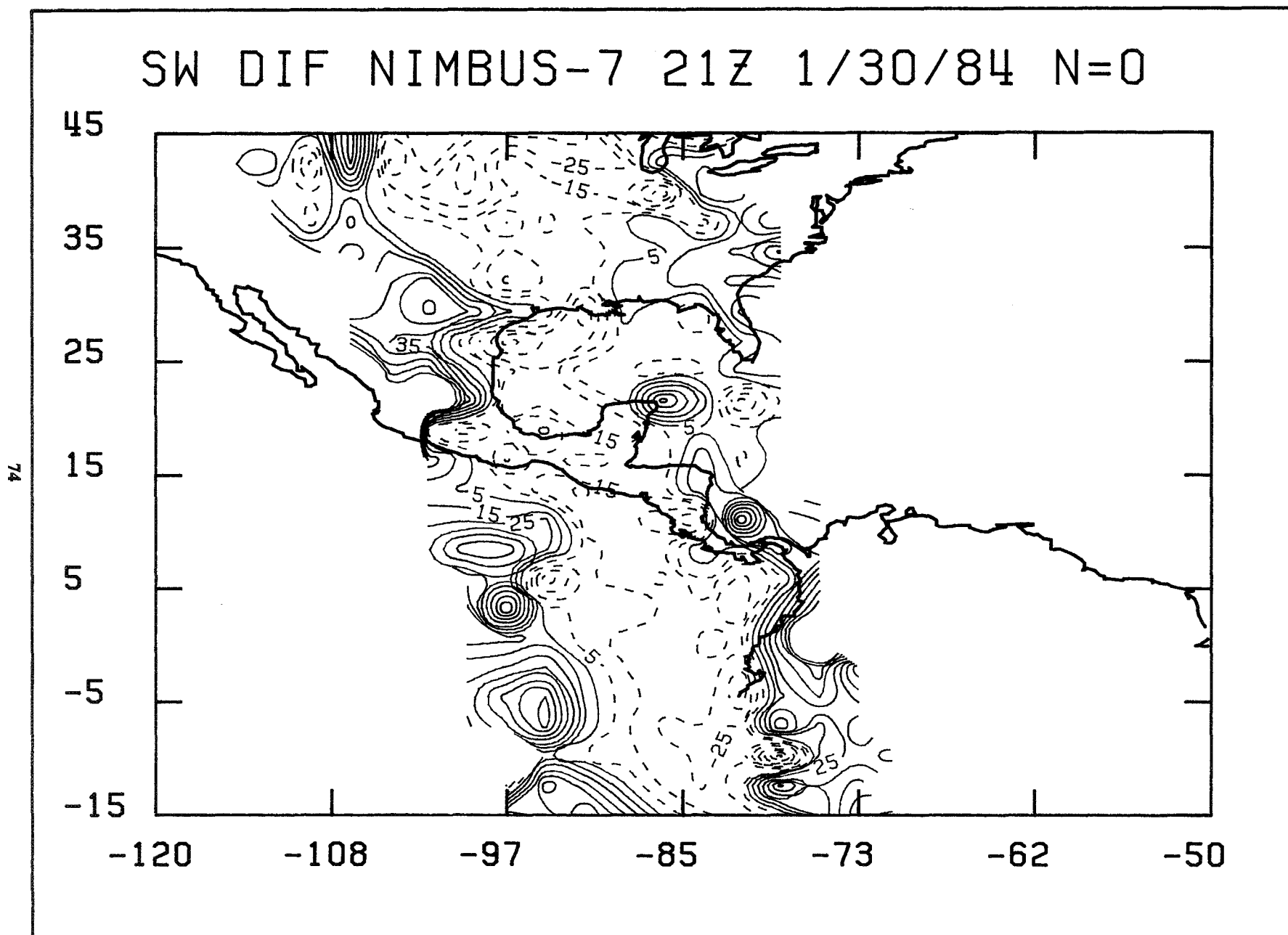
Figure 20. A set of four profiles of anisotropic factor for clear ocean illustrating the dependence on satellite zenith angle and degree of anisotropy.

ERBE VS SCALED ANISOTROPIC MODEL
(RELAZ = 270–240/60–90 SZA = 53–60)

SW ADM ERR ACA 21Z 7/17/83 N=1.69
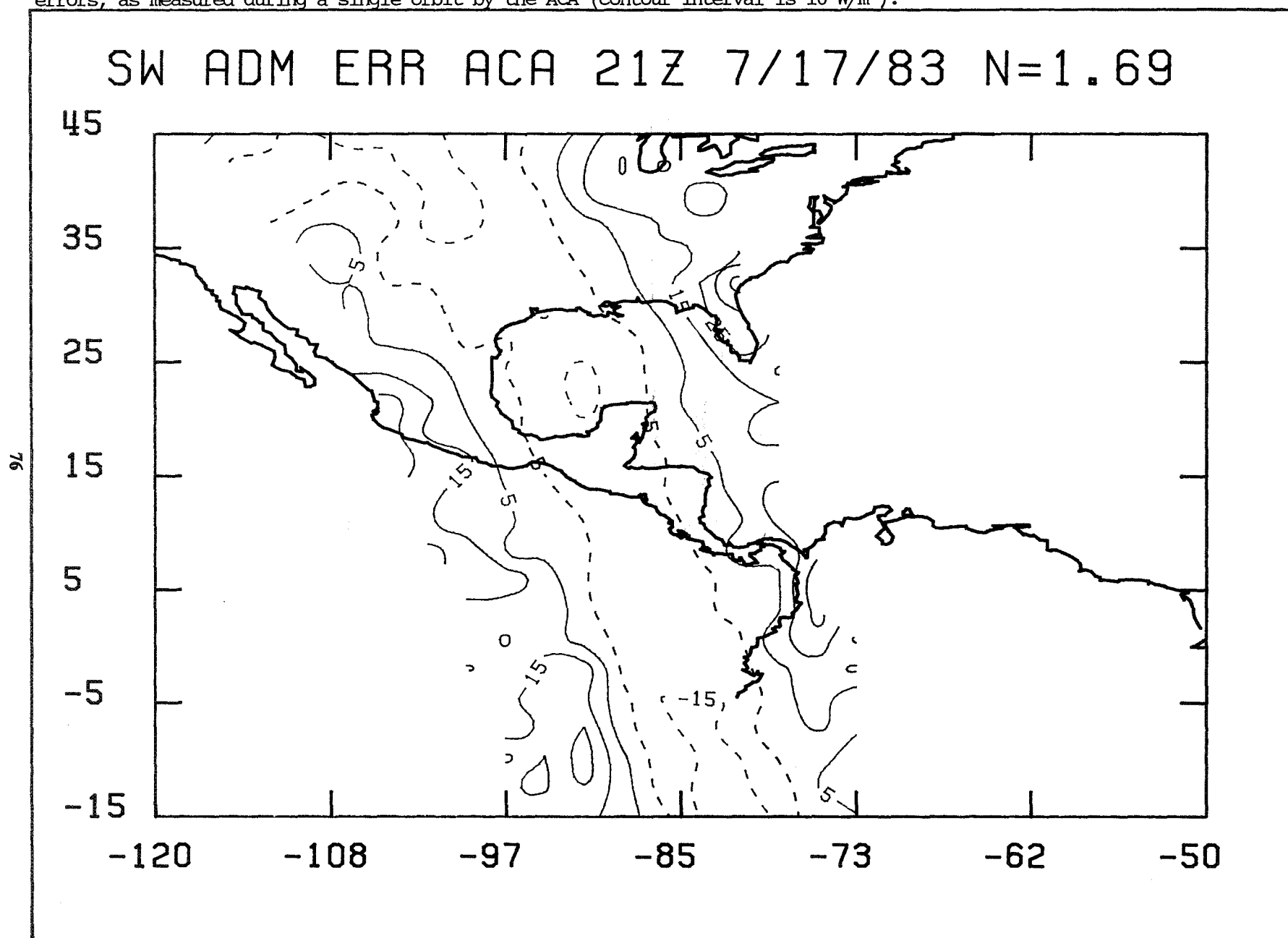
Figure 21b. As in Figure 21a, but as measured during a single orbit by the CERES-I.

SW ADM ERR CERES 21Z 7/17/83 N=1.69
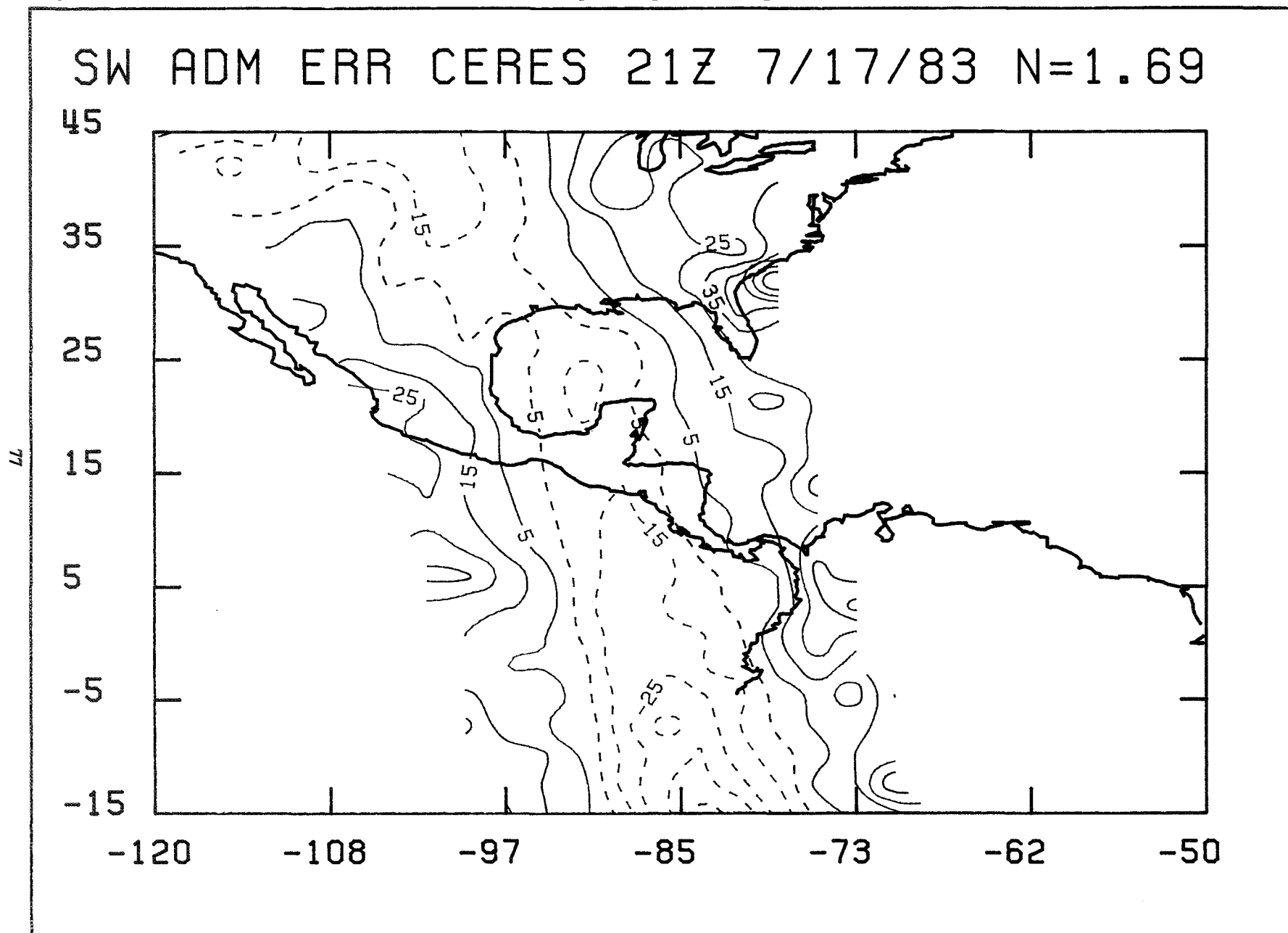
Figure 21c. As in Figure 21a, but as measured during a single orbit by the CSR.
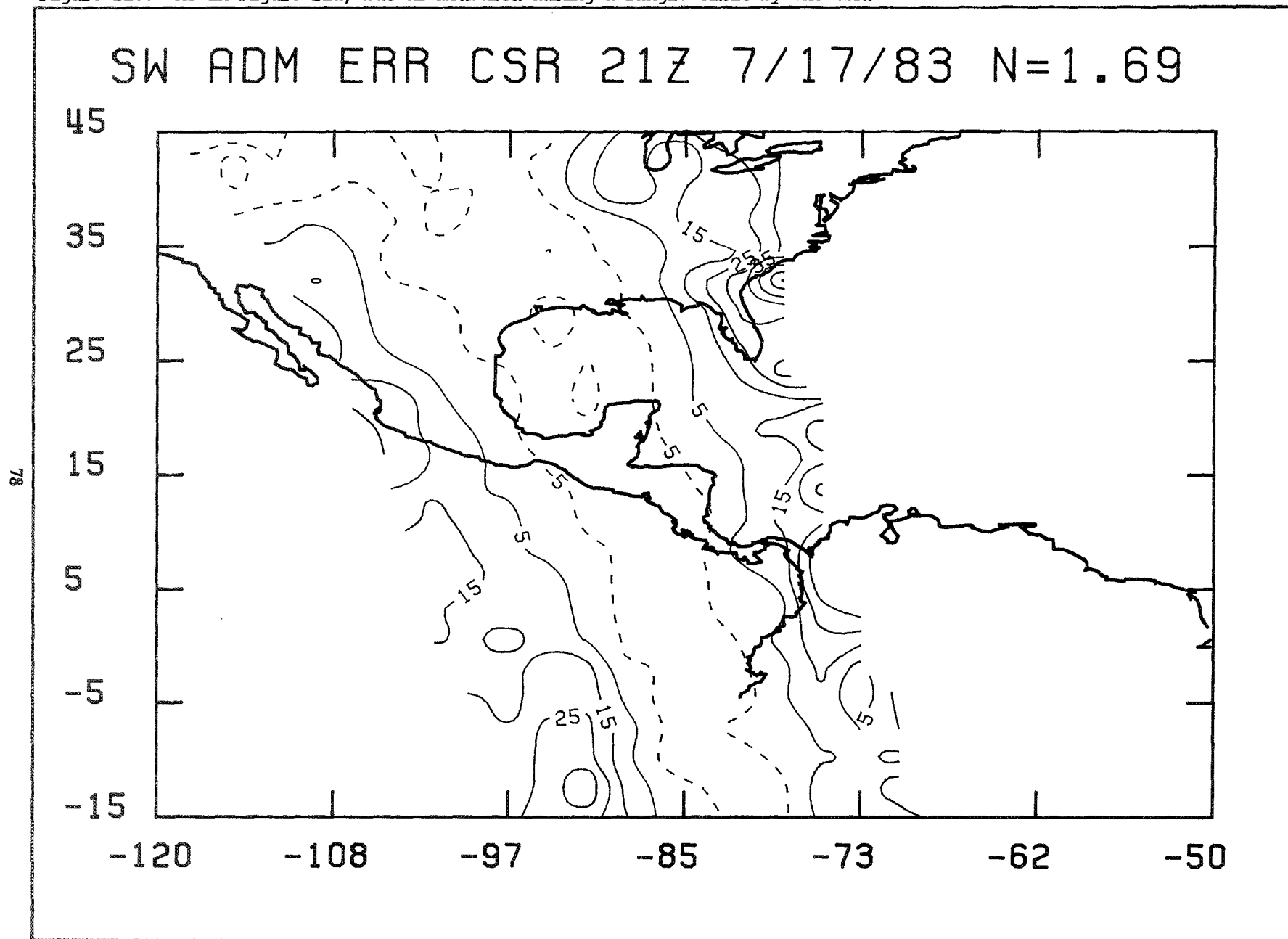
SW ADM ERR ERBE 21Z 7/17/83 N=1.69
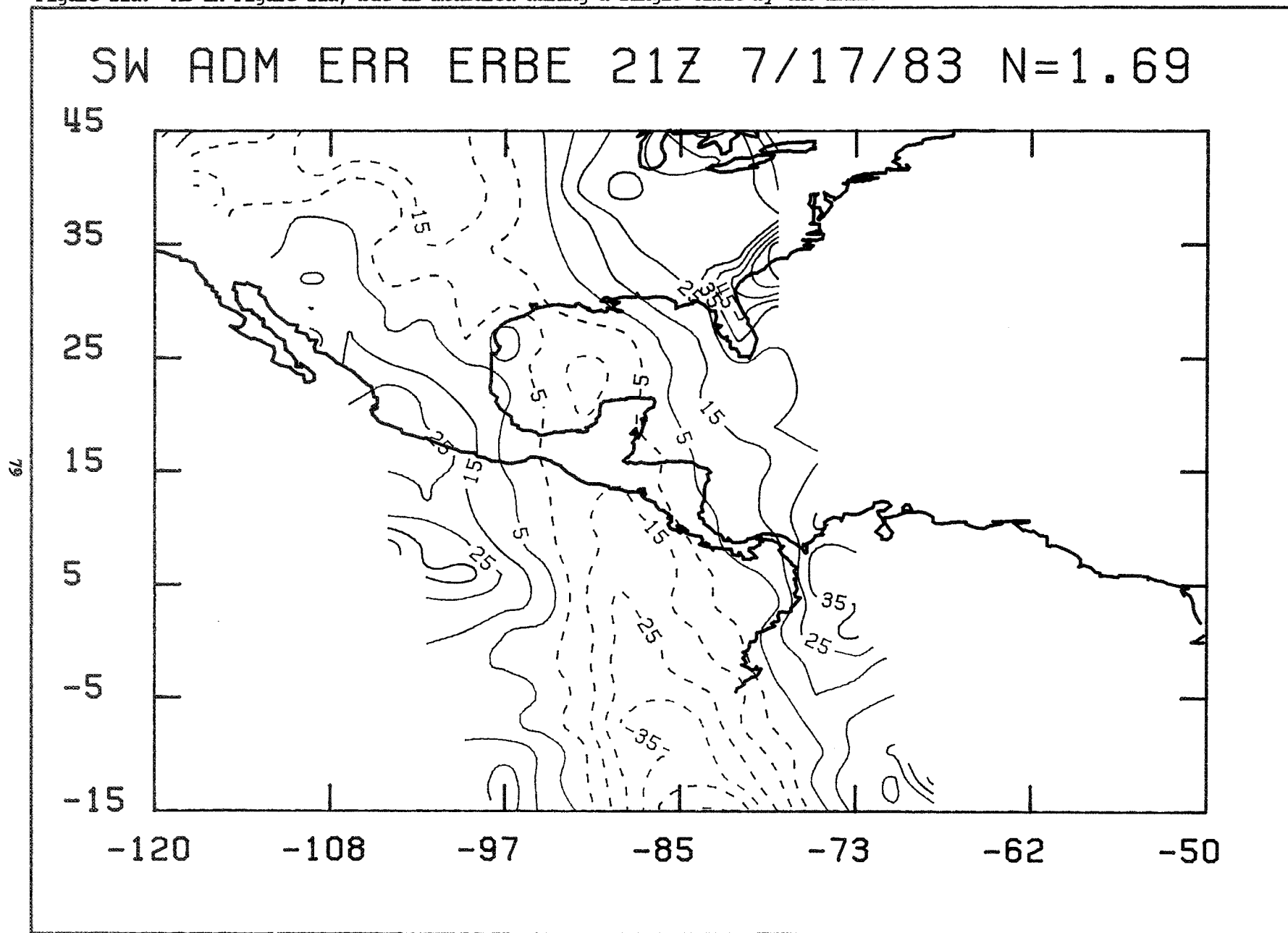
Figure 21e. As in Figure 21a, but as measured during a single orbit by the Nimbus-7 ERB.
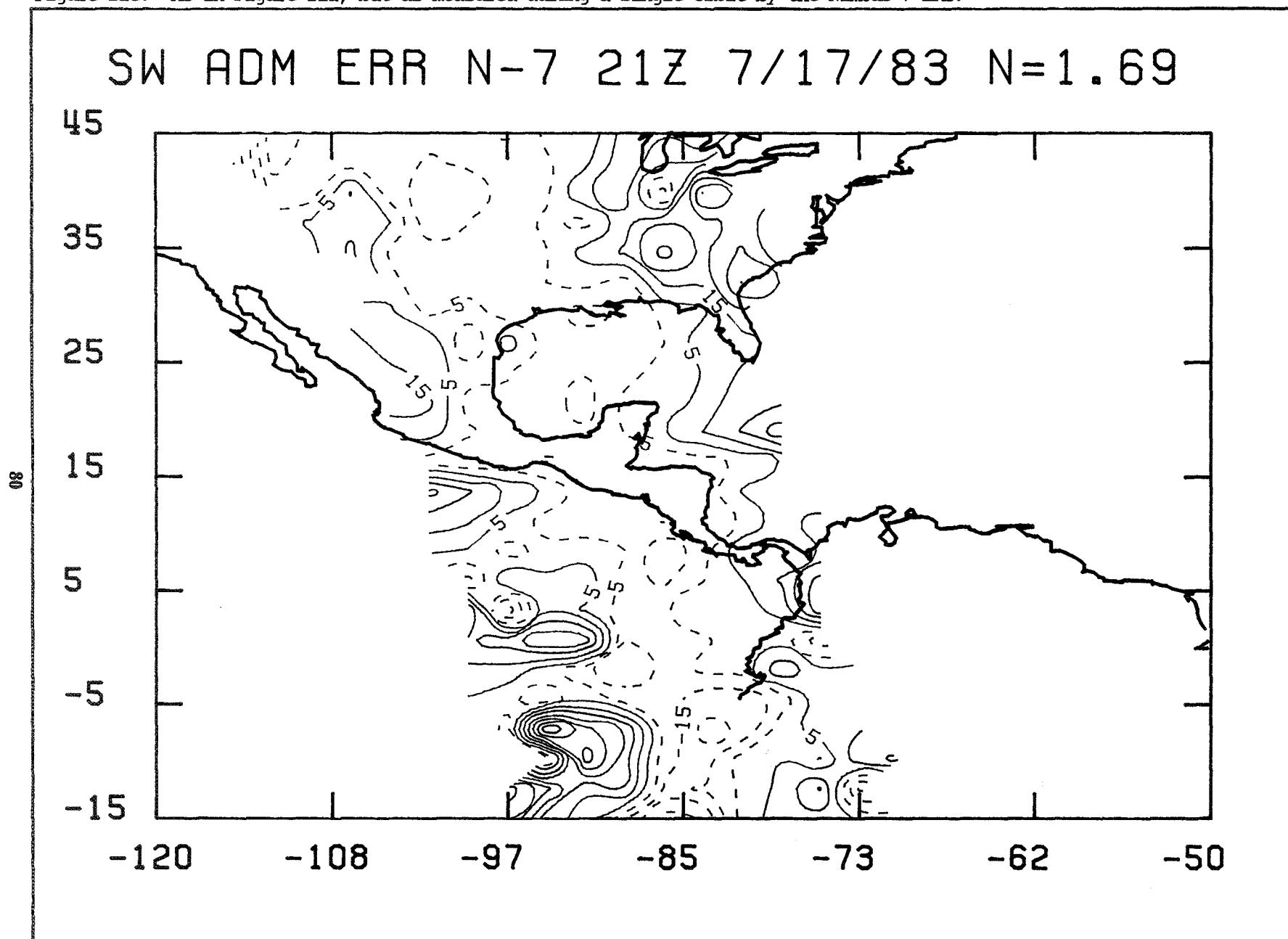

SW ADM ERR N-7 21Z 7/17/83 N=1.69

Figure 22a.   The errors in shortwave TOA flux relative to the truth field for 21Z January 30, 1984, due to angular sampling errors, as measured during a single orbit by the ACA (contour interval is 10 W/m^2).
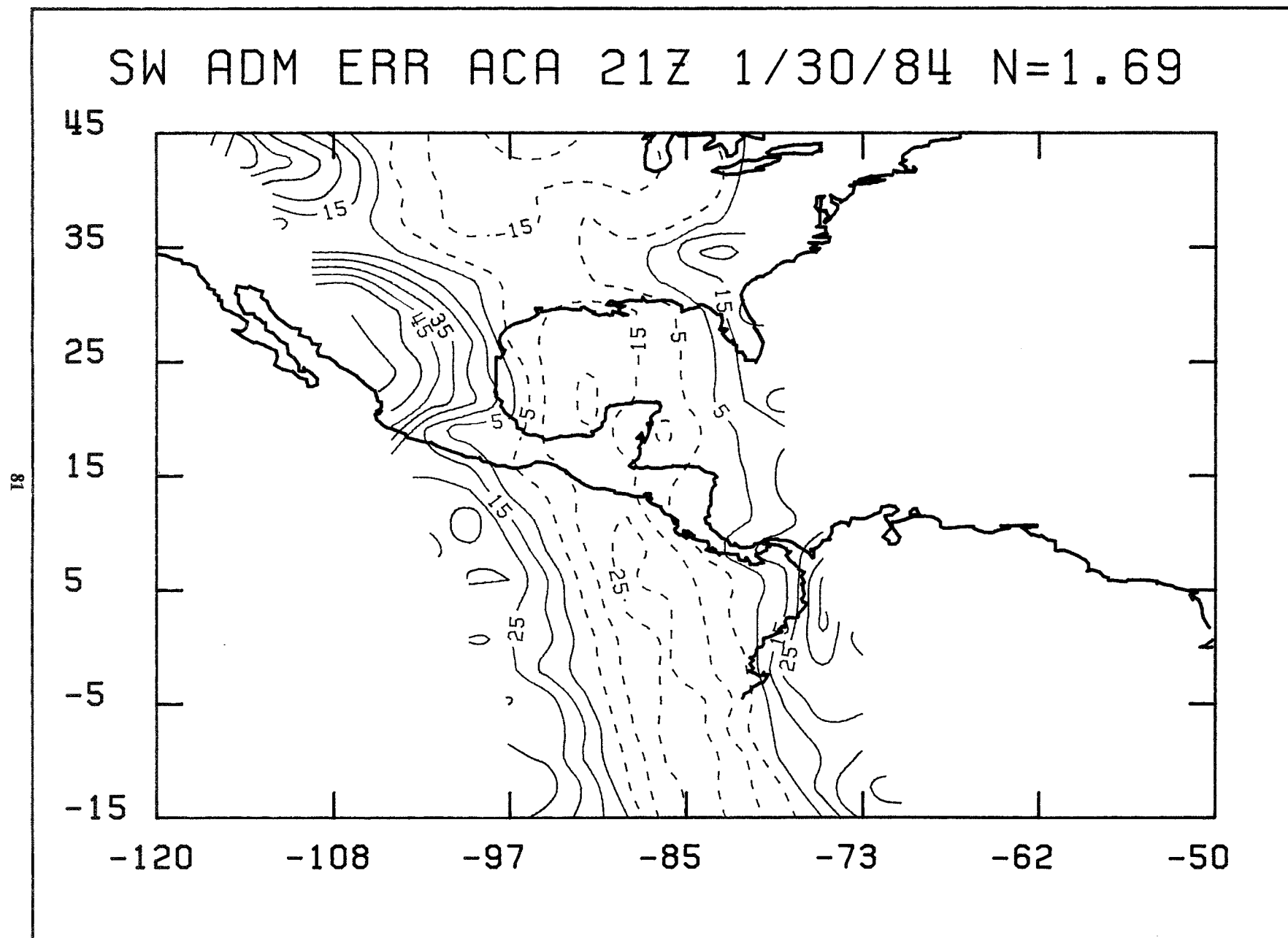

SW ADM ERR ACA 21Z 1/30/84 N=1.69

Figure 22b. As in Figure 22a, but as measured during a single orbit by the CERES-I.
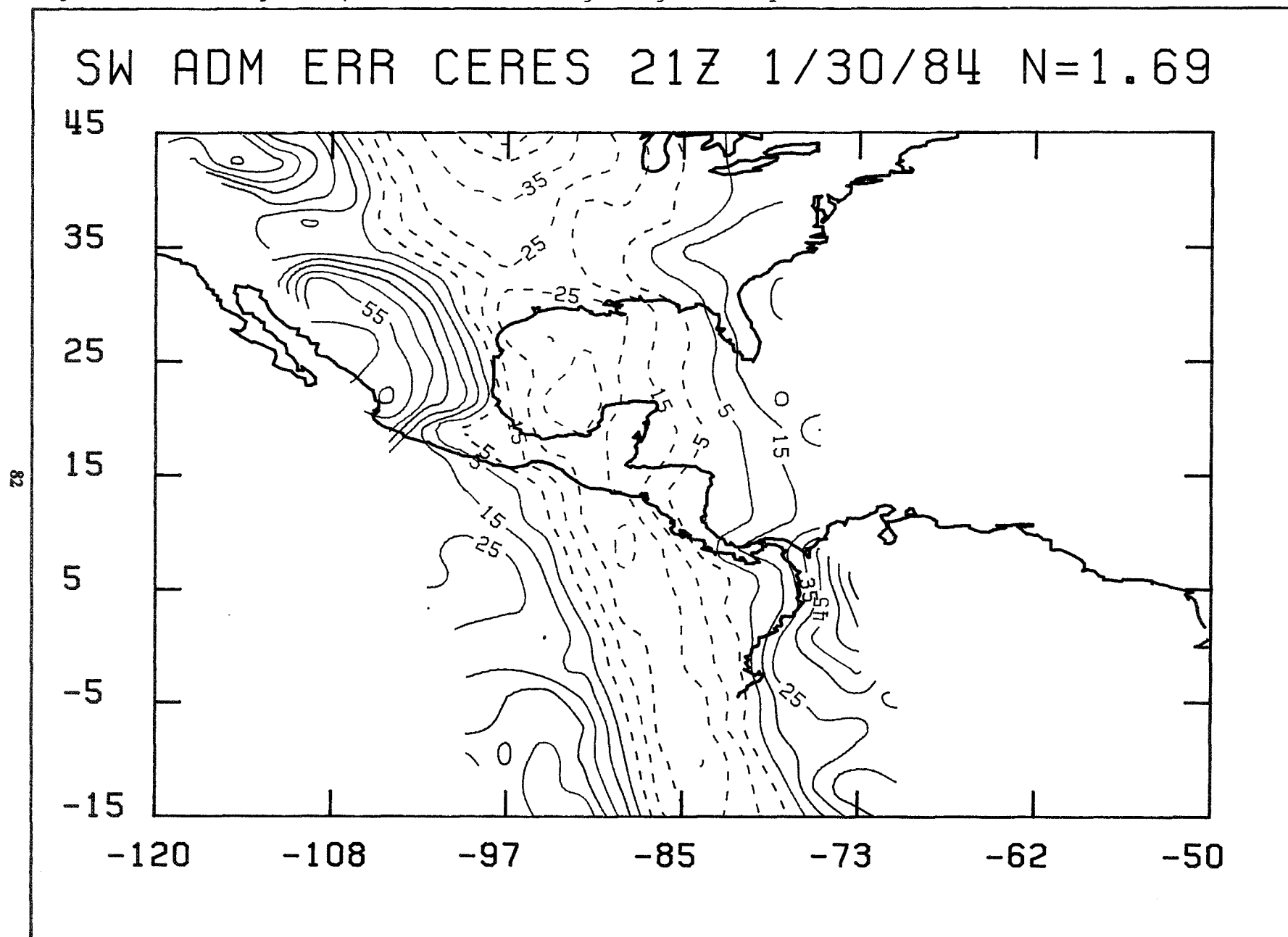
SW ADM ERR CERES 21Z 1/30/84 N=1.69

SW ADM ERR CSR 21Z 1/30/84 N=1.69
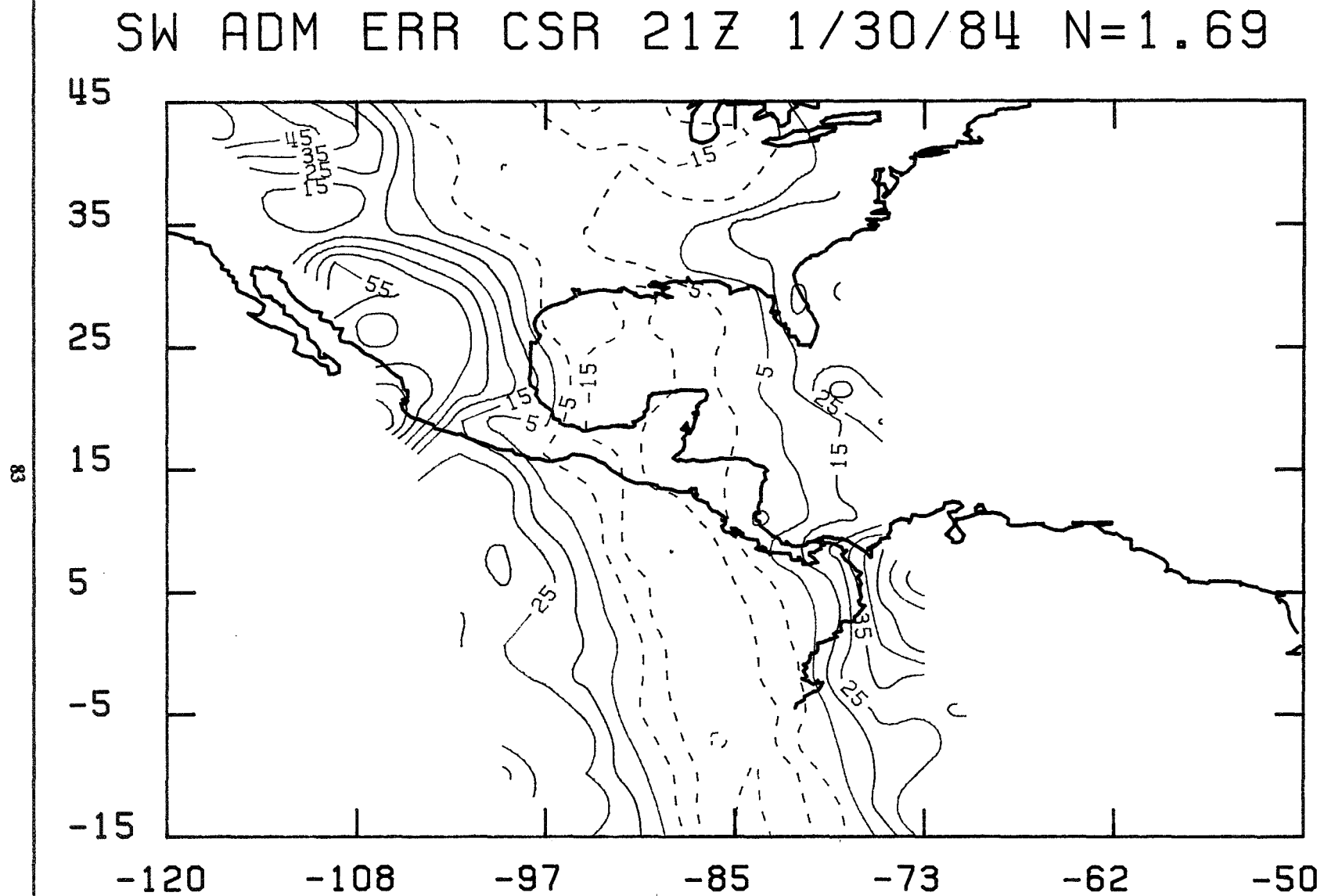
Figure 22d. As in Figure 22a, but as measured during a single orbit by the ERBE.

SW ADM ERR ERBE 21Z 1/30/84 N=1.69
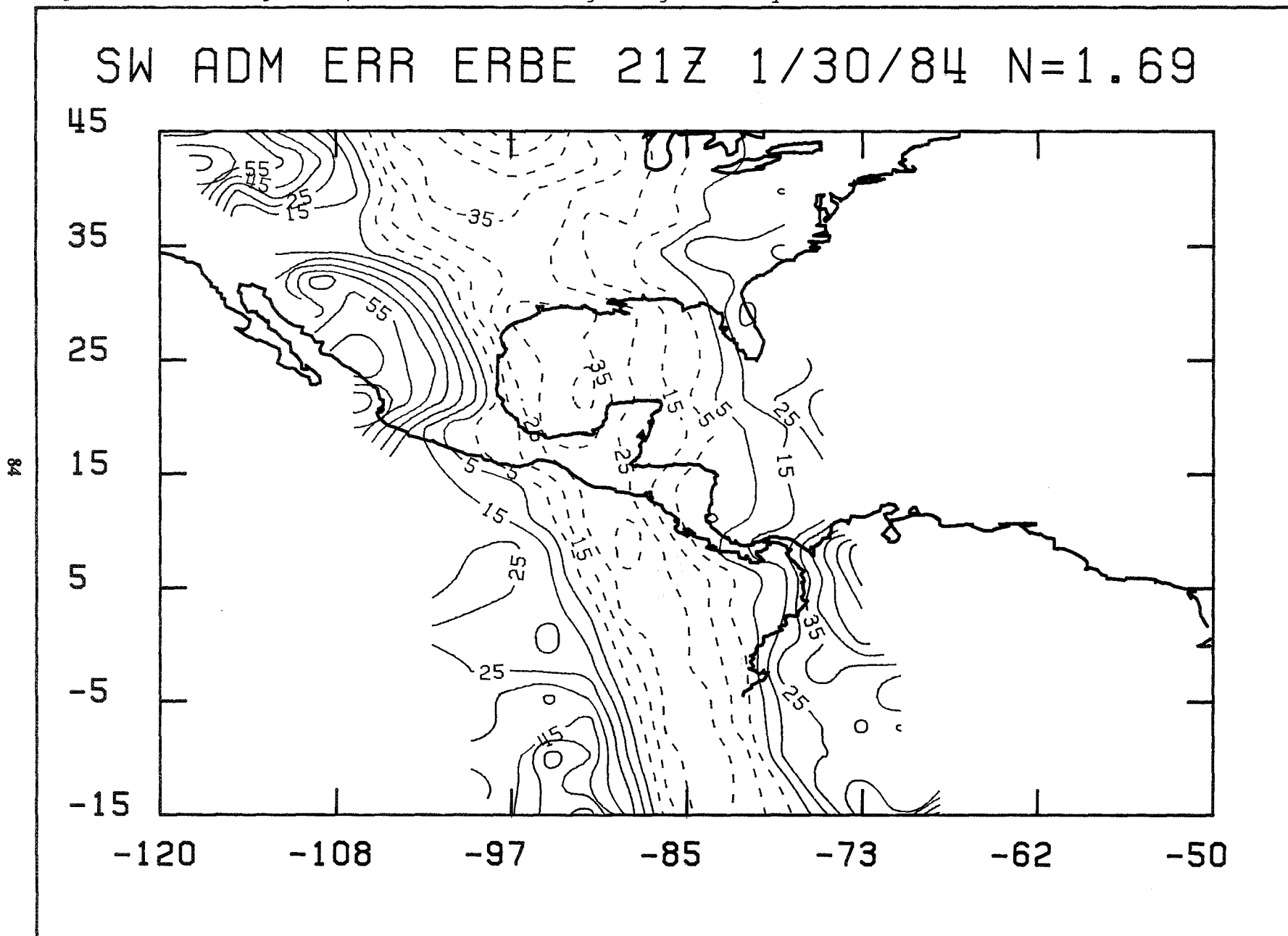
Figure 22e. As in Figure 22a, but as measured during a single orbit by the Nimbus-7 ERB.

SW ADM ERR N-7 21Z 1/30/84 N=1.69
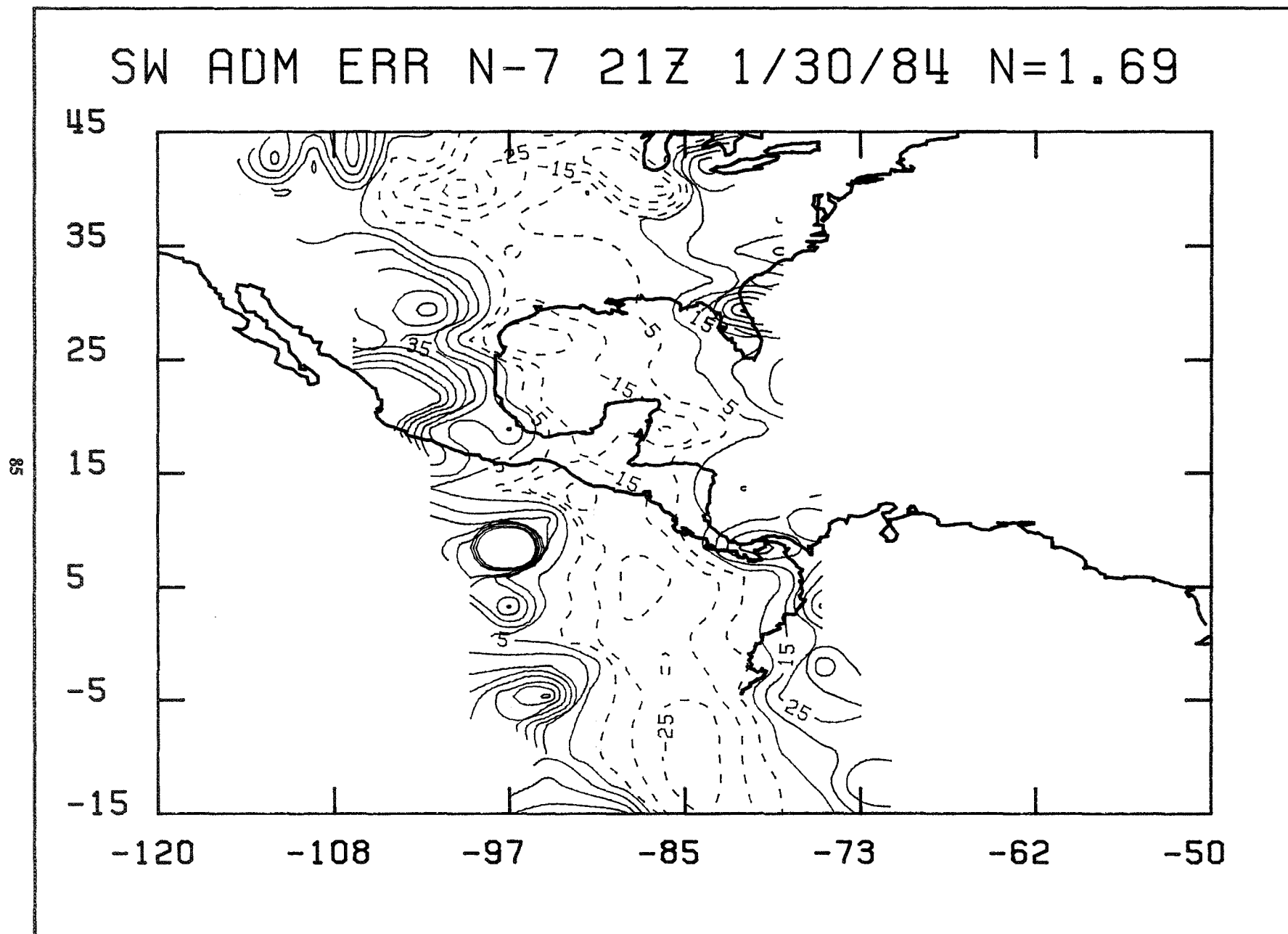
3.3 TOTAL MEASUREMENT ERRORS

Total regional bias errors (with N=1.69) are shown for July and January, respectively, in Figures 23a through 23e and Figures 24a through 24e for the five radiometers. The figures illustrate the total error patterns that arise during an AN afternoon overpass (21Z) of the study domain having a local Equator crossing time of about 3:15 PM (86°W). Readily noticeable in the error contours of all instruments is the characteristic gradient from negative values near nadir to positive values, near the edge of the scan swath. This behavior is due to the systematic variation of ADM errors with increasing satellite zenith angle that we have previously noted and which is here combined with random distributions of spatial sampling error. Also noticeable are zonal variations in ADM error for the CERES-I and ERBE instruments which are evident in the changing amplitude of the near-nadir error trough. This is discussed in a later section.

3.4 TIME-AVERAGED ERRORS

A complete set of tables summarizes the results of the simulation study. Both the TOA shortwave and longwave irradiances are considered in terms of "orbital" bias, STD, and RMS errors. GOES synoptic image times of 15Z and 21Z are presented for equator crossings at 109°W, 86°W, and 63°W for each of the five candidate scanner configurations. The effects of both spatial sampling errors (N=1) and the combination of spatial sampling and bidirectional modelling errors (N=0.59 and N=1.69) are analyzed for both the six-day average of daily instantaneous errors and the error of the six-day average instantaneous fields.

Table 11 contains the statistical summary (spatial RMS error, mean bias, and standard deviation about the mean bias) for the six days of simulations performed for July 1983 with the 15Z GOES image. The longitudes of 109°W, 86°W, and 63°W cover the simulation domain for a range of local times three to eight hours earlier than the image time (i.e., 7 to 12 AM local time). Corresponding variations in the angle of illumination and the level of solar insolation are present in the three sets of orbits. Daily instantaneous flux errors are derived from the ensemble of regional satellite estimates, Eq.(31), and errors, Eq.(29), when collected over identical, single orbit passes of the study area on each of six days. Ensemble RMS errors were computed using Eq.(41) where M is the total number of observations in the 6-day sample, typically about 6x200=1200. Because the number of targets sampled during an orbit was the same each day, the ensemble regional bias is equal to the mean orbital regional bias when averaged for six days. Ensemble STD errors were obtained from the RMS and bias components using Eq.(53). Errors in the 6-day mean instantaneous fluxes consider the error properties of the time-averaged fields. Here the instantaneous reference fluxes, Eq.(30), and satellite estimates are first averaged for six days to obtain regional mean values. RMS, STD, and BIAS errors are then computed over an orbital swath using the time-averaged fields. Table 12 contains similar summaries, however the GOES image is taken at 21Z, providing local times across the domain which range from 1 to 6 PM. Tables 13 and 14 provide the simulation statistics for the 15Z and 21Z GOES images for the six days of simulation during January 1984.

When only spatial sampling errors are present, the measurements are all largely unbiased. Due to the high instantaneous insolation values, particularly at 86°W and 63°W for the 15Z image, the shortwave flux errors greatly exceed those of the longwave fluxes. The shortwave errors are generally larger in July than January due to the solar declination, as the simulation domain lies more within the northern hemisphere than the southern (15°S to 45°N). In this set of experiments, the spatial sampling ability of the scanner, as governed by its instantaneous field of view size, sampling rate, and scan pattern, largely determines the sensor's performance. In general, the two cross-track scanners (ERBE and CERES-I) perform the best under the specified conditions, with the lowest RMS errors. The CERES-I and ERBE

Figure 23a. The errors in shortwave TOA flux relative to the truth field for 21Z July 17, 1983, due to total sampling errors (angular plus spatial), as measured during a single orbit by the ACA (contour interval is 10 W/m^2).

SW DIF ACA 21Z 7/17/83 N=1.69
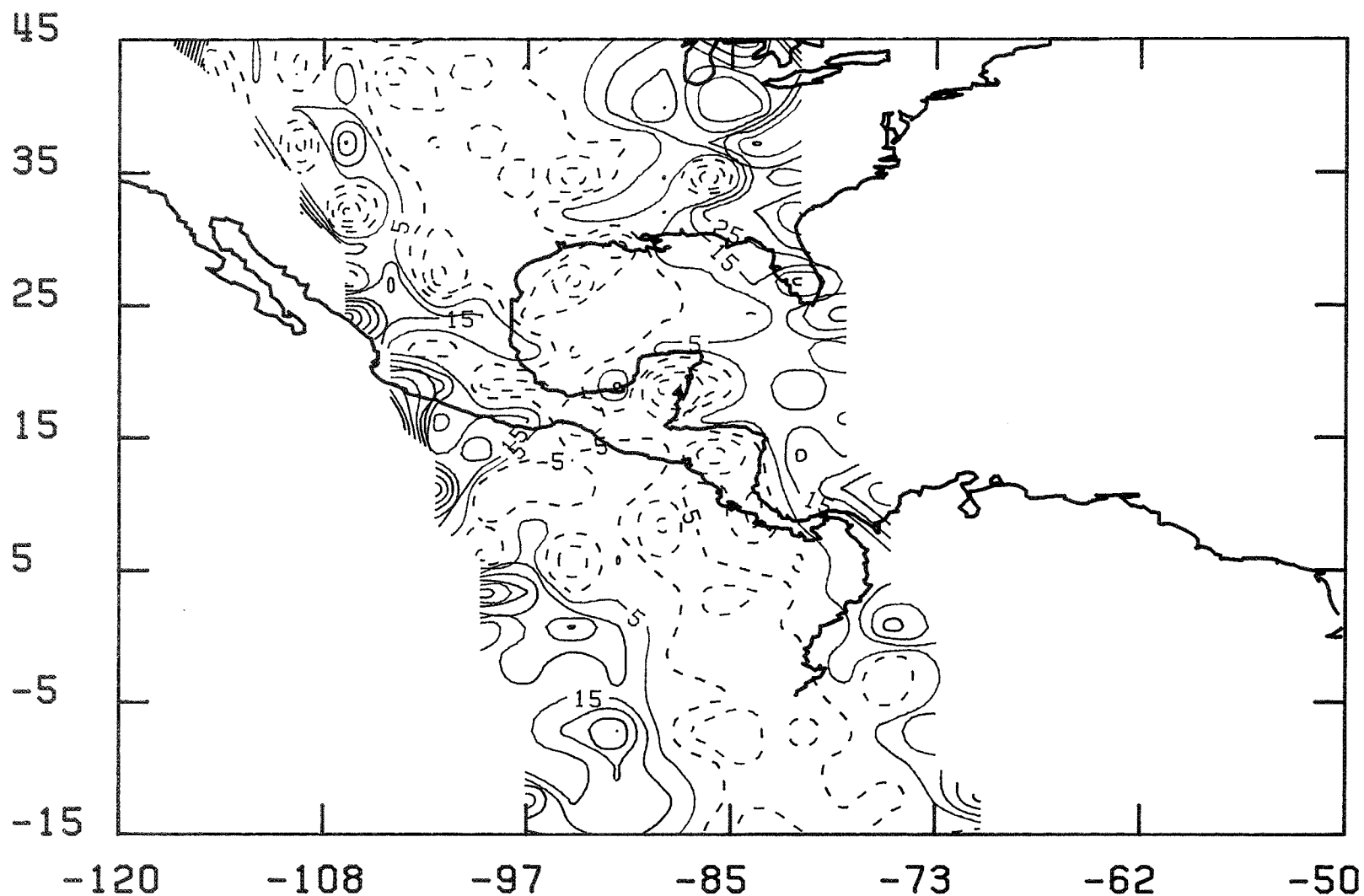
SW DIF CERES 21Z 7/17/83 N=1.69
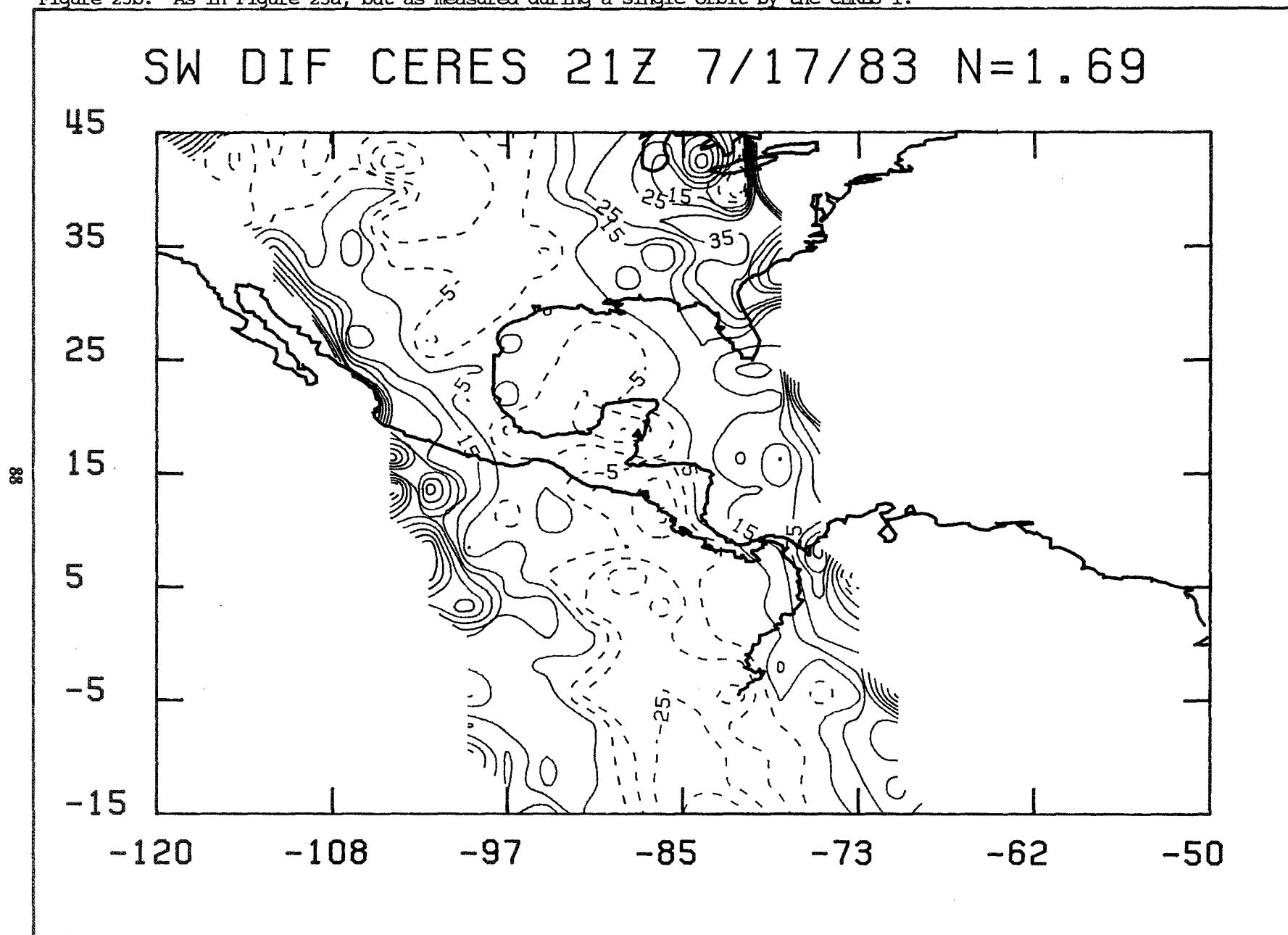
Figure 23c. As in Figure 23a, but as measured during a single orbit by the CSR.

SW DIF CSR 21Z 7/17/83 N=1.69
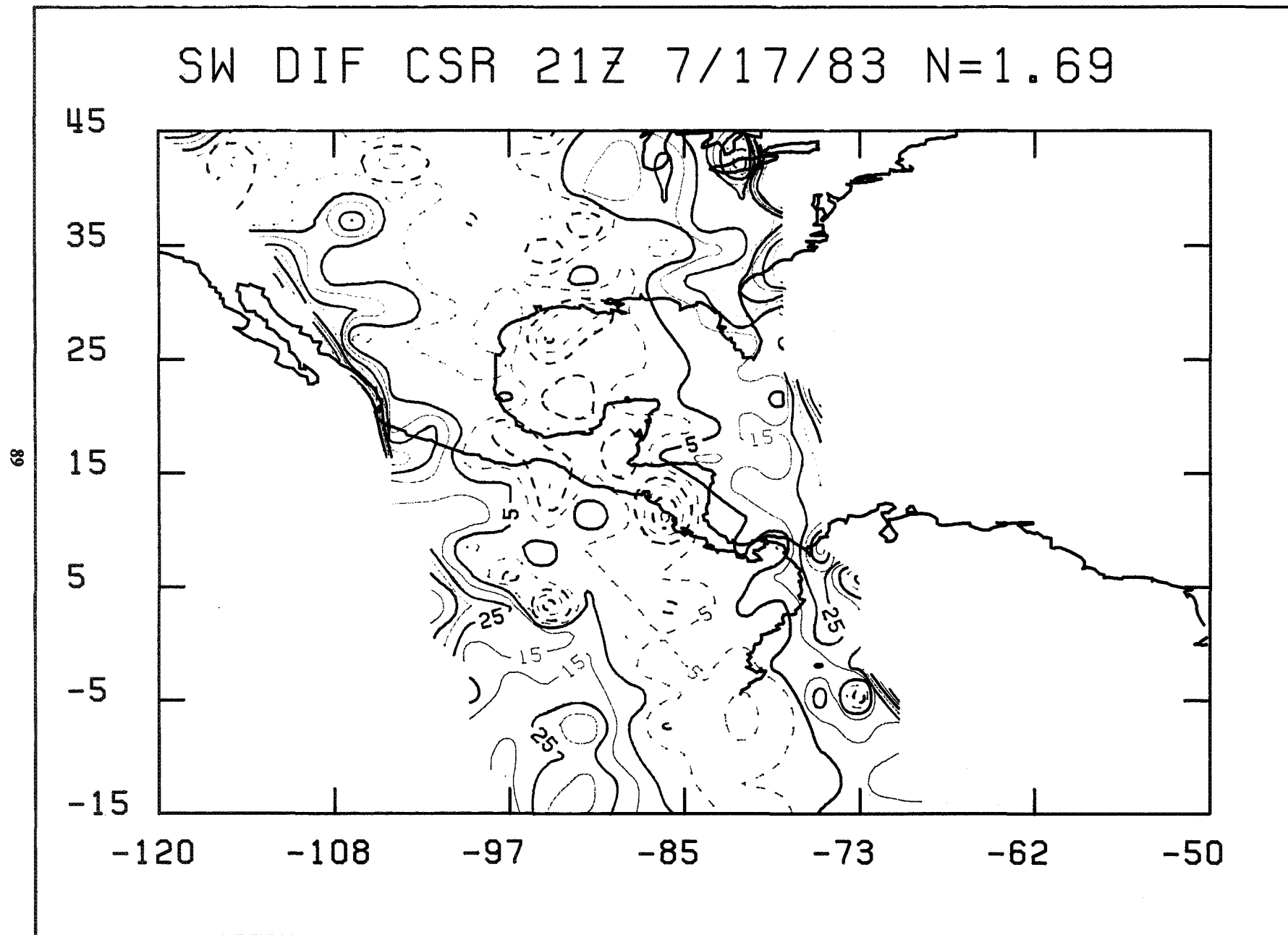
Figure 23d. As in Figure 23a, but as measured during a single orbit by the ERBE.
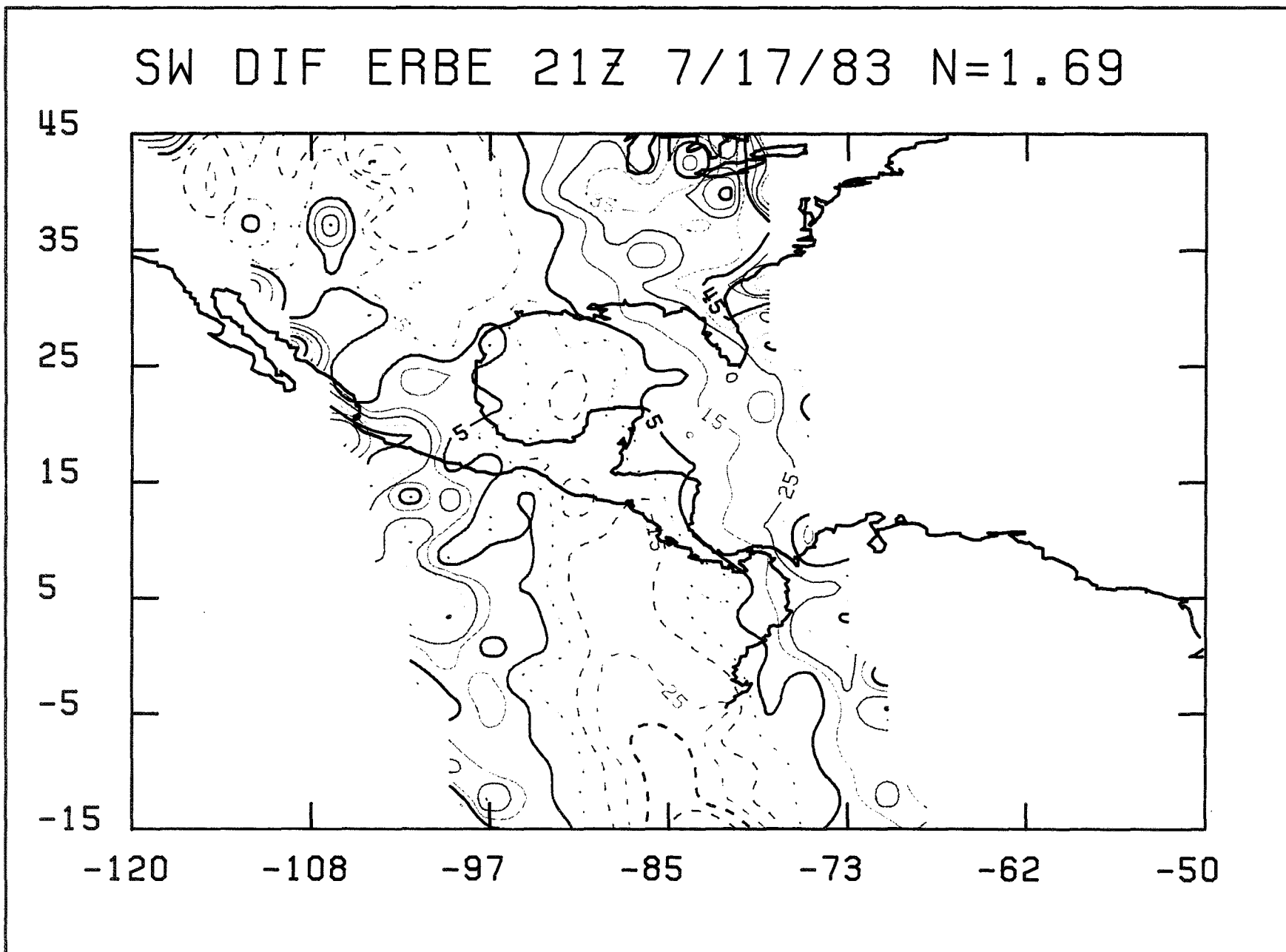
SW DIF ERBE 21Z 7/17/83 N=1.69

SW DIF NIMBUS-7 21Z 7/17/83 N=1.69
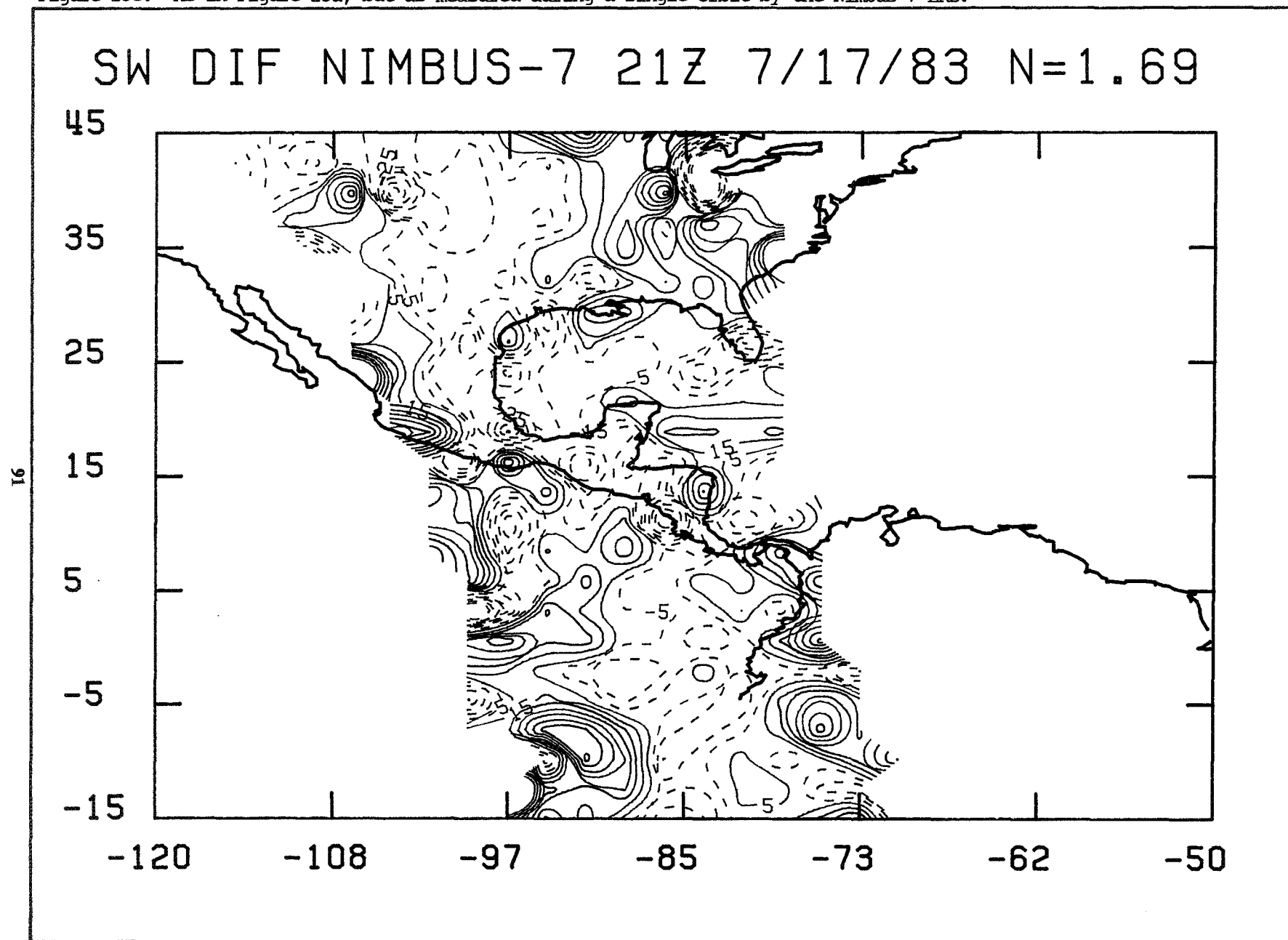
Figure 24a. The errors in shortwave TOA flux relative to the truth field for 21Z January 30, 1984, due to total sampling errors (angular plus spatial), as measured during a single orbit by the ACA (contour interval is 10 W/m^2).


SW DIF ACA 21Z 1/30/84 N=1.69

SW DIF CERES 21Z 1/30/84 N=1.69
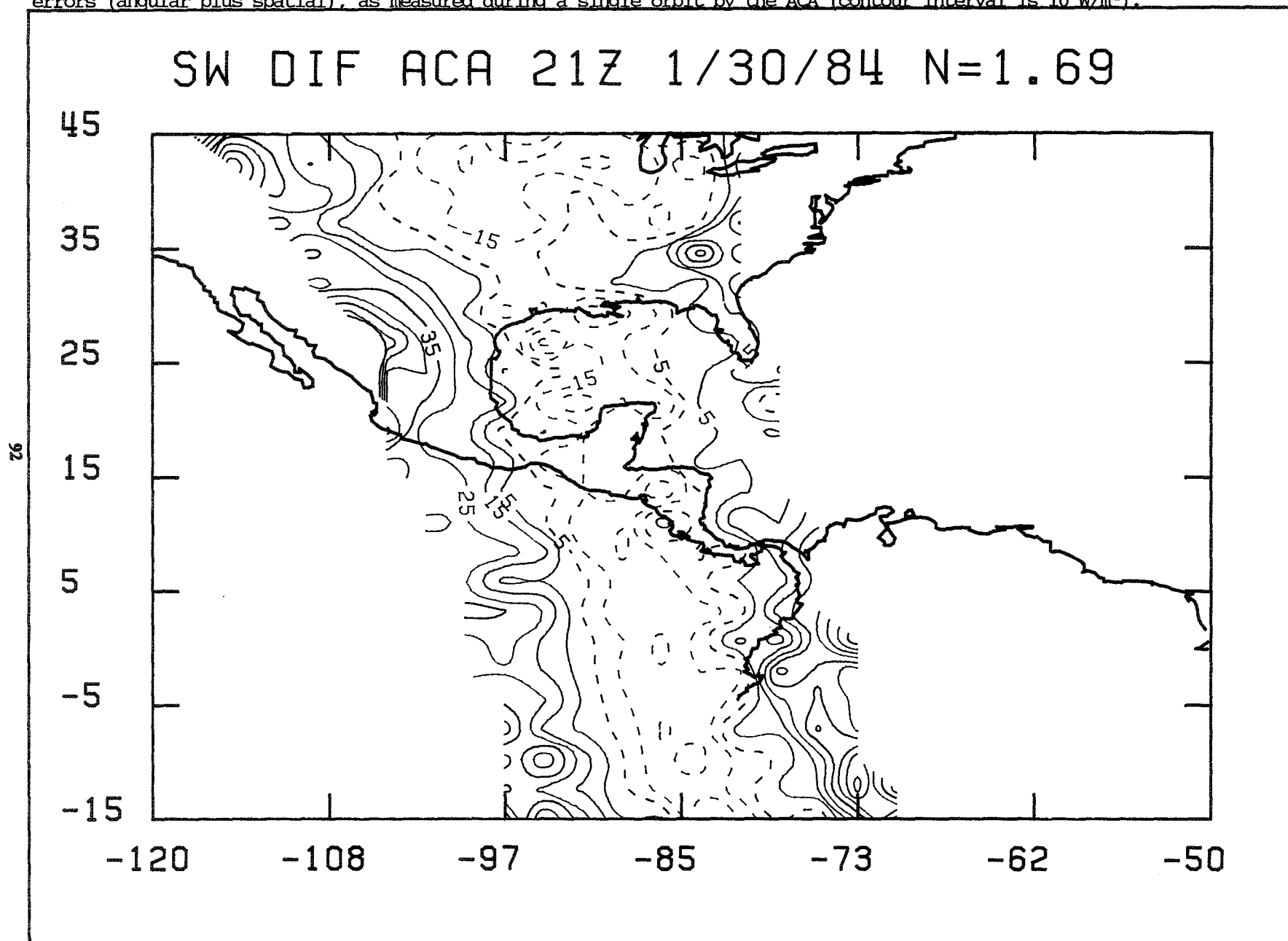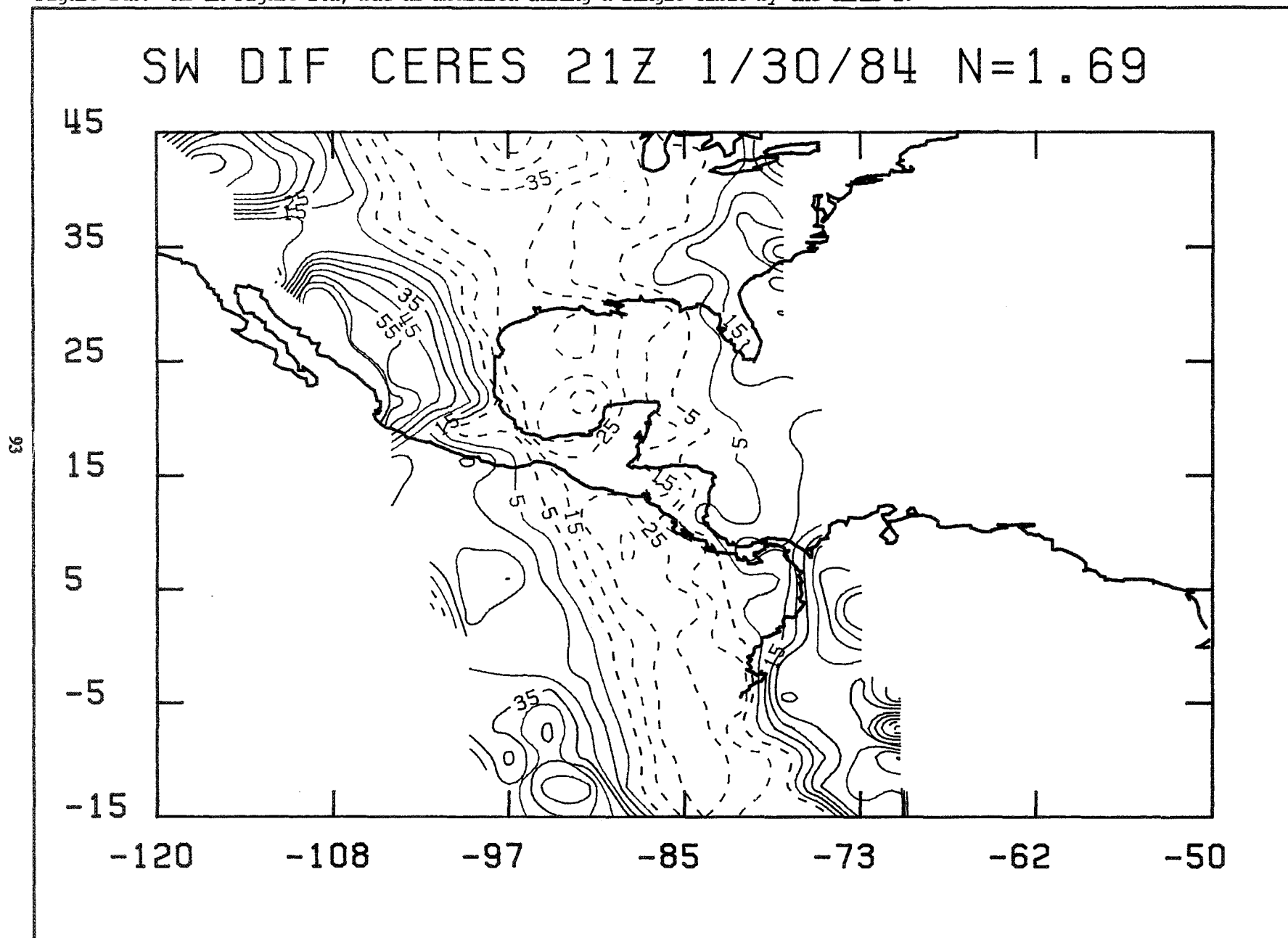
Figure 24c. As in Figure 24a, but as measured during a single orbit by the CSR.

SW DIF CSR 21Z 1/30/84 N=1.69
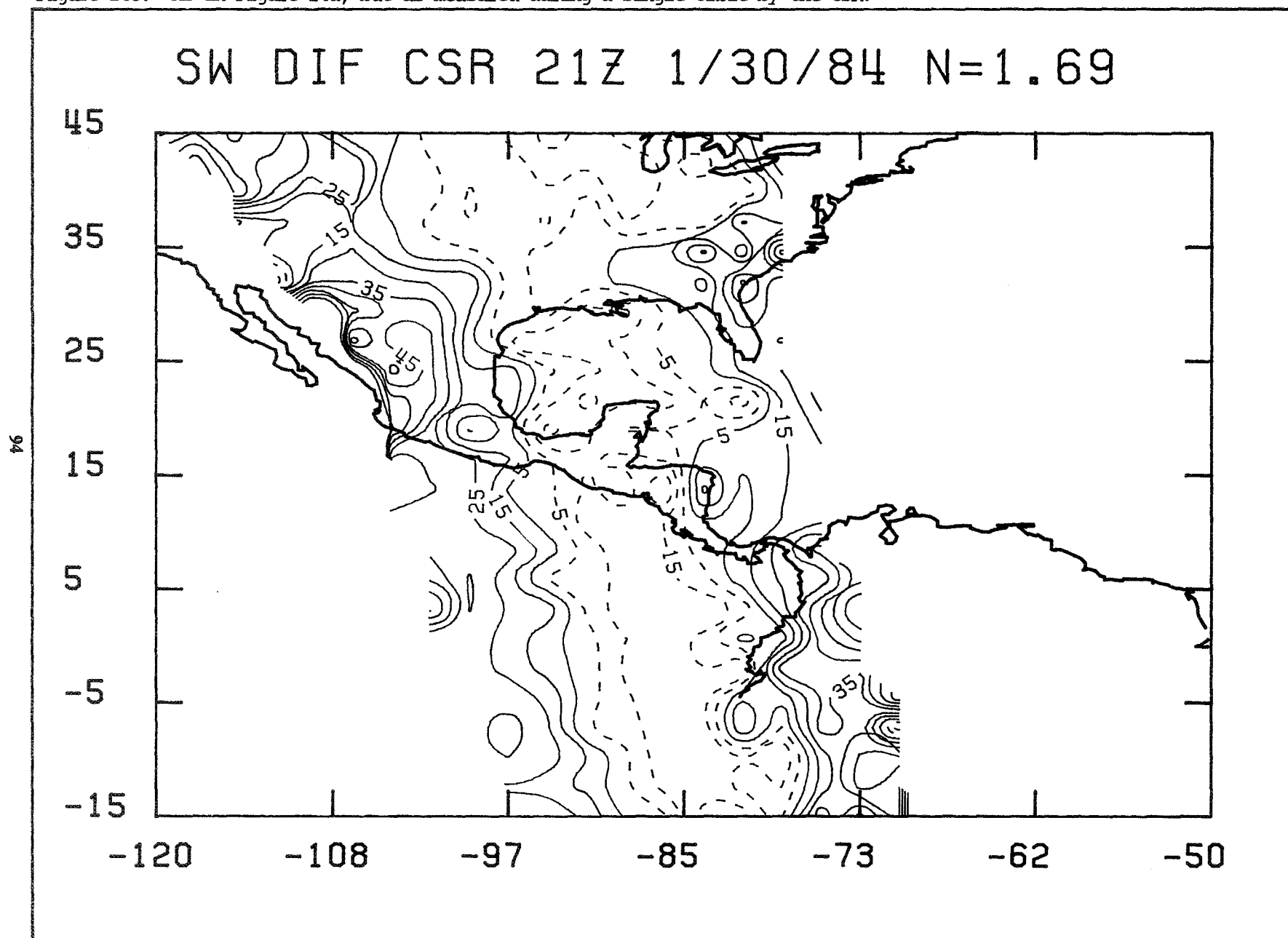
Figure 24d. As in Figure 24a, but as measured during a single orbit by the ERBE.
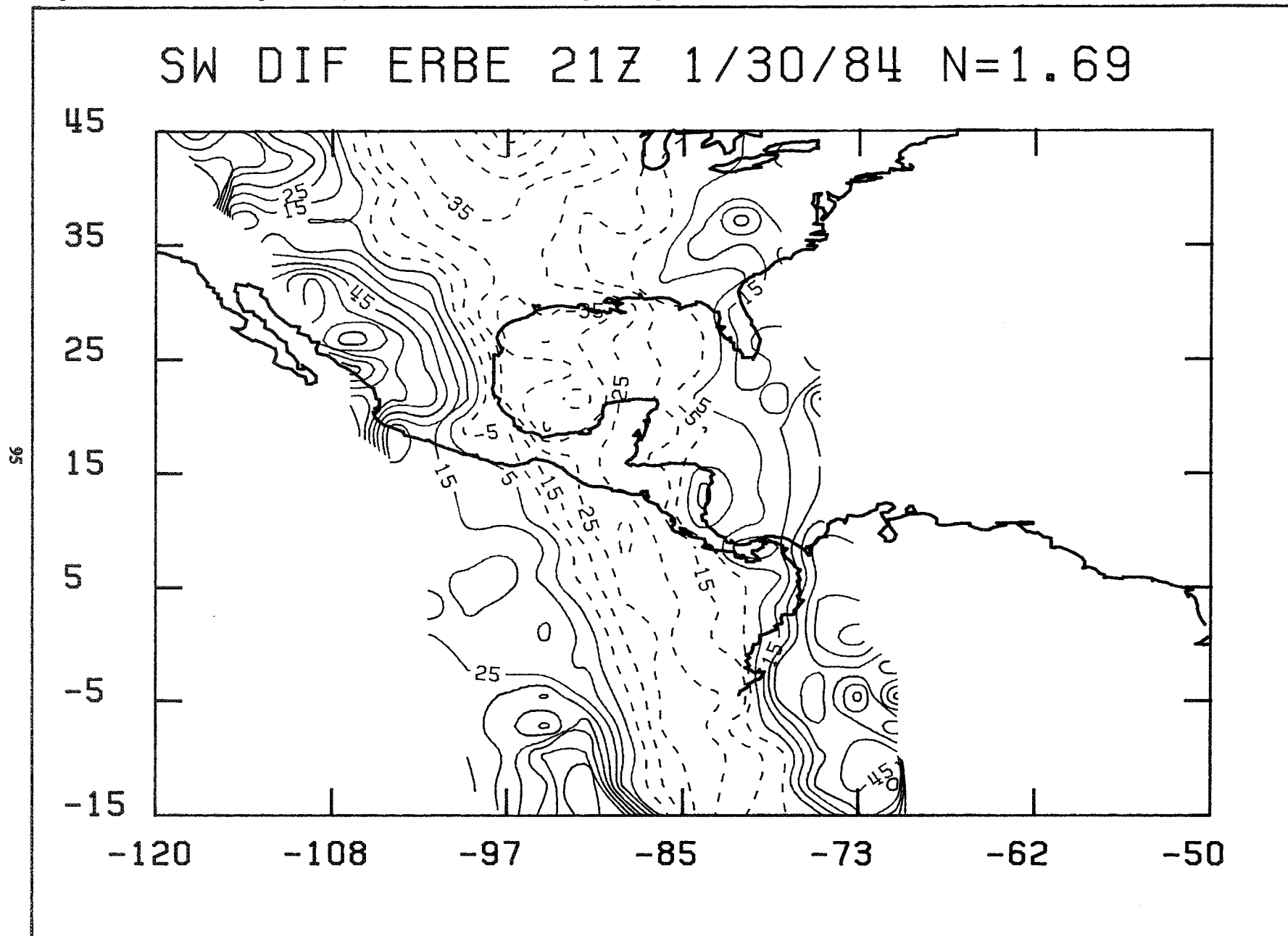
SW DIF ERBE 21Z 1/30/84 N=1.69

SW DIF NIMBUS-7 21Z 1/30/84 N=1.69

Table 11. ERBI Simulation Study Statistical Results for July 1983 at 15Z for N = 0

SHORTWAVE

ERROR IN 6-DAY MEAN INSTANTANEOUS FLUXES (W/m^2)

	109°W			86°W			63°W		
RADIOMETER	RMS	STD	BIAS	RMS	STD	BIAS	RMS	STD	BIAS
ACA	4.14	4.14	0.02	7.60	7.59	0.39	5.94	5.93	0.31
CERES	4.66	4.62	0.64	5.34	5.33	0.31	3.91	3.91	-0.06
CSR	3.56	3.56	0.04	5.54	5.53	0.20	5.05	5.04	0.31
ERBE	9.34	9.24	1.40	6.20	6.16	0.68	3.49	3.49	0.11
NIMBUS-7	7.08	7.05	0.63	14.63	14.62	-0.59	14.69	14.68	0.58

DAILY INSTANTANEOUS FLUX ERROR FROM 6-DAY SAMPLE SIZE (W/m^2)

ACA	8.29	8.29	0.02	13.47	13.47	0.39	12.01	12.00	0.31
CERES	7.98	7.96	0.64	9.32	9.32	0.31	8.33	8.33	-0.06
CSR	8.76	8.76	0.04	11.14	11.14	0.20	9.80	9.79	0.31
ERBE	9.58	9.56	1.40	10.14	10.12	0.68	8.19	8.19	0.11
NIMBUS-7	14.40	14.39	0.63	27.88	27.87	-0.59	27.39	27.38	0.58

LONGWAVE

ERROR IN 6-DAY MEAN INSTANTANEOUS FLUXES (W/m^2)

	109°W			86°W			63°W		
RADIOMETER	RMS	STD	BIAS	RMS	STD	BIAS	RMS	STD	BIAS
ACA	1.12	1.12	-0.01	1.45	1.45	-0.04	1.09	1.09	-0.02
CERES	1.37	1.35	-0.22	1.04	1.03	-0.06	0.73	0.73	0.03
CSR	0.92	0.91	-0.08	1.18	1.18	-0.03	0.94	0.94	-0.05
ERBE	3.27	3.23	-0.54	1.32	1.31	-0.15	0.68	0.68	0.03
NIMBUS-7	2.16	2.16	-0.11	3.10	3.10	0.08	2.15	2.15	0.04

DAILY INSTANTANEOUS FLUX ERROR FROM 6-DAY SAMPLE SIZE (W/m^2)

ACA	2.26	2.26	-0.01	2.88	2.88	-0.04	2.42	2.42	-0.02
CERES	2.14	2.13	-0.22	2.03	2.03	-0.06	1.67	1.67	0.03
CSR	2.27	2.26	-0.08	2.47	2.47	-0.03	2.02	2.02	-0.05
ERBE	2.75	2.75	-0.54	2.27	2.27	-0.15	1.63	1.63	0.03
NIMBUS-7	4.15	4.15	-0.11	6.38	6.38	0.08	4.78	4.78	0.04

OBSERVATION REJECTION CRITERIA:

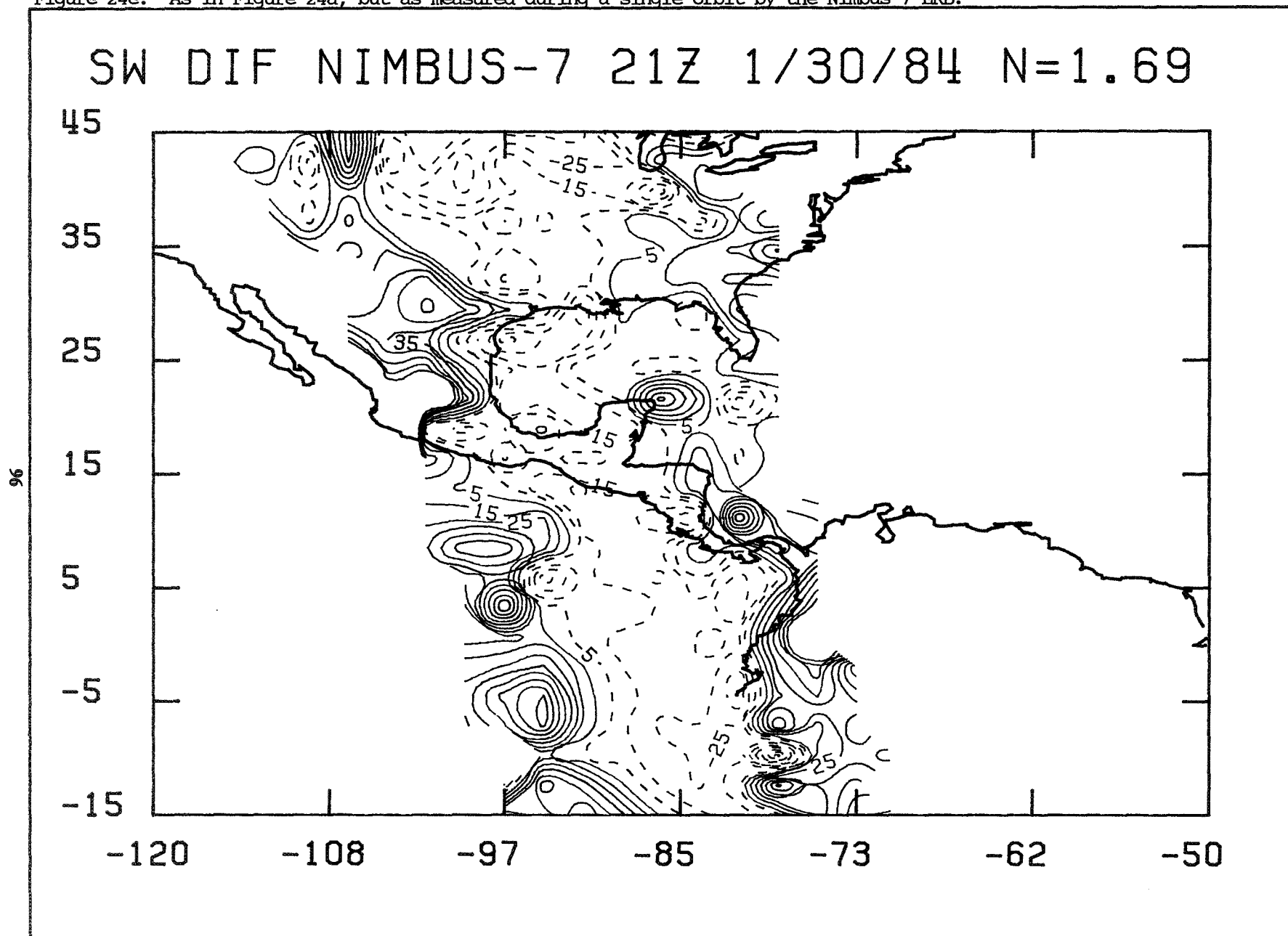Reject if: [1]Satellite Zenith Angle > 70; [2]Solar Zenith Angle > 86; [3]Shortwave Bidirectional Reflectance > 2.

Table 12. ERBI Simulation Study Statistical Results for July 1983 at 21Z for N = 0

SHORTWAVE

ERROR IN 6-DAY MEAN INSTANTANEOUS FLUXES (W/m^2)

	109°W			86°W			63°W		
RADIOMETER	RMS	STD	BIAS	RMS	STD	BIAS	RMS	STD	BIAS
ACA	5.40	5.36	-0.61	6.29	6.29	0.20	4.29	4.29	-0.04
CERES	4.34	4.31	-0.54	4.87	4.86	-0.11	2.89	2.89	-0.07
CSR	5.45	5.43	-0.47	5.84	5.84	-0.09	4.15	4.13	0.42
ERBE	5.23	5.23	-0.26	5.48	5.47	-0.23	3.40	3.40	0.10
NIMBUS-7	12.84	12.84	-0.16	13.59	13.58	0.55	10.70	10.63	1.23

DAILY INSTANTANEOUS FLUX ERROR FROM 6-DAY SAMPLE SIZE (W/m^2)

ACA	13.31	13.30	-0.61	13.06	13.06	0.20	7.94	7.94	-0.04
CERES	9.14	9.12	-0.54	9.38	9.38	-0.11	5.48	5.48	-0.07
CSR	11.31	11.30	-0.47	11.25	11.25	-0.09	7.51	7.49	0.42
ERBE	9.50	9.49	-0.26	10.06	10.06	-0.23	5.90	5.90	0.10
NIMBUS-7	25.82	25.82	-0.16	26.74	26.74	0.55	18.92	18.90	1.23

LONGWAVE

ERROR IN 6-DAY MEAN INSTANTANEOUS FLUXES (W/m^2)

	109°W			86°W			63°W		
RADIOMETER	RMS	STD	BIAS	RMS	STD	BIAS	RMS	STD	BIAS
ACA	1.37	1.36	0.15	1.69	1.69	-0.06	1.60	1.60	0.00
CERES	1.10	1.10	0.09	1.24	1.24	0.01	0.95	0.95	-0.01
CSR	1.15	1.15	0.01	1.50	1.50	0.01	1.48	1.47	-0.15
ERBE	1.57	1.57	-0.01	1.47	1.47	+0.04	1.10	1.10	0.00
NIMBUS-7	2.30	2.30	0.12	3.66	3.66	-0.11	3.41	3.41	-0.17

DAILY INSTANTANEOUS FLUX ERROR FROM 6-DAY SAMPLE SIZE (W/m^2)

ACA	2.89	2.89	0.15	3.42	3.42	-0.06	3.15	3.15	0.00
CERES	2.04	2.04	0.09	2.40	2.40	0.01	1.97	1.97	-0.01
CSR	2.48	2.48	0.01	2.85	2.85	0.01	2.70	2.70	-0.15
ERBE	2.39	2.39	-0.01	2.53	2.53	0.04	2.04	2.04	0.00
NIMBUS-7	5.12	5.12	0.12	7.17	7.17	-0.11	6.32	6.32	-0.17

OBSERVATION REJECTION CRITERIA:

Reject if: [1]Satellite Zenith Angle > 70; [2]Solar Zenith Angle > 86; [3]Shortwave Bidirectional Reflectance > 2.

Table 13. ERBI Simulation Study Statistical Results for January 1984 at 15Z for N = 0

SHORTWAVE

ERROR IN 6-DAY MEAN INSTANTANEOUS FLUXES (W/m^2)

	109°W			86°W			63°W		
RADIOMETER	RMS	STD	BIAS	RMS	STD	BIAS	RMS	STD	BIAS
ACA	2.33	2.33	0.15	8.89	8.89	0.39	5.56	5.56	0.13
CERES	1.45	1.44	-0.19	4.16	4.15	-0.19	4.63	4.62	-0.26
CSR	2.27	2.27	0.15	5.62	5.60	0.52	5.95	5.94	0.28
ERBE	1.69	1.68	-0.17	4.58	4.57	-0.22	3.83	3.83	0.15
NIMBUS-7	4.02	4.01	0.24	15.00	15.00	-0.78	12.57	12.56	0.56

DAILY INSTANTANEOUS FLUX ERROR FROM 6-DAY SAMPLE SIZE (W/m^2)

	RMS	STD	BIAS	RMS	STD	BIAS	RMS	STD	BIAS
ACA	4.95	4.94	0.15	11.55	11.54	0.39	11.59	11.59	0.13
CERES	3.22	3.21	-0.19	6.52	6.52	-0.19	8.19	8.19	-0.26
CSR	4.77	4.77	0.15	9.11	9.09	0.52	10.53	10.53	0.28
ERBE	3.55	3.54	-0.17	6.76	6.76	-0.22	7.27	7.26	0.15
NIMBUS-7	9.85	9.84	0.24	21.82	21.80	-0.78	24.78	24.77	0.56

LONGWAVE

ERROR IN 6-DAY MEAN INSTANTANEOUS FLUXES (W/m^2)

	109°W			86°W			63°W		
RADIOMETER	RMS	STD	BIAS	RMS	STD	BIAS	RMS	STD	BIAS
ACA	0.88	0.88	0.01	1.34	1.34	-0.01	1.05	1.05	-0.01
CERES	0.65	0.65	0.07	0.65	0.64	0.07	0.85	0.85	0.08
CSR	0.80	0.80	-0.01	0.76	0.76	0.00	1.05	1.05	-0.03
ERBE	0.69	0.68	0.04	0.75	0.75	0.05	0.69	0.68	-0.02
NIMBUS-7	1.50	1.50	0.03	2.60	2.60	0.15	2.19	2.19	0.01

DAILY INSTANTANEOUS FLUX ERROR FROM 6-DAY SAMPLE SIZE (W/m^2)

	RMS	STD	BIAS	RMS	STD	BIAS	RMS	STD	BIAS
ACA	1.69	1.69	0.01	1.92	1.92	-0.01	2.34	2.34	-0.01
CERES	1.10	1.10	0.07	1.10	1.10	0.07	1.59	1.58	0.08
CSR	1.42	1.42	-0.01	1.50	1.50	0.00	2.02	2.02	-0.03
ERBE	1.15	1.15	0.04	1.24	1.24	0.05	1.31	1.31	-0.02
NIMBUS-7	3.44	3.44	0.03	3.85	3.84	0.15	4.53	4.53	0.01

OBSERVATION REJECTION CRITERIA:

Reject if: [1]Satellite Zenith Angle > 70; [2]Solar Zenith Angle > 86; [3]Shortwave Bidirectional Reflectance > 2.

Table 14. ERBI Simulation Study Statistical Results for January 1984 at 21Z for N = 0

SHORTWAVE

ERROR IN 6-DAY MEAN INSTANTANEOUS FLUXES (W/m^2)

	109°W			86°W			63°W		
RADIOMETER	RMS	STD	BIAS	RMS	STD	BIAS	RMS	STD	BIAS
ACA	4.29	4.26	-0.53	5.84	5.81	0.49	3.27	3.25	0.30
CERES	2.99	2.98	-0.26	3.99	3.98	0.24	4.24	4.20	0.57
CSR	4.00	4.00	-0.19	5.45	5.45	0.07	3.35	3.34	0.26
ERBE	3.27	3.27	-0.09	3.88	3.88	-0.22	3.19	3.19	0.25
NIMBUS-7	8.53	8.53	0.11	13.77	13.76	-0.43	8.36	8.31	0.84

DAILY INSTANTANEOUS FLUX ERROR FROM 6-DAY SAMPLE SIZE (W/m^2)

ACA	9.37	9.36	-0.53	8.83	8.82	0.49	6.36	6.35	0.30
CERES	5.64	5.63	-0.26	5.91	5.91	0.24	5.12	5.11	0.57
CSR	7.41	7.41	-0.19	7.88	7.88	0.07	5.70	5.70	0.26
ERBE	5.83	5.83	-0.09	6.03	6.03	-0.22	4.85	4.85	0.25
NIMBUS-7	17.22	17.22	0.11	19.02	19.00	-0.43	13.58	13.57	0.84

LONGWAVE

ERROR IN 6-DAY MEAN INSTANTANEOUS FLUXES (W/m^2)

	109°W			86°W			63°W		
RADIOMETER	RMS	STD	BIAS	RMS	STD	BIAS	RMS	STD	BIAS
ACA	0.93	0.92	0.10	1.34	1.34	-0.02	1.44	1.43	-0.13
CERES	0.59	0.59	0.03	0.85	0.85	0.05	1.30	1.30	-0.03
CSR	0.79	0.79	-0.02	1.00	1.00	0.08	1.36	1.36	-0.07
ERBE	0.60	0.60	0.02	0.86	0.86	0.10	1.07	1.07	-0.06
NIMBUS-7	1.36	1.36	-0.14	3.16	3.16	0.18	3.34	3.34	-0.07

DAILY INSTANTANEOUS FLUX ERROR FROM 6-DAY SAMPLE SIZE (W/m^2)

ACA	1.87	1.87	0.10	2.18	2.18	-0.02	2.90	2.90	-0.13
CERES	1.07	1.06	0.03	1.38	1.38	0.05	2.10	2.10	-0.03
CSR	1.36	1.36	-0.02	1.69	1.68	0.08	2.50	2.50	-0.07
ERBE	1.23	1.23	0.02	1.52	1.52	0.10	1.92	1.92	-0.06
NIMBUS-7	2.99	2.99	-0.14	4.77	4.76	0.18	5.97	5.97	-0.07

OBSERVATION REJECTION CRITERIA:

Reject if: [1]Satellite Zenith Angle > 70; [2]Solar Zenith Angle > 86; [3]Shortwave Bidirectional Reflectance > 2.

instruments are the only scanners able to retrieve TOA flux estimates, in the absence of ADM error, with an error of not more than 10 Wm^{-2} (User Requirements from ERBRR-87 (1988)). The Nimbus-7 ERB scanner, with its lower sampling rate, returns the highest spatial sampling errors, confirming the Nimbus-7 ERB experiment team's choice of a somewhat larger 4.5° grid (2070 target areas) upon which to grid its fields, thereby reducing the error, albeit at a somewhat lower spatial resolution.

The sampling errors are reduced when the six-day averaged fields are considered. The reduction rate for the errors, however, is somewhat slower than that (about 80%) expected by the square root of the sample size, with the errors dropping by a factor of about two for a six-fold increase in the number of days observed. This is because meteorological data, on adjacent days, typically are serially correlated. The implication to the corresponding monthly averages would be an error reduction of about a factor of five, with the RMS monthly instantaneous shortwave flux accuracy in the neighborhood of 2 to 3 Wm^{-2}. It is interesting that spatial sampling errors behave almost as if they were perfectly random.

Tables 15 through 18 provide statistical summaries for an alternative set of simulations, though for the identical set of sampling periods and GOES image times presented above in Tables 11 through 14. In this next experiment, a systematic departure from the reference bidirectional reflectance models is introduced. We find that all of the instruments perform more poorly under these conditions, as the measurements are inverted using the reference reflectance models which are inconsistent with the "true" Earth reflectance models. The total error is a combination of two fundamental error sources, spatial and angular. In this realization, with a 1.69 factor enhancement to the anisotropy of the "true" scene, the cross-track scanners do not perform as well as the two conical scanners (CSR and ACA). This behavior is due to the rapid growth of the total error in the cross-track scanners due to their vulnerability to ADM errors, as each element of the scene is viewed only once from a fixed Earth-Sun-satellite geometry. In the conical scanners, the measurements are taken about a series of concentric rings, each with a different satellite zenith angle. Many scene elements are viewed by detectors in several rings at different azimuth/zenith angle combinations, allowing the forward, backward and sideward anisotropic errors to partially cancel. The growth of error due to ADM error propagation is largest in the pure cross-track configuration (ERBE) with the hybrid cross-track scanner (CERES-I) showing a less-rapid error growth. The Nimbus-7 ERB, with its forward, side and back-viewing scan pattern, is somewhat insensitive to ADM errors as is the case of the conical scanners. Unlike the previous simulation, where ADM error was neglected, we find some significant evidence of systematic bias errors in the measurements, with the cross-track scanners the most prone to this bias contamination.

A complete set of profiles (Figures 25a through 25c and 26a through 26c) is provided relating the total shortwave RMS sampling error over the simulation domain to the degree of bidirectional model error (i.e., the anisotropy scale factor N). Continuous variations in N are shown in the figures, although only two anisotropic experiments were conducted in July (N=0.59 and N=1.69) and one in January (N=1.69). Intermediate results are obtained for these "orbital" statistics using Eqs. (46) and (47). In Eq.(46) we show that a relationship between the RMS^2 of the angular sampling error at different N experiments allows us to infer all angular sampling errors from the result of a single experiment. Total RMS errors are then derived for different N-experiments by varying N_2 in Eq.(47) with both RMS$^2_{SPATIAL}$ and RMS$^2_{ANGULAR}$ constant. Resulting total RMS error profiles are provided for the shortwave measurements taken by all five candidate radiometers (ACA, CERES-I, CSR, ERBE, and Nimbus-7) for the six day sampling periods in January and July. Both the six-day average of the daily errors (Figure 25), as well as the error of the six-day average fields (Figure 26), are portrayed. A range of local time and ascending-node combinations are achieved, with equator crossings at 109°W, 86°W, and 63°W. The effects of both spatial sampling errors and bidirectional modelling errors can be identified in these representations. The results with sampling error alone, having been found to yield approximately the

Table 15. ERBI Simulation Study Statistical Results for July 1983 at 15Z for N = 1.69

SHORTWAVE

ERROR IN 6-DAY MEAN INSTANTANEOUS FLUXES (W/m^2)

RADIOMETER	109°W			86°W			63°W		
	RMS	STD	BIAS	RMS	STD	BIAS	RMS	STD	BIAS
ACA	29.68	29.55	-2.73	17.68	17.63	1.32	10.10	10.06	0.90
CERES	40.02	39.99	-1.52	22.00	21.38	5.10	10.71	9.78	4.37
CSR	33.07	32.88	3.62	18.86	18.49	3.71	9.55	9.49	1.00
ERBE	43.90	43.88	1.45	24.16	23.06	7.19	12.56	10.77	6.47
NIMBUS-7	33.76	33.51	-4.06	20.81	20.73	-1.74	17.99	17.96	0.47

DAILY INSTANTANEOUS FLUX ERROR FROM 6-DAY SAMPLE SIZE (W/m^2)

	RMS	STD	BIAS	RMS	STD	BIAS	RMS	STD	BIAS
ACA	30.82	30.70	-2.73	21.12	21.08	1.32	14.66	14.63	0.90
CERES	41.06	41.03	-1.52	23.84	23.29	5.10	13.52	12.79	4.37
CSR	34.44	34.25	3.62	21.54	21.22	3.71	13.25	13.22	1.00
ERBE	45.18	45.16	1.45	26.01	25.00	7.19	15.31	13.87	6.47
NIMBUS-7	36.92	36.64	-4.06	31.69	31.64	-1.74	29.72	29.72	0.47

LONGWAVE

ERROR IN 6-DAY MEAN INSTANTANEOUS FLUXES (W/m^2)

RADIOMETER	109°W			86°W			63°W		
	RMS	STD	BIAS	RMS	STD	BIAS	RMS	STD	BIAS
ACA	2.79	2.79	0.12	3.00	2.98	-0.30	2.88	2.86	-0.29
CERES	4.94	4.55	1.93	4.75	4.65	0.96	4.77	4.58	1.34
CSR	4.05	3.29	-2.37	4.56	3.44	-3.00	4.48	3.34	-2.99
ERBE	5.92	5.47	2.27	5.58	5.40	1.38	5.50	5.18	1.86
NIMBUS-7	4.40	4.30	-0.95	5.19	5.03	-1.26	4.83	4.67	-1.26

DAILY INSTANTANEOUS FLUX ERROR FROM 6-DAY SAMPLE SIZE (W/m^2)

	RMS	STD	BIAS	RMS	STD	BIAS	RMS	STD	BIAS
ACA	3.40	3.40	0.12	3.93	3.92	-0.30	3.63	3.62	-0.29
CERES	5.18	4.80	1.93	5.08	4.99	0.96	5.05	4.87	1.34
CSR	4.58	3.91	-2.37	5.12	4.15	-3.00	4.87	3.84	-2.99
ERBE	6.19	5.75	2.27	5.88	5.72	1.38	5.74	5.43	1.86
NIMBUS-7	5.50	5.42	-0.95	7.59	7.49	-1.26	6.45	6.33	-1.26

OBSERVATION REJECTION CRITERIA:

Reject if: [1]Satellite Zenith Angle > 70; [2]Solar Zenith Angle > 86; [3]Shortwave Bidirectional Reflectance > 2.

Table 16. ERBI Simulation Study Statistical Results for July 1983 at 21Z for N = 1.69

SHORTWAVE

ERROR IN 6-DAY MEAN INSTANTANEOUS FLUXES (W/m^2)

	109°W			86°W			63°W		
RADIOMETER	RMS	STD	BIAS	RMS	STD	BIAS	RMS	STD	BIAS
ACA	6.87	6.87	0.05	13.35	13.34	0.67	18.14	17.73	-3.83
CERES	9.51	9.16	2.54	16.87	16.82	1.28	23.84	23.40	-4.57
CSR	8.36	8.34	-0.55	14.12	13.89	2.50	18.06	18.00	1.43
ERBE	12.23	11.43	4.35	19.14	19.03	2.06	26.37	26.13	-3.54
NIMBUS-7	17.75	17.71	1.14	20.26	20.26	0.07	22.07	21.78	-3.58

DAILY INSTANTANEOUS FLUX ERROR FROM 6-DAY SAMPLE SIZE (W/m^2)

	109°W			86°W			63°W		
ACA	14.41	14.41	0.05	17.72	17.71	0.67	19.70	19.33	-3.83
CERES	13.60	13.36	2.54	19.40	19.30	1.28	25.04	24.63	-4.57
CSR	14.51	14.50	-0.55	17.88	17.70	2.50	19.81	19.76	1.43
ERBE	15.67	15.06	4.35	21.57	21.47	2.06	27.69	27.47	-3.54
NIMBUS-7	28.83	28.81	1.14	31.11	31.11	0.07	28.07	27.84	-3.58

LONGWAVE

ERROR IN 6-DAY MEAN INSTANTANEOUS FLUXES (W/m^2)

	109°W			86°W			63°W		
RADIOMETER	RMS	STD	BIAS	RMS	STD	BIAS	RMS	STD	BIAS
ACA	2.54	2.52	0.29	3.03	3.02	-0.27	3.07	3.06	-0.22
CERES	5.05	4.63	2.01	4.66	4.54	1.05	4.64	4.45	1.33
CSR	4.09	3.36	-2.32	4.49	3.46	-2.87	4.57	3.52	-2.92
ERBE	6.07	5.59	2.38	5.43	5.20	1.55	5.55	5.25	1.80
NIMBUS-7	4.55	4.47	-0.83	5.59	5.41	-1.40	5.44	5.28	-1.31

DAILY INSTANTANEOUS FLUX ERROR FROM 6-DAY SAMPLE SIZE (W/m^2)

	109°W			86°W			63°W		
ACA	3.61	3.60	0.29	4.29	4.28	-0.27	4.12	4.11	-0.22
CERES	5.35	4.96	2.01	5.14	5.03	1.05	5.01	4.83	1.33
CSR	4.70	4.09	-2.32	5.17	4.31	-2.87	5.15	4.24	-2.92
ERBE	6.37	5.91	2.38	5.86	5.65	1.55	5.86	5.58	1.80
NIMBUS-7	6.42	6.37	-0.83	8.26	8.14	-1.40	7.60	7.48	-1.31

OBSERVATION REJECTION CRITERIA:

Reject if: [1]Satellite Zenith Angle > 70; [2]Solar Zenith Angle > 86; [3]Shortwave Bidirectional Reflectance > 2.

Table 17. ERBI Simulation Study Statistical Results for January 1984 at 15Z for N = 1.69

SHORTWAVE

ERROR IN 6-DAY MEAN INSTANTANEOUS FLUXES (W/m^2)

		109°W			86°W			63°W	
RADIOMETER	RMS	STD	BIAS	RMS	STD	BIAS	RMS	STD	BIAS
ACA	21.36	20.07	-7.31	14.90	14.02	-5.02	9.63	9.31	-2.46
CERES	32.75	30.51	-11.92	22.95	19.87	-11.47	19.68	15.86	-11.65
CSR	20.48	20.46	-1.01	12.70	12.66	1.03	9.25	9.08	1.78
ERBE	36.04	34.04	-11.83	26.56	23.22	-12.91	24.21	19.53	-14.30
NIMBUS-7	25.39	24.10	-7.98	24.12	23.11	-6.89	19.88	19.88	-0.31

DAILY INSTANTANEOUS FLUX ERROR FROM 6-DAY SAMPLE SIZE (W/m^2)

ACA	22.20	20.91	-7.31	16.93	16.18	-5.02	14.50	14.29	-2.46
CERES	33.36	30.98	-11.92	24.21	21.32	-11.47	21.32	17.85	-11.65
CSR	21.47	21.44	-1.01	15.28	15.24	1.03	13.55	13.43	1.78
ERBE	36.59	34.30	-11.83	27.76	25.58	-12.91	25.51	21.12	-14.30
NIMBUS-7	27.30	25.68	-7.98	30.14	29.34	-6.89	29.71	29.71	-0.31

LONGWAVE

ERROR IN 6-DAY MEAN INSTANTANEOUS FLUXES (W/m^2)

		109°W			86°W			63°W	
RADIOMETER	RMS	STD	BIAS	RMS	STD	BIAS	RMS	STD	BIAS
ACA	2.40	2.39	0.21	2.83	2.82	-0.13	2.70	2.69	-0.23
CERES	4.65	4.18	2.03	4.61	4.41	1.35	4.48	4.27	1.35
CSR	3.68	3.01	-2.11	4.15	3.23	-2.60	4.25	3.28	-2.71
ERBE	5.38	4.74	2.55	5.41	5.08	1.85	5.27	4.99	1.72
NIMBUS-7	4.14	4.07	-0.76	4.81	4.69	-1.08	4.55	4.41	-1.12

DAILY INSTANTANEOUS FLUX ERROR FROM 6-DAY SAMPLE SIZE (W/m^2)

ACA	2.79	2.78	0.21	3.13	3.13	-0.13	3.44	3.43	-0.23
CERES	4.75	4.26	2.03	4.72	4.51	1.35	4.71	4.51	1.35
CSR	3.84	3.23	-2.11	4.35	3.50	-2.60	4.63	3.75	-2.71
ERBE	5.50	4.82	2.55	5.51	5.20	1.85	5.42	5.14	1.72
NIMBUS-7	5.01	4.98	-0.76	5.58	5.47	-1.08	6.04	5.94	-1.12

OBSERVATION REJECTION CRITERIA:

Reject if: [1]Satellite Zenith Angle > 70; [2]Solar Zenith Angle > 86; [3]Shortwave Bidirectional Reflectance > 2.

Table 18. ERBI Simulation Study Statistical Results for January 1984 at 21Z for N = 1.69

SHORTWAVE

ERROR IN 6-DAY MEAN INSTANTANEOUS FLUXES (W/m^2)

RADIOMETER	109°W			86°W			63°W		
	RMS	STD	BIAS	RMS	STD	BIAS	RMS	STD	BIAS
ACA	8.09	8.00	-1.19	16.88	16.79	-1.74	24.58	23.77	-6.23
CERES	11.92	11.64	-2.56	23.99	23.88	-2.30	33.69	32.67	-8.23
CSR	8.67	8.52	1.60	17.44	17.26	2.46	25.47	25.47	-0.16
ERBE	14.14	13.88	-2.70	26.27	26.21	-1.87	37.15	36.39	-7.50
NIMBUS-7	12.02	11.99	0.77	23.56	23.32	-3.35	28.31	27.44	-6.97

DAILY INSTANTANEOUS FLUX ERROR FROM 6-DAY SAMPLE SIZE (W/m^2)

RADIOMETER	RMS	STD	BIAS	RMS	STD	BIAS	RMS	STD	BIAS
ACA	11.69	11.63	-1.19	18.92	18.84	-1.74	25.52	24.64	-6.23
CERES	13.20	12.95	-2.56	25.18	25.08	-2.30	34.85	33.76	-8.23
CSR	11.02	10.90	1.60	19.28	19.12	2.46	26.78	26.78	-0.16
ERBE	15.30	15.06	-2.70	27.45	27.39	-1.87	37.32	36.13	-7.50
NIMBUS-7	19.21	19.19	0.77	28.16	27.96	-3.35	31.07	30.17	-6.97

LONGWAVE

ERROR IN 6-DAY MEAN INSTANTANEOUS FLUXES (W/m^2)

RADIOMETER	109°W			86°W			63°W		
	RMS	STD	BIAS	RMS	STD	BIAS	RMS	STD	BIAS
ACA	2.43	2.42	0.22	2.87	2.86	-0.19	2.98	2.96	-0.29
CERES	4.58	4.16	1.90	4.67	4.51	1.23	4.33	4.07	1.50
CSR	3.85	3.11	-2.26	4.17	3.22	-2.65	4.08	3.19	-2.55
ERBE	5.43	4.89	2.37	5.30	5.00	1.76	5.03	4.57	2.09
NIMBUS-7	4.27	4.14	-1.07	5.05	4.93	-1.08	5.28	5.15	-1.17

DAILY INSTANTANEOUS FLUX ERROR FROM 6-DAY SAMPLE SIZE (W/m^2)

RADIOMETER	RMS	STD	BIAS	RMS	STD	BIAS	RMS	STD	BIAS
ACA	2.94	2.93	0.22	3.36	3.36	-0.19	3.83	3.82	-0.29
CERES	4.68	4.27	1.90	4.81	4.65	1.23	4.71	4.44	1.50
CSR	4.05	3.36	-2.26	4.43	3.55	-2.65	4.67	3.92	-2.55
ERBE	5.54	5.01	2.37	5.47	5.18	1.76	5.28	4.74	2.09
NIMBUS-7	5.02	4.90	-1.07	6.19	6.09	-1.08	7.23	7.14	-1.17

OBSERVATION REJECTION CRITERIA:

Reject if: [1]Satellite Zenith Angle > 70; [2]Solar Zenith Angle > 86; [3]Shortwave Bidirectional Reflectance > 2.
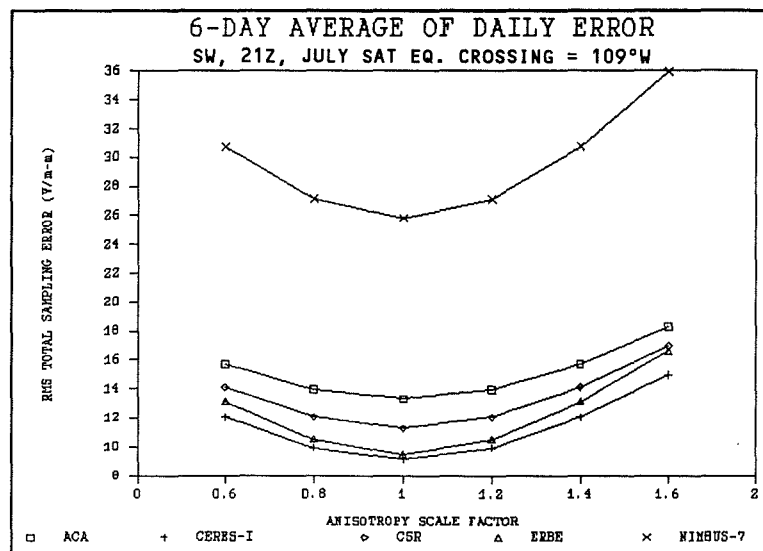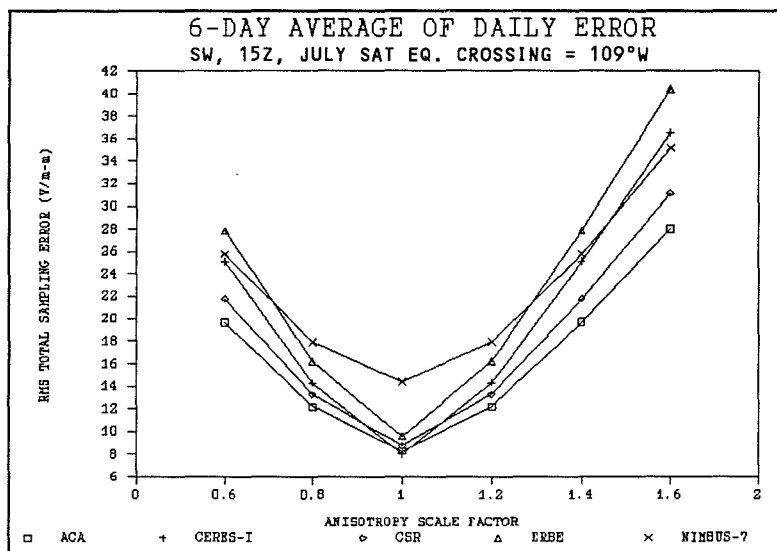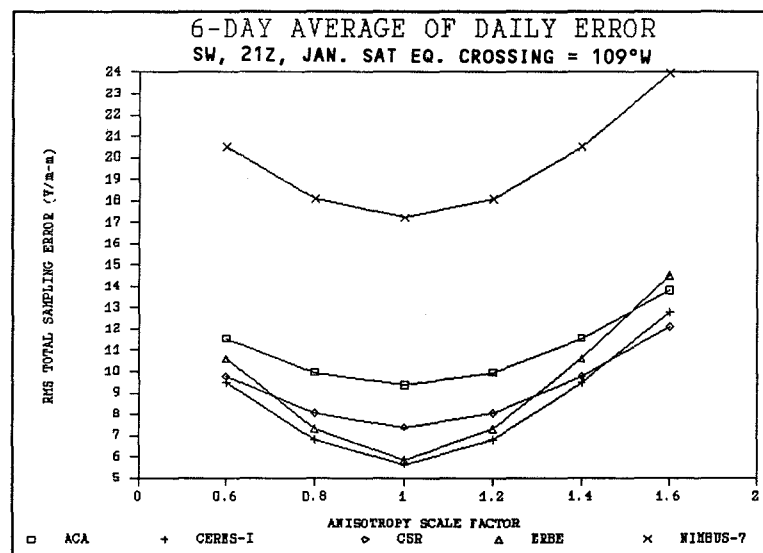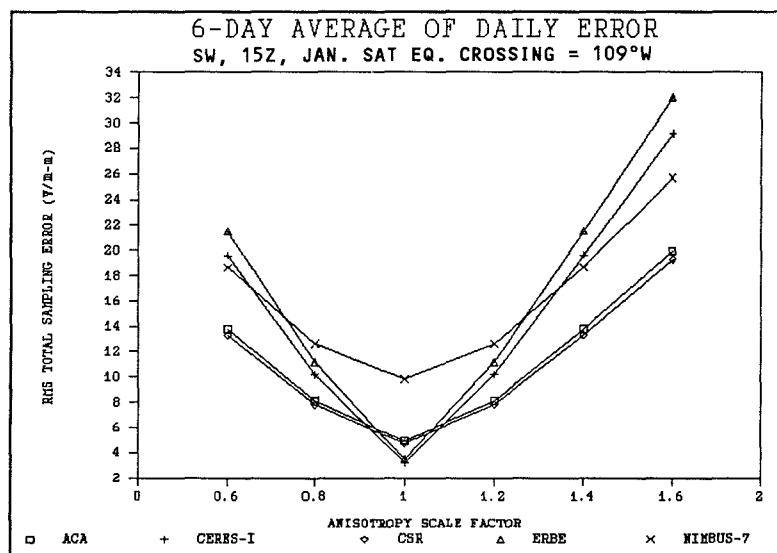
Figure 25a. Profiles of daily total RMS sampling error (W/m²) for the TOA shortwave flux estimates as a function of anisotropic scale factor (averaged over the six days of the simulation) for 15Z and 21Z January and July at equator-crossing longitude of 109°W.
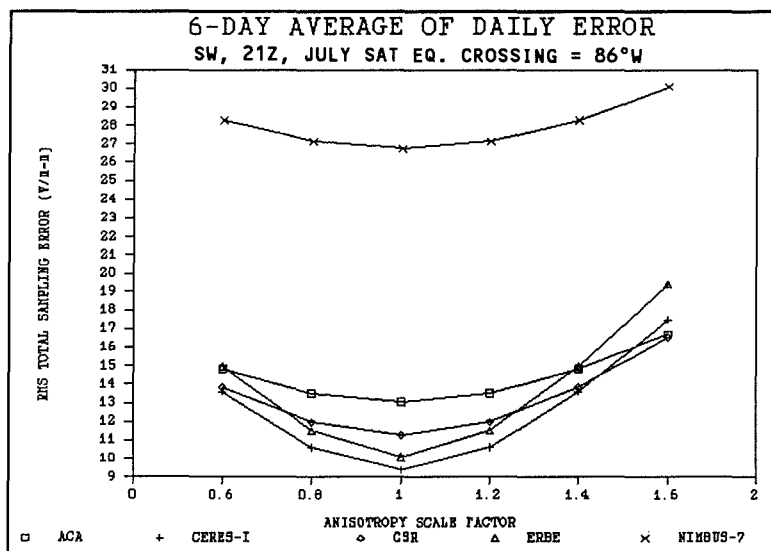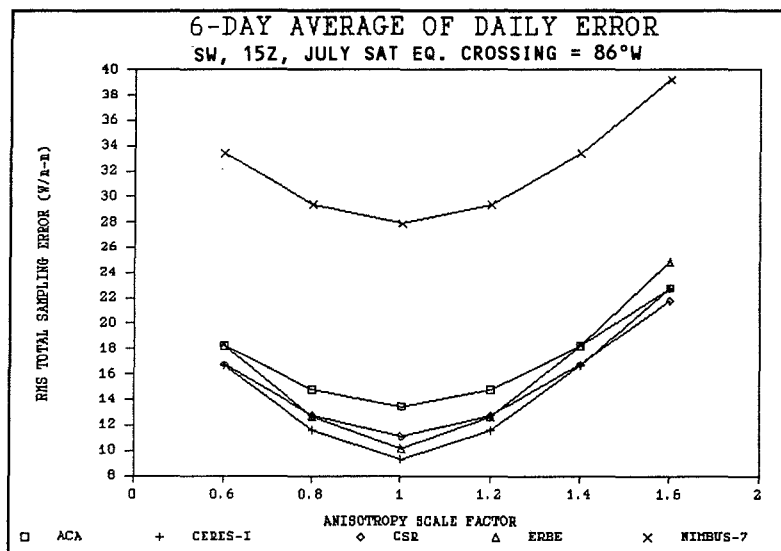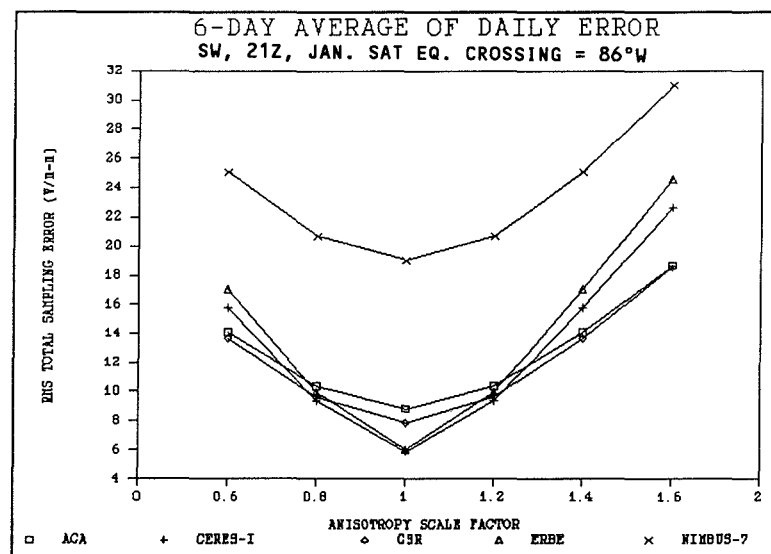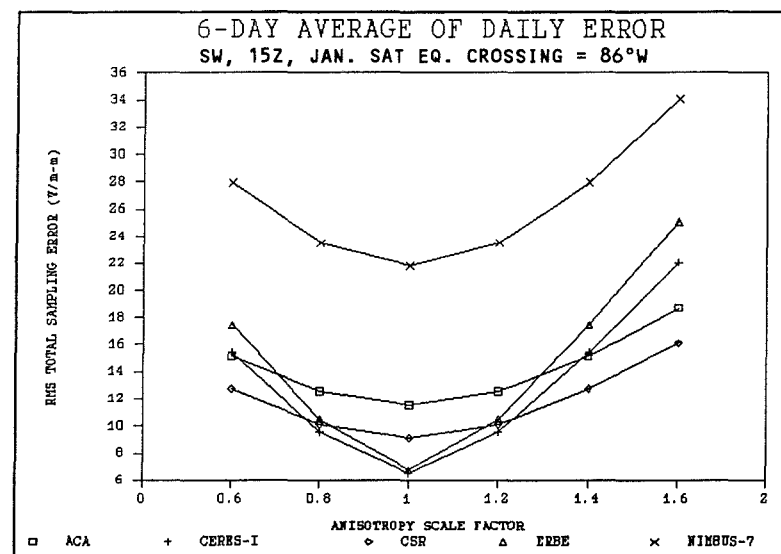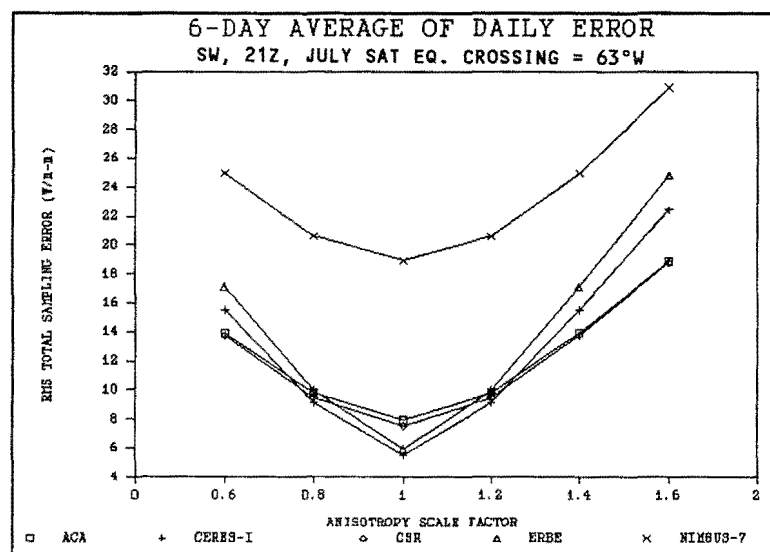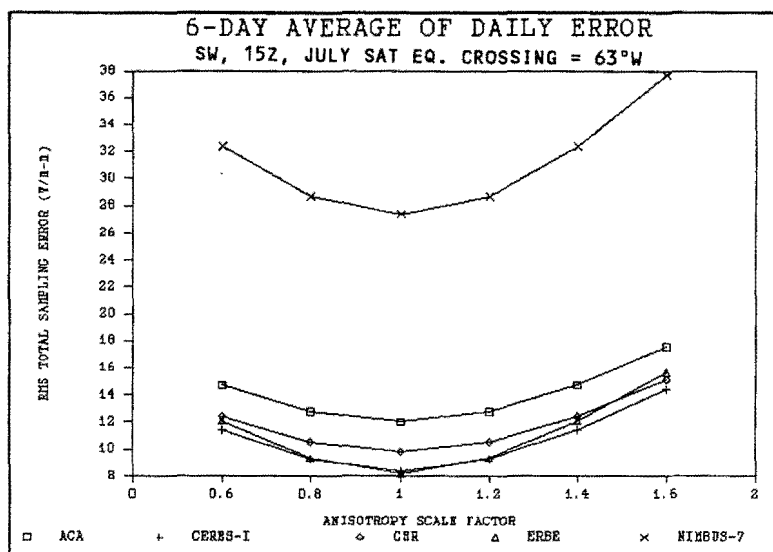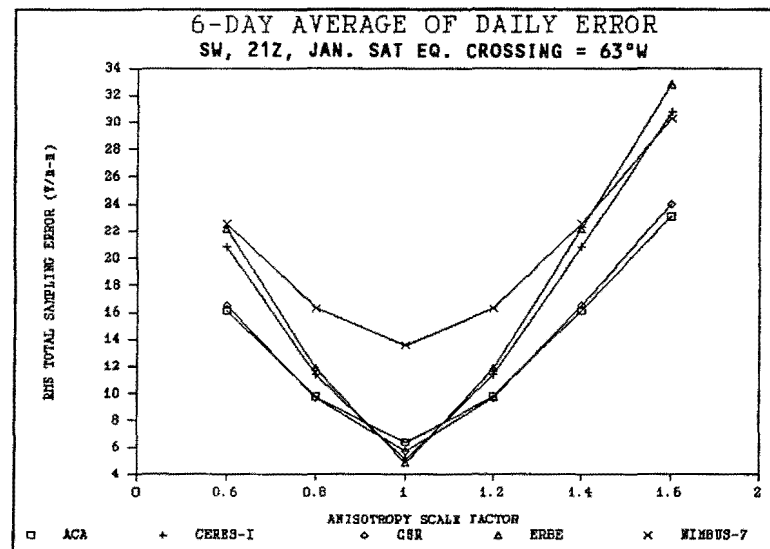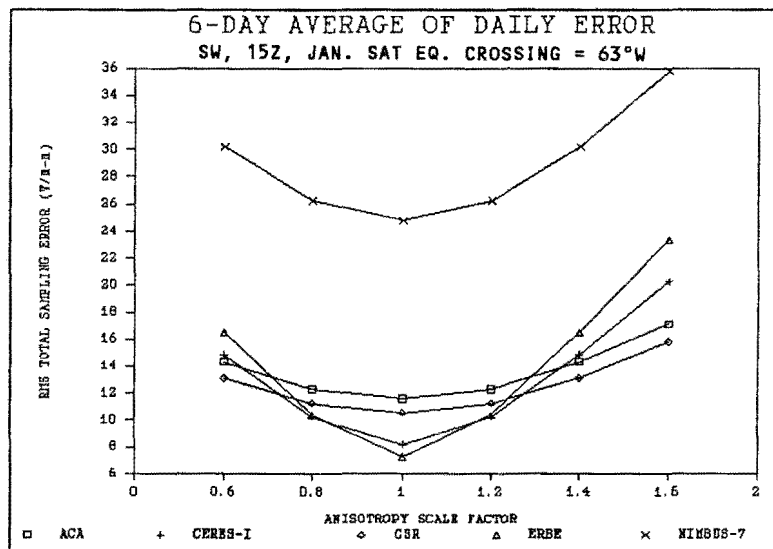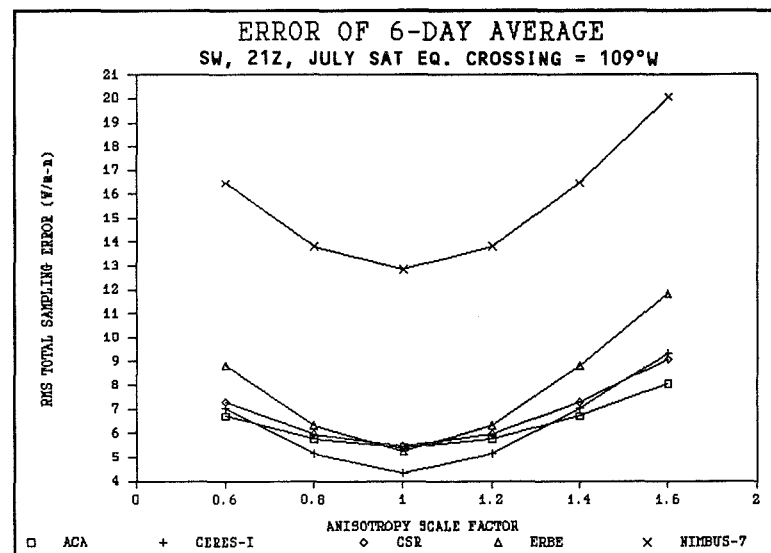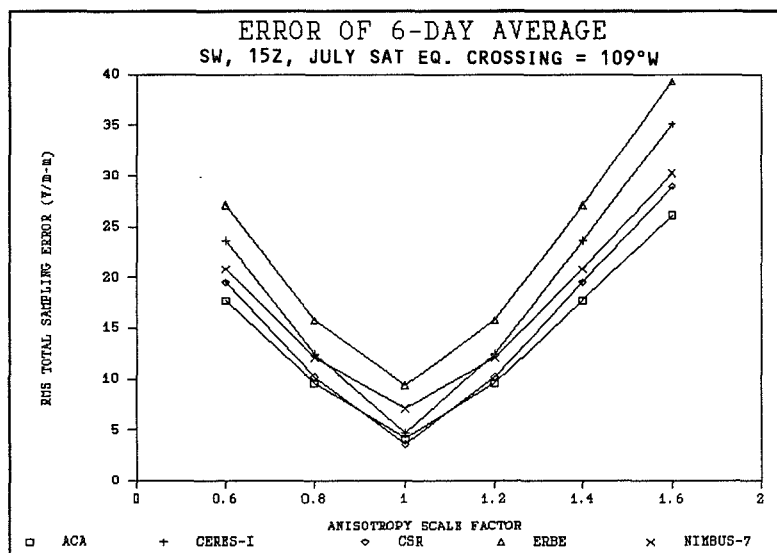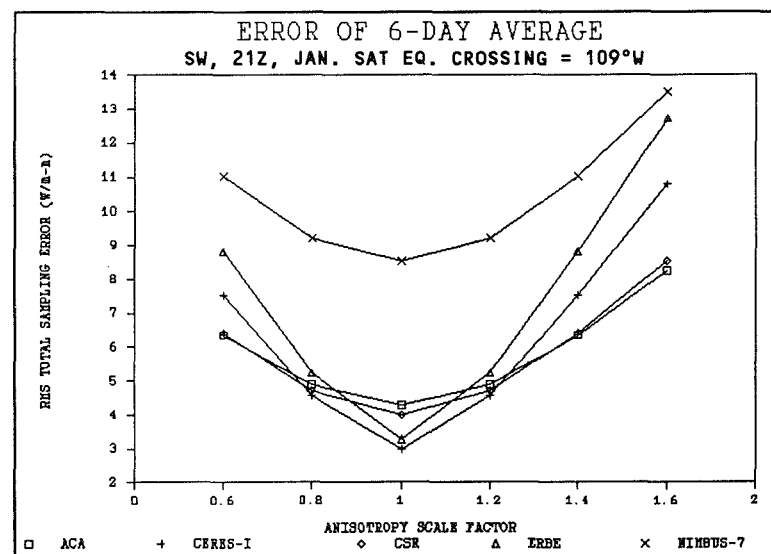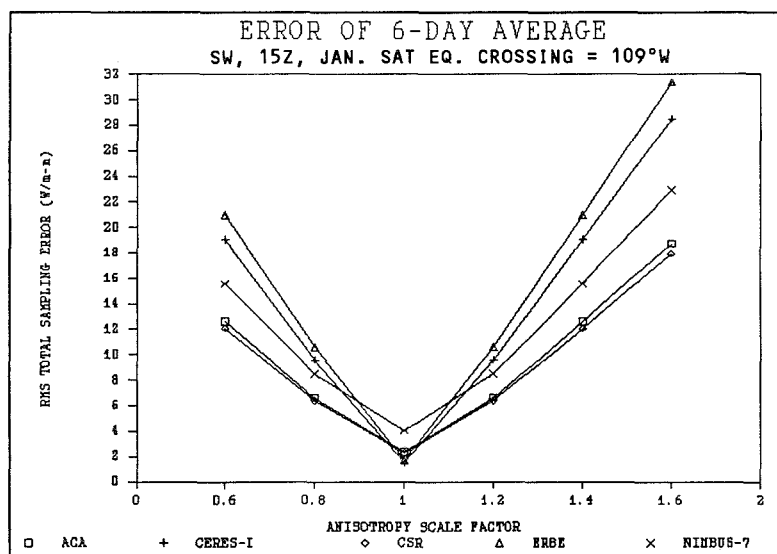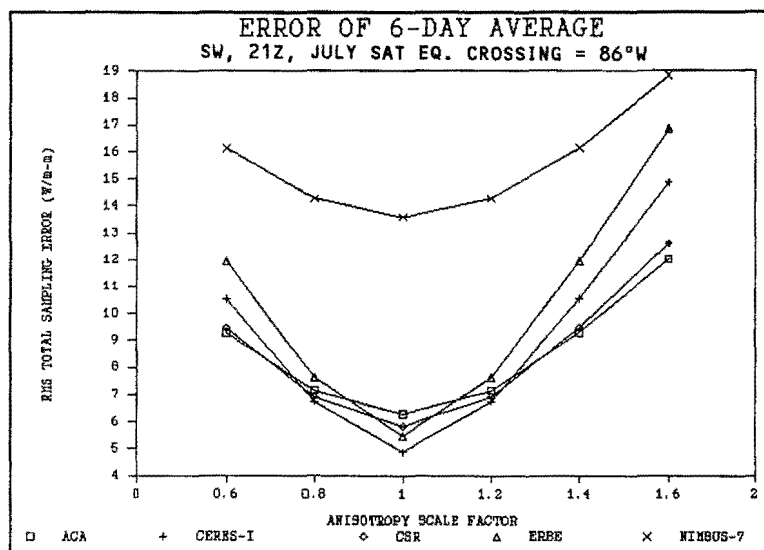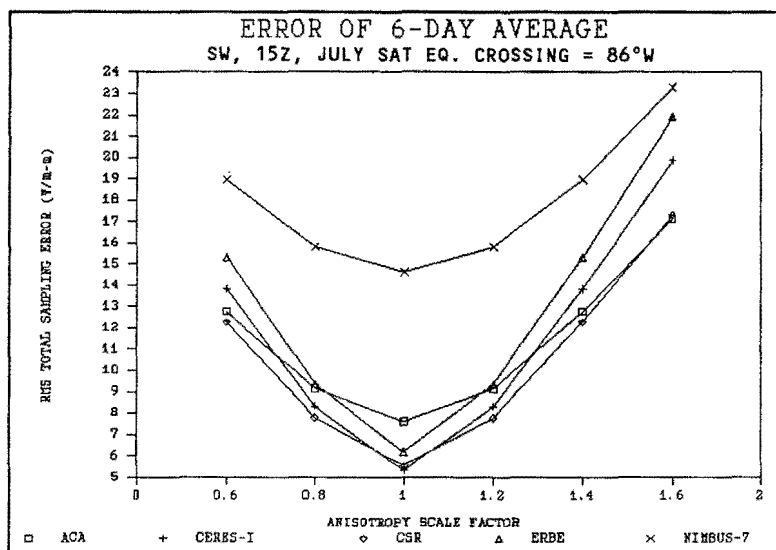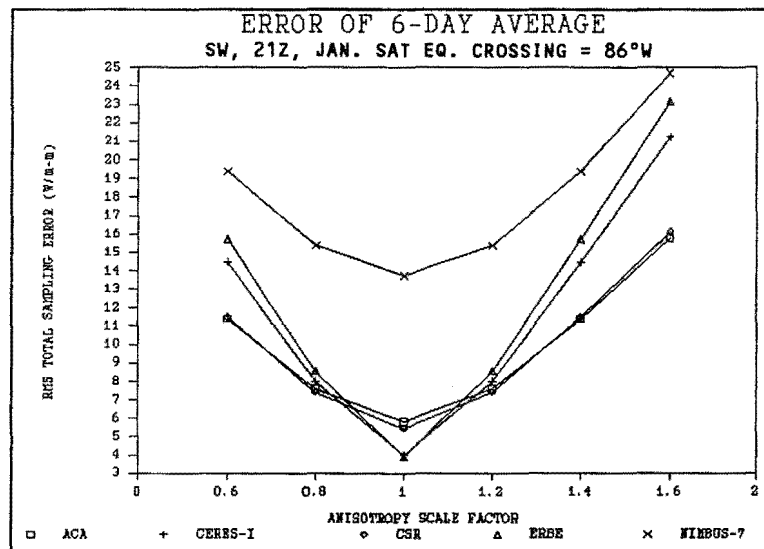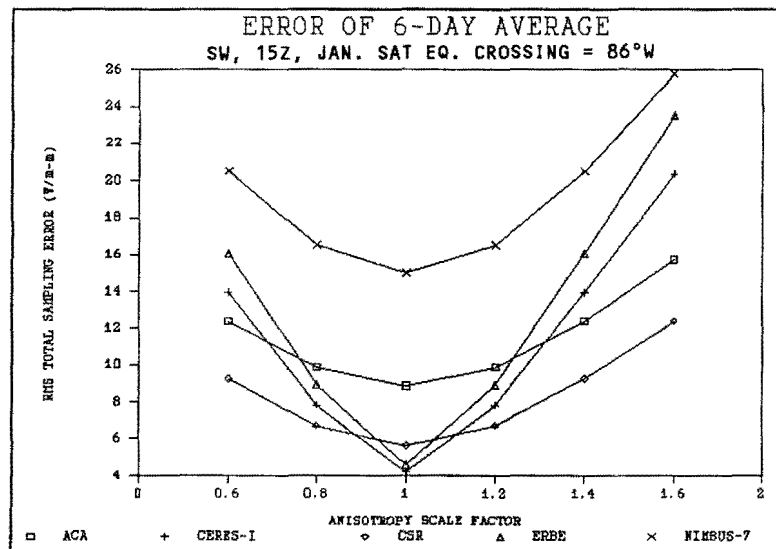
Figure 25b. Profiles of daily total RMS sampling error (W/m^2) for the TOA shortwave flux estimates as a function of anisotropic scale factor (averaged over the six days of the simulation) for 15Z and 21Z January and July at equator-crossing longitude of 86°W.

Figure 25c. Profiles of daily total RMS sampling error (W/m²) for the TOA shortwave flux estimates as a function of anisotropic scale factor (averaged over the six days of the simulation) for 15Z and 21Z January and July at equator-crossing longitude of 63°W.
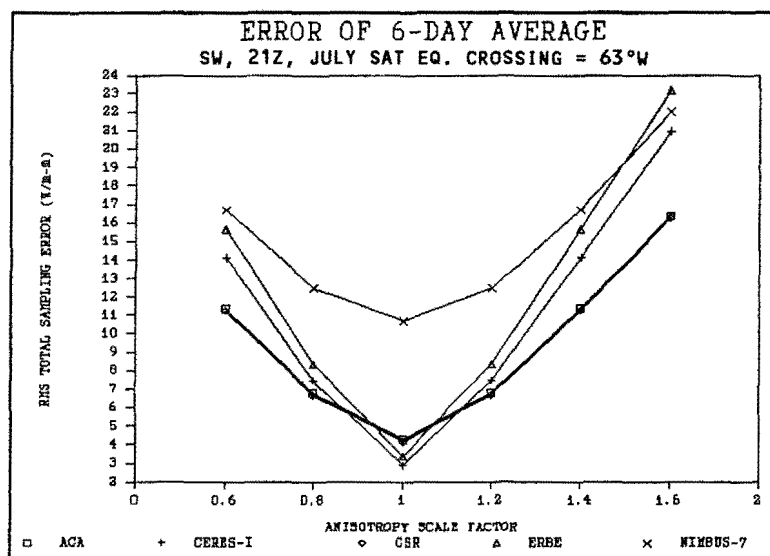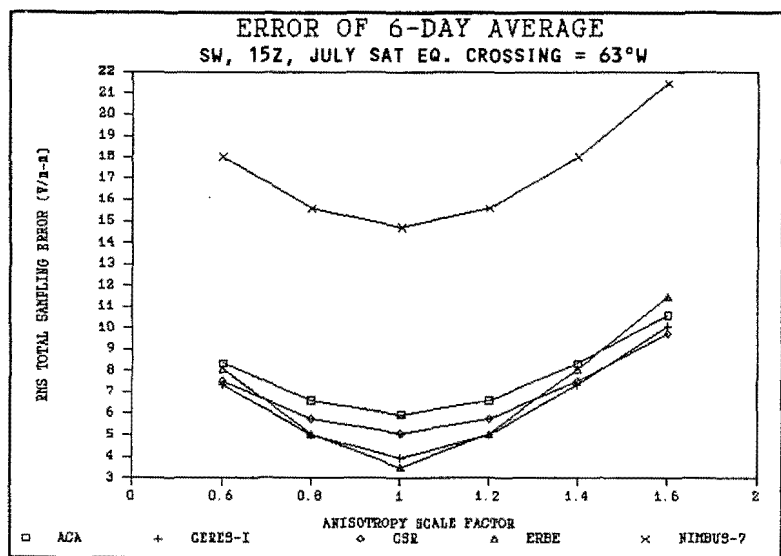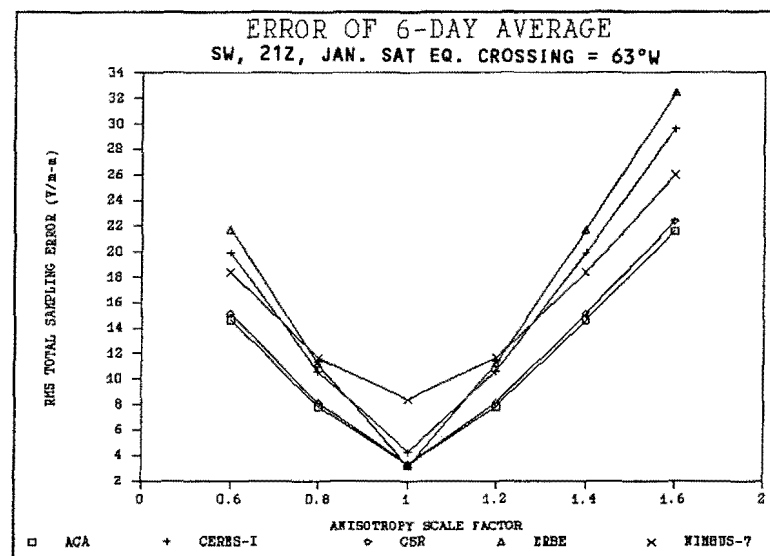
Figure 26a. Profiles of the six-day averaged total RMS sampling error (W/m²) for the TOA shortwave flux estimates as a function of anisotropic scale factor for 15Z and 21Z January and July at equator-crossing longitude of 109°W.
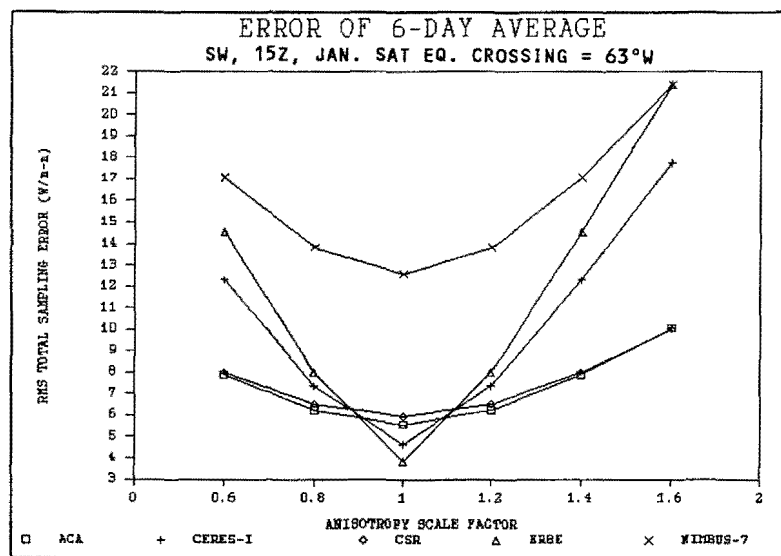
Figure 26b. Profiles of the six-day averaged total RMS sampling error (W/m^2) for the TOA shortwave flux estimates as a function of anisotropic scale factor for 15Z and 21Z January and July at equator-crossing longitude of 86°W.

ERROR OF 6-DAY AVERAGE
SW, 15Z, JAN. SAT EQ. CROSSING = 63°W

ERROR OF 6-DAY AVERAGE
SW, 21Z, JAN. SAT EQ. CROSSING = 63°W

ERROR OF 6-DAY AVERAGE
SW, 15Z, JULY SAT EQ. CROSSING = 63°W

ERROR OF 6-DAY AVERAGE
SW, 21Z, JULY SAT EQ. CROSSING = 63°W

Figure 26c. Profiles of the six-day averaged total RMS sampling error (W/m^2) for the TOA shortwave flux estimates as a function of anisotropic scale factor for 15Z and 21Z January and July at equator-crossing longitude of 63°W.

same error as an N=1 experiment, are plotted at N=1 and the angular modelling errors have an increased contribution as the scale factor departs from unity, according to Eq.(46).

A discussion of the total sampling error includes the competing effects of the spatial and angular error components. We have seen that, in general, cross-track scanners are better spatial samplers than their biaxial counterparts, but tend to accumulate greater angular sampling errors. These statements are supported in Figures 25 and 26 which summarizes the results of many anisotropic scaling experiments conducted at 21Z and using a 3:15 PM (fixed equator crossing at 86°W) local orbiting platform. Each of the five prototype radiometers was flown for each of six days in July 1983 including the 15th and 17th-21st days of the month and for January 25-30, 1984. RMS flux errors were obtained across the analysis field for each day and averaged over the six-day period. These values are taken to be representative of the typical daily RMS errors that can be attained by the individual instruments.

Immediately obvious from Figures 25 and 26 is that cross-track scanning radiometer error curves (CERES-I and ERBE) tend to cross those of biaxial scanners (ACA, CSR, and Nimbus-7) at some given value of the anisotropy scaling factor N. This result is a consequence of better sampling characteristics of the cross-track instruments in the limit where the ADM error vanishes. On the figure, this limit is nearly met at N=1 (i.e., no systematic departure from ERBE model) which then indicates the approximate magnitude of the spatial sampling error which cannot be represented in these figures. We recall that it is obtained from a unique simulation experiment in which both the reference field radiances and the satellite flux estimates are generated using isotropic ADMs. Thus, the spatial-only sampling error case corresponds to N=0 in both the reference field and satellite ADMs and cannot be represented by a point on these curves for which the data represent satellite retrievals with N=1. As N moves away from unity, the cross-track scanner angular modeling errors increase more rapidly than the biaxial instruments and eventually overtake them in their total error amounts.

Figures 27a and 27b present the bias between the satellite-observed and the reference shortwave flux. The bias is presented as a function of latitude for six days in January and July for an anisotropic perturbation N = 1.69. The two curves illustrate the biases for the ERBE cross-track scanner (ERBE) and the conically scanning radiometer (CSR). The ERBE results indicate a marked latitudinally dependent bias, with positive errors of 10 to 20 Wm^{-2} near the solar declination for each season. In the winter hemispheres (away from the Sun), the ERBE bias changes sign and reaches 10 Wm^{-2}. In contrast, the biases of the CSR estimates do not indicate a strong latitudinally dependent bias.

In the ERBE and other cross-track scanner designs, the viewing geometry is perpendicular to the subsatellite track. Every region sampled by the satellite is viewed from a single set of angles (satellite and solar zenith angles and, most importantly, relative azimuth). Typically, angular reflectance models exhibit the greatest departure from isotropy in the solar principal plane, and the least departures at azimuth angles perpendicular to this plane. Also, in this latter direction, the surface is reflecting less energy than an isotropic surface over a larger range of zenith angles than occurs in the principal plane, (cf. Figure 20). If the "real" reflectance of the scene is more anisotropic than the mean models used to convert from radiance to flux (i.e., N > 1), then the errors in the observed fluxes relative to the reference fluxes will generally be positive for observations in the principal plane, and negative for observations at azimuths more perpendicular to the principal plane. The latitudinal dependence of the ERBE bias can now be understood as the result of the scan plane rotating with respect to the solar principal plane as the satellite orbits. At latitudes near the solar declination, the scan plane is near the principal plane, so the error is positive. As the satellite enters the winter hemisphere, the scan plane rotates away from the principal plane, introducing negative biases.

Figure 27a. Six-day mean latitudinal bias of satellite-observed shortwave flux estimates for January. Error profiles are shown for the CSR (biaxial) and ERBE (cross-track) scanners for an N = 1.69 anisotropic Earth/atmosphere model at 21Z for a satellite Equator crossing at 86°W.
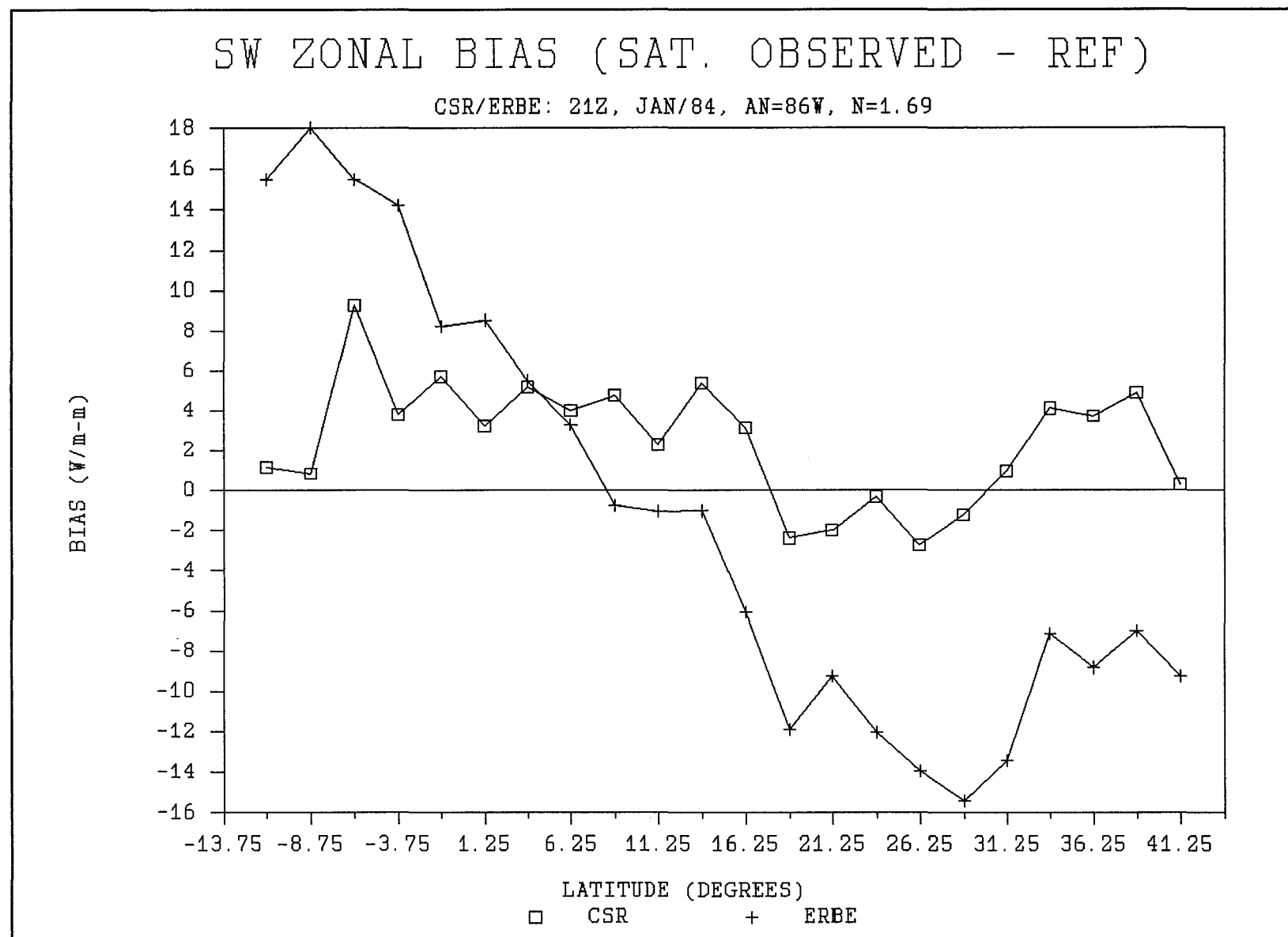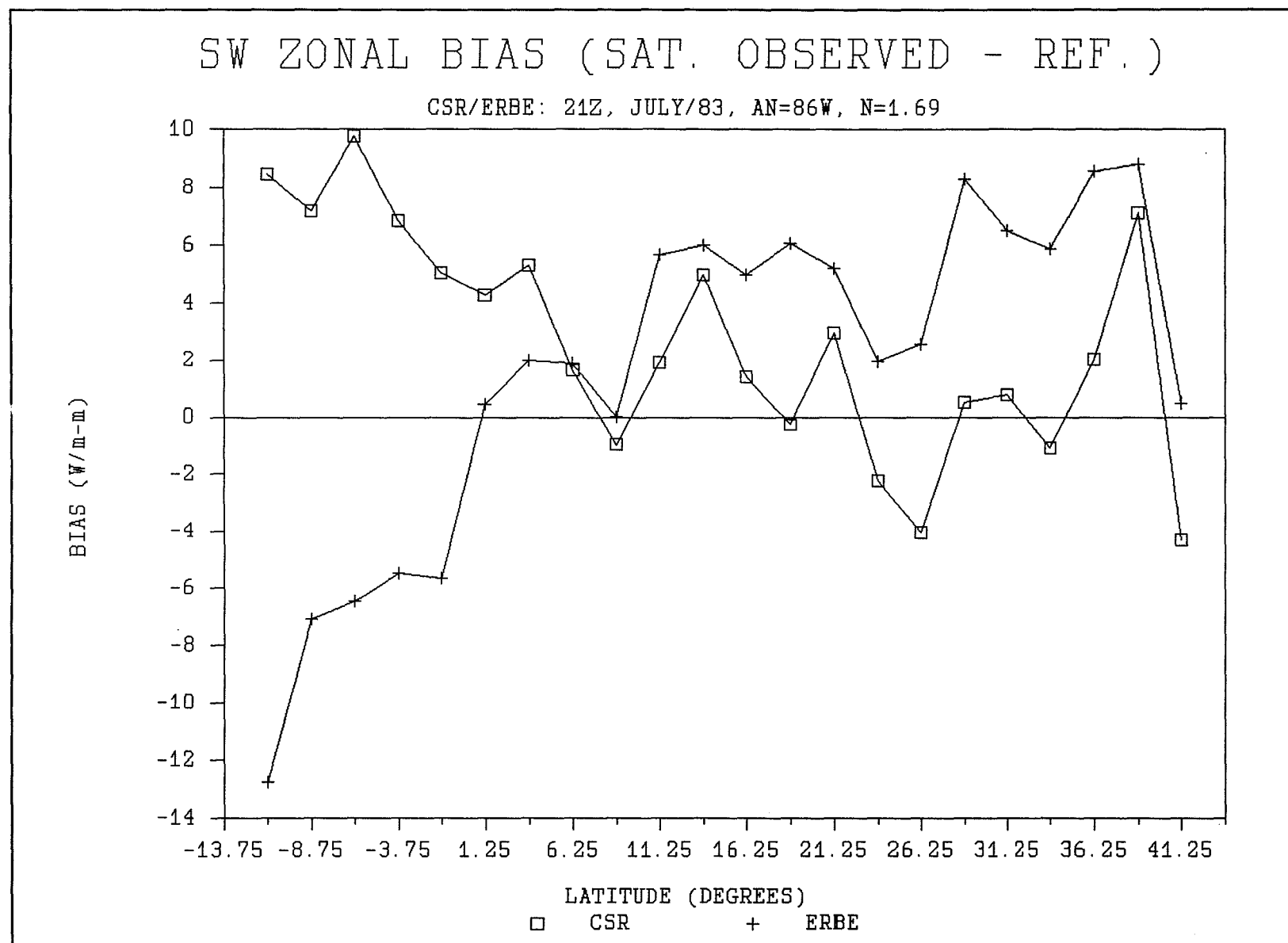
Figure 27b. Same as Figure 27a, but for July.

SW ZONAL BIAS (SAT. OBSERVED - REF.)

CSR/ERBE: 21Z, JULY/83, AN=86W, N=1.69

LATITUDE (DEGREES)

□   CSR   +   ERBE

The CSR, unlike ERBE, is able to view target regions at multiple azimuth angles within the same latitude zone. This capability allows a cancellation of anisotropic errors to take place as a target is viewed from ahead, the side, and the rear of the satellite. As a direct consequence, as illustrated in the figures, the CSR biases do not vary strongly with latitude. This feature is, in fact, a major strength of observations taken by CSR designs relative to cross-track scanners.

These same geometrical sampling differences between the ERBE and CSR-type instruments, in the presence of systematic angular model error, also cause generally greater variance in the bias for regions within a latitude zone for the cross-track scanner compared to the rotating azimuth scanner. This is shown in Figures 27c and 27d where the zonal standard deviations of regional bias error are plotted for January and July, respectively.

Figure 27c. Latitude variation of the standard deviation of daily regional satellite shortwave flux error. Curves are shown for the CSR (biaxial) and ERBE (cross-track) scanners for an N = 1.69 anisotropic Earth/atmosphere model at 21Z and for a satellite Equator crossing at 86°W.
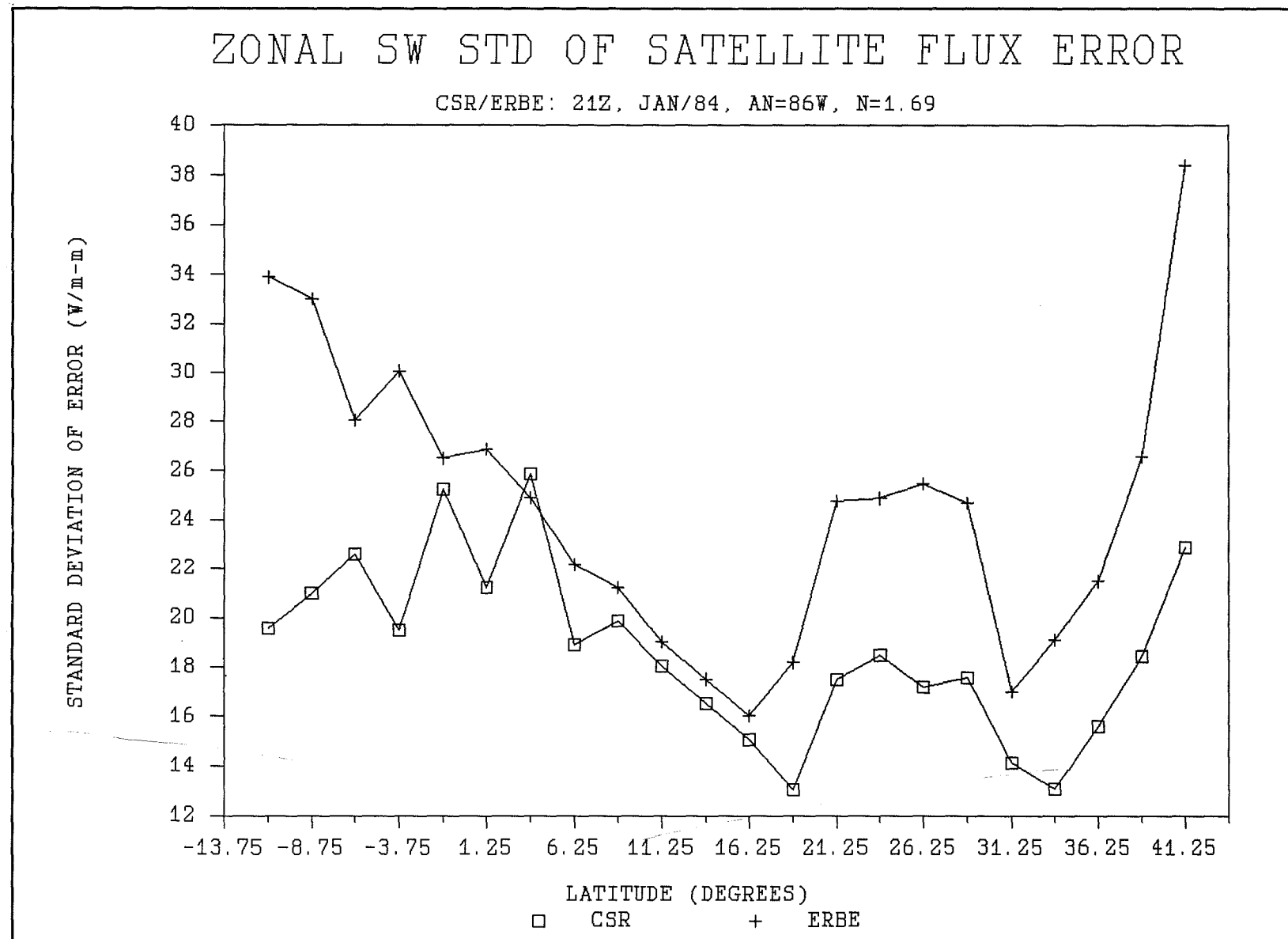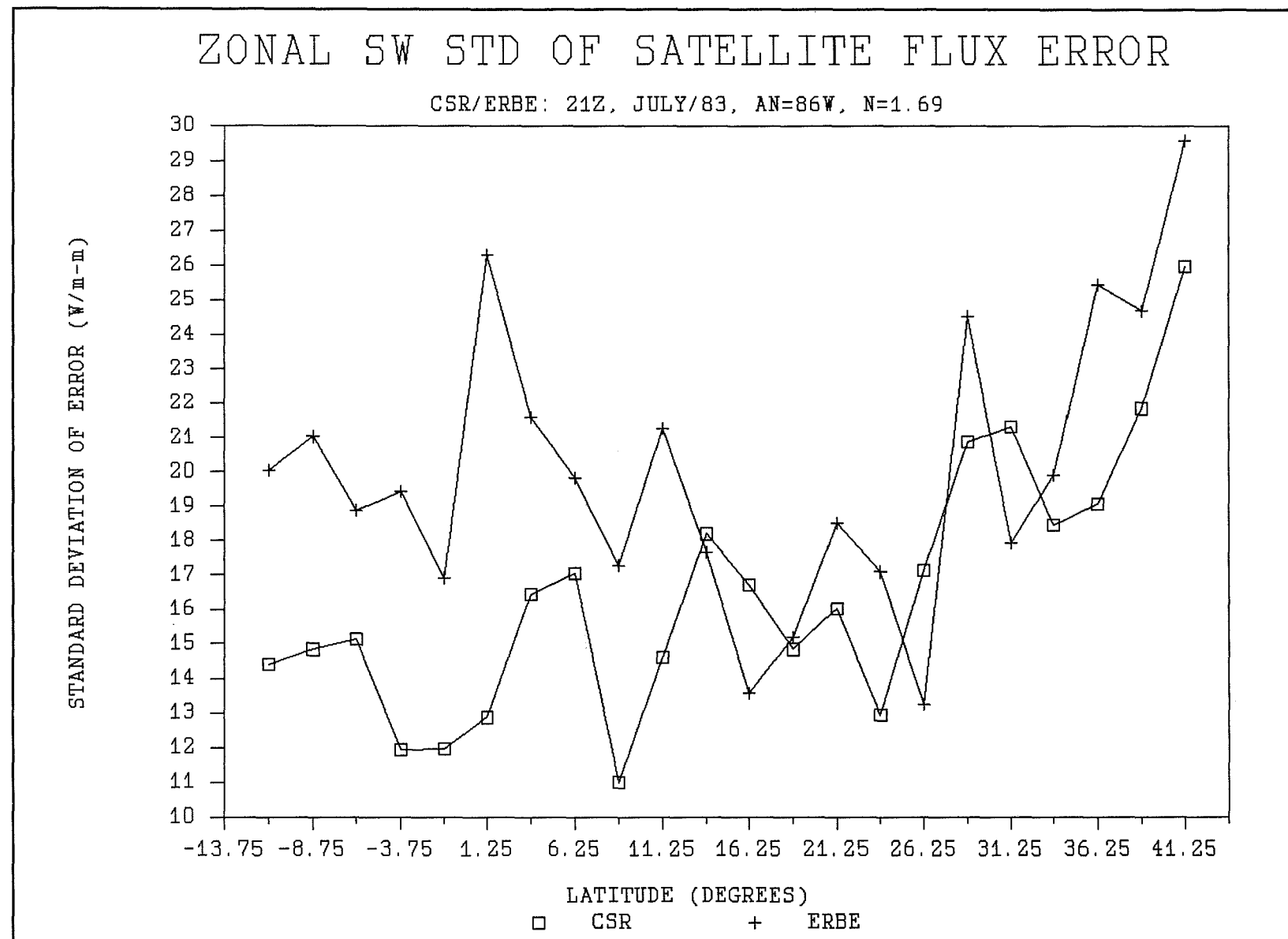
Figure 27d.   Same as Figure 27c, but for July.

ZONAL SW STD OF SATELLITE FLUX ERROR

CSR/ERBE: 21Z, JULY/83, AN=86W, N=1.69

4. CONCLUDING REMARKS

The two primary sources of error encountered in radiation budget measurements are caused by the non-uniform sampling of the radiance field at the TOA and by the use of incorrect ADM's in the inversion of the satellite altitude observations to TOA flux estimates. In the limit, where the ADM error vanishes (due to the assumption of correctly specified ADM's), the accuracy of each of the candidate scanner designs is determined by the instrument's ability to map out the TOA radiance field in a uniform manner. This lower limit can be improved through attention to the design of the scanning pattern, through the elimination of overlapping or widely scattered sensor footprints; alternatively, optimum time and space averaging schemes may be employed. As errors in the ADM's are encountered, the total error exceeds the minimum (spatial sampling) error. These additional errors are due to the fact that only a finite number of mean ADM's for broad scene categories may be used, while each scene realization is composed of a unique ADM. The problem is further compounded by the potential for scene misidentification, where an incorrect ADM will be assigned to the radiance inversion.

4.1 THE EFFECTS OF ADM ERROR

As errors in the ADM accumulate, the corresponding component of the error variance increases. In this study, ADM errors are specified by using mean statistical models and a linear relationship in terms of the degree of anisotropy. The rate of ADM error increase depends on the scanning pattern and the Earth-Sun-satellite geometry. A cross-track scanner in a near-noon orbit scans at relative azimuths to the Sun of 0° and 180° near the solar declination and toward higher latitudes a transition near 90° takes place. In the former, when the Earth scene is more anisotropic than assumed in the mean models, the limb radiance will be higher and the nadir radiance will be lower than the model. The scanner will then incur systematic underestimates (overestimates) in the fluxes from radiance observations in the nadir (limb) direction. A scanner that samples uniformly in all angles will benefit in the presence of ADM error through the cancellation of errors in targets where views are obtained from different look angles. We have shown two-axis scanning radiometers to be significantly less sensitive to ADM errors than a simple cross-track scanner. Instruments which offer angular coverage in both zenith and relative azimuth are approximately one-half as sensitive to ADM error as a simple cross-track scanner when instantaneous fluxes are considered for a single orbit.

4.2 THE EFFECTS OF SPATIAL SAMPLING ERROR

The measurement accuracy can be only as good as accuracy in the absence of ADM considerations. Here, the uniformity of mapping of the TOA radiances is crucial to an optimal set of measurements. The cross-track scanners (ERBE and CERES-I) do well in this regard and incur the lowest errors. It may, nevertheless, be possible to improve their minimum error limits through attention to the design of the viewing aperture, sampling rate, and processing techniques which eliminate overlapping or widely scattered observations within a 2.5° target area.

4.3 TRADEOFFS IN INSTRUMENT DESIGN

This study assumes that scanner measurement error can be summarized in terms of only two fundamental, instrument-dependent characteristics: spatial sampling error and ADM error. The ideal instrument would minimize both. The biaxial scanning radiometers have been shown to be significantly less sensitive to ADM errors than a simple cross-track scanner by providing cancellation of opposing ADM errors made at different viewing angles. Under conditions of large ADM variability, they will yield the least errors in retrieved TOA fluxes. Our results show, however, that cross-track scanners are likely to outperform biaxial and conical scanners, for Earth radiation budget measurements, providing that realistic anisotropy

scale factors for the atmosphere (N) do not exceed the range between 0.7 and 1.3 (error $\leq$ 30%). The Nimbus-7 ERB instrument, with its low data rate and nonuniform spatial coverage, yields the greatest spatial sampling error. This may be expected, however, because the scan design was not optimized for mapping the radiation budget but for the development of a first generation of ADMs. For this range of N values, the biaxial scanner designs yield RMS errors larger than (but close to) those of the cross-track scanners. As the two errors combine, the total RMS error increases, approaching the ADM asymptote for large ADM error. Clearly, the cross-track scanners do best in the absence of ADM error. However, in the presence of increasing error in the angular models, the biaxial scanners provide the best set of measurements. Based on our results, the selection of the optimum scanner design for ERBI involves a compromise between a cross-track scan pattern that uniformly maps the Earth's surface and evenly samples the incident radiances, and a circular or conical scan pattern that obtains multiple samples of a given region at various satellite zenith and relative azimuth angles to minimize ADM errors. Because the CERES instrument is composed of both a simple cross-track scanner and a second component that rotates the scan plane through 180° every 30 to 45 seconds, it contains elements of the optimal scanner design. The simple cross-track scanner provides the uniform spatial coverage required for small spatial sampling errors while the rotating azimuth plane radiometer assures greater angular coverage and reduced ADM errors. Results presented here indicate that, although total RMS errors for CERES are reduced below those for ERBE and the biaxial scanners for N < 1.3, they grow with increasing N at a faster rate than errors for the ACA or CSR. For values of N > 1.3, the CERES performs better than ERBE, but being a compromise design, it may no longer be the minimum-error design.

4.4 ISSUES RELATED TO ADM ERROR MAGNITUDES

A key issue that must be considered in interpreting the simulation results is the amount of systematic ADM variability (departures from the mean models) that is truly present at 2.5° regional resolution. Indications of the error magnitudes can be obtained from the ERBE models themselves by imposing systematic misclassifications by one scene class (e.g., clear versus partly cloudy, partly cloudy versus mostly cloudy, etc.). We performed this exercise for both overestimations and underestimations of the cloud amount and found that systematic, long-term errors in the amount of anisotropy of 20% are likely. Also, the error analysis of ERBE scanner data (Barkstrom et al., 1989) is consistent with ADM errors of less than 30%. Random components of the resultant ADM error (over small spatial or temporal scales) cancel quickly and are unimportant. When target fluxes, observed from six days of orbits with the same equator crossing longitude, are averaged before being statistically analyzed, it is found that the spatial sampling errors decrease almost as if they were random (i.e., 80% of the square root of the number of days sampled, implying that daily observations are very nearly linearly independent and uncorrelated), while the ADM errors decrease, but by a lesser amount. However, in six consecutive days, satellite orbits systematically move in equator-crossing longitude, by about 2° to 3° per day. Since the ADM errors are usually systematically of opposite signs near nadir and near the limb, ADM errors will tend to cancel when averaged over six consecutive days. This will be studied as part of our next phase of this simulation work, where the error in the diurnally averaged radiation budget parameters will be evaluated.

4.5 INSTRUMENT RECOMMENDATIONS

If systematic ADM errors are indeed less than 30%, the CERES-I, ERBE and CSR, in order of increasing error, provide the most accurate instantaneous flux estimates, within 2 to 3 W/m² of each other. However, the magnitude of this error is right at the 10 W/m² accuracy requirement of the user community (NOAA, 1988). Therefore, in order to more confidently satisfy this requirement, it may be necessary to modify these instruments' scan and field-of-view designs, and/or the data processing software system, with the specific objective of reducing the sampling error, which dominates the ADM error.

More advanced data processing algorithms, such as methods which fit a functional surface representation of the measured field and integrate the fitted function over the grid cell, offer the potential for further improvement of the radiation budget estimates. While this enhancement may require a matrix inversion for each of 10,000 regions observed daily for each wavelength sampled, the sizing of a slightly more powerful computer for the data processing may in fact offer a highly cost-effective alternative or complement to further refinement of the instruments' designs.

4.6 SUMMARY

Identical studies of instantaneous error have been completed for many days, two seasons, and several satellite equator crossing longitudes. These results are all consistent with the above conclusions. Also, the longwave flux errors have been found to have the same space and time characteristics as for the shortwave fluxes, but the errors are only about 25% of the shortwave errors.

Instantaneous flux errors are composed of non-uniform spatial sampling and ADM variability errors. Cross-track scanners have least spatial sampling error, but are most sensitive to ADM variability. The effects of ADM variability, at the 10-km scale, cancel when random, but do not cancel when systematic. For biaxial scanners, spatial sampling dominates ADM variability errors for all N values tested. However, for cross-track scanners, the above is only true for N values between 0.7 and 1.3. Thus, optimum scanner design critically depends on the N value which represents true ADM variability. Shortwave spatial sampling errors are at the limit of user accuracy requirements (10 W/m^2). Therefore, future ERBI system designs should emphasize minimizing non-uniform spatial sampling error.

REFERENCES

Barkstrom, B., E. Harrison, L. Smith, R. Green, J. Kibler, R. Cess, and the ERBE Science Team, 1989: Earth Radiation Budget Experiment (ERBE) Archival and April 1985 Results, *Bull. Amer. Meteor. Soc.*, **70**, 1254-1262.

Barkstrom, B. R., 1984: The Earth Radiation Budget Experiment (ERBE), *Bull. Amer. Meteor. Soc.*, **65**, 1170-1185.

Green, R. N., 1980: The Effect of Directional Radiation Models on the Interpretation of Earth Radiation Budget Measurements, *J. Atmos. Sci.*, **37**, 2298-2313.

Hoffman, J., 1989: New Sensor Monitors Earth's Energy Budget, Photonics Spectra, pp. 147.

Jacobowitz, H., L. L. Stowe, and J. R. Hickey, 1978: The Nimbus-7 User's Guide, NASA, Greenbelt, MD 20771, 33-69.

Krishnamurti, T. N., H. S. Bedi, K. Engels, A. Weiner, K. Kuma, K. Canpana, and L. Kimoto, 1988: Comparison of Cloud Cover From General Circulation Models and ISCCP Data Sets, Report prepared for the Fourth CAS/JSC Working Group on Numerical Experimentation, WMO, Toronto, 68 pages.

Minnis, P., and E. F. Harrison, 1984a: Diurnal Variability of Regional Cloud and Surface Radiative Parameters Derived From GOES Data, III, November 1978 radiative parameters, *J. Clim. Appl. Meteor.*, **23**, 1032-1051.

Minnis, P. and E. F. Harrison, 1984b: Diurnal Variability of Regional Cloud and Surface Radiative Parameters Derived From GOES Data, I, Analysis Method, *J. Clim. Appl. Meteorol.*, **23**, 993-1011.

Muench, H. Stuart, 1981: Calibration of Geosynchronous Satellite Video Sensors, Air Force Geophysics Laboratory, Report AFGL-TR-81-0050, pp. 25.

NOAA, 1988: Report of the Earth Radiation Budget Requirements Review - 1987. L. L. Stowe, Editor, NOAA Tech. Rept. NESDIS-41, U.S. Dept. of Commerce, Washington, DC, 119 pages.

Raschke, E., T. H. Vonder Haar, M. Pasternak, and W. R. Bandeen, 1973: The Radiation Balance of the Earth-Atmosphere System From Nimbus-3 Radiation Measurements, NASA TN D-7249, 73, pp. [NTIS-N73-21702].

Rossow, W. B., F. Mosher, E. Kinsella, A. Arking, M. Desbois, E. Harrison, P. Minnis, E. Ruprecht, G. Seze, C. Simmer, and E. Smith, 1985: ISCCP Cloud Algorithm Intercomparison, *J. Clim. Appl. Meteor.*, **24**, 877-903.

SBRC, 1980: Visible Infrared Spin-Scan Radiometer Atmosphere Sounder (VAS) for a Geostationary Operational Environmental Satellite (GOES), Volume 1, Sections 1 through 5, VAS-E GOES Data Book, prepared under Contract No. NAS5-24342 (HAC PA 44-10899A, Div. 44) for NASA/Goddard Space Flight Center, Greenbelt, MD 20771.

Smith, E. A. and D. R. Phillips, 1972: Autoamted Cloud Tracking Using Precisely Aligned Digital ATS Pictures, IEEE Transactions on Computers, Vol. C-21, No. 7, 715-729.

Stowe, L. L., P. Ardanuy, R. Hucek, P. Abel, and H. Jacobowitz, 1988: Evaluating the Design of Satellite Scanning Radiometers for Earth's Radiation Budget Measurements with Computer Simulations, IRS, Lille, France, Deepak Publishing, 232-235.

Suttles, J. T., R. N. Green, P. Minnis, G. L. Smith, W. F. Staylor, B. A. Wielicki, I. J. Walker, D. F. Young, V. R. Taylor, and L. L. Stowe, 1988: Angular Radiation Models for the Earth-Atmosphere System, Volume I: Shortwave Radiation, NASA RP 1184, 147 pp.

Suttles, J. T., R. N. Green, G. L. Smith, B. A. Wielicki, I. J. Walker, V. R. Taylor, and L. L. Stowe, 1989: Angular Radiation Models for the Earth-Atmosphere System, Volume II: Longwave Radiation, NASA RP 1184, 87 pp.

Taylor, V. R. and L. L. Stowe, 1984: Reflectance Characteristics of Uniform Earth and Cloud Surfaces Derived From Nimbus-7 ERB, *J. Geophys. Res.*, **89**, 4987-4996.

Taylor, V. R. and L. L. Stowe, 1986: Revised Reflectance and Emission Models From Nimbus-7 ERB Data, Extended Abstracts, *Sixth Conf. on Atmospheric Radiation*, Williamsburg, Amer. Meteor. Soc., J19-J22.

Wielicki, B. A. and R. N. Green, 1989: Cloud Identification for ERBE Radiative Flux Retrieval, *J. Appl. Meteor.*, **28**, 1131-1146.

Wirth, J., E. Raschke, B. Bauche, and D. Hennings, 1986: Measurement of Radiative Properties Using the Conical Scan Radiometer, Institut für Geophysik und Meteorologie, University of Cologne, Kerpener Str. 13, D-5000 Köln 41, Germany, 7 pages.

(continued from inside cover)

NESDIS 26 Monthly and Seasonal Mean Outgoing Longwave Radiation and Anomalies. Arnold Gruber, Marylin Varnadore, Phillip A. Arkin and Jay S. Winston, October 1987. (PB87 160545/AS)

NESDIS 27 Estimation of Broadband Planetary Albedo from Operational Narrowband Satellite Measurements. James Wydick, April 1987. (PB88 107644/AS)

NESDIS 28 The AVHRR/HIRS Operational Method for Satellite Based Sea Surface Temperature Determination. Charles Walton, March 1987. (PB88 107594/AS)

NESDIS 29 The Complementary Roles of Microwave and Infrared Instruments in Atmospheric Sounding. Larry McMillin, February 1987. (PB87 184917/AS)

NESDIS 30 Planning for Future Generational Sensors and Other Priorities. James C. Fisher, June 1987. (PB87 220802/AS)

NESDIS 31 Data Processing Alogorithms for Inferring Stratospheric Gas Concentrations from Balloon-Based Solar Occultation Data. I-Lok Chang (American University) and Michael P. Weinreb, April 1987. (PB87 196424)

NESDIS 32 Precipitation Detection with Satellite Microwave Data. Yang Chenggang and Andrew Timchalk, June 1988. (PB88 240239)

NESDIS 33 An Introduction to the GOES I-M Imager and Sounder Instruments and the GVAR Retransmission Format. Raymond J. Komajda (Mitre Corp) and Keith McKenzie, October 1987. (PB88 132709)

NESDIS 34 Balloon-Based Infrared Solar Occultation Measurements of Stratospheric O3, H20, HNo3, and CF2C12. Michael P. Weinreb and I-Lok Chang (American University), September 1987. (PB88 132725)

NESDIS 35 Passive Microwave Observing From Environmental Satellites, A Status Report Based on NOAA's June 1-4, 1987, Conference in Williamsburg, VA. James C. Fisher, November 1987. (PB88 208236)

NESDIS 36 Pre-Launch Calibration of Channels 1 and 2 of the Advanced Very High Resolution Radiometer. C. R. Nagaraja Rao, October 1987. (PB88 157169/AS)

NESDIS 39 General Determination of Earth Surface Type and Cloud Amount Using Multispectral AVHRR Data. Irwin Ruff and Arnold Gruber, February 1988. (PB88 199195/AS)

NESDIS 40 The GOES I-M System Functional Description. Carolyn Bradley (Mitre Corp), November 1988.

NESDIS 41 Report of the Earth Radiation Budget Requirements Review - 1987, Rosslyn, VA, 30 March-3 April 1987. Larry L. Stowe (Editor), June 1988.

NESDIS 42 Simulation Studies of Improved Sounding Systems. H. Yates, D. Wark, H. Aumann, N. Evans, N. Phillips, J. Sussking, L. McMillin, A. Goldman, M. Chahine and L. Crone, February 1989.

NESDIS 43 Adjustment of Microwave Spectral Radiances of the Earth to a Fixed Angle of Progagation. D. Q. Wark, December 1988. (PB89 162556/AS)

NESDIS 44 Educator's Guide for Building and Operating Environmental Satellite Receiving Stations. R. Joe Summers, Chambersburg Senior High, February 1989.

NESDIS 45 Final Report on the Modulation and EMC Consideration for the HRPT Transmission System in the Post NOAA-M Polar Orbiting Satellite ERA. James C. Fisher (Editor), June 1989. (PB89 223812/AS)

NESDIS 46 MECCA Program Documentation. Kurt W. Hess, September 1989.

NESDIS 47 A General Method of Using Prior Information in a Simultaneous Equation System. Lawrence J. Crone, David S. Crosby and Larry M. McMillin, October 1989.

NESDIS 49 Implementation of Reflectance Models in Operatioal AVHRR Radiation Budget Processing. V. Ray Taylor, February 1990.

NESDIS 50 A Comparison of ERBE and AVHRR Longwave Flux Estimates. A. Gruber, R. Ellingson, P. Ardanuy, M. Weiss, S. K. Yang, (Contributor: S.N. Oh).

NESDIS 51 The Impact of NOAA Satellite Soundings on the Numerical Analysis and Forecast System of the People's Republic of China. A. Gruber and W. Zonghao, May 1990.

NESDIS 52 Baseline Upper Air Network (BUAN) Final Report. A. L. Reale, H. E. Fleming, D. Q. Wark, C. S. Novak, F. S. Zbar, J. R. Neilon, M. E. Gelman and H. J. Bloom, October 1990.

NESDIS 53 NOAA-9 Solar Backscatter Ultraviolet (SBUV/2) Instrument and Derived Ozone Data: A Status Report Based on a Review on January 29, 1990. Walter G. Planet, June 1990.

NESDIS 54 Evaluation of Data Reduction and Compositing of the NOAA Global Vegetation Index Product: A Case Study. K. P. Gallo and J. F. Brown, July 1990.

NESDIS 55 Report of the Workshop on Radiometric Calibration of Satellite Sensors of Reflected Solar Radiation, March 27-28, 1990, Camp Springs, MD. Peter Abel (Editor), July 1990.

NESDIS 56 A Noise Level Analysis of Special 10-Spin-Per-Channel VAS Data. Donald W. Hillger, James F. W. Purdom and Debra A. Lubich, February 1991.

NESDIS 57 Water Vapor Imagery Interpretation and Applictions to Weather Analyis and Forecasting. Roger B. Weldon and Susan J. Holmes, April 1991.

NOAA SCIENTIFIC AND TECHNICAL PUBLICATIONS

The National Oceanic and Atmospheric Administration was established as part of the Department of Commerce on October 3, 1970. The mission responsibilities of NOAA are to assess the socioeconomic impact of natural and technological changes in the environment and to monitor and predict the state of the solid Earth, the oceans and their living resources, the atmosphere, and the space environment of the Earth.

The major components of NOAA regularly produce various types of scientific and technical information in the following kinds of publications:

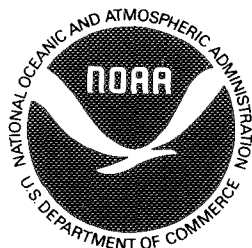PROFESSIONAL PAPERS - Important definitive research results, major techniques, and special investigations.

CONTRACT AND GRANT REPORTS - Reports prepared by contractors or grantees under NOAA sponsorship.

ATLAS - Presentation of analyzed data generally in the form of maps showing distribution of rainfall, chemical and physical conditions of oceans and atmosphere, distribution of fishes and marine mammals, ionospheric conditions, etc.

TECHNICAL SERVICE PUBLICATIONS - Reports containing data, observations, instructions, etc. A partial listing includes data serials; prediction and outlook periodicals; technical manuals, training papers, planning reports, and information serials; and miscellaneous technical publications.

TECHNICAL REPORTS - Journal quality with extensive details, mathematical developments, or data listings.

TECHNICAL MEMORANDUMS - Reports of preliminary, partial, or negative research or technology results, interim instructions, and the like.